



Université  
de Toulouse

# THÈSE

En vue de l'obtention du

## DOCTORAT DE L'UNIVERSITÉ DE TOULOUSE

**Délivré par :**

Institut National Polytechnique de Toulouse (Toulouse INP)

**Discipline ou spécialité :**

Signal, Image, Acoustique et Optimisation

---

**Présentée et soutenue par :**

Mme YANNA CRUZ CAVALCANTI

le mercredi 31 octobre 2018

**Titre :**

Factor analysis of dynamic PET images

---

**Ecole doctorale :**

Mathématiques, Informatique, Télécommunications de Toulouse (MITT)

**Unité de recherche :**

Institut de Recherche en Informatique de Toulouse (I.R.I.T.)

**Directeur(s) de Thèse :**

M. NICOLAS DOBIGEON

M. CLOVIS TAUBER

**Rapporteurs :**

Mme IRÈNE BUVAT, CNRS PARIS

M. SAID MOUSSAOUI, ECOLE CENTRALE NANTES

**Membre(s) du jury :**

M. CHRISTIAN JUTTEN, UNIVERSITE JOSEPH FOURIER, Président

M. ANTOINE SOULOUMIAC, CEA SACLAY, Membre

M. CLOVIS TAUBER, UNIVERSITE DE TOURS, Membre

Mme CAROLINE PETITJEAN, UNIVERSITE DE ROUEN, Membre

M. NICOLAS DOBIGEON, INP TOULOUSE, Membre

M. SIMON STUTE, CEA GRENOBLE, Invité

M. THOMAS OBERLIN, INP TOULOUSE, Membre



*A Deus, por sua generosidade nas bênçãos que me concede.  
À minha mãe, por me dar a vida e me permitir vivê-la em plenitude.  
Ao meu marido Vinicius, que esteve ao meu lado em cada passo  
dessa longa jornada pelo conhecimento.*

*“Tudo posso naquele que me fortalece.” Filipenses 4:13*



# Acknowledgments

The journey in the search for knowledge is challenging and everlasting. It often requires effort, commitment, persistence and a lot of resilience. My journey has only just begun, but a big step has definitely been taken. The obstacles that have come into my way until this day could never be overcome without the support and encouragement of the people there are to be referred to.

First and foremost, I would like to express my sincere gratitude to my supervisors Dr Nicolas Dobigeon, Dr Clovis Tauber and Dr Thomas Oberlin for giving me the opportunity to achieve this Ph.D. thesis. I am also thankful for their guidance, patience, constructive criticism and advice, which have enabled me to complete this project successfully. Additionally, I would like to acknowledge the bureaucratic support from Dr Dobigeon in my arrival in France and many other moments throughout this Ph.D. Dr Dobigeon has also been my professor during graduation and has inspired me with his knowledge to pursue research. Along with Dr Clovis Tauber, he gave me my first professional opportunity in a short internship at IRIT in 2012, for which I am truly grateful to both of them.

For this dissertation, I would like to thank Dr Irène Buvat and Dr Said Moussaoui for taking the time, despite their busy schedules, to study my work and report on my thesis. I would also like to thank Dr Christian Jutten for accepting to chair my jury and the board of examiners, Dr Caroline Petitjean and Dr Antoine Souloumiac, for their time and insightful questions. Additionally, I thank Dr Simon Stute for accepting the invitation to attend my thesis defence and providing me with the datasets that I needed for my simulations.

This thesis work would not have been successful without the scientific collaboration of many people. In particular, I would like to thank Dr Cédric Févotte and Dr Vinicius Ferraris for the stimulating discussions.

I gratefully acknowledge the funding sources that made my Ph.D. work possible. I was funded by the Brazilian Ministry of Education in a 3-year international doctorate program. I hope to have the opportunity of bringing back to Brazil all the knowledge and experience that I have acquired in France since my graduation (also financed by the Brazilian government). I believe that science and technology have the power of changing the world. My main goal in everything that I have done so far is to be able to improve people's lives through knowledge. Thus, I hope with all my heart to have the opportunity to bring science to people, allowing technology to change their lives through my work.

Moreover, I thank the help and support of IRIT secretaries, Mrs Sylvie Armengaud, Mrs Sylvie Eichen,

---

Mrs Annabelle Sansus and Mrs Isabelle Vasseur that do a remarkable work for all IRIT members. I would also like to thank all the members of the SC group that have contributed immensely to my personal and professional time at IRIT. I thank my past and current fellow labmates: Adrien, Louis, Olivier, Dylan, Mouna, Jessica, Pierre-Antoine, Tatsumi, Etienne and Baha for the enormous support, great conversations and pleasant companionships. I could not also forget all the other past and current members of the SC group: Sébastien, Marie, Herwig, Charly, Benoît, Claire, Yassine, Alberto, Maxime and Dana. I would also like to thank the members of the Inserm laboratory for their hospitality during my short stay at Tours.

Above all, I would like to thank my family for all their love and encouragement. I thank my parents, Lucimar e Yêso, who supported me in all my pursuits. Their constant love and encouragement is the foundation on which everything else is built. I thank my grandmother Paulina for her love and prayers. Finally, I thank my loving, encouraging, and patient husband Vinicius whose faithful support kept me going. To all of you, I dedicate this thesis.

# Abstract

Thanks to its ability to evaluate metabolic functions in tissues from the temporal evolution of a previously injected radiotracer, dynamic positron emission tomography (PET) has become an ubiquitous analysis tool to quantify biological processes. Several quantification techniques from the PET imaging literature require a previous estimation of global time-activity curves (TACs) (herein called *factors*) representing the concentration of tracer in a reference tissue or blood over time. To this end, factor analysis has often appeared as an unsupervised learning solution for the extraction of factors and their respective fractions in each voxel.

Inspired by the hyperspectral unmixing literature, this manuscript addresses two main drawbacks of general factor analysis techniques applied to dynamic PET. The first one is the assumption that the elementary response of each tissue to tracer distribution is spatially homogeneous. Even though this homogeneity assumption has proven its effectiveness in several factor analysis studies, it may not always provide a sufficient description of the underlying data, in particular when abnormalities are present. To tackle this limitation, the models herein proposed introduce an additional degree of freedom to the factors related to specific binding. To this end, a spatially-variant perturbation affects a nominal and common TAC representative of the high-uptake tissue. This variation is spatially indexed and constrained with a dictionary that is either previously learned or explicitly modelled with convolutional nonlinearities affecting non-specific binding tissues. The second drawback is related to the noise distribution in PET images. Even though the positron decay process can be described by a Poisson distribution, the actual noise in reconstructed PET images is not expected to be simply described by Poisson or Gaussian distributions. Therefore, we propose to consider a popular and quite general loss function, called the  $\beta$ -divergence, that is able to generalize conventional loss functions such as the least-square distance, Kullback-Leibler and Itakura-Saito divergences, respectively corresponding to Gaussian, Poisson and Gamma distributions. This loss function is applied to three factor analysis models in order to evaluate its impact on dynamic PET images with different reconstruction characteristics.

**Keywords:** dynamic PET images, blind source separation, unsupervised learning, non-convex optimization, majorization-minimization algorithms.





# Résumé

La tomographie par émission de positrons (TEP) est une technique d'imagerie nucléaire non-invasive qui permet de quantifier les fonctions métaboliques des organes à partir de la diffusion d'un radiotraceur injecté dans le corps. Alors que l'imagerie statique est souvent utilisée afin d'obtenir une distribution spatiale de la concentration du traceur, une meilleure évaluation de la cinétique du traceur est obtenue par des acquisitions dynamiques. En ce sens, la TEP dynamique a suscité un intérêt croissant au cours des dernières années, puisqu'elle fournit des informations à la fois spatiales et temporelles sur la structure des prélèvements de traceurs en biologie *in vivo*. Les techniques de quantification les plus efficaces en TEP dynamique nécessitent souvent une estimation de courbes temps-activité (CTA) de référence représentant les tissus ou une fonction d'entrée caractérisant le flux sanguin. Dans ce contexte, de nombreuses méthodes ont été développées pour réaliser une extraction non-invasive de la cinétique globale d'un traceur, appelée génériquement analyse factorielle.

L'analyse factorielle est une technique d'apprentissage non-supervisée populaire pour identifier un modèle ayant une signification physique à partir de données multivariées. Elle consiste à décrire chaque voxel de l'image comme une combinaison de signatures élémentaires, appelées *facteurs*, fournissant non seulement une CTA globale pour chaque tissu, mais aussi un ensemble des coefficients reliant chaque voxel à chaque CTA tissulaire. Parallèlement, le démelange - une instance particulière d'analyse factorielle - est un outil largement utilisé dans la littérature de l'imagerie hyperspectrale. En imagerie TEP dynamique, elle peut être très pertinente pour l'extraction des CTA, puisqu'elle prend directement en compte à la fois la non-négativité des données et la somme-à-une des proportions de facteurs, qui peuvent être estimées à partir de la diffusion du sang dans le plasma et les tissus.

Inspiré par la littérature de démelange hyperspectral, ce manuscrit s'attaque à deux inconvénients majeurs des techniques générales d'analyse factorielle appliquées en TEP dynamique. Le premier est l'hypothèse que la réponse de chaque tissu à la distribution du traceur est spatialement homogène. Même si cette hypothèse d'homogénéité a prouvé son efficacité dans plusieurs études d'analyse factorielle, elle ne fournit pas toujours une description suffisante des données sous-jacentes, en particulier lorsque des anomalies sont présentes. Pour faire face à cette limitation, les modèles proposés ici permettent un degré de liberté supplémentaire aux facteurs liés à la liaison spécifique. Dans ce but, une perturbation spatialement variante est introduite en complément d'une CTA nominale et commune. Cette variation est indexée spatialement et contrainte avec un dictionnaire,

---

qui est soit préalablement appris ou explicitement modélisé par des non-linéarités convolutives affectant les tissus de liaisons non-spécifiques. Le deuxième inconvénient est lié à la distribution du bruit dans les images PET. Même si le processus de désintégration des positrons peut être décrit par une distribution de Poisson, le bruit résiduel dans les images TEP reconstruites ne peut généralement pas être simplement modélisé par des lois de Poisson ou gaussiennes. Nous proposons donc de considérer une fonction de coût générique, appelée  $\beta$ -divergence, capable de généraliser les fonctions de coût conventionnelles telles que la distance euclidienne, les divergences de Kullback-Leibler et Itakura-Saito, correspondant respectivement à des distributions gaussiennes, de Poisson et Gamma. Cette fonction de coût est appliquée à trois modèles d'analyse factorielle afin d'évaluer son impact sur des images TEP dynamiques avec différentes caractéristiques de reconstruction.

**Mots-clés:** images TEP dynamiques, séparation aveugle des sources, apprentissage non supervisé, optimisation non convexe, algorithmes de majoration-minimisation.



---

# Abbreviations

ADMM	Alternated direction method of multipliers
ANC	Abundance nonnegativity constraint
ASC	Abundance sum-to-one constraint
AUC	Area under the curve
BCCB	Block circulant matrix with circulant blocks
BCD	Block-coordinate descent
BCM	Beta compositional model
BPT	Binary partition trees
BSS	Blind source separation
CAPES	Coordenação de Aperfeiçoamento de Ensino Superior
CLS	Constrained least squares
CLT	Central limit theorem
CM	Compartmental modelling
CT	Computed tomography
DPE	Doutorado Pleno no Exterior
ECG	Electrocardiograms
EEG	Electroencephalograms
ELMM	Extended linear mixing model
EM	Expectation maximization
EMG	Electromyograms
FADS	Factor analysis of dynamic structures
FBP	Filtered-back projection
FCLS	Fully constrained least squares
fMRI	Functional magnetic resonance imaging
FOV	Field-of-view
FRTM	Full reference tissue compartment model

---

GNCM	Generalized normal compositional models
ICA	Independent component analysis
INSERM	Institut National de la Santé et de la Recherche Médicale
KL	Kullback-Leibler
LMM	Linear mixing models
LOR	Line-of-response
LRM	Local reference model
MLE	Maximum likelihood estimators
MM	Maximization-minimization
MNF	Minimum noise fraction
MRI	Magnetic resonance image
NCM	Normal compositional models
NMF	Nonnegative matrix factorization
NMSE	Normalized mean square error
nSB	Non-specific binding
OSEM	Ordered subset expectation maximization
OSP	Orthogonal subspace projection
PALM	Proximal alternating linearized minimization
PCA	Principal component analysis
PET	Positron emission tomography
PLMM	Perturbed linear mixing model
PNMM	Parametrically nonlinear mixing model
PSF	Point spread function
PSNR	Peak signal-to-noise ratio
PVE	Partial volume effect
Q-Q	Quantile-Quantile
rLMM	Robust linear mixing model
rNMF	Robust nonnegative matrix factorization
ROI	Regions-of-interest
SB	Specific binding

SBF	Specific binding factor
SLMM	Specific binding linear mixing model
SUnSAL	Sparse unmixing by variable splitting and augmented Lagrangian
SUV	Standardized uptake value
SVCA	Supervised cluster analysis
SVD	Singular value decomposition
SVM	Support vector machine
TAC	Time-activity curve
TOF	Time-of-flight
TSPO	Translocator protein
VCA	Vertex component analysis

# Contents

<b>Introduction</b>	<b>1</b>
<b>I General context</b>	<b>7</b>
<b>1 Dynamic Positron Emission Tomography</b>	<b>9</b>
1.1 Positron Emission Tomography (PET): a brief overview . . . . .	10
1.2 Physical principles of acquisition . . . . .	10
1.2.1 Radioisotopes . . . . .	10
1.2.2 Positron decay in PET . . . . .	12
1.2.3 Coincidence detection . . . . .	13
1.2.4 Time-of-flight . . . . .	15
1.2.5 Photon-tissue interaction . . . . .	15
1.3 Reconstruction and corrections . . . . .	16
1.3.1 Reconstruction process . . . . .	16
1.3.2 Standard corrections . . . . .	18
1.4 Dynamic PET imaging . . . . .	19
1.5 Properties of PET images . . . . .	20
1.5.1 Partial volume effect . . . . .	21
1.5.2 Noise . . . . .	22
1.6 Quantification . . . . .	23

1.6.1	Standardized uptake value (SUV)	23
1.6.2	Parametric imaging methods	24
1.6.3	Challenges of quantification	30
1.7	Conclusion	31
<b>2</b>	<b>Blind source separation in multi-band imaging</b>	<b>33</b>
2.1	From non-parametric methods to factor analysis in dynamic PET	34
2.2	A brief overview on blind source separation (BSS)	35
2.2.1	Linear model	38
2.2.2	Classical approaches	38
2.3	Factor analysis in PET	41
2.3.1	SVD-based factor analysis	41
2.3.2	Optimization-based factor analysis	42
2.4	Hyperspectral unmixing	44
2.4.1	Endmember extraction	46
2.4.2	Abundance estimation	47
2.5	Nonlinear unmixing	49
2.5.1	Bilinear models	50
2.5.2	Postnonlinear mixing model	52
2.6	Handling the variability in linear models	52
2.6.1	Endmember bundles	53
2.6.2	Local spectral unmixing	53
2.6.3	Computational models	54
2.7	Conclusion	56
<b>II</b>	<b>Development of algorithms for dynamic PET images unmixing</b>	<b>57</b>
<b>3</b>	<b>Unmixing dynamic PET images with variable specific binding kinetics</b>	<b>59</b>
3.1	Introduction	59
3.2	Variability on specific binding kinetics	61
3.3	Method	62
3.3.1	Specific binding linear mixing model (SLMM)	62
3.3.2	Problem formulation	66
3.4	Algorithm implementation	68
3.4.1	PALM: general principle	69
3.4.2	Optimization with respect to $\mathbf{M}$	70
3.4.3	Optimization with respect to $\mathbf{A}$	71
3.4.4	Optimization with respect to $\mathbf{B}$	72
3.5	Evaluation on Synthetic Data	73
3.5.1	Synthetic data generation	73
3.5.2	Compared methods	77
3.5.3	Hyperparameter influence	79
3.5.4	Results	79
3.5.5	Impact of the deconvolution	83
3.6	Evaluation on Real Data	86
3.6.1	PET data acquisition	86
3.6.2	Results	87
3.7	Discussion	94
3.7.1	Performance of the method	94
3.7.2	Flexibility of the method	95
3.8	Conclusion	96
<b>4</b>	<b>Factor analysis of dynamic PET images: beyond Gaussian noise</b>	<b>97</b>
4.1	Introduction	98
4.2	Factor analysis techniques	99

4.3	Divergence measure . . . . .	100
4.3.1	Noise in PET images . . . . .	100
4.3.2	The $\beta$ -divergence . . . . .	105
4.4	Block-coordinate descent algorithm . . . . .	106
4.4.1	Majorization-minimization algorithm . . . . .	109
4.4.2	Update of the factor TACs $\mathbf{M}$ . . . . .	110
4.4.3	Update of the factor proportions $\mathbf{A}$ . . . . .	111
4.4.4	Update of the internal variability $\mathbf{B}$ . . . . .	113
4.5	Experiments with synthetic data . . . . .	115
4.5.1	Synthetic data generation . . . . .	115
4.5.2	Compared methods . . . . .	116
4.5.3	Performance measures . . . . .	117
4.5.4	Results on Phantom I . . . . .	118
4.5.5	Results on Phantom II . . . . .	119
4.6	Experiments with real data . . . . .	129
4.6.1	Real data acquisition . . . . .	129
4.6.2	Results . . . . .	129
4.7	Conclusion . . . . .	131
<b>5</b>	<b>Towards parametric nonlinear unmixing of dynamic PET images</b>	<b>135</b>
5.1	Introduction . . . . .	135
5.2	Proposed model . . . . .	138
5.3	Derivation of the objective function . . . . .	139
5.4	A PALM algorithm . . . . .	140
5.4.1	Optimization with respect to $\mathbf{M}$ . . . . .	140
5.4.2	Optimization with respect to $\mathbf{A}$ . . . . .	142
5.4.3	Optimization with respect to $\mathbf{B}_i$ . . . . .	142
5.4.4	Optimization with respect to $\alpha_{ki}$ . . . . .	143
5.5	Evaluation on synthetic data . . . . .	143
5.5.1	Synthetic data generation . . . . .	143
5.5.2	Compared methods . . . . .	147
5.5.3	Results and discussion . . . . .	149
5.6	Evaluation on real data . . . . .	153
5.6.1	PET data settings . . . . .	153
5.6.2	Results and discussion . . . . .	153
5.7	Conclusion . . . . .	155
	<b>List of publications</b>	<b>159</b>
	<b>Conclusions and perspectives</b>	<b>161</b>
<b>A</b>	<b>Appendix to chapter 3</b>	<b>167</b>
A.1	Solutions to the optimization sub-problems . . . . .	167
A.1.1	Resolution with respect to $\mathbf{A}$ . . . . .	167
A.1.2	Resolution with respect to $\mathbf{M}$ . . . . .	168
A.1.3	Resolution with respect to $\mathbf{B}$ . . . . .	168
A.2	The whitening transform . . . . .	169
A.2.1	Noise whitening . . . . .	171
A.3	An ADMM approach . . . . .	172
A.3.1	Problem formulation . . . . .	172
A.4	An ADMM-based algorithm . . . . .	174
A.4.1	ADMM: general principle . . . . .	174
A.4.2	Optimization with respect to $\mathbf{A}$ . . . . .	175
A.4.3	Optimization with respect to $\mathbf{M}$ . . . . .	176
A.4.4	Optimization with respect to $\mathbf{B}$ . . . . .	177
A.4.5	Constraints and penalization terms . . . . .	177
A.4.6	Solutions to the optimization sub-problems . . . . .	180



<b>B Appendix to chapter 5</b>	<b>183</b>
B.1 Solutions to the optimization sub-problems	183
B.1.1 Resolution with respect to $\mathbf{m}_k$	183
B.1.2 Resolution with respect to $\tilde{\mathbf{A}}$	185
B.1.3 Resolution with respect to $\mathbf{A}_K$	186
B.1.4 Resolution with respect to $\mathbf{B}_i$	186
B.1.5 Resolution with respect to $\alpha_i$	187
<b>Bibliography</b>	<b>188</b>

# List of Figures

1.1 PET acquisition scheme	11
1.2 Illustration of a $\beta^+$ decay [JP05]	12
1.3 Non-collinearity due to conservation of the momentum. [JP05]	13
1.4 Detection of positron annihilation	13
1.5 Illustration of annular arrays of small crystals [JP05]. View of a PET scanner from the annular plane (left) and view along the axis of the scanner (right).	15
1.6 Effects of the interaction of radiation with matter [JP05]	16
1.7 Line-of-response (right) and point correspondent to the LOR in a sinogram (left) [Rey07]	17
1.8 Illustration of a 3D+time dynamic PET image.	20
1.9 The transaxial resolution includes a tangential component and a radial component. By moving the radioactive source away from the tomographic axis, the probability that the incident photons interact with the scintillators of several detectors before being absorbed increases. It is therefore more difficult to define precisely the place of interaction of the 511 keV gamma rays when the distance to the axis increases, this is why the spatial resolution is degraded in this direction [MAI12].	21
1.10 Tissue-fraction effect due to sampling. (B) spill-out of the black structure with the value of 10 over the gray structure with the value of 5, (C) spill-in of the gray structure into the black one, (D) final result from both spill-in and spill-out effects.[SBB07]	22
1.11 Configuration of the classic three-compartment kinetic model used in many imaging studies.	25
1.12 Configuration of the classic three-compartment kinetic model used in many imaging studies.	26
1.13 Configuration of the classic reference three-tissue kinetic model used in many imaging studies.	27
2.1 A measured PET voxel is composed by the contributions of each ROI tissue TAC in the corresponding studied region.	36
2.2 Illustration of a mixing system	38
2.3 Illustration of the factor analysis scheme	44
2.4 An observed hyperspectral voxel is composed by the contributions of each material in the final spectral response.	45
2.5 Illustration of the simplex for a mixing matrix of 3 factors (a similar representation was introduced in [Bar80]). The filled circles represent the vertices of the simplex, corresponding to the factors and empty circles are the TACs.	46
2.6 Photons interacting with several materials produces nonlinearities.	50
2.7 Illustration of a simplex with : (a) endmember without variability, (b) endmember bundles and (c) endmembers as a multivariate probability distribution [HDT15].	53
3.1 Samples of TACs inside the high-uptake region (thalamus for healthy subjects and thalamus plus stroke for unhealthy subjects) of 10 real images of different patients, as delimited by a specialist.	62
3.2 Simplex with one varying factor.	63

3.3	Graphical representation of SLMM. . . . .	64
3.4	Estimation scheme . . . . .	67
3.5	Diagram of voxel neighbourhood structure for three dimensions, where the blue voxel is the one considered and the red ones are its direct neighbours. . . . .	67
3.6	15 <sup>th</sup> time-frame of the dynamic PET phantom: from left to right, transversal, sagittal and coronal views. . . . .	74
3.7	Synthetic image generation scheme. The red ellipses constitute the ground truth data used for quantitative assessment. . . . .	74
3.8	Ground truth of factors (right) and corresponding proportions(left), extracted from SUnSAL/N-findr . . . . .	76
3.9	Left: variability basis element $\mathbf{v}_1$ identified by PCA. Right: generated SBFs (blue) and the nominal SBF signature (red). . . . .	77
3.10	Variability matrix B randomly generated. . . . .	77
3.11	15 <sup>th</sup> time-frame of 3D-generated image with PSF and a 15dB noise: from left to right, transversal, sagittal and coronal planes. . . . .	77
3.12	Factor proportion maps of the 15 <sup>th</sup> time-frame obtained for SNR=15dB corresponding to the specific gray matter, white matter, gray matter and blood, from left to right. The first 3 columns show a transaxial view while the last one shows a sagittal view. All images are in the same scale [0,1]. . . . .	80
3.13	TACs obtained for SNR = 15dB. For the proposed SLMM algorithm, the represented SBF TAC corresponds to the empirical mean of the estimated spatially varying SBFs $\mathbf{m}_{1,1}, \dots, \mathbf{m}_{1,N}$ . . . . .	81
3.14	Ground-truth (left) and estimated (right) SBF variability. . . . .	81
3.15	Factor proportion maps of the 15 <sup>th</sup> time-frame obtained for SNR=15dB corresponding to the specific gray matter, white matter, gray matter and blood, from left to right. The first 3 columns show a transaxial view while the last one shows a sagittal view. . . . .	84
3.16	TACs obtained for SNR=15dB. For the proposed SLMM algorithm, the represented SBF corresponds to the empirical mean of the estimated spatially varying SBFs $\mathbf{m}_{1,1}, \dots, \mathbf{m}_{1,N}$ . . . . .	85
3.17	Ground-truth (left) and estimated (right) SBF variability. . . . .	85
3.18	Variability basis elements of first subject (left) and second subject (right) . . . . .	86
3.19	Factor proportion maps of the first stroke subject. The first 3 columns show a transaxial view while the last one shows a sagittal view. From left to right: the specific gray matter, white matter, non-specific gray matter and blood. . . . .	88
3.20	TACs obtained by estimation from the first subject image. . . . .	89
3.21	From top to bottom: MRI ground-truth of the stroke area for the first stroke subject, SBF coefficient maps estimated by K-means, NMF, VCA, LMM, SLMM and SBF variability estimated by SLMM. . . . .	90
3.22	Factor proportion maps of the second stroke subject. The first 3 columns show a transaxial view while the last one shows a sagittal view. From left to right: the specific gray matter, white matter, non-specific gray matter and blood. . . . .	91
3.23	TACs obtained by estimation from the second stroke subject image. . . . .	92
3.24	From top to bottom: MRI ground-truth of the stroke area for the second stroke subject, SBF coefficient maps estimated by K-means, NMF, VCA, LMM, SLMM and SBF variability estimated by SLMM. . . . .	93
4.1	Empirical covariance, mean and variance of a randomly chosen region. . . . .	101
4.2	Empirical SNR for each frame of time (in dB) . . . . .	102
4.3	Histogram study in 4 different regions of the image and 4 different time frames . . . . .	104
4.4	$\beta$ -divergence $d_\beta(y = 1 x)$ as a function of $x$ . . . . .	106
4.5	15 <sup>th</sup> time-frame of 6it image: from left to right, transversal, sagittal and coronal planes. . . . .	116
4.6	15 <sup>th</sup> time-frame of 50it image: from left to right, transversal, sagittal and coronal planes. . . . .	116
4.7	PSNR mean and standard deviation obtained on the 6it (left) and 50it (right) images after factorization with $\beta$ -NMF with fixed (top) and estimated (bottom) factor TACs over 64 samples. . . . .	118
4.8	PSNR mean and standard deviation obtained on the 6it (left) and 50it (right) images after factorization with $\beta$ -LMM with fixed (top) and estimated (bottom) factor TACs over 64 samples. . . . .	120
4.9	From left to right: factor proportions from specific gray matter, non-specific gray matter, white matter and blood for one 6it sample, estimated with fixed $\mathbf{M}$ . . . . .	122

4.10	Variability matrices estimated with fixed $\mathbf{M}$ on a 6it sample. . . . .	122
4.11	From left do right: factor proportions from specific gray matter, non-specific gray matter, white matter and blood for one 50it sample, estimated with fixed $\mathbf{M}$ . . . . .	123
4.12	Variability matrices estimated with fixed $\mathbf{M}$ on a 50it sample. . . . .	123
4.13	From left do right: factor proportions from specific gray matter, non-specific gray matter, white matter and blood for one 6it sample. . . . .	124
4.14	$\beta$ -SLMM TACs for $\beta = 0, 1, 2$ corresponding to the specific binding factor, gray matter, white matter and blood for one 6it sample. . . . .	125
4.15	Variability matrices estimated on a 6it sample. . . . .	125
4.16	From left do right: factor proportions from specific gray matter, non-specific gray matter, white matter and blood for one 50it sample. . . . .	126
4.17	$\beta$ -SLMM TACs for $\beta = 0, 1, 2$ corresponding to the specific binding factor, gray matter, white matter and blood for one 50it sample. . . . .	127
4.18	Variability matrices estimated on a 50it sample. . . . .	127
4.19	From left do right: factor proportions from non-specific gray matter, white matter and blood obtained with $\beta$ -SLMM for $\beta = 0, 1, 2$ . . . . .	130
4.20	From top to bottom: MRI ground truth of the stroke zone, factor proportions from specific gray matter and variability matrices obtained with $\beta$ -SLMM for $\beta = 0, 1, 2$ . . . . .	132
4.21	TACs corresponding to the specific binding factor, gray matter, white matter and blood. . . . .	133
5.1	Synthetic image generation scheme. The red ellipses constitute the ground truth data used for quantitative assessment. . . . .	144
5.2	Ground truth of factors (right) and corresponding proportions(left), extracted by SUNSAL/N-findr	145
5.3	Binding potential maps w.r.t. the free fraction of radioligand per tissue. . . . .	146
5.4	Factors (blue) and TACs generated from the 2-tissue reference model. . . . .	147
5.5	15 <sup>th</sup> time frame of 3D-generated image with PSF and a 15dB noise: from left to right, transversal, sagittal and coronal planes. . . . .	147
5.6	Factor proportion maps obtained from the synthetic image corresponding to the gray matter, white matter and blood, from left to right. The first 2 columns show a transaxial view while the last one shows a sagittal view. All images are in the same scale $[0, 1]$ . . . . .	150
5.7	Factor TACs estimated from the synthetic image . . . . .	151
5.8	From top to bottom: ground-truth, initial and PNMM estimations of $BP.f_T$ . The first column corresponds to the gray matter and the second to the white matter. Note that for DEPICT $BP.f_T$ was estimated for the whole image using the respective tissue TAC as reference. . . . .	151
5.9	From left to right: SLMM factor proportion related to the SBF, SLMM variability result and DEPICT $BP.f_T$ estimation using the white and gray matters as reference TACs, respectively. . . . .	152
5.10	Factor proportion maps obtained from the real image corresponding to the gray matter, white matter and blood, from left to right. The first 2 columns show a transaxial view while the last one shows a sagittal view. All images are in the same scale $[0, 1]$ . . . . .	154
5.11	Factor TACs estimated from the real image . . . . .	154
5.12	From top to bottom: stroke region, initial gray matter factor proportion, gray matter factor proportion estimated by PNMM, DEPICT $BP.f_T$ using the gray matter TAC as reference and PNMM $BP.f_T$ for the gray matter. . . . .	156
5.13	From top to bottom: stroke region, initial white matter factor proportion, white matter factor proportion estimated by PNMM, DEPICT $BP.f_T$ using the white matter TAC as reference and PNMM $BP.f_T$ for the white matter. . . . .	157
5.14	From top to bottom: stroke region, SB factor proortion estimated by SLMM and interval variability estimated by SLMM. . . . .	158

# List of Tables

3.1	factor proportion, factor and variability penalization hyperparameters for LMM and SLMM with SNR= 15dB . . . . .	78
3.2	Normalized Mean Square Errors of the estimated variables $\mathbf{A}_1$ , $\mathbf{A}_{2:K}$ , $\tilde{\mathbf{M}}^1$ , $\mathbf{M}^{2:K}$ and $\mathbf{B}$ for K-means, VCA, NMF, LMM and SLMM . . . . .	82
3.3	Factor proportion, factor and variability penalization parameters for SLMM with no deconvolution, wiener pre-deconvolution and joint deconvolution with SNR = 15dB. . . . .	83
3.4	NMSE of estimated parameters for SLMM with no deconvolution, with Wiener pre-deconvolution and with joint deconvolution for SNR=15dB . . . . .	83
4.1	Summary of NMF, LMM and SLMM under (4.2) . . . . .	100
4.2	Stopping criterion and variability penalization parameters . . . . .	121
4.3	Mean NMSE of $\mathbf{A}_1$ , $\mathbf{A}_{2:K}$ and $\mathbf{A}_1 \circ \mathbf{B}$ and PSNR of reassembled images estimated by $\beta$ -LMM and $\beta$ -SLMM with fixed $\mathbf{M}$ over the 64 samples, for different values of $\beta$ . . . . .	121
4.4	Mean NMSE of $\mathbf{A}_1$ , $\mathbf{A}_{2:K}$ , $\tilde{\mathbf{M}}^1$ , $\mathbf{M}^{2:K}$ and $\mathbf{A}_1 \circ \mathbf{B}$ and PSNR of reassembled image estimated by $\beta$ -LMM and $\beta$ -SLMM with $\mathbf{M}$ estimated over the 64 samples, for different values of $\beta$ . . . . .	128
5.1	Parameters . . . . .	147
5.2	NMSE of $\mathbf{A}$ , $\mathbf{M}$ and $\mathbf{BP}$ as chosen in initialization and after conducting PNMM-unmixing . . . .	152

# Introduction

## Context and objective of the thesis

Positron emission tomography (PET) is a non-invasive nuclear imaging technique that allows the organ metabolic functions to be quantified from the diffusion of an injected radiotracer within the body. This technique enables the distinction of different tissues from metabolism particularities not easily apparent in other biomedical image modes, which may help to diagnose various pathologies, ranging from cancers to epilepsy. Additionally to diagnostic interests, PET has also been increasingly promoted for the follow-up of treatment or disease evolution. While static imaging is often performed in order to obtain a map of the spatial distribution of tracer concentration, the best evaluation of tracer kinetics is achieved in dynamic acquisitions [Muz+12]. In this sense, dynamic PET has received increasing interest, since it provides both spatial and temporal information on the pattern of tracer uptakes within an *in vivo* context. To provide interpretable results, PET images have to pass through a process called quantification [Buv07]. It consists in exploring the variations of the concentration of radiopharmaceuticals or radiotracers over time, characterized by time-activity curves (TACs), to estimate the kinetic parameters that describe the studied process. The most effective quantification techniques in dynamic PET often require an estimation of reference TACs representing tissues or an input function characterizing the blood flow. In this context, many methods were developed to perform a non-invasive extraction of the global kinetics of a tracer, generically referred to as factor analysis.

Factor analysis refers to several unsupervised learning techniques that aim to identify physically meaningful patterns from multivariate data [HJA85; JH91]. It consists in describing each voxel of the image as a combination of elementary signatures, called *factors*, providing not only an overall TAC that describes each tissue but also a set of coefficients relating each voxel with each tissue TAC [Bar80]. This description underlies the assumption that any perturbations affecting the kinetic process under study are negligible, thus each tissue contains a spatially homogeneous tracer concentration. In the dynamic PET literature, two main approaches have stood out. The first one is based on singular value decomposition (SVD) or apex-seeking [Pao+82; CBD84], while the second one tries to directly estimate the factors and their respective fractions through optimization schemes [SDG00]. Among the second group, nonnegative matrix factorization techniques naturally appeared as a solution to take the nonnegativity of PET data into account [Lee+01b]. It also allowed for a divergence measure that

matches the Poissonian nature of the count-rates in PET, the Kullback-Leibler (KL) divergence [Kim+01], while the previous methods often relied on the assumption of a Gaussian noise through the use of a Frobenius norm on the cost function.

Meanwhile, unmixing - a specific instance of factor analysis - is a widely employed tool in the hyperspectral imagery literature [Bio+12; Dob+09]. In dynamic PET imaging, it can be very relevant for the extraction of factor TACs, since it directly takes into account both the nonnegativity of the data and the sum-to-one of the factor proportions that can be derived from the diffusion of blood in plasma and tissues. Over the last decades, cutting-edge techniques have been developed by the hyperspectral unmixing community to deal with several limitations of general blind source separation (BSS) solutions. It is the case of the homogeneity assumption embedded in the description of linear mixing models (LMM). Hyperspectral data can often present nonlinearities [NB09; Dob+14b] or spectral variability [ZH14; HDT15], which yielded new models and solutions that modify the LMM structure of standard unmixing. Moreover, as in dynamic PET, several BSS methods assume the noise to follow a Gaussian distribution. Borrowing techniques from the audio literature [FI11], a hyperspectral unmixing solution was also developed to generalize the model of the underlying noise on data [FD15].

Therefore, the main goal of this work is to develop practical contributions to dynamic PET applications that overcome the above-mentioned issues. The strategies adopted in this manuscript adapt the solutions developed in the hyperspectral literature to fit the particularities of PET data. To this end, we introduce in Chapter 3 a novel perturbation model that handles the variability of high-uptake tissues, often neglected in factor analysis techniques. The solution capitalizes on a previous model from the hyperspectral literature that generalizes the standard LMM with an additive spatially indexed term. The variability term is described by a previously learned dictionary and its corresponding map of coefficients. Based on a Gaussian assumption on the noise, the chosen cost function is the Frobenius norm. Then, Chapter 4 generalizes this solution to deal with different shapes of noise distribution, from Gamma and Poisson to Gaussian, including undetermined distributions in-between. This is done by means of the  $\beta$ -divergence. Finally, Chapter 5 presents a perspective work that benefits from the physiological knowledge inherent to parametric imaging of PET data to propose a nonlinear unmixing framework.

The work presented in this thesis has been carried out in the Institut de Recherche en Informatique de Toulouse (France), within the Signal and Communication group, in collaboration with the University of Tours and the Institut National de la Santé et de la Recherche Médicale (INSERM). This thesis has been funded by the Coordenação de Aperfeiçoamento de Ensino Superior (CAPES), attached to the Brazilian Ministry of Education, in the program “Doutorado Pleno no Exterior (DPE)”.

## Structure of the manuscript

**Part I** introduces the general context of this thesis and reviews the state-of-the-art methods that provide the technical basis of this work. It comprises two chapters.

- **Chapter 1** introduces more thoroughly the relevance of dynamic PET for clinical assessment, that is in the heart of this work. It further discusses several effects of acquisition and reconstruction affecting the quality of the final data. Finally, it presents the main challenges related to quantification and its need for a previous estimation of reference TACs or the input function.
- **Chapter 2** recalls the key theoretical tools and practical concepts of blind source separation applied to multivariate data analysis. After a brief review on general non-parametric methods applied in the PET literature for extraction of global TACs, it presents factor analysis as a more general alternative. Then it summarizes some of the solutions to the BSS problem and provides a brief history of factor analysis in the PET domain. Hyperspectral unmixing is subsequently detailed with its nonlinear and spectral-variability instances, preparing the reader to the developments that are to follow.

**Part II** gathers the contributions of this thesis to the factor analysis problem applied to the dynamic PET domain. The content of its three chapters is described hereafter.

- **Chapter 3** introduces an unmixing approach to deal with the variability inherent to specific binding tissues. While factor analysis assumes the classes to be spatially homogeneous, after a careful examination of real data, we decided to propose an approach that no longer disregards possible fluctuations on the rate of tracer concentration in voxels affected by specific binding. Therefore, based on a previous perturbation model that explicitly accounts for spatial factor variability [TDT16a], we derive a formulation that allows fluctuations solely to the specific binding factor. Moreover, we constrain these variations to be described by a previously learned dictionary according to a spatial map that provides the amount of variation in each voxel of the image. The noise is considered to be Gaussian and the Frobenius norm is used to evaluate the level of fit between the data and the proposed model. The variables of this model are estimated using an optimization algorithm that ensures convergence of the iterates to a critical point, namely proximal alternating linearized minimization (PALM) [BST13]. The performance of the proposed unmixing method is evaluated on synthetic and real data. A comparison with state-of-the-art algorithms that do not take factor variability into account allows the interest of the proposed unmixing solution to be appreciated.
- **Chapter 4** further generalizes the approach proposed in the previous chapter to a framework that is more adaptable to different noise distributions. To this end, it resorts to a class of divergences that are related to a wide family of distributions that include the Gamma, Poisson and Gaussian distributions.

This divergence is called the  $\beta$ -divergence. Due to its possibly nonsmooth nature, this divergence is not easily adaptable to all optimization algorithms. Therefore, we apply a majorization-minimization (MM) technique that results on multiplicative updates and that is often used to resolve this kind of problem [FI11]. A similar MM solution has also been applied to deal with nonlinearities in hyperspectral unmixing in [FD15]. We derive new updates particularly suited to the model introduced in the previous chapter. Three algorithms are then evaluated on synthetic data:  $\beta$ -NMF,  $\beta$ -LMM and  $\beta$ -SLMM. The  $\beta$ -NMF is a standard approach from the audio domain [FI11], while  $\beta$ -SLMM is the approach developed throughout this chapter and  $\beta$ -LMM is its particular instance which neglects spatial variability. Simulations are conducted on two sets of synthetic data: with and without variability. Results obtained on real data are also evaluated.

- **Chapter 5** introduces a more prospective work that directly relates the kinetics of specific binding tissues with non-specific binding ones through nonlinear unmixing. It capitalizes on data-driven parametric imaging methods [GGC01] to provide a physical description of the underlying PET data. This characterization is introduced in the factor analysis formulation to yield a novel nonlinear unmixing model designed for PET image analysis. This model also explicitly introduces global kinetic parameters that allow for a direct estimation of the binding potential with respect to (w.r.t.) the free fractions in each non-specific binding tissue. As a high number of variables have to be estimated, once again the PALM algorithm is used to minimize the corresponding objective function. The algorithm is evaluated on synthetic and real data to show the potential interest of the approach.

## Main contributions

**Chapter 3.** The contribution of this chapter lies in the introduction of a model that explicitly takes into account the variability on the specific binding factor time-activity-curve, until now neglected in the PET literature. The proposed decomposition relies on a new interpretation of the spatial heterogeneity of PET images. A joint deconvolution step is also considered in the analysis. Proximal gradient updates are computed for each variable, allowing for the inclusion of elaborate constraints [Con15] and nonsmooth penalizations. The proposed approach yields competitive performances and variability estimates on both synthetic and real data.

**Chapter 4.** The  $\beta$ -divergence is first introduced to the PET domain. The model proposed in the previous chapter is adapted with this flexible data-fitting term, yielding a novel algorithm. Exhaustive simulations conducted on both synthetic and real data show that optimal results for images with different reconstruction parameters may be obtained with different values of  $\beta$ . As a perspective, this study shows that the  $\beta$ -divergence has a potential interest in several steps of the dynamic PET pipeline.



**Chapter 5.** This chapter introduces a new paradigm for factor analysis in dynamic PET, capitalizing on parametric imaging. It studies the potential interest of jointly conducting nonlinear unmixing with global kinetic parameter estimation in a reference tissue compartment model framework, by considering each non-specific binding tissue as a reference. An elementary synthetic data example and a real data simulation show the promising perspective of this contribution.



## Part I.

# General context



# Dynamic Positron Emission Tomography

## Contents

1.1	Positron Emission Tomography (PET): a brief overview . . . . .	<b>10</b>
1.2	Physical principles of acquisition . . . . .	<b>10</b>
1.2.1	Radioisotopes . . . . .	10
1.2.2	Positron decay in PET . . . . .	12
1.2.3	Coincidence detection . . . . .	13
1.2.4	Time-of-flight . . . . .	15
1.2.5	Photon-tissue interaction . . . . .	15
1.3	Reconstruction and corrections . . . . .	<b>16</b>
1.3.1	Reconstruction process . . . . .	16
	Data arrangement into a sinogram . . . . .	16
	Reconstruction methods . . . . .	17
1.3.2	Standard corrections . . . . .	18
	Attenuation correction . . . . .	18
	Scatter and random correction . . . . .	19
1.4	Dynamic PET imaging . . . . .	<b>19</b>
1.5	Properties of PET images . . . . .	<b>20</b>
1.5.1	Partial volume effect . . . . .	21
1.5.2	Noise . . . . .	22
1.6	Quantification . . . . .	<b>23</b>
1.6.1	Standardized uptake value (SUV) . . . . .	23
1.6.2	Parametric imaging methods . . . . .	24
	Compartmental modelling (CM) . . . . .	24
	Data-driven methods . . . . .	28
1.6.3	Challenges of quantification . . . . .	30
1.7	Conclusion . . . . .	<b>31</b>

This chapter introduces the principle and objectives of dynamic positron emission tomography (PET). It further discusses the main challenges that hamper its analysis. To this end, Section 1.1 provides a brief overview of PET imaging. Section 1.2 describes the physical properties of this imaging technique from tracer injection to acquisition of dynamic frames, while Section 1.3 discusses the posterior tomographic reconstruction procedure as well as further corrections. Section 1.4 briefly exposes the advantages that this nuclear imaging method offers for the *in vivo* study of organ metabolism. General properties of both static and dynamic PET are detailed on Section 1.5. Finally, the quantification of PET images is explained in Section 1.6 through the introduction of

two relevant techniques: standardized uptake value and parametric imaging.

## 1.1. Positron Emission Tomography (PET): a brief overview

PET is a functional imaging technique that explores the physiology of organs. It is able to deliver relevant information on dysfunctions, which will precede the appearance of morphological abnormalities such as cancer and dementia, hardly detectable by anatomical imagery. The general principle of PET is the scintigraphy, which consists in injecting a radioactive tracer intravenously. The radiolabelled tracer is composed of a radioisotope attached to a molecule with specific affinity towards an organ or function within an organ. After fixation, it disintegrates emitting a positron that will be annihilated with an electron of the environment after a short course of a few millimetres. This annihilation produces two gamma photons of 511keV that leave in the same direction but opposite senses and may be detected in coincidence by the ring detectors situated around the patient, thus reporting the presence of a molecular target. The place of emission of each detected pair of photons lies on the line joining two detection points, the so-called line-of-response (LOR). When the number of detected pairs of photons is sufficient, the distribution of the radiopharmaceutical in the body of the subject can be reconstructed, using mathematical techniques or algorithms of reconstruction. This procedure provides a three-dimensional image with the quantitative information on the metabolic activity of an organ through the measure of the concentration of radiotracer in the body. Fig. 1.1 shows the scheme of a PET acquisition.

In clinical PET applications, static imaging is often performed in order to obtain a map of the spatial distribution of tracer concentration. However, the best evaluation of tracer kinetics, i.e., the dynamic process of tracer uptake and retention, is achieved through the examination of changes in tracer concentration in the body over time, which prevents static imaging bias on the description of tracer metabolism [Muz+12]. In this sense, dynamic PET has received increasing attention over the last years, since it provides both spatial and temporal information about the pattern of tracer uptakes on *in vivo* biology. A single tracer injection allows knowledge on a large amount of information about the rate of ongoing metabolic events. Dynamic PET provides a series of frames of sinogram data with varying durations that can reach from seconds to hours. Nonetheless, as an outcome of its short acquisition intervals, especially on the earlier frames that are kept short to capture the fast kinetics right after tracer injection, dynamic PET data is highly corrupted by noise.

## 1.2. Physical principles of acquisition

### 1.2.1. Radioisotopes

Radioactivity is a natural physical phenomenon through which unstable atomic nucleus, known as radioisotopes, spontaneously transforms into more stable atomic nucleus losing energy through the emission of radiation, such

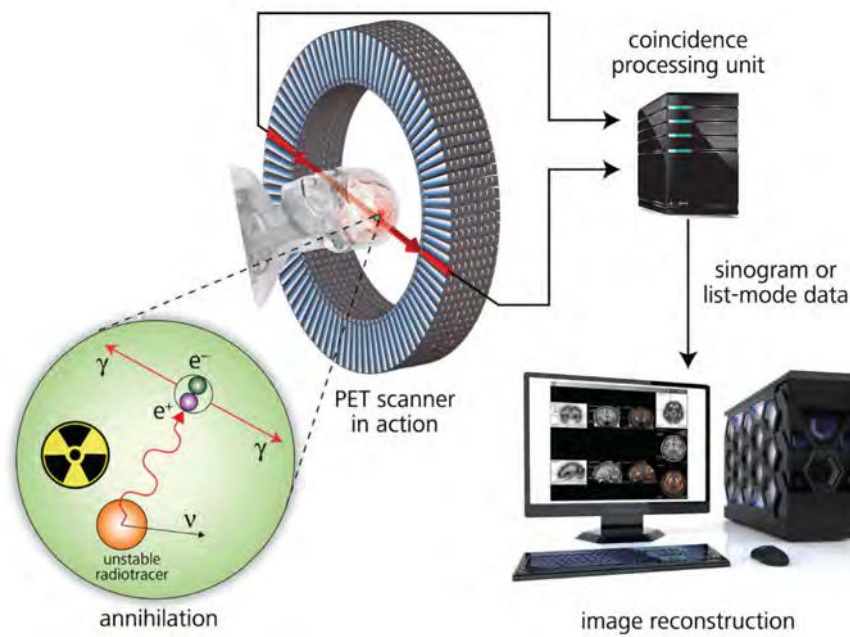


Figure 1.1.: PET acquisition scheme

as  $\alpha$ ,  $\beta^+$  and  $\beta^-$  rays which are frequently followed by high energy photon emission or  $\gamma$  rays.

Radioactive decay, which in physics corresponds to the transformation of matter into energy, occurs when the electric charge of an atom is unbalanced. The possible situations of instability are as follows:

- nucleons excess: emission of  $\alpha$  particles;
- neutrons excess: transformation of neutron into proton, emitting electrons ( $\beta^-$  decay);
- protons excess: transformation of proton into neutron, emitting positrons ( $\beta^+$  decay), showed in Fig. 1.2.

Radioisotopes that have a positive charge excess are used as positron emitters. They are bonded with an organic molecule to form radiopharmaceuticals. The most relevant group of these compounds is the radiotracers, used in PET to diagnose abnormalities in the body tissues. We can divide them into three main categories:

- the first one includes tracers with an excellent emission rate, but a short half-life, which is the indicator that determines the time required to reduce the radioisotope activity to the half. They can only be produced and synthesized at research centres that have a PET scan because of their short duration. Some examples:  $^{11}\text{O}$ ,  $^{13}\text{N}$ ,  $^{11}\text{C}$ ;
- the second one comprises the radioisotopes with long-duration, which includes  $^{18}\text{F}$ , the most used isotope due to its long duration.  $^{76}\text{Br}$  is also part of this group, but as it has a high positron emission kinetic energy, which can be dangerous, it is only used for therapeutic purposes;

- finally, the group with very short duration but coming from isotopic generators of very long-duration, which are used for the calibration of PET scans.

The main radiotracer used in PET is  $^{18}\text{F}$ -FDG, a glucose analog. It is obtained by replacing the normal hydroxyl group by the positron-emitting radionuclide fluorine-18. As glucose consumption is disturbed by numerous dysfunctions,  $^{18}\text{F}$ -FDG turns out to be an excellent radiotracer for several diseases.

### 1.2.2. Positron decay in PET

Due to its high positive charge, as stated previously, PET radioisotopes undergo  $\beta^+$  decay (Fig. 1.2), i.e., when a proton transforms into a neutron, releasing a positron  $\beta^+$  (particle analogous to the electron, but with opposite charge) and a neutrino  $\nu$ . The positron is released with a certain kinetic energy and, as it passes through the tissue, it ionizes neighboring electrons, losing energy. When resting state is reached, it combines with an electron from the tissue to form a positronium. Then, the positron-electron pair suffers annihilation, which releases two  $\gamma$  rays of 511keV in opposite sense, that is, with 180 degrees of separation between them. The principle of PET imaging is based on the detection of these two  $\gamma$  photons of 511keV by the PET scan crystals in order to determine the place of annihilation. An example of  $\beta^+$  emission is the decay of fluorine-18 ( $^{18}\text{F}$ ) into stable oxygen-18 ( $^{18}\text{O}$ ):

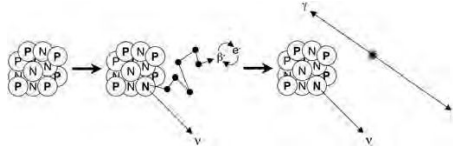


Figure 1.2.: Illustration of a  $\beta^+$  decay [JP05]

Two major physical phenomena of this process negatively affect the spatial resolution of the PET scan: positron range and non-collinearity of  $\gamma$  rays.

- **Positron range:** The event of annihilation does not detect the emission of the positron itself. After emission, the positron follows a dentition trajectory through the tissue and interacts with it through ionization. There is a distance between annihilation and decay that is called free-course and depends on the initial energy of the positron and the composition of the tissue, in particular its density. For low-energy positron emitters, this distance in soft tissues is small (for instance, 0.5 mm for the  $^{18}\text{F}$ ). For high-energy positron emitters, it will highly affect resolution.
- **Non-collinearity of  $\gamma$  rays:** For a positron to combine with an electron from the tissue, it must lose all its energy and have the same kinetic energy as that due to the tissue temperature. Although the



positronium is at the same temperature as the tissue, its angular momentum is not negligible, since photons have little angular momentum compared to energy and they must maintain the same momentum of the positronium. If the positronium is moving in the same direction as one of the photons, this photon will have more energy than the other, but generally this effect does not significantly affect PET scan detection. If the positronium is moving in a direction perpendicular to the annihilation photons, due to conservation of momentum, they will be slightly non-collinear (non-collinearity is, in average, typically of the order of less than 1 degree), resulting in a loss of resolution of 1 to 2 mm. Fig. 1.3 illustrates this process.

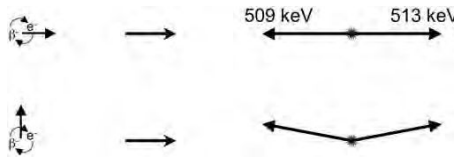


Figure 1.3.: Non-collinearity due to conservation of the momentum. [JP05]

Radioisotopes with excess of protons may also decay by electron capture, but these will not be detected by a PET scan. To disintegration by  $\beta^+$  decay, the isotope needs to have at least 1,02MeV more energy than the isotope for which it decays.

### 1.2.3. Coincidence detection

If two detectors on opposite sides of the patient detect an event at about the same time, then annihilation occurred somewhere along the straight line between the detectors, as illustrated by Fig. 1.4. This straight line is called the LOR. The key to PET acquisition is precisely the ability to identify these coincidental events.

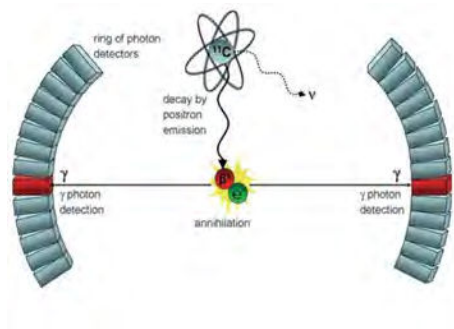


Figure 1.4.: Detection of positron annihilation

In order to detect the simultaneous arrival of the two  $\gamma$  rays in opposite directions, it is essential to have two detectors on opposite sides of the patient in all directions. Therefore, detectors are usually constructed as

annular arrays of small crystals that are placed around the patients, as showed in Fig. 1.4. The area defined by crystals where annihilation occurs is tubular (and not simply a line). In analog systems, each detector is formed by a scintillation crystal and a photomultiplier <sup>1</sup>. Detection is then performed if the two  $\gamma$  rays arrive at the same time with the same energy. In this case, simultaneity is defined by a coincidence circuit, which is based on two windows:

- **the temporal window:** is usually in the range of 5 to 16 ns. In practice, when the first photon is detected, the time window is started and remains open for a given time  $\tau$ . Every photon detected while the time window is open will be associated with the first photon. A new pair of photons can only be detected after the window is closed.
- **the energy window:** detects photons with an energy comprised within a range with mean value of approximately 511eV. It is useful to neglect the arrival of photons from scattering, which have a lower energy and prevent pile-up effects in which the crystal receive energy from several photons.

Several phenomena directly affecting image resolution can be identified:

- **True coincidences:** when two photons of the annihilation event are detected by crystals in opposite directions as a photopick;
- **Scattered coincidences:** when one of the photons goes through a Compton effect, altering its LOR due to the interaction of a  $\gamma$  ray with an electron of the tissue;
- **Random coincidences:** when two photons from different annihilations are detected as originating from the same annihilation.

The interaction of photons entering the detectors with electrons from the crystal occurs either through the photoelectric effect, where the full photon energy is transmitted to the crystal, or through the Compton effect that, due to its scintillation, only transmits part of the energy. The light energy generated is then transferred to the photocatode of the photomultiplier tube through a light guide. The role of the photocatode is to transform the light energy into electrons that are directed to the first dynode to be multiplied by the factor of secondary emission. The signal coming out of the photomultiplier provides a measurable electrical impulse whose integral is proportional to the energy of the photon that has entered the crystal. During the integration time, which depends on the rate of light decrease in the crystal, the detector is not able to measure another event. This phenomenon, called dead time, is responsible for losses in sensitivity to high counts. In general, the density, as well as the energetic and temporal resolutions, affects the performance of different PET imaging devices.

---

<sup>1</sup>Recently, digital PET detectors were developed to overcome the limitations of conventional photomultiplier technology. This topic will not be further detailed in this work for brevity purposes.

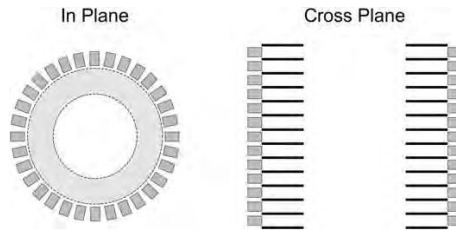


Figure 1.5.: Illustration of annular arrays of small crystals [JP05]. View of a PET scanner from the annular plane (left) and view along the axis of the scanner (right).

#### 1.2.4. Time-of-flight

The photons released during the course of a PET scan reach the detectors at *almost* the same time. The key to understand the concept of time-of-flight (TOF) relies on the “almost”. TOF is the time difference between the detection of photons released during coincident events. The measurement of the difference in arrival times allows to more accurately identify the location of the annihilation event along the line between the two detectors. With TOF PET scanners then, each event is more informative. The key limitation to building a TOF scanner is the time taken by the scintillation process within the crystals.

#### 1.2.5. Photon-tissue interaction

Before reaching the detector, the photons pass through the patient and some of them interact with the tissue. There are three possible interactions between the 511keV photons and the tissue: the photoelectric effect, the Compton effect and the Rayleigh scattering, which are shown in Fig. 1.6

- **Photoelectric effect:** In the photoelectric effect, the photon is completely absorbed by an electron from the atom, overcoming the binding energy and releasing the electron with kinetic energy corresponding to the rest of the photon energy. This phenomenon usually happens with low-energy photons and high atomic number atoms.
- **Compton effect:** In the Compton effect, or incoherent scattering, the annihilation photon interacts with an electron from an upper layer. The photon loses a part of its energy and is dispersed in a new direction, while the electron leaves the valence layer. The Compton effect contributes to the attenuation of  $\gamma$  rays. The effect of the Compton diffusion on the final resolution of the PET image depends on several instrumental considerations of the machine.
- **Rayleigh scattering:** Rayleigh dispersion or coherent dispersion occurs when a photon bounces the atoms in the matrix without causing ionization. The photon changes direction and there is therefore a change in the moment, which is transferred to the atoms of the matrix. However, such dispersion is not frequent at 511 kV in the tissue and can be ignored.

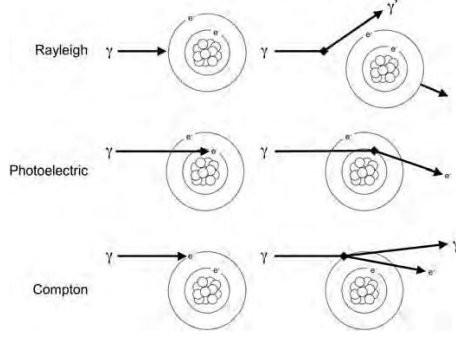


Figure 1.6.: Effects of the interaction of radiation with matter [JP05]

Due to the small angle of the scattered photons, the apparent attenuation may be smaller than the actual attenuation. The coefficient of the apparent attenuation depends on the geometry and the energy resolution of the system. Actual attenuation can be measured with experimental configurations that exclude almost all dispersed photons. A closely collimated, i.e. directed, source and detector allow only non-scattered photons to reach the detector. In some cases, the attenuation coefficient serves as the input parameter used during reconstruction. A lower value than the actual value can be used to account for small angle dispersion.

## 1.3. Reconstruction and corrections

### 1.3.1. Reconstruction process

PET data is constructed through the projection of the location of coincidences occurring within the object of study (e.g., an organ). Therefore a step of tomographic reconstruction becomes essential to recognize the object from its projection.

#### Data arrangement into a sinogram

The elementary PET data are the LORs connecting a pair of detectors that are placed in coincidence. The coincidences recorded on each LOR may be arranged in a matrix called sinogram. Each row of this matrix corresponds to a different angle of the one-dimensional projection. The number of columns is equivalent to the number of LORs for each measurement angle. Sinograms may have, for instance, 256 rows of measurement angles while 192 pairs of detectors for an angular position. Each element of the sinogram represents a LOR between two detectors.

Figure 1.7 shows two detectors  $d_1$  and  $d_2$  connected by an LOR that corresponds to a point of the sinogram. The sum of the coincidences detected within this LOR is allocated in the position defined by  $s_1$  and  $\phi_1$ . Each event accepted by the coincidence circuits adds a unity to the total value of this point of the sinogram.

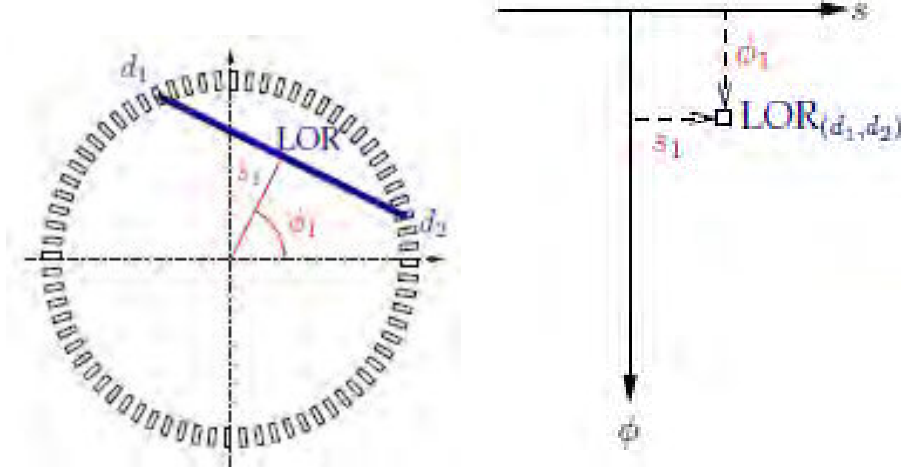


Figure 1.7.: Line-of-response (right) and point correspondent to the LOR in a sinogram (left) [Rey07]

PET data corresponding to one acquisition time may be of two or three dimensions. In “2D” mode, the system only registers the coincidences occurring between two crystals belonging to the same ring or two neighboring rings. To this end, the scanner is equipped with septa between the detection rings in order to stop annihilation photons whose direction correspond to a high copolar angle. In “3D” mode, the LORs are not only in the axial plane, but also at a considerable angle to these planes and for each angle there is a stack of planes.

### Reconstruction methods

After detection and allocation of coincidences, the next step consists of computing the radioactivity distribution within the field of view (FOV) with the information recorded in the sinogram. There are two main techniques of reconstruction: filtered back-projection and iterative reconstruction.

- **Filtered back-projection:** This method is generally applied aiming to implement Fourier reconstruction. The first step of the algorithm consists on filtering each line of the sinogram with a ramp filter that is generally combined with a low-pass filter to prevent noise amplification. Then the method proceeds to the backprojection of filtered projections for each different measured angle. The major advantages of this method are its speed, low complexity and good performance when tracer binding is rather homogeneous. On the other hand, it amplifies the statistical noise of the acquired data.
- **Iterative reconstruction:** Iterative algorithms are initialized with a random estimation of the solution and iteratively proceed to the reconstruction and projection operations. Reconstruction consists of acquiring a frame of the image from the sinogram. The inverse operation, i.e., calculating the sinogram of a given frame, is called projection. In each iteration, the projection of the current solution is compared to the measured projection. The error between those two is supposed to decrease in the next iteration and

the process continue until this error is smaller than a previously defined criterion, meaning the algorithm has converged. Iterative reconstruction allows a more robust modelling of the effects occurring in the PET scan and therefore is more general than Fourier reconstruction. However, it presents a high computational cost and, consequently, is much slower than the latter one. Nonetheless, this drawback has been overcome by our current computational resources that allows the use of these algorithms for clinical practice. The preferred iterative algorithms for reconstruction are based on expectation maximization (EM). The most frequently used method accelerates EM by an ordered subset, corresponding to the acronym OSEM.

### 1.3.2. Standard corrections

Several coincidences are detected in PET image acquisition, but just a few hold relevant information about the place of annihilation as stated in Section 1.2.3. Furthermore, the interaction of the photon with the tissue (detailed in 1.2.5) when passing through the patient before getting to the detector attenuates the signal. In order to correct the deteriorated signal, different strategies were proposed. Some examples of corrections are described in the following.

#### Attenuation correction

Attenuation occurs when the emitted photons are absorbed before reaching the detector. In a PET scan, it is mainly due to the effects presented in Section 1.2.5. Attenuation correction is then applied to obtain a more realistic representation of the radiotracer distribution from the obtained deteriorated information.

Attenuation correction is easily modeled along a line, knowing the linear attenuation coefficient at each point of space and for an energy of 511keV. Once these parameters are known, it is sufficient to calculate the integral of the attenuation coefficient along each LOR. To this end, a projection step is performed through an image of the attenuation coefficient, in order to compute the set of corrective factors corresponding to these integrals (one by LOR). Whatever the point of annihilation of the coincidence detected along the line joining the two crystals, the total distance traveled by these two photons is the same. The amount of attenuating material traversed is, therefore, the same. Thus, attenuation on an LOR does not depend on the location of annihilation.

The main challenge when applying this method of correction relies on the determination of the set of linear attenuation coefficients. In practice, a mean coefficient for each voxel of the reconstructed image is defined and an image of the linear attenuation coefficients is produced. This image is often called *attenuation map*. This map is measured by means of an acquisition in transmission carried out either by a computed tomography (CT) scanner or by an external source emitting 511 keV annihilation photons. Currently, most PET scans are coupled to a CT scanner that estimates the attenuation coefficients for given values of photon energy. The final attenuation map is obtained by converting it to correspond to 511keV.

## Scatter and random correction

In a clinical PET scan conditions, the effects presented in Section 1.2.3 are an important source of inaccuracy. To reduce these negative effects, some techniques were developed for correction of random and scattered coincidences.

- **Correction of random coincidences:** There are two most currently used methods to estimate the distribution of random coincidences and its variants. The first method uses the measurement of the count rate of events detected by each crystal. It therefore assumes that the tomograph is able to record these data. At the end of the acquisition, an estimation of the number of random coincidences per LOR is inferred from the number of events detected by each crystal of the LOR within a coincidence window. This method has two disadvantages: in most cases, it overestimates the amount of random coincidences, and it does not take into account the characteristics of the coincidence detection chain (dead time and multiple coincidence processing). In addition, event rates may vary throughout the acquisition. A second effective and simple way of avoiding random coincidences is through temporal windows, as described in Section 1.2.3. The advantage of this method is that the estimate of random coincidences has exactly the same characteristics as the raw coincidences [Stu10].
- **Correction of scattered coincidences:** The correction of scattered coincidences has been explored in many works. The first category of methods assumed that after correction of all phenomena except scattering, the coincidences detected outside the patient or object are scattered coincidences. The contours of the patient or object are either obtained directly via CT, if available, or estimated from a first reconstruction of the PET data after correction for attenuation and random coincidences. Since the distribution of the scattered coincidences is a low frequency signal, the tails of this distribution are measured outside the patient or the object in the sinograms and then completed by adjustment with different functions in order to estimate the distribution of the coincidences scattered inside the patient or the object (always in the sinograms). A second category of methods explores the fact that only the events detected around 511keV are of interest. It is based on energy windowing, as detailed in Section 1.2.3. The challenge in this case is to determine whether a low energy received is due to the limited energy resolution of the crystals, or to a hypothetical previous scatter. Many other methods were proposed in the literature that will not be detailed in this review but can be consulted in [Stu10].

## 1.4. Dynamic PET imaging

Dynamic PET imaging consists of acquiring a series of static PET images in different frame durations after the injection of the radiopharmaceutical, followed by its reconstruction. The frames of time may vary according to

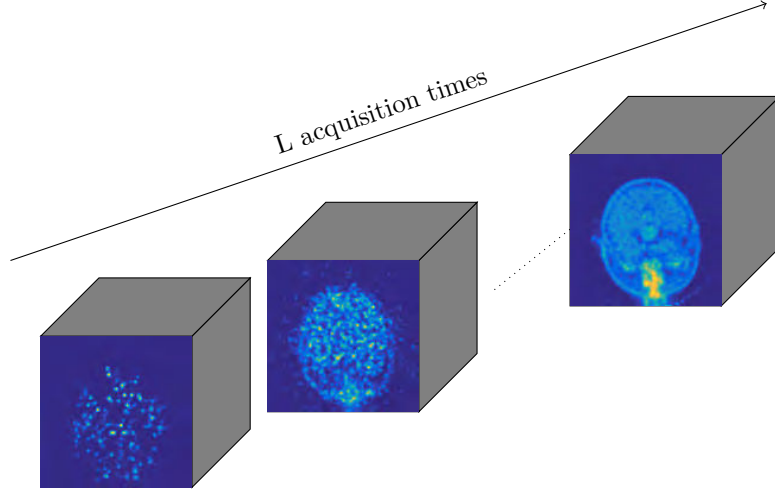


Figure 1.8.: Illustration of a 3D+time dynamic PET image.

the study being made and can be very short in order to detect the quick variations in radiotracer concentration after injection or very long when less noisy images are required. Fig. 1.8 shows an illustration of a dynamic PET image with three-dimensional frames.

The main interest of dynamic imaging is to assess the concentration distribution of the tracer in the organs as a function of time. It is used to explore the functionality of organs over time in *in vivo* applications. It has proven its relevance in many applications from cancer [Muz+12] to neuroinflammation[Lav+15].

Dynamic PET acquisition can be achieved using two general approaches:

- acquisitions in list mode, if the PET scan contains this mode. This acquisition allows a storage of each event, with the instant of detection, the number of the corresponding LOR, and the energy of the photon detected. In this mode, the  $L$  times of acquisition will be specified after the process, where the sinogram will be divided into  $L$  frames followed by an individual reconstruction of each image frame.
- standard dynamic acquisition, which consists in pre-specifying the different time steps before acquisition and saving each detected event in the corresponding sinogram at each time step. Then the sinograms are reconstructed independently for each time step [RTZ]. The final set of dynamic images obtained holds the information on the kinetics of the radiotracer in the FOV.

## 1.5. Properties of PET images

As stated in Sections 1.2 and 1.3, PET image acquisition and reconstruction are affected by several phenomena that can bias the quantification, making its analysis a challenging task. In this section, we describe some characteristics of PET images that should be considered in any quantitative analysis.



### 1.5.1. Partial volume effect

Spatial resolution can be defined as the smallest discernible detail in an image [GW08], i.e., it represents the smallest distance between two distinguishable objects. In PET images, the detector size plays the main role in determining spatial resolution, but some other effects such as non-collinearity, positron range, penetration into the detector, among others, are also relevant (refer to [Mos11] for more details). Due to the cylindrical geometry of the scanners, the spatial resolution is non-stationary in the FOV, i.e., it varies according to the location of measurement, as shown in Fig. 1.9.

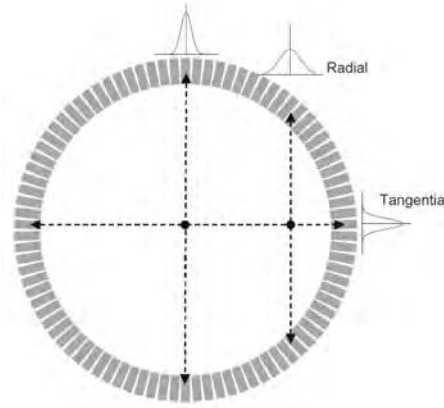


Figure 1.9.: The transaxial resolution includes a tangential component and a radial component. By moving the radioactive source away from the tomographic axis, the probability that the incident photons interact with the scintillators of several detectors before being absorbed increases. It is therefore more difficult to define precisely the place of interaction of the 511 keV gamma rays when the distance to the axis increases, this is why the spatial resolution is degraded in this direction [MAI12].

Meanwhile, another procedure that deeply affects the reconstructed images is the sampling, which produces the tissue-fraction effect. The voxels in the reconstructed image may contain heterogeneous tissues, i.e., tissues with different metabolic activities. Therefore, as each PET voxel contains a definite volume, it may only partially present the desired tissue, being the averaging of the activity of different emission sources.

The effects from both spatial resolution and sampling constitute the Partial volume effect (PVE). It represents the mix of different signals into the same voxel due to these phenomena. The limited spatial resolution spreads the signal coming from a given object into a larger number of voxels than the real voxels that represent this structure. Hence, it produces spill-out of radioactivity from a high-activity region into the surrounding tissue and spill-in from surrounding tissues with high-activity into the volume of interest. The impact of the PVE is shown in Fig. 1.10

The extent of the PVE depends on spatial resolution, sampling, the contrast of a structure with respect to its surrounding environment and the size of the volume of interest.

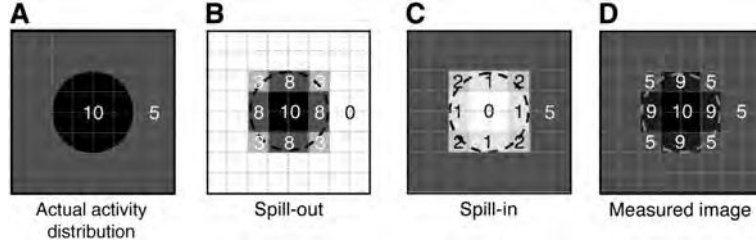


Figure 1.10.: Tissue-fraction effect due to sampling. (B) spill-out of the black structure with the value of 10 over the gray structure with the value of 5, (C) spill-in of the gray structure into the black one, (D) final result from both spill-in and spill-out effects.[SBB07]

### 1.5.2. Noise

Positron emission is a random process and the tomographic acquisition is done with a limited amount of time. Therefore, the measured data is corrupted by a high statistical noise and its posterior reconstruction estimates the noisy radioactivity distribution. Even though the positron decay process can be described by a Poisson distribution, the observed noise in reconstructed images has not a simple Poisson or Gaussian shape, especially when non-linear iterative image reconstruction methods are used, such as ordered subset expectation maximization (OSEM). The noise in OSEM images is known to be object dependent, with higher noise in regions with high uptake compared to low uptake ones [Raz+05; BLL01]. Parameters values, such as the number of reconstruction iterations, may also change the aspect and the correlation within the noise significantly. Moreover, post-processing corrections and filtering operated by modern PET systems significantly alter the nature of the noise, thus corrupting the final reconstructed images. Modelling the noise on this final data, thus becomes a highly challenging task [WTB94].

Considering the difficulties in characterizing the noise properties in PET images, many works assumes that the data is corrupted by a Gaussian noise [Fes94; CHB97; Kam09]. This assumption may also be substantiated by the central limit theorem (CLM) [Tro59], which presents the Gaussian distribution as a limiting form of the Poisson distribution (and others) when the mean value is very large. Thus, the Poisson parameter becomes both the mean and variance for this Gaussian limiting distribution of a originally Poissonian data. Hybrid distributions, such as Poisson-Gaussian [MOM00] and Poisson-Gamma [Ira+11], have also been proposed in an attempt to take into account the various phenomena occurring in the data. The work of Teymurazyan et al. [Tey+12] tried to determine the statistical properties of data reconstructed by filtered-back projection (FBP) and iterative EM algorithms. While FBP reconstructed images were sufficiently described by a normal distribution, the Gamma statistics were a better fit for EM reconstructions. The recent work of Mou et al. [MHO17] further studied the Gamma behaviour that can be found on PET reconstructed data.

Another aspect to take into account when studying the properties of the noise is that its properties can change from one frame to another. In a PET scan, activity contrast between organs varies from frame to frame

because of changes in the tracer distribution over time. Dynamic PET uses time frames with varying durations to capture the initial fast changes in tracer distribution while minimizing the data size. The frame durations in a dynamic PET scan may range from a few seconds to several minutes or hours. As a result, the noise level varies significantly from frame to frame [CQ10]. The frames in dynamic PET are often considered independent consequently producing poor image statistics on each time frames, what affects mainly the shorter ones. More advanced approaches indicate that improvements can be obtained through removal of the assumption of time-frame independence, which can feed through to improved functional parameter estimates [Hon+08].

## 1.6. Quantification

Emission tomography is a great tool to assess the quantitative characterization of *in vivo* functional and molecular processes. To this end, voxel values in the reconstructed PET images have to be converted into an interpretable physical quantity, namely radiotracer concentration that reveals the targeted physiological process, further allowing for the derivation of the parameters of interest characterizing molecular processes from the physiological model that describes the system. Such quantitative interpretation of PET images is often referred to as *quantification* [Buv07].

Quantitative assessment is extremely appealing for many applications, as it results in much superior information than the only visual inspection of images, with less user-dependency [TTA12]. While visual assessment may be a sufficient tool for initial diagnosis and staging, quantification is especially relevant for differential diagnosis and evaluation of therapeutic efficacy, benefiting from the comparison of (semi)quantitative indices before and after treatment. Moreover, only a quantitative analysis of data can provide the necessary parameters to evaluate the pharmacokinetics properties and efficacy of drugs, such as peak time, clearance, area-under-the-curve (AUC) in plasma, healthy tissues and tumours. In the future, this ability will become even more relevant to the selection of the most appropriate tracer for each application. Quantification techniques may be applied in the voxel level or may require the definition of regions-of-interest (ROI) from which the TACs will be extracted. These ROIs may correspond to blood regions or non-specific binding regions. When using ROIs, the TACs are obtained with two main steps that consist, in a first moment, in ROI demarcation and then, averaging of the TACs in one ROI. In the following, two of the main quantitative methodologies that are currently used in PET will be described and completed by an analysis of the challenges that are still to be addressed.

### 1.6.1. Standardized uptake value (SUV)

SUV is the most commonly employed semi-quantitative method in clinical practice, in particular for static imaging. It consists on the ratio between the radiotracer concentration in a certain ROI and the injected

activity, divided by a normalization factor

$$\text{SUV} = \frac{R_c}{\frac{I_a}{NF}}, \quad (1.2)$$

where the  $R_c$  is the radiotracer concentration (e.g.,  $\text{kMq/ml}$ ) measured with PET in the ROI,  $I_a$  is the total injected activity (e.g.  $\text{MBq}$ ) and  $NF$  is a normalization factor, e.g., body weight, body surface area and square meters, computed from the height and weight of the patient.

However, the SUV depends significantly on several different factors making it difficult to compare SUVs computed in different centres when the experimental procedures are even slightly different, e.g., the time interval between injection and scanning, the settings characterizing image acquisition, the reconstruction algorithm.

On the other hand, despite the current lack of a standardized and reliable SUV protocol, when computed in the same centre with the same settings, SUV remains a simple and effective tool for assessing treatment response to therapy, for diagnosis and other evaluations in clinical routine.

### 1.6.2. Parametric imaging methods

Tracer kinetic modelling techniques are used to estimate biologically interpretable parameters by describing the TACs in a region-of-interest with mathematical models. A wide range of techniques models the PET signals based on compartmental analysis of the tracer. These approaches may be divided in two major groups: model-driven methods and data-driven methods, as defined by [Gun+02]. Model-driven methods are based on a previously chosen compartmental model, whereas data-driven techniques do not need any *a priori* decisions about the most appropriate model structure. In model-driven methods, micro or macro parameters of the system are estimated from a previously defined compartmental structure. Meanwhile, data-driven methods derive macro system parameters from a less constrained description of the kinetic processes of a tracer.

#### Compartmental modelling (CM)

Compartment modelling, also known as kinetic modelling, is the most accurate method to describe the kinetic behaviour occurring within the voxel in a dynamic PET dataset. While it has been explored for a long time, it still has significant traction thanks to its quantitative accuracy. In CM, the tracer is assumed to be exchanged between compartments, where each compartment represents a physiological or biochemical entity. There are several different types of compartment models described in the literature, e.g., 1-tissue, 2-tissues and 3-tissues models. While some of them require an arterial blood or plasma input function, such as those that are used for the quantification of blood flow [KS48], cerebral metabolic rate for glucose [Sok+77; Phe+79] and for neuroreceptor ligand binding [Min+84], others are based on reference tissue models [Blo+89; Cun+91; Hum+92; LH96]. The selection of a given compartment model is based on the radiotracer under study [Gun+97; Inn+07], but most of the models consider that the measured signal in a given voxel is the sum of the comprising

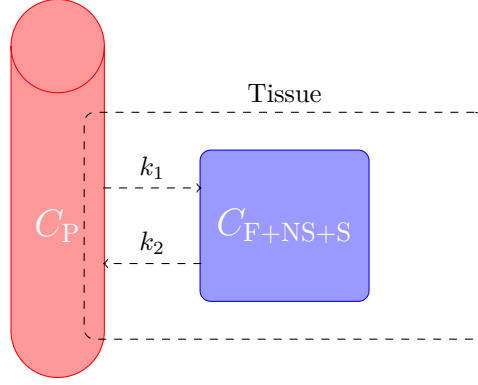


Figure 1.11.: Configuration of the classic three-compartment kinetic model used in many imaging studies.

compartments. Moreover, the rates at which the radiotracer is transferred are given by first-order differential equations.

Figs. 1.11, 1.12 and 1.13 illustrate three models currently applied in dynamic PET, where F stands for free, NS for nonspecific, S for specifically bound tracer in tissue and the  $k$ s are rate constants describing the rate of tracer exchange between compartments.  $C_P$  represents the radioligand concentration in arterial plasma and  $V_p$  represents the fraction of arterial plasma appearing in the tissue.  $C_T$  is the total tissue concentration of tracer. For all models, it can be considered that the TAC of the voxel is a linear combination that accounts for the blood volume by a spillover term governed by  $V_p$  :

$$C_{PET} = V_p C_P + (1 - V_p) C_T. \quad (1.3)$$

In the following, the three mentioned models are further detailed in terms of  $C_T$ .

- **1-tissue model:** In the 1-tissue model [KS48] depicted in Fig. 1.11, the radioligand is assumed to move between the plasma compartment  $C_P$  that represents the radioligand concentration in arterial plasma, and the tissue compartment  $C_{F+NS+S}$  that contains the concentration of radioligand on free, nonspecific and specific tissues. The total tissue concentration of tracer is given by

$$C_T = K_1 e^{-k_2 \mathbf{t}} * C_P, \quad (1.4)$$

where  $\mathbf{t} = [t_1, \dots, t_L]^T$  are the times of acquisition, which are previously known and  $*$  stands for temporal convolution. For simplification purposes, throughout this work we will use the notation  $e^\theta$  as an element-wise operation, i.e., when  $\theta$  is a vector it will produce a vector in which each element is the exponential of the corresponding element in vector  $\theta$ .

- **2-tissue model:** Figure 1.12 presents the compartmental structure for the 2-tissue compartmental model [Min+84], where the radioligand is assumed to move between three compartments:  $C_P$ ,  $C_{F+NS}$  that

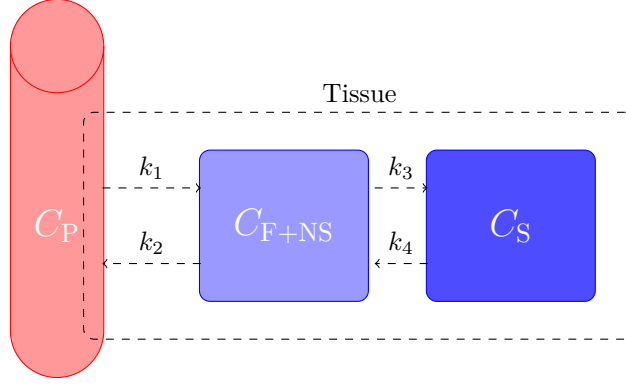


Figure 1.12.: Configuration of the classic three-compartment kinetic model used in many imaging studies.

represents the free plus non-specific compartment, and  $C_S$  represents the specifically bound compartment. The exchange between compartments are subject to rate constants  $k_j$  ( $j = 1, \dots, 4$ ) [HBS16]. The total tissue concentration is computed as

$$C_T = \frac{K_1}{\alpha_2 - \alpha_1} [(k_3 + k_4 - \alpha_1)e^{-\alpha_1 t} + (\alpha_2 - k_3 - k_4)e^{-\alpha_2 t}] * C_P, \quad (1.5)$$

where

$$\alpha_{1,2} = \frac{k_2 + k_3 + k_4 \pm \sqrt{(k_2 + k_3 + k_4)^2 - 4k_2k_4}}{2}. \quad (1.6)$$

- **Full reference tissue compartment model (FRTM):** An alternative to using a known input function consists in using a region of reference that is supposed to be devoided of the target of the radiotracer. The advantage of this method consists in reducing the degree of invasiveness and the level of complexity of the scanning protocol as well as data analysis procedures, as no arterial cannulation and sampling are required. Moreover, labeled metabolites that can bias the measurements of plasma concentration in arterial blood are no longer an issue with this technique [LH96]. Fig. 1.13 depicts the compartmental structure for the FRTM [Blo+89; Cun+91; LH96]. To successfully apply this model, it is essential to choose a reference region with no specific binding. Also, the distribution volume in the tissue of interest has to equal that in the reference tissue, i.e.,  $\frac{K_1}{k_2} = \frac{K'_1}{k'_2}$ <sup>2</sup>. In that case, the PET signal becomes:

$$C_T = R_1(C_R + b_1 C_R * e^{-\alpha_1 t} + b_2 C_R * e^{-\alpha_2 t}), \quad (1.7)$$

where  $R_1$  represents the tracer delivery ratio between the tissue of interest and the reference region

<sup>2</sup>the primes (') refer to the reference tissue parameters.

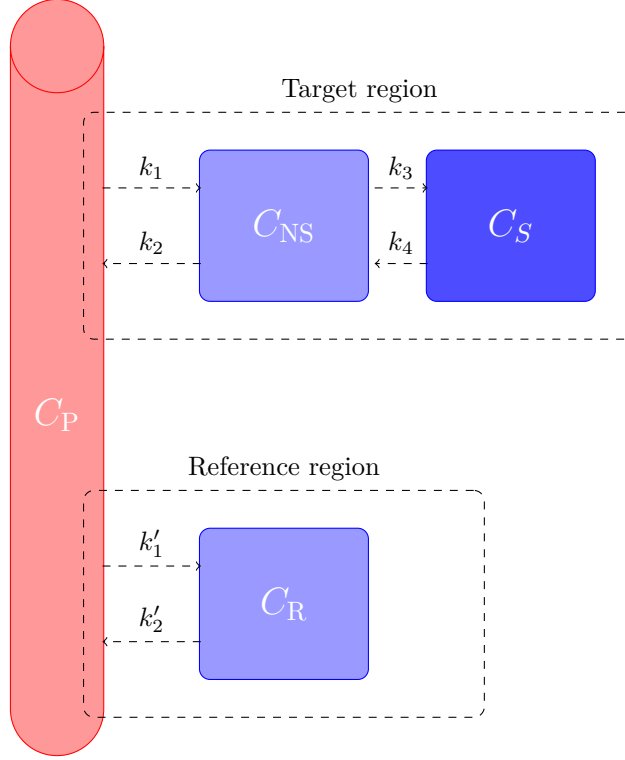


Figure 1.13.: Configuration of the classic reference three-tissue kinetic model used in many imaging studies.

$(R_1 = \frac{K_1}{K'_1} = \frac{k_2}{k'_2})$ , with

$$b_1 = \frac{(k_3 + k_4 - \alpha_1)(\alpha_1 - k_2/R_1)}{\sqrt{(k_2 + k_3 + k_4)^2 - 4k_2k_4}}, \quad (1.8)$$

$$b_2 = \frac{(\alpha_2 - k_3 - k_4)(\alpha_2 - k_2/R_1)}{\sqrt{(k_2 + k_3 + k_4)^2 - 4k_2k_4}}. \quad (1.9)$$

The binding potential is  $BP = \frac{k_3}{k_4}$ . Gunn et al. [GGC01] further developed the binding potential relationship as

$$\begin{aligned} BF.f_T &= R_1 \left( 1 + \frac{b_1}{\alpha_1} + \frac{b_2}{\alpha_2} \right) - 1 \\ &= \frac{\frac{K_1}{k_2} \left( 1 + \frac{k_3}{k_4} \right)}{\frac{K'_1}{k'_2}} - 1, \end{aligned} \quad (1.10)$$

where  $f_T$  is the free fraction of radioligand in tissue.

Considering both the 2-tissue and reference compartment models, the assumption of constant kinetic patterns seems appropriate for the blood compartment as well as non-specific binding tissues, since they present some homogeneity besides some perfusion difference (e.g. white matter versus gray matter). Therefore, their contribution to the voxel TAC should be fairly proportional to the fraction of this type of tissue in the voxel.

CM is considered the “gold standard” in PET quantification thanks to its reliability and its independence on

scanning time or plasma clearance, in contrast with the SUV. However, its complex acquisition protocol, that requires dynamic scanning and arterial blood sampling to measure the time course of plasma concentration of tracer (also called input function), is a great limitation of the method. Simplifications based on non-invasive estimation of the input function or employment of the reference-region approach are currently being studied to better facilitate the use of CM in clinical practice.

### Data-driven methods

Graphical analysis [Gje82; PBF83] and spectral analysis [CJ93] are among the group of data-driven methods. Graphical methods consist in estimating macroparameters (which are combinations of microparameters) by appropriately transforming the multiple time measurements of plasma and tissue uptake data. There are two types of graphical methods: the Patlak plot [PBF83] and the Logan plot [Log00], which can be applied to irreversible and reversible tracers, respectively.

In this work, we will be especially interested in the general theory introduced by Gunn et al. [GGC01] for plasma and reference input models. Inspired by spectral analysis, it characterizes the compartmental system in terms of its impulse response, as summarized hereafter.

- **Plasma input models:** Spectral analysis [CJ93] describes the system impulse response as a positive sum of exponentials and considers the plasma or blood input function as input, which yields

$$C_T = \left( \sum_{i=1}^V b_i e^{-\alpha_i t} \right) * C_P, \quad (1.11)$$

where the coefficients  $b_i$  and  $\alpha_i$  describe the kinetics of the tracer and  $V$  is the total number of tissue compartments in the target tissue. Moreover, the coefficients  $b_i$  are constrained to be nonnegative which is true as this is a plasma input model. In this formulation, the blood volume is neglected in the target tissue.

Gunn et al. [GGC01] constructs a general model for blood and plasma in a basis function framework that writes

$$C_T = (1 - V_B) \left( \sum_{i=0}^V b_i e^{-\alpha_i t} \right) * C_P + V_B C_B, \quad (1.12)$$

where  $C_B$  is the tracer activity concentration in blood,  $V_B$  is its corresponding fraction and the delivery of the tracer to the tissue is given by  $K_1 = \sum_{i=1}^V b_i$ . Moreover, Gunn differentiates the models with reversible and irreversible kinetics.

- (i) **Reversible kinetics** ( $\alpha_i > 0$ ): The volume of distribution  $V_D$  of plasma input models exhibiting



reversible kinetics is given by the integral of the impulse response function, which gives

$$V_D = \sum_{i=0}^V \frac{b_i}{\alpha_i}.$$

- (ii) **Irreversible kinetics** ( $\alpha_{k(i \neq 0)} > 0$ ,  $\alpha_{k0} = 0$ ): In the case of irreversible kinetics models, the irreversible uptake rate constant from plasma,  $K_I$ , is given by

$$K_I = b_0.$$

- **Reference tissue input models:** The reference tissue input model is defined as

$$C_T = ((1 + b_0)\delta(\mathbf{t}) + \sum_{i=1}^V b_i e^{-\alpha_i \mathbf{t}}) * C_R, \quad (1.13)$$

where  $C_T$  is the target tissue,  $V$  is the sum of the total number of tissue compartments in both the target and reference tissues,  $C_R$  is the reference tissue TAC chosen to describe the studied ROI,  $\delta(\mathbf{t})$  is the impulse function and the ratio of delivery of the tracer between the target and reference tissues is  $R_1 = 1 + b_0$ . In the case of reference tissue input models, it is natural to assume that negative coefficients  $b_i$  can also be encountered [Gun+02]. As in [Gun+02], in this definition, the presence of blood volume is neglected in both the target and reference tissue. In [GGC01], a definition including the blood volume is presented.

- (i) **Reversible target tissue kinetics** ( $\alpha_i > 0$ ): From the set of reversible models, [GGC01] derives the relation

$$1 + b_0 + \sum_{i=1}^V \frac{b_i}{\alpha_i} = \frac{V_D}{V'_D},$$

with  $V_D$  and  $V'_D$  the total volume of distribution in the target and reference tissues, respectively. This relation allows for a direct computation of the binding potential with respect to the free fractions of the radioligand in tissue ( $f_T$ ), i.e.,  $BP.f_T$ . It is given by:

$$BP.f_T = b_0 + \sum_{i=1}^V \frac{b_i}{\alpha_i}. \quad (1.14)$$

- (ii) **Irreversible kinetics** ( $\alpha_{(i \neq 0)} > 0$ ,  $\alpha_0 = 0$ ) In the case of irreversible kinetics in the target tissue and reversible kinetics in the reference tissue, the normalized irreversible uptake rate constant from plasma is given by

$$\frac{K_I}{V'_D} = b_V.$$

This general formulation is transparent because it returns information about the underlying compartmental structure. The number of nonzero coefficients returned corresponds to the model order. However, the real underlying configuration, i.e., if compartments are in series or in parallel, is indistinguishable. In particular, for reference tissue input models, a model order of four, for instance, may present seven possible configurations.

### 1.6.3. Challenges of quantification

While quantification techniques from the PET literature present a sufficiently accurate performance in several clinical applications, some challenges inherent to this general problem leave room for improvements. As previously discussed, while the SUV is a very simple and efficient approach, it is not able to benefit from the temporal information of dynamic PET and produces biased results, as a consequence of its applications on static images. Parametric imaging capitalizes on the temporal information of dynamic PET. However, it is very complex and requires the estimation of a high number of parameters. There are many possible sources of errors and uncertainties in kinetic parameters obtained through model-driven methods based on CM. First, they need a previous knowledge on the model that better fits the tracer under study. However, even if we choose an appropriate model, to compute each parameter of the model is a highly challenging task and may still oversimplify the underlying kinetics of the tracer. The variation in the number of detected photons caused by the random nature of radioactive decay is of course always a major source of error. As previously stated, other sources may include: the camera detectors and electronics, image acquisition protocol, image reconstruction algorithm with corrections (attenuation, random and scattered coincidences, detector uniformity, decay) and so on. Moreover, PET image noise leads to quantitative inaccuracy that can cause both bias and uncertainty in measured entities such as SUV and kinetic parameters. Data-driven methods seem to be more robust and, consequently, more complex. Besides the computation of parameters, which already imposes a non-unique problem, it also carries the challenge of knowing which compartmental configuration better fits the estimated parameters.

There is, of course, potentially a huge interest in including kinetic parameters in clinical applications. However, despite the potential benefits, full kinetic modelling for monitoring treatment response is rarely used, since it requires time-consuming dynamic scanning, is more complicated and less reproducible than SUV based methods. Moreover, they require a knowledge of the activity concentration in arterial blood or a reference tissue, what makes kinetic modelling tricky for the clinical routine, being today mainly utilized for research applications. To improve the quality of parametric imaging results, we have to be able to provide a high-quality arterial input function and/or reference tissue TAC. This remains a challenge, especially for radiotracers that do not have any anatomical regions that can be a priori considered to be devoid of specific binding (e.g. radiotracers of neuroinflammation).

## 1.7. Conclusion

This chapter provided an overall view of the PET image domain and the relevance of dynamic PET. After summarizing the acquisition and reconstruction processes, roughly describing all the effects affecting data, we discussed the relevance of quantification and the current methods to apply it. The main challenges in PET image quantification were also discussed. The next chapters will try to overcome some of the obstacles presented in this chapter. The first one is the need for a non-invasive estimation of reference TACs from non-specific tissues. The undetermined nature of PET noise, a main challenge for quantification, will also be addressed. Moreover, the complexity encountered in parametric imaging and its main drawbacks will be confronted.



# Blind source separation in multi-band imaging

## Contents

2.1	From non-parametric methods to factor analysis in dynamic PET . . . . .	<b>34</b>
2.2	A brief overview on blind source separation (BSS) . . . . .	<b>35</b>
2.2.1	Linear model . . . . .	38
2.2.2	Classical approaches . . . . .	38
2.3	Factor analysis in PET . . . . .	<b>41</b>
2.3.1	SVD-based factor analysis . . . . .	41
2.3.2	Optimization-based factor analysis . . . . .	42
2.4	Hyperspectral unmixing . . . . .	<b>44</b>
2.4.1	Endmember extraction . . . . .	46
2.4.2	Abundance estimation . . . . .	47
2.5	Nonlinear unmixing . . . . .	<b>49</b>
2.5.1	Bilinear models . . . . .	50
2.5.2	Postnonlinear mixing model . . . . .	52
2.6	Handling the variability in linear models . . . . .	<b>52</b>
2.6.1	Endmember bundles . . . . .	53
2.6.2	Local spectral unmixing . . . . .	53
2.6.3	Computational models . . . . .	54
	Statistical approaches . . . . .	54
	Deterministic approaches . . . . .	55
2.7	Conclusion . . . . .	<b>56</b>

This manuscript is based on factor analysis and matrix factorization techniques borrowed from the multi-band imaging literature. Indeed, multi-band imaging is now in the heart of various applications, including Earth observation [Bio+12], microscopy [DB12], astronomy [DTS07] and functional imaging, among others. State-of-the-art factor analysis techniques have been further developed in these domains in the last years and some applications have shown a greater advance on this topic than others have. For this reason, the techniques developed throughout this manuscript have been inspired by matrix factorization methods from the hyperspectral domain, rather than the PET domain that is our main application.

This chapter presents the fundamental models and algorithms that underlie this work. To this end, Section 2.1 discusses the main methods used for the extraction of elementary TACs for clinical PET analysis. Section 2.2 introduces the concept of blind source separation and the linear combination model that is the basis of most of

these methods. It also briefly summarizes classical matrix factorization algorithms for blind source separation. In particular, Section 2.3 introduces factor analysis methods from the PET literature while Section 2.4 presents some unmixing methods proposed in the hyperspectral literature that will provide the fundamentals for the methods developed throughout this manuscript. Section 2.5 summarizes the main nonlinear models from the hyperspectral imaging literature. The variability encountered in linear mixtures, which is a topic that recently raised interest in the hyperspectral community with applications to Earth observation, is addressed in Section 2.6. Section 2.7 concludes the chapter. The approaches presented in this chapter will inspire the techniques subsequently developed along this thesis for the PET domain.

## 2.1. From non-parametric methods to factor analysis in dynamic

### PET

As discussed in the last chapter, compartmental models (CMs) are one of the most accurate ways to quantify the distribution of radiotracer in a PET image. Some of the most well established CMs [GGC01] in PET require an arterial blood or plasma input function [KS48; Sok+77; Phe+79], while others require a reference tissue TAC [Blo+89; Cun+91; Hum+92; LH96]. Either way, an estimation of reference TACs representing tissues or an input function characterizing the blood flow is required.

In this context, many methods were developed in order to perform a non-invasive extraction of the global kinetics of reference TACs. Segmentation has constantly appeared as a relevant tool in the analysis of dynamic PET, generally categorized in the domain as supervised or unsupervised clustering of TACs. Many unsupervised approaches have been proposed based on the hypothesis that voxels with homogeneous behaviors can be identified by analysing the similarity between their TACs. Ashburner et al. [Ash+96] applied a clustering treatment based on the shapes of the pixel TACs rather than their absolute scaling while Brankov et al. [Bra+03] used a similarity metric for clustering. An algorithm similar to K-means was proposed by Wong et al. [Won+02] that improved the standard method with a least-square distance that assures within-cluster cost minimization. A parametric imaging algorithm with components extraction based on an average linkage method for hierarchical cluster was presented by Zhou et al. [Zho+02] while Guo et al. [Guo+03] combined hierarchical linkage to a precluster in a two-stage clustering process. Krestyannikov et al. [KTR06] used the least-square method to cluster PET data in the projection space. Maroy et al. [Mar+08] proposed a method of local means analysis also based in hierarchical linkage. Clustering the sinogram domain by maximizing the posterior probability was proposed by Kamasak [Kam09]. Cheng Liao and Qi [CQ10] developed a weighted multiphase level set method to achieve segmentation. A method based on spectral clustering where data mapped into a high dimensional space is clustered to a low-dimensional space of the Laplacian matrix was proposed by Mouysset et al. [Mou+13].

In clinical PET research for microglial activation, the supervised cluster analysis (SVCA) algorithm proposed

by Turkheimer et al. [Tur+07] has been often used as an automatic approach for reference tissue kinetics extraction. It is based on the segmentation of PET voxels by analysing the differences in time-activity curves (TACs). The algorithm SVCA6 for brain imaging requires 6 predefined kinetic classes that describe the gray matter (reference tissue), white matter, skull, blood, soft tissue and one additional class for microglial activation. Each voxel of the image is described by a linear combination of the class kinetics. Indeed, this linearity assumption for voxel decomposition can be envisioned in the light of CM that considers that the resultant signal is composed by the sum of the contribution of each compartment representing a physiological structure. The last step of SVCA6 consists in a linear regression procedure that computes the contribution of each class to each voxel. A modified method considering only 4 kinetic classes (SVCA4), i.e., excluding bone and soft tissue zones, was proposed by Boellaard et al. [Boe+08]. It requires a previously defined brain mask which can be acquired from a magnetic resonance image (MRI) of the subject. Fig. 2.1 presents an illustration of this assumption, where each region of the brain is expected to contain blood, specific gray (sGray) matter, non-specific gray (nsGray) matter and white matter elements. As a result of a smaller number of classes, precision was improved. Tomasi et al. [Tom+08] proposed a method with the ability of improving even further the precision of SVCA with an image-derived blood TAC [Yaq+12]. The blood input function automatic extraction consists in selecting the 10 pixels with maximum area under the curve (AUC) in the first 5 frames, where the blood peak concentration should be present.

Still aiming at extraction of reference TACs, factor analysis has naturally appeared as a more general and flexible way to perform TAC tissue extraction in the PET domain [Bar80; CBD84; Wu+95]. It consists in describing each voxel of the image as a linear combination of all other voxels, providing not only an overall TAC that describes each tissue but also a matrix of coefficients that present the relation of each voxel with each tissue TAC. The experiments reported in [Lee+01b; Pad+12; Sch13] showed the interest of applying factor analysis in the PET domain in a constrained framework, where both TACs and coefficients are assumed to be positive, which is coherent with the knowledge that we have on reconstructed PET images.

Factor analysis techniques belong to a group of generic methods that aim at tackling blind source separation (BSS) problems. The next section further discusses BSS, its mathematical formulation and possible solutions.

## 2.2. A brief overview on blind source separation (BSS)

An effective way to improve signal quality and extract as much information as possible from an observed signal is to recognize all the agents affecting the resulting data and possibly selecting the ones of greatest interest. This rationale may be behind our brain selective attention, i.e., its ability to focus on a particular stimulus while neglecting a wide range of other stimuli perceived by our natural sensors. A classical example is the cocktail party effect [Aro92], which basically highlights our ability to focus on a single conversation despite of

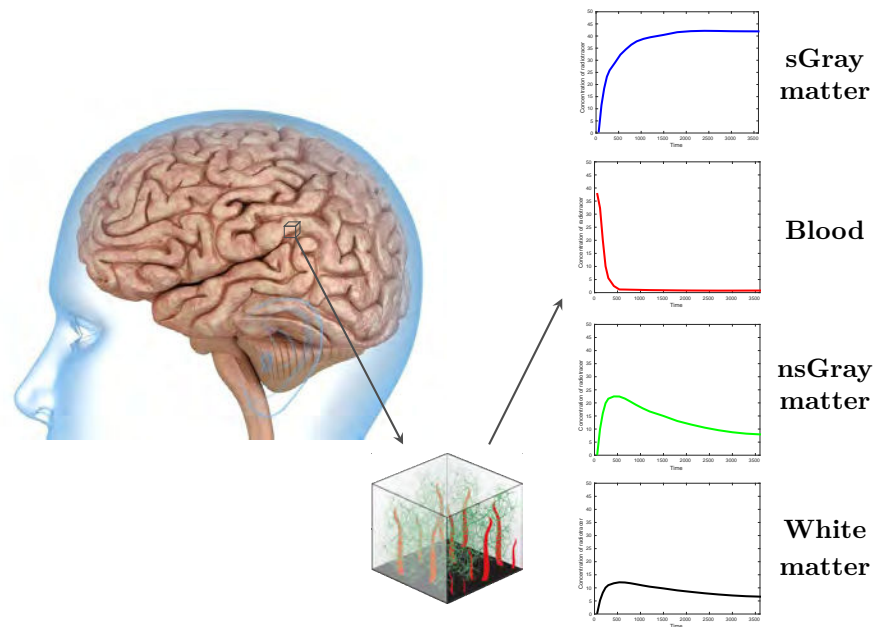


Figure 2.1.: A measured PET voxel is composed by the contributions of each ROI tissue TAC in the corresponding studied region.



a noisy-room situation.

This kind of problem is commonly referred to as blind source separation (BSS). Introduced in the mid-80s [HJA85; JH91], BSS is an unsupervised learning tool that consists in separating a mixture of *a priori* unknown signals by identifying the underlying mixing system.

BSS has been advocated as a relevant and efficient tool to identify the underlying synthesis occurring in multivariate signals acquired in various applicative contexts, ranging from Earth science [Bio+12] to experimental physics [DB12]. Historically, it has been widely used for the audio and biomedical signal processing domains. In audio applications, it is used to describe different speech signals in one conversation [CC97]; to characterize and separate speech and music background [LBO97; Van03]; to describe sounds issued from different musical instruments [KP00], among others [Vin+03]. In the biomedical domain, it was widely applied to characterize electrophysiology signals, such as electroencephalograms (EEG) [VO00], electrocardiograms (ECG) [DDV00], electromyograms (EMG) [Far+04; Far+03]. It was also applied in functional imaging, such as functional magnetic resonance imaging (fMRI) [McK+98] and PET [Wu+95].

Besides the above-mentioned classical applications, the same problem can be found in a long list of other domains. It is the case of chemometrics, where it was used to identify the different spectra constituting a chemical substance [GPH04; Mou05]. In telecommunications, it was applied for radio surveillance [CT03], interference reduction [XB99] and cognitive radio [ZXY09]. Hyperspectral imaging for Earth Observation also has several examples of the use of linear combination models [ND05a; DKS06].

The first step to distinguish each signal altering the perceived data is to identify its corresponding mixing system. Let  $\mathbf{M} = [\mathbf{m}_1, \dots, \mathbf{m}_K]$  be a matrix of  $K$  elementary sources, with  $\mathbf{m}_k \in \mathbb{R}^L$  the  $k$ th source and  $\mathbf{Y} = [\mathbf{y}_1, \dots, \mathbf{y}_N]$  the matrix comprising the  $N$  observed signals, denoted by  $\mathbf{y}_n \in \mathbb{R}^L$ , for  $n = 1 \dots N$ . The relation between the source signals and the observed ones is illustrated in Fig. 2.2 and can be defined as

$$\mathbf{Y} = \mathcal{S}(\mathbf{M}), \quad (2.1)$$

where  $\mathcal{S}$  denotes the mixing system and the noise that depends on the physical phenomena affecting the latent (i.e. unobserved) data. The system  $\mathcal{S}$  is often mathematically characterized with an approximation of the observation matrix  $\mathbf{Y}$  by a model, denoted as  $\mathbf{X}(\boldsymbol{\theta})$  such that

$$\mathbf{Y} \approx \mathbf{X}(\boldsymbol{\theta}), \quad (2.2)$$

where  $\boldsymbol{\theta}$  contains the latent variables belonging to the model, where  $\mathbf{M} \in \boldsymbol{\theta}$ , and the approximation symbol  $\approx$  generalizes the relation between the model and the measured data.

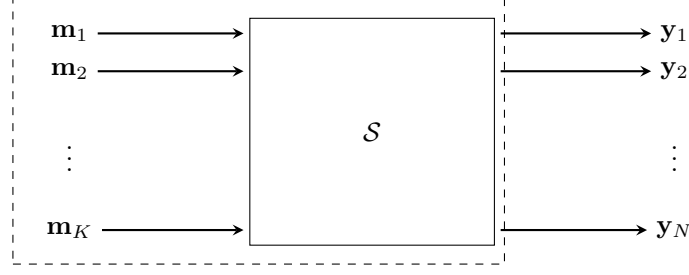


Figure 2.2.: Illustration of a mixing system

### 2.2.1. Linear model

In a wide bunch of applications from the signal and image processing domains, a sufficiently general assumption is that each approximation variable  $\mathbf{x}_n \in \mathbb{R}^L$  is composed by a linear combination of the  $K$  elementary signals (or sources) and their respective mixing coefficients. More explicitly, this model is mathematically expressed as

$$\mathbf{x}_n = \sum_{k=1}^K a_{k,n} \mathbf{m}_k, \quad (2.3)$$

where  $\mathbf{m}_k$  is the *factor* corresponding to the  $k^{th}$  source,  $a_{k,n}$  is the *coefficient* that represents the influence of the  $k^{th}$  source in the  $n^{th}$  signal. In matrix form, (2.3) simply writes

$$\mathbf{X} = \mathbf{M}\mathbf{A}, \quad (2.4)$$

where  $\mathbf{X} = [\mathbf{x}_1, \dots, \mathbf{x}_N]$  is a  $L \times N$  matrix comprising the approximated data,  $\mathbf{M}$  is a  $L \times K$  matrix of *factors*,  $\mathbf{A} = [\mathbf{a}_1, \dots, \mathbf{a}_N]$  is a  $K \times N$  matrix containing the coefficients, also known as *activations*. In this case,  $\theta = \{\mathbf{M}, \mathbf{A}\}$ .

### 2.2.2. Classical approaches

Among the most classical BSS solutions to this problem are singular-value decomposition (SVD), principal component analysis (PCA) [Bis06], independent component analysis (ICA) [Com94], nonnegative matrix factorization (NMF) [LS00] and sparse coding [OF96] (also called dictionary learning [Kre+03; Fer+ed]).

PCA is a multivariate analysis method that aims at identifying the most relevant trends and patterns on data through dimension reduction. High-dimensional data is often highly correlated and one of the challenges of PCA when dealing with this kind of input is to transform this large number of variables into a smaller number of uncorrelated *principal components*. To this end, it searches for the direction of maximum variance in the input space. Thus, the first principal component contains most of data variability and each following component accounts for the remaining variability not represented in the precedent ones.

A routine for performing PCA starts with the computation of a measure of data variability. From multivariate statistics, recall that the variance  $\sigma^2$  is an one-dimensional measure of the spread of data in a dataset. In multi-dimensional data, however, it is often useful to know how much the dimensions vary from the mean with respect to each other. Therefore, covariance appears as a good way to compare two dimensions. For two variables  $[\mathbf{X}]_1 \in \mathbb{R}^N$  and  $[\mathbf{X}]_2 \in \mathbb{R}^N$ , it is mathematically defined as

$$\text{cov}([\mathbf{X}]_1, [\mathbf{X}]_2) = \frac{1}{N-1} \sum_{l=1}^L (x_{1l} - \mu_1)(x_{2l} - \mu_2), \quad (2.5)$$

where  $\mu_1$  and  $\mu_2$  are the mean of the variable  $[\mathbf{X}]_1$  and  $[\mathbf{X}]_2$  in the  $\mathbb{R}^N$  dimension, respectively. Data covariance computation is essential to PCA. The matrix formulation concerning a data set may be written as  $\text{cov}(\mathbf{X}) = \mathbf{X}_\mu \mathbf{X}_\mu^T$  with  $\mathbf{X}_\mu$  the centered data, i.e., after mean subtraction.

SVD is often used as a method for PCA, since they are both based on finding an uncorrelated description of both  $\mathbf{M}$  and  $\mathbf{A}$  through orthogonalization [WEG87]. SVD consists on decomposing  $\mathbf{X}$  in (2.4) as follows

$$\mathbf{X} \approx \mathbf{U} \mathbf{S} \mathbf{V}^T, \quad (2.6)$$

where  $\mathbf{S}$  is a diagonal matrix of singular values whose elements are arranged in descending order of magnitude,  $\mathbf{V}$  is composed by the eigenvectors of  $\text{cov}(\mathbf{X})$  and  $\mathbf{U}$  is the matrix of projections of  $\mathbf{X}$  onto  $\text{cov}(\mathbf{X})$ .

After covariance computation, the first step of a SVD routine is to find a number  $K$  of non-zero eigenvalues of the covariance matrix to constitute the non-square matrix  $\mathbf{S}$  with a diagonal formed by their square root in descending order of magnitude. All non-diagonal elements of  $\mathbf{S}$  are set to zero. Then, the eigenvectors of  $\text{cov}(\mathbf{X})$  are arranged in the same order as their corresponding eigenvalues to form  $\mathbf{V}$ . The projection matrix  $\mathbf{U}$  may be computed as  $\mathbf{u}_k = s_k^{-1} \mathbf{X} \mathbf{v}_k$  with  $k = [1, \dots, K]$ . SVD can be used to find the component vectors of PCA. Truncated SVD performs filtering by discarding the eigenvectors with negligible eigenvalues, while keeping the eigenvectors associated with the  $K$  largest eigenvalues.

While in PCA the eigenvectors point out the direction of maximum variation, ICA tries to decompose the data into an additive series of statistically independent non-Gaussian vectors [HO00]. It is relevant to highlight that uncorrelation is not the same as statistical independence, since that, in uncorrelated data, the value of one variable may still provide information about the others. Beyond uncorrelation, statistical independence between variables means that they are uniquely defined, i.e., knowing the value of one of them provides absolutely no information on the others. To this end, it iteratively updates  $\mathbf{M}$  in equation (2.4) so as to maximize or minimize a given cost function that measures independence and non-Gaussianity, e.g., mutual information, entropy, kurtosis (fourth moment). A drawback of ICA is that statistical independence can be rarely ensured in practice [Fri98; ND05a].

Even though these approaches have proven their effectiveness in various domains, its performance is compromised when sources are correlated or present a strong statistical relation. Among the principal challenges, these approaches face the non-uniqueness and the undetermined nature of the optimization problem [DS04]. In order to reduce the number of possible solutions, although not entirely solving the non-uniqueness problem, additional assumptions can be made on data. They can be expressed in terms of penalizations and constraints. It is the case of NMF and sparse coding. Indeed, linear decomposition can be formulated as an optimization problem which consists in estimating the parameter vector  $\boldsymbol{\theta}$  assumed to belong to a set denoted  $\mathcal{C}$  with the possible complementary penalizations  $R(\boldsymbol{\theta})$ . It is mathematically described as

$$\hat{\boldsymbol{\theta}} \in \arg \min_{\boldsymbol{\theta} \in \mathcal{C}} \left\{ \mathcal{D}(\mathbf{Y}|\mathbf{X}(\boldsymbol{\theta})) + R(\boldsymbol{\theta}) \right\} \quad (2.7)$$

where  $\mathcal{D}(\cdot|\cdot)$  is a measure of dissimilarity between the observed data  $\mathbf{Y}$  and the proposed model that should depend on the noise properties of the signal.

In the standard NMF formalism [LS00], to provide an additive and part-based description of the data, nonnegative constraints are assumed for the signatures and respective coefficients

$$\mathbf{A} \succeq \mathbf{0}_{K,N}, \quad \mathbf{M} \succeq \mathbf{0}_{L,K}, \quad (2.8)$$

where  $\mathbf{0}_{W,H}$  denotes the  $W \times H$ -matrix made of 0's and  $\succeq$  stands for a component-wise inequality. The corresponding NMF optimization problem has been largely considered in the literature.

Sparse coding searches a compact representation of data by penalizing  $\mathbf{A}$  so as to enforce sparsity. The most direct way to recover a  $k$ -sparse matrix, i.e., a matrix with at most  $k$  non-zero elements, is through the  $\ell_0$  operator, mathematically written as  $\|\mathbf{A}\|_0$ , that denotes the number of non-zero entries in the matrix  $\mathbf{A}$ . However, this operator is very difficult to adapt to most classical optimization problems. For its adaptability, in particular its ability to be written as a linear programming problem, one of the most popular tools to induce sparsity is the  $\ell_1$ -norm, also called the LASSO regularizer [Tib96]. Mathematically written as  $\|\mathbf{A}\|_1$ , it produces shrinkage on data depending on the value of its corresponding tuning parameter, that works as a baseline in order to set more or less coefficients to zero. To define them as penalizations for  $\mathbf{A}$  in problem (2.7), we write  $R(\mathbf{A}) = \|\mathbf{A}\|_0$  or  $R(\mathbf{A}) = \|\mathbf{A}\|_1$ . In general, sparsity is relevant in many applications, since, in practice, it takes the form of variable or feature selection, increasing interpretability of the solution [Bac+12]. Moreover, it can be combined in various different ways with different techniques, including NMF [Hoy04].

In the following section, a brief summary of the BSS methods applied in the PET domain will be presented. Subsequently, to provide the basis of the methods developed throughout this thesis, BSS methods from the hyperspectral literature will be further detailed.

## 2.3. Factor analysis in PET

In the search for a non-invasive extraction of the blood input function as well as an unsupervised estimation of reference tissue TACs to help in quantification, BSS methods, namely factor analysis or matrix factorization, raised a lot of interest in the dynamic PET community.

Factor analysis consists in interpreting each voxel TAC of the image as a linear combination of  $K$  elementary factor TACs, corresponding to distinct tissues, and their respective coefficients, as illustrated in Fig. 2.3. In this work, we will categorize factor analysis in dynamic PET with two generations of methods: SVD-based and optimization-based.

### 2.3.1. SVD-based factor analysis

The first generation is mainly based on apex-seeking and SVD for extraction of principal components or factors. Based on previous studies made on principal component analysis for quantitative evaluation on medical imaging [Sch79; Mor90], Barber [Bar80] was the first to effectively propose a matrix factorization-based analysis technique for gamma camera imaging. The main assumption of this method is that tissues are spatially homogeneous with respect to a given tracer and therefore a single TAC is able to characterize the variation of tracer concentration over time for all points within an organ. Moreover, while pure voxels of a tissue would present the most extreme values of their corresponding coefficient, overlapping voxels would be identified with coefficient values partitioned between each mixing factor. Indeed, Barber defines the coefficients in a voxel as summing to one and determines that they have to be positive so as to represent a physically realistic situation. This technique, referred to as factor analysis of dynamic structures (FADS), was further developed by Di Paola et al. [Pao+82] and applied by Cavailloles et al. [CBD84] for non-invasive gated cardiac studies under positivity constraints. Nijran and Barber [NB85; NB86] highlighted the relevance of providing physiological *a priori* information on at least one of the factors to reduce the number of possible solutions to the problem. As an example, they used the differential equations from a three-compartment model to describe the tracer flow in the kidney, considered as the factor of interest. The impact of poor identification of factors was discussed in [Hou84]. Houston [Hou86] further addressed the identification of physiologically meaningful factors, by the use of set theory and clustering, while the work in [Sam+87] tried to achieve the same goal by the use of rotation procedures. In a posterior work, Samal et al. [Sam+87] investigated the ambiguous nature of general factor analysis problems applied to dynamic PET. In [NB88], the relevance of constraints on providing physically meaningful factors for FADS approaches is studied. Nakamura et al. [NSK89] evaluated the performance of a factor analysis method based on the maximum entropy principle in dynamic radionuclide images. In [Dae+90], a background correction is implemented within factor analysis.

Buvat et al. [Buv+93] proposed a target apex-seeking method that identifies a factor when knowing part or

the entirety of its shape. In its first decades, FADS was inherently associated with PCA and factors extraction was mainly based on orthogonality or apex-seeking principles. Indeed, Bernali et al. [Ben+93] summarized the step-by-step procedure applied in the domain until its publication as the following:

- First, a preprocessing step that often consists on clustering and selection of TACs is conducted on data to improve SNR;
- Then, an orthogonal analysis (often SVD) is applied to the selected TACs to reduce dimensionality, producing basis vectors;
- An oblique rotation of the previously estimated basis vectors is then conducted to obtain non-orthogonal factor TACs, representative of tissues and blood.
- Finally, an oblique projection of the image is used to produce factor coefficients.

In their work, they analysed an appropriate metric for orthogonal and oblique analysis, proposing an iterative statistical method based on the fixed-effect model [Cau86] to explicitly take into account physical considerations of data. The method allowed the direct application of nonnegativity and normalization to the factor proportions as a step of the iterative procedure. It also enabled the modeling of Poisson or Gaussian noise in the data. In [Ben+94], the interest of directly applying *a priori* knowledge of data into factor analysis was further investigated.

Furthermore, Wu et al. [Wu+95] applied FADS to extract the blood TACs from dynamic FDG-PET studies and the method was successfully validated in a breast cancer study into humans when compared to aortic plasma. Houston et al. [HS97] compared different FADS methods in renal dynamic studies, showing that they work well when the compartments are homogeneous and non-homogeneous without pathology. However, the presence of an abnormality in the tissues lowers the performance of factor analysis. A realistic estimation of the blood input function also appeared to be of relevance for the good performance of FADS methods.

### 2.3.2. Optimization-based factor analysis

In opposition to the previous SVD-based approaches, the second generation of methods is based on optimization. A Monte-Carlo-simplex iterative method was first introduced in the domain by Bazin et al. [Baz+80]. Van Daele et al. [Dae+91] proposed a vertex-finding algorithm that is based on the minimization of a function of the vertices. Sitek et al. [SDG00] applied a conjugate gradient algorithm to conduct FADS on cardiac images by minimizing a least square function such as in the optimization problem posed in (2.7) with

$$\mathcal{D}(\mathbf{Y}|\mathbf{MA}) = \|\mathbf{Y} - \mathbf{MA}\|_F^2, \quad (2.9)$$

where  $\|\cdot\|_F$  is the Frobenius norm and is associated with a Gaussian assumption on the noise or the approximation residual. The article also proposed a post-processing step to reduce the non-uniqueness encountered on factor analysis approaches. Instead of using a constraint to impose nonnegativity, as in standard NMF, the proposed method applied a penalization in both  $\mathbf{M}$  and  $\mathbf{A}$  that was defined as

$$R_+(\boldsymbol{\theta}) = \sum_{l=1}^L \sum_{k=1}^K \lambda_M H(m_{lk}) + \sum_{k=1}^K \sum_{n=1}^N \lambda_A H(a_{kn}), \quad (2.10)$$

where  $\lambda_M$  and  $\lambda_A$  determine the trade-off between its respective penalization term and the data-fitting term with

$$H(\theta) = \begin{cases} \theta^2, & \text{if } \theta < 0, \\ 0, & \text{if } \theta \geq 0. \end{cases} \quad (2.11)$$

The works of Sitek et al. [SGH02] further improved nonnegative FADS with a penalization that promoted non-overlapping regions in each voxel aiming at tackling the non-uniqueness problem inherent of factor analysis. El Fakhri et al. [El +05] validated the approach with the extraction of left and right ventricle factor TACs in cardiac dynamic PET. In [El +06], factor analysis is further generalized to a five-dimensional framework that includes three spatial dimensions, one temporal dimension and a photon-energy dimension.

In another direction, independent component analysis (ICA) has been widely advocated to solve BSS problems. Thus, naturally, ICA has also been considered to analyse PET images, e.g., to segment various cardiac tissues and blood [Lee+01a; Che+07; Mar+10]. However, ICA assumes statistical independence of the sources, which significantly lowers its performance when the sources to be recovered are correlated and short-numbered, as encountered when analysing PET images [ND05a]. Furthermore, ICA not necessarily provides physically meaningful factors since it does not impose nonnegativity constraints.

Meanwhile, Lee et al. [Lee+01b] popularized NMF with multiplicative updates as a solution to explicitly consider nonnegativity while adapting the divergence measure  $\mathcal{D}(\mathbf{Y}|\mathbf{MA})$  to the Poissonian nature of the noise distribution in the count-rates with the Kullback Leibler (KL) divergence. The KL-divergence  $\mathcal{K}(\mathbf{Y}|\mathbf{X})$  writes

$$\mathcal{K}(\mathbf{Y}|\mathbf{X}) = \sum_{l=1}^L \sum_{n=1}^N y_{ln} \log \frac{x_{ln}}{y_{ln}}. \quad (2.12)$$

Kim et al [Kim+01] applied KL-NMF to the extraction of the carotid input function followed by a partial volume correction. A scale-corrected NMF was used in [BSK07] for estimation of the vascular TAC in 5 healthy subjects injected with [18F]-Altanserin. Padilla et al. [Pad+12] applied NMF for dimension reduction, followed by a support vector machine (SVM) classifier for the diagnosis of Alzheimer disease. Schulz et al. [Sch13] compared NMF and standard factor analysis performances in the distinction between the myocardial tracer concentration and the blood input function. NMF presented superior results. A more deterministic

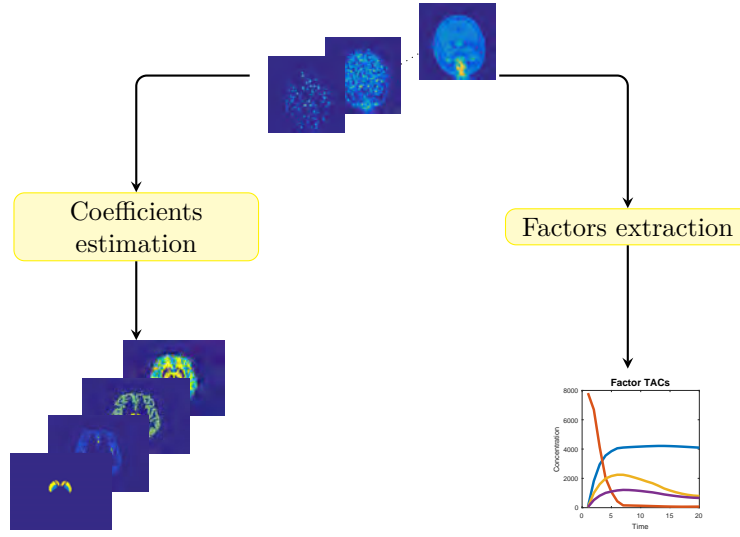


Figure 2.3.: Illustration of the factor analysis scheme

approach was proposed by Ouedraogo et al. [Oue+14] to perform BSS on the non-negative data domain. It is a geometrical method based on the simplicial cone shrinking concept. More recently, Filippi et al. [FDM17] applied a non-negative factor analysis approach with an additional penalization on the factor proportions based on pre-defined regions of interest for each tissue.

## 2.4. Hyperspectral unmixing

This manuscript focuses on dynamic PET images and is mainly inspired by several methods proposed in the hyperspectral imaging literature, in particular for Earth observation. Multispectral and hyperspectral imaging consists in the acquisition and processing of images whose pixels are characterized by tens to hundreds different wavelength channels, in opposition to single-valued gray-level images or even three-channel red, green and blue (RGB) images. These channels provide the reflectance spectrum of the surfaces captured in the image, i.e. the response of the surface to visible light that depends on absorption features caused by pigments. In Earth observation applications, this deeper spectral information allows to differentiate materials in a scene from its reflectance.

The constitution of pixels in hyperspectral images is often described with linear mixing models (LMM) that consist of a linear combination of *endmembers*, that contain the spectral signature of a given material on the observed scene, and *abundances*, which correspond to the proportion of each endmember in each voxel, as shown in Fig. 2.4. This mixture is often explained by the limited spatial resolution of hyperspectral sensors. Hyperspectral unmixing then consists of the identification of these elements described by LMM. It is a valuable technique widely applied in the hyperspectral imagery literature, especially in remote sensing for Earth



observation [Bio+12; BN08; Amm+14; Dob+09; IBP11].

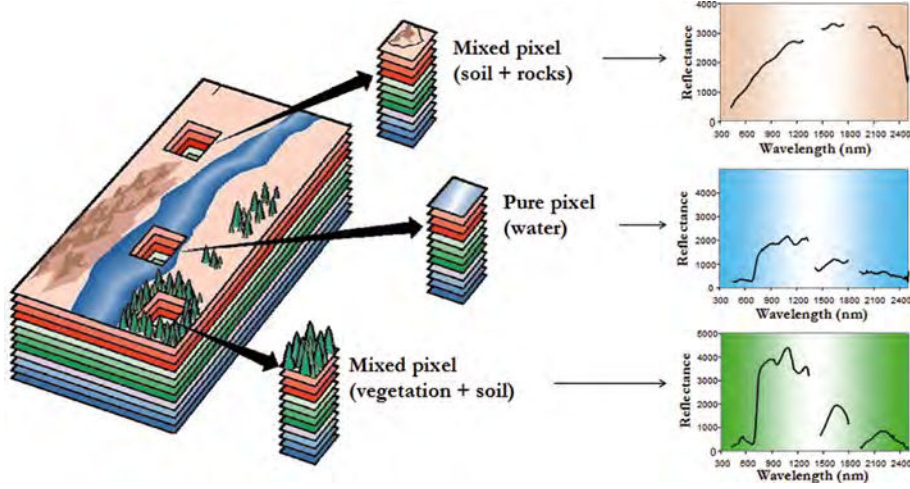


Figure 2.4.: An observed hyperspectral voxel is composed by the contributions of each material in the final spectral response.

The factorization (2.4) and constraints (2.8) that describe a typical NMF can also be envisaged under the light of LMM. As already stated, BSS problems may lead to several solutions and further assumptions on data may reduce the set of search. Thus, additionally to the nonnegativity constraints defined in (2.8), LMM generally assumes the following abundance sum-to-one constraint (ASC)

$$\mathbf{A}^T \mathbf{1}_K = \mathbf{1}_N \quad (2.13)$$

where  $\mathbf{1}_N$  is the  $N$ -dimensional vector made of ones.

This constraint forces the abundances to be interpreted as concentrations [Kes03]. Therefore, all factor proportion vectors lie inside the unit (or probability)  $(K - 1)$ -simplex, denoted as  $\Delta_K$  and defined by  $\Delta_K = \{\mathbf{a} \in \mathbb{R}^K, \forall k \in [1, \dots, K], a_k \geq 0 \text{ and } \sum_{k=1}^K a_k = 1\}$ . Similarly, the TAC  $\mathbf{x}_n$  belong to the convex set whose simplices are the columns of  $\mathbf{M}$ , represented by a  $(K - 1)$ -simplex in  $\mathbb{R}^L$  [Bio+12]. Fig. 2.5 shows an example of a simplex defined by  $K = 3$  elementary factors. A simplex can be interpreted as a generalization of a triangle to higher dimensions, i.e., in a  $k$ -dimensional subspace, a  $k$ -simplex is a subset defined by the simplest  $(k - 1)$ -dimensional object of this subspace. The rationale behind this definition is the fact that a high-dimensional data can actually be defined on a subspace of much lower dimension. This geometric interpretation for LMMs led to a two-step strategy that became the most common way to perform hyperspectral unmixing: endmember extraction followed by abundance estimation.

In this work, a parallel between hyperspectral images and dynamic PET images is drawn, where the TACs of PET, constituted by temporal samples, correspond to spectra, constituted by spectral bands. This allows us to address dynamic PET with approaches not yet applied in the domain.

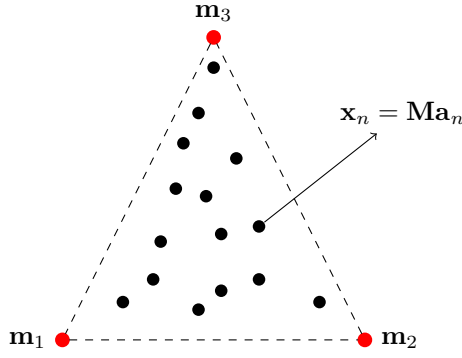


Figure 2.5.: Illustration of the simplex for a mixing matrix of 3 factors (a similar representation was introduced in [Bar80]). The filled circles represent the vertices of the simplex, corresponding to the factors and empty circles are the TACs.

### 2.4.1. Endmember extraction

Endmember extraction requires *a priori* knowledge (or estimation) of the number of classes. In general, it is based on the computation of a simplex whose vertices are the endmembers, as in Fig. 2.5. Many approaches proposed in the literature are built on the *pure pixel* hypothesis [Pla+04]. A pure pixel is solely constituted by one material in the scene, i.e., there is no mixing in its composition. The mentioned hypothesis assumes that for each material in the observed image, there is at least one pure pixel. Otherwise said, we observe the vertices of the simplex. As the pure-pixel approaches are very popular in the domain, in the following, a brief review on two standard and effective techniques will be provided. These techniques, called N-findr [ZP09; CWT11; Cha+11] and vertex component analysis (VCA) [ND05b], will be used for comparison purposes throughout this work.

N-findr consists in searching for the simplex with the largest volume among the possible simplices in the data subspace. It assumes that this simplex of maximum volume will be most likely specified by the purest pixels. The vertices of this simplex will define the endmembers. N-findr often applies dimensionality reduction as a preprocessing step, e.g., by conducting minimum noise fraction (MNF) transformation or a PCA and maintaining the  $K$  main eigenvectors. The algorithm is initialized with a set of endmembers randomly extracted from the input data. The volume of the convex hull whose facets are delineated from this initial endmember set is computed. An exhaustive search is conducted in order to find the points that comprise the smallest convex set containing the data. This is done by replacing each endmember position in this set by each pixel in the hyperspectral data and recalculating the volume in each replacement so as to find the greater one. If none of the recalculated volumes is greater than the initial one, then no endmember is replaced. Otherwise, the combination with maximum volume is retained.

The first step of VCA also consists of dimensionality reduction through SVD or PCA. Then data are projected onto the subspace previously identified and a projected projection is applied. The concept of projected projection

or perspective projection comes from geometry [Cra94] and consists in projecting each voxel  $\mathbf{y}_n$  from the observed dataset onto the plane  $\mathbf{y}_n^T \mathbf{u} = 1$ , where  $\mathbf{u} \in \mathbb{R}^K$  is chosen so that  $\mathbf{y}_n^T \mathbf{u} > 0$ . This is equivalent to rescaling each observation voxel  $\mathbf{y}_n$  such that  $\tilde{\mathbf{y}}_n = \frac{\mathbf{y}_n}{\mathbf{y}_n^T \mathbf{u}}$ ,  $\forall n$ . The initial  $K$ -dimensional cone is thus transformed into a  $K - 1$ -simplex, making the algorithm more robust with respect to scaling variations of the data. The algorithm is initialized with randomly generated vectors and data is projected onto a direction orthogonal to the subset spanned by the identified endmembers. From this random group of endmembers, the data point maximizing the projection is identified as an endmember. This is iteratively done until each endmember signature correspond to the extreme of the projection, in an exhaustive search.

Both algorithms rely on the search for extreme points on the data distribution. However, this mechanism increases their sensitivity to outliers or noise, especially when the SNR is low. They are, nonetheless, very popular in the hyperspectral domain for endmember extraction.

### 2.4.2. Abundance estimation

Once the endmembers have been extracted, abundances can be estimated in a convex framework. Two main variants of the corresponding optimization problem may be pointed out.

- **Constrained least squares (CLS):** only the abundance nonnegativity constraint (ANC) is considered.

$$\hat{\mathbf{A}} = \arg \min_{\mathbf{A}} \frac{1}{2} \|\mathbf{Y} - \mathbf{MA}\|_F^2, \quad \text{s.t.} \quad \mathbf{A} \succeq \mathbf{0}_{K,N} \quad (2.14)$$

- **Fully constrained least squares (FCLS):** both the ANC and the ASC are considered.

$$\hat{\mathbf{A}} = \arg \min_{\mathbf{A}} \frac{1}{2} \|\mathbf{Y} - \mathbf{MA}\|_F^2, \quad \text{s.t.} \quad \mathbf{A} \succeq \mathbf{0}_{K,N}, \quad \mathbf{1}_K^T \mathbf{A} = \mathbf{1}_N^T \quad (2.15)$$

where  $\hat{\mathbf{A}}$  is the estimated abundance. In classic applications, the noise is generally assumed to be Gaussian, which makes the Frobenius norm  $\|\cdot\|_F^2$  a suitable choice for the data-fitting term.

A widely used algorithm to solve this problem is presented in [HC01]. The method, based on an orthogonal subspace projection (OSP), rewrites the problem in (2.3) as

$$\mathbf{x}_n = \mathbf{d}a_{r,n} + \mathbf{U}\mathbf{s}, \quad (2.16)$$

where  $\mathbf{d} = \mathbf{m}_r$  is an endmember of interest that is selected from matrix  $\mathbf{M}$  for classification,  $a_{r,n}$  its corresponding abundance,  $\mathbf{U}$  of size  $L \times K - 1$  and  $\mathbf{s}$  of size  $K - 1 \times 1$  are the matrices containing the remaining endmembers and abundances, respectively. This formulation allows the definition of an OSP to annihilate  $\mathbf{U}$  from the observed

voxel  $\mathbf{y}_n$ , such as

$$\mathbf{P}_{\text{OSP}}(\mathbf{y}_n) = \mathbf{d}^T \mathbf{P}_{\mathbf{U}}^\perp(\mathbf{y}_n), \quad (2.17)$$

where

$$\mathbf{P}_{\mathbf{U}}^\perp(\mathbf{y}_n) = \mathbf{I} - \mathbf{U}\mathbf{U}^\# \quad (2.18)$$

with  $\mathbf{U}^\# = (\mathbf{U}^T \mathbf{U})^{-1} \mathbf{U}^T$  the pseudo-inverse of  $\mathbf{U}$ . The solution to this least square problem with ASC is

$$\hat{\mathbf{a}}_n = \mathbf{P}_{\mathbf{M},1}^\perp \alpha + (\mathbf{M}^T \mathbf{M})^{-1} \mathbf{1} [\mathbf{1}^T (\mathbf{M}^T \mathbf{M})^{-1} \mathbf{1}]^{-1}, \quad (2.19)$$

where  $\alpha$  is the solution to unconstrained least square problem given by

$$\alpha = (\mathbf{M}^T \mathbf{M})^{-1} \mathbf{M}^T \mathbf{y}_n \quad (2.20)$$

and

$$\mathbf{P}_{\mathbf{M},1}^\perp = \mathbf{I} - (\mathbf{M}^T \mathbf{M})^{-1} \mathbf{1} [\mathbf{1}^T (\mathbf{M}^T \mathbf{M})^{-1} \mathbf{1}]^{-1} \mathbf{1}^T \quad (2.21)$$

with  $\mathbf{1}$  a  $K \times 1$  vector of ones.

More recently, a more efficient solution based on the alternated direction method of multipliers (ADMM) was proposed [BF10]. In this strategy, the abundance constraints are taken into account as Lagrange multipliers. The general principle of ADMM, detailed in [Boy+11], is presented in Appendix A.4.1. Below, the implementation of FCLS into ADMM, also used for comparison throughout this manuscript, is summarized.

Optimizing (2.15) with respect to  $\mathbf{A}$  is equivalent to solving the following problem for each voxel:

$$\mathbf{a}_n = \arg \min_{\mathbf{a}_n} \left\{ \frac{1}{2} \|\mathbf{y}_n - \mathbf{M}\mathbf{a}_n\|_2^2 \text{ s.t. } \mathbf{a}_n \succeq \mathbf{0}_K, \mathbf{a}_n^T \mathbf{1}_K = 1 \right\}. \quad (2.22)$$

After introducing the splitting variable  $\mathbf{w}_n^{(\mathbf{A})} \in \mathbb{R}^K$  for  $n = 1, \dots, N$  such that

$$\underbrace{\begin{pmatrix} \mathbf{I}_K \\ \mathbf{1}_K^T \end{pmatrix}}_{\mathbf{Q}} \mathbf{a}_n + \underbrace{\begin{pmatrix} -\mathbf{I}_K \\ \mathbf{0}_K^T \end{pmatrix}}_{\mathbf{R}} \mathbf{w}_n = \underbrace{\begin{pmatrix} \mathbf{0}_K \\ 1 \end{pmatrix}}_{\mathbf{s}}, \quad (2.23)$$

the resulting scaled augmented Lagrangian is expressed as

$$\mathcal{L}_{\mu_n^{(\mathbf{A})}}(\mathbf{a}_n, \mathbf{w}_n^{(\mathbf{A})}, \boldsymbol{\lambda}_n^{(\mathbf{A})}) = \frac{1}{2} \|\mathbf{y}_n - \mathbf{M}\mathbf{a}_n\|_2^2 + \frac{\mu_n^{(\mathbf{A})}}{2} \|\mathbf{Q}\mathbf{a}_n + \mathbf{R}\mathbf{w}_n^{(\mathbf{A})} - \mathbf{s} + \boldsymbol{\lambda}_n^{(\mathbf{A})}\|_2^2 + \iota_{\mathbb{R}^+}(\mathbf{w}_n^{(\mathbf{A})}), \quad (2.24)$$

where  $\iota_{\mathbb{R}^+}(\cdot)$  is the indicator function defined on the positive quadrant. Algorithm 1 provides the final ADMM. Another approach to account for ANC and ASC is the projected gradient scheme that benefits from the abundance projection onto the simplex, efficiently computed by Condat [Con15].

**Algorithm 1:** ADMM optimization w.r.t.  $\mathbf{A}$ 


---

**Data:**  $\mathbf{Y}, \mathbf{A}^{(0)}, \mu_n^{(0)}$   
**Result:**  $\mathbf{A}$   
**begin**  
    **for**  $n = 1$  **to**  $N$  **do**  
         $k \leftarrow 1$   
         $\lambda_n^{(\mathbf{A})^{(0)}} = \mathbf{0}$   
         $\mathbf{w}_n^{(\mathbf{A})^{(0)}} = \mathbf{0}$   
        **while** *stopping criterium not satisfied* **do**  
             $\mathbf{a}_n^{(k)} \leftarrow \arg \min_{\mathbf{a}_n} \mathcal{L}_{\mu_n^{(\mathbf{A})^{(k-1)}}}(\mathbf{a}_n, \mathbf{w}_n^{(\mathbf{A})^{(k-1)}}, \lambda_n^{(\mathbf{A})^{(k-1)}})$   
             $\mathbf{w}_n^{(\mathbf{A})^{(k)}} \leftarrow \arg \min_{\mathbf{w}_n^{(\mathbf{A})}} \mathcal{L}_{\mu_n^{(\mathbf{A})^{(k-1)}}}(\mathbf{a}_n^{(k)}, \mathbf{w}_n^{(\mathbf{A})}, \lambda_n^{(\mathbf{A})^{(k-1)}})$   
             $\lambda_n^{(\mathbf{A})^{(k)}} \leftarrow \lambda_n^{(\mathbf{A})^{(k-1)}} + \mathbf{Q}\mathbf{a}_n^{(k)} + \mathbf{R}\mathbf{w}_n^{(\mathbf{A})^{(k)}} - \mathbf{s}$   
             $k \leftarrow k + 1$   
         $\mathbf{a}_n \leftarrow \mathbf{a}_n^{(k)}$

---

Other approaches have been proposed in the domain when data are not expected to contain pure pixels [Pla+12]. Finally, many statistical approaches based on hierarchical Bayesian models [Dob+09] and NMF were also widely used.

However, all those LMM-based approaches are subjected to several limitations because the observations may present nonlinearities and spectral variability. In the hyperspectral domain, nonlinearities may happen due to the interaction of the light that reaches the sensor with several different materials, bouncing on objects several times [NB09]. To deal with these effects, nonlinear mixing models and their corresponding unmixing algorithms appeared, raising a fertile branch of research in the hyperspectral community. Next section will present a brief summary on the topic and more comprehensive reviews can be found in [HPG14; Dob+14b].

Meanwhile, spectral variability can be caused by changes on lightening and the environment during the acquisition process, since reflectance depends on the incidence of light as well as the viewing angle. Therefore, the interest on endmember variability in the hyperspectral domain has increased in recent years [ZH14; HDT15] and many works have pointed out to this kind of approach. Indeed, in practice, all materials present intra-class variability, inducing local modifications in the spectrum of pure materials. Section 2.6 will present different ways to approach this problem based on the definition of a local simplex that will take the variability into account while trying to maintain a correctly located pure pixel vertex.

## 2.5. Nonlinear unmixing

Two main assumptions are necessary for the linear mixture assumption to hold: the mixing process must occur at a macroscopic scale and the photons that reach the sensor must interact with only one material. Otherwise, nonlinear effects must occur, as presented in Fig. 2.6. Thus, nonlinear spectral mixture models have recently

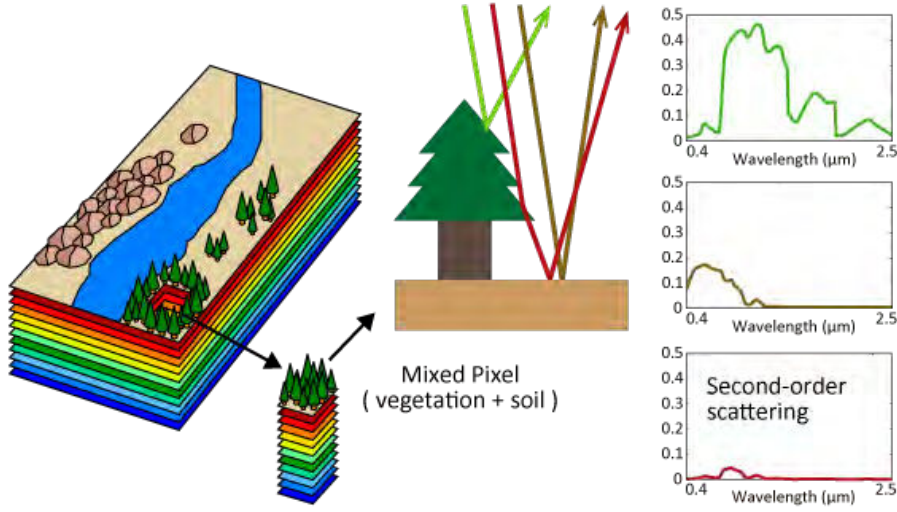


Figure 2.6.: Photons interacting with several materials produces nonlinearities.

received particular attention in hyperspectral image processing [Dob+14b; Dob+14a]. In the following, we will provide a brief summary on a group of these models that inspired the nonlinear model developed for PET applications that will be presented in Chapter 5. This group can be characterized by the following general formulation:

$$\mathbf{x}_n = \mathbf{M}\mathbf{a}_n + \boldsymbol{\mu}(\mathbf{M}, \mathbf{a}_n, \mathbf{b}_n), \quad (2.25)$$

where in addition to a linear contribution similar to LMM, the observed pixel is also composed of an additive nonlinear term  $\boldsymbol{\mu}(\cdot)$  that may depend on the factors matrix  $\mathbf{M}$ , the factor proportion coefficients  $\mathbf{a}_n$  and additional nonlinearities coefficients  $\mathbf{b}_n$ , introduced to adjust the amount of nonlinearity in each pixel. Among the models represented by (2.25) are the bilinear models [ADT11], the quadratic-linear model [Meg+14], the postnonlinear model [Alt+11] and the bilinear-bilinear model [EG14]. The next paragraphs describe the bilinear and postnonlinear models.

### 2.5.1. Bilinear models

In hyperspectral imaging, the photons suffer scattering effects before reaching the sensor. In an attempt to model these effects, a wide class of nonlinear models defines the nonlinear component  $\boldsymbol{\mu}(\mathbf{M}, \mathbf{a}_n, \mathbf{b}_n)$  from (2.25) as [ADT11]

$$\boldsymbol{\mu}(\mathbf{M}, \mathbf{a}_n, \mathbf{b}_n) = \sum_{i=1}^{K-1} \sum_{j=i+1}^K b_{i,j,n} \mathbf{m}_i \circ \mathbf{m}_j, \quad (2.26)$$

with

$$\mathbf{m}_i \circ \mathbf{m}_j = \begin{bmatrix} m_{1i}m_{1j} \\ \vdots \\ m_{Li}m_{Lj} \end{bmatrix}. \quad (2.27)$$

The set of nonlinearity coefficients  $\{b_{i,j,n}\}$  adjusts the amount of nonlinearity between each pair of materials  $\mathbf{m}_i$  and  $\mathbf{m}_j$  in the  $n^{th}$  voxel. The definition of these coefficients, as well as the constraints considered for each variable, is what mainly differentiates the various bilinear models of the literature.

The model proposed in [Som+09; NB09] includes the coefficients  $\{b_{i,j,n}\}$  into the nonnegativity and sum-to-one constraints from the factor proportions, yielding

$$\mathbf{x}_n = \mathbf{M}\mathbf{a}_n + \sum_{i=1}^{K-1} \sum_{j=i+1}^K b_{i,j,n} \mathbf{m}_i \circ \mathbf{m}_j \quad (2.28)$$

with

$$\begin{cases} a_{kn} \geq 0, & \forall k, \forall n \\ b_{i,j,n} \geq 0, & \forall n, \forall i \neq j \\ \sum_{k=1}^K a_{kn} + \sum_{i=1}^{K-1} \sum_{j=i+1}^K b_{i,j,n} = 1, & \forall n \end{cases} \quad (2.29)$$

When  $b_{i,j,n} = 0, \forall i \neq j$ , the model in (2.28) reduces to the standard LMM. However, when the coefficients are non-zero, the factor proportions no longer follow the sum-to-one constraint.

The approach introduced in [Fan+09] defines the nonlinearity coefficients as the product of the factor proportions  $b_{i,j,n} = a_{in}a_{jn}$ , leading to

$$\mathbf{x}_n = \mathbf{M}\mathbf{a}_n + \sum_{i=1}^{K-1} \sum_{j=i+1}^K a_{in}a_{jn} \mathbf{m}_i \circ \mathbf{m}_j \quad (2.30)$$

with the standard unmixing constraints applied to the factor proportions. The rationale behind this relation between the nonlinear coefficients and the amount of linear contributions  $a_{in}$  and  $a_{jn}$  comes from the fact that a pixel containing more of a given material is more subjected to nonlinear interactions. If a material is not present in one pixel, it cannot interact with other materials. However, this bilinear model is not an extension of the LMM.

In order to relate both the nonlinear coefficients to the linear factor proportions and provide an extension of the LMM, Halimi et al. [Hal+11] introduced a generalized bilinear model (GBM) that weights the products of the factor proportions  $a_{in}a_{jn}$  with additional free parameters  $\gamma_{i,j,n} \in (0, 1)$ , leading to  $b_{i,j,n} = \gamma_{i,j,n}a_{in}a_{jn}$  and

$$\mathbf{x}_n = \mathbf{M}\mathbf{a}_n + \sum_{i=1}^{K-1} \sum_{j=i+1}^K \gamma_{i,j,n} a_{in}a_{jn} \mathbf{m}_i \circ \mathbf{m}_j. \quad (2.31)$$

### 2.5.2. Postnonlinear mixing model

Altmann et al. [Alt+11] proposed a nonlinear model that introduces a second-order polynomial expansion of the nonlinearity

$$\begin{aligned}\boldsymbol{\mu}(\mathbf{M}, \mathbf{a}_n, \mathbf{b}_n) &= b_n(\mathbf{M}\mathbf{a}_n) \circ (\mathbf{M}\mathbf{a}_n), \\ &= b_n \sum_{i=1}^K \sum_{j=1}^K a_{in} a_{jn} \mathbf{m}_i \circ \mathbf{m}_j,\end{aligned}\tag{2.32}$$

leading to

$$\mathbf{x}_n = \mathbf{M}\mathbf{a}_n + b_n \sum_{i=1}^K \sum_{j=i+1}^K a_{in} a_{jn} \mathbf{m}_i \circ \mathbf{m}_j.\tag{2.33}$$

This model has shown great flexibility on describing several nonlinearities not only for unmixing purposes [Alt+11] but also to detect nonlinear mixtures in the observed image [ADT13]. Moreover, this model allows the amount of nonlinearity to be governed by a unique parameter  $b_n$  in each pixel, differently from the previous bilinear models. Additionally to the interaction between materials, it also models the interaction of similar materials.

## 2.6. Handling the variability in linear models

In the hyperspectral domain, due to the scene environment (e.g., different lightening, atmospheric effects) or the intrinsic characteristics of the object, the assumption that a given material can be fully characterized by a single signature may not sufficiently describe reality.

Considering that the endmembers are sources, and that the abundances are mixing coefficients, in the hyperspectral imaging domain, endmember variability refers to the fact that a spectral signature of a given material can vary either in the spatial domain of the image, the temporal domain, or both. In this work, we will focus on spatial variability, which has a direct correlation to kinetics variability in the PET domain.

In order to deal with spatial spectral variability, various statistical and deterministic models were proposed in the hyperspectral unmixing literature [ZH14; DCJ16]. These methods, illustrated in Fig. 2.7, can be categorized according to their fundamental basis in four different classes: endmember bundles, local spectral unmixing, computational models and parametric models (that will not be further developed in this manuscript). In the following, a brief summary of the first three categories will be presented. The interested reader is invited to consult detailed surveys on the domain [ZH14; DCJ16; Som+11].



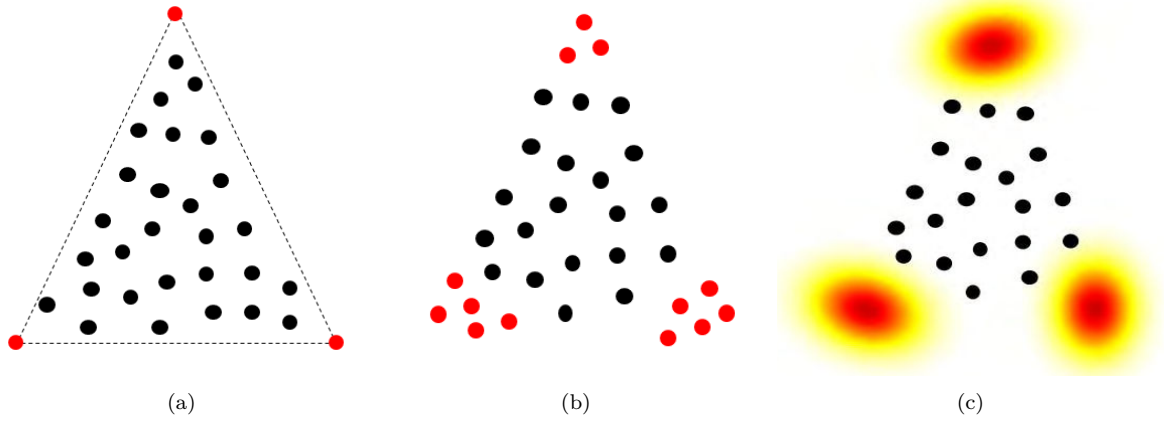


Figure 2.7.: Illustration of a simplex with : (a) endmember without variability, (b) endmember bundles and (c) endmembers as a multivariate probability distribution [HDT15].

### 2.6.1. Endmember bundles

In the first approach, different spectra describing the response of one material under various experimental conditions are grouped into one set (or *bundle*) that will characterize one endmember. The sets may either be previously available or be learned from data. The simplest way to automate the extraction of each bundle dictionary consists in randomly choosing subsets and then estimating their internal endmembers [Som+12]. Recently, another approach for endmember bundles extraction was proposed by [Uez+16b]. It uses the shape of the spectral curve to identify a set of similar endmember spectra within each class, making it more robust to illumination variations that produce scale changes. Once the bundles are grouped, the task becomes abundance estimation that may be done with any state-of-the-art unmixing algorithms [BF10], or techniques of sparse unmixing [IBP11], Gaussian processes [Uez+16a] or endmember selection procedures [Hey+16]. Each element of a bundle has its own associated abundance map. The global abundance of a bundle is finally computed by simply summation of the contributions of each abundance instance of the corresponding bundle.

### 2.6.2. Local spectral unmixing

In the local spectral unmixing framework, unmixing is conducted in data subsets, i.e., both endmembers and corresponding abundances are computed for each previously defined subgroup of data. The idea here is that variability may be mitigated through a local approach. This is especially true for hyperspectral imaging, where different lightening in a whole scene may provide different endmembers for a single material, while this material may be locally expressed by a single endmember, assuming uniformity in the chosen subsets [ZGC13]. The simplest way to construct these subsets is through sliding windows [Goe+13; Can+11], even though it does not ensure meaningful samples. To optimize the segmentation of samples, a strategy based on binary partition trees (BPT) [Veg+14b] is applied. BPT provides meaningful regions of the image at different scales through

a hierarchical segmentation, where, at each iteration, the two most similar regions are merged. A drawback of local spectral unmixing is the impossibility of acquiring global abundances, which is generally expected in unmixing approaches. A solution is to perform *a posteriori* grouping of these local abundances.

### 2.6.3. Computational models

In this thesis, we will be especially interested in computational models. Contrary to bundles or local approaches, these techniques explicitly include the variability into the estimation model. Therefore, a material is often represented with a reference endmember that is allowed to locally vary. The challenge here is to correctly determine the flexibility trade-off that will capture variability while avoiding endmember merging, i.e., to mix endmember information within the variability. Moreover, as the variability itself is often not explicitly modeled, its physical interpretation is a difficult task. Both statistical and deterministic approaches were proposed with this underlying philosophy and are detailed hereafter.

#### Statistical approaches

Statistical approaches consist in modelling endmembers as multivariate probability distributions. Among these approaches, normal compositional models (NCM) [Ech+10] allow the spatially indexed endmembers to follow a normal distribution, i.e.,

$$y_{ln} = \sum_{k=1}^N a_{kn} \mathbf{m}_{kn}, \text{ with } \mathbf{m}_{kn} \sim \mathcal{N}(\bar{\mathbf{m}}_k, \sigma^2 \mathbf{I}_L). \quad (2.34)$$

A generalization of this method, proposed in [HDT15], allows for a deeper expression of the variability with an additive noise that accounts for mismodelling. The approach, denoted generalized NCM (GNCM), solves the following problem

$$\begin{aligned} y_{ln} &= \sum_{k=1}^N a_{kn} \mathbf{m}_{kn} + \mathbf{r}_n, \\ \mathbf{m}_{kn} &\sim \mathcal{N}(\bar{\mathbf{m}}_k, \sigma^2 \mathbf{I}_L), \quad \mathbf{r}_n \sim \mathcal{N}(\mathbf{0}_L, \Psi_n^2 \mathbf{I}_L), \end{aligned} \quad (2.35)$$

where  $\mathbf{r}_n$  is an additive noise and  $\Psi_n^2$  is the noise variance for which a prior enforcing small values is assigned. This formulation provides information on the spatial and spectral variability of each material at each pixel.

Another method similar to the NMC is the Beta compositional model (BCM). It replaces the endmember Gaussian prior by the beta distribution, which is better adapted for some materials, such as the grass. The BCM mixture model proposed in [Du+14] writes

$$y_{ln} = \sum_{k=1}^N a_{kn} \mathbf{m}_{kn}, \text{ with } \mathbf{m}_{kn} \sim \mathcal{B}(\alpha_{l,k}, \beta_{l,k}), \quad (2.36)$$

where  $\mathcal{B}$  is the beta distribution and its corresponding parameters  $\alpha_{l,k}$  and  $\beta_{l,k}$  are previously learned from data.

### Deterministic approaches

A novel class of methodologies promotes a more flexible modelling of the variability through its explicit mathematical expression. An extended LMM (ELMM) accounting for scaling variations was proposed in [Veg+14a; Dru+16]. This model is particularly relevant when dealing with hyperspectral images since changes on lightening in a scene induce the same spectral response to be represented at different scales. The ELMM simplifies the Hapke model [Hap81; Hap93] while taking into account the geometry of the scene. It is mathematically defined as

$$\mathbf{X} = \mathbf{M}(\Psi \circ \mathbf{A}) + \mathbf{R}, \quad (2.37)$$

where  $\mathbf{R}$  is the matrix accounting for noise and mismodelling errors, “ $\circ$ ” is the point-wise product and  $\Psi$  is a  $K \times N$  matrix containing the scaling factors that describe local variations in the spectral response.

To further address the problem of hyperspectral variability, Thouvenin et al. [TDT16a; TDT16b] proposed an additive and spatially varying representation of endmember perturbation. The final model, called Perturbed LMM (PLMM), is defined as

$$\mathbf{y}_n = \sum_{k=1}^K a_{k,n}(\mathbf{m}_k + \mathbf{d}\mathbf{m}_{k,n}) + \mathbf{r}_n, \quad \text{for } n = 1, \dots, N, \quad (2.38)$$

where  $\mathbf{d}\mathbf{m}_{k,n}$  denotes the perturbation of the  $k$ th endmember in the  $n$ th pixel and  $\mathbf{r}_n$  once again accounts for the noise. While providing relevant information on the spatial distribution of the variability in a scene, the PLMM does not address the semantic ambiguity resulting from the physical nature of the observed variability [Tho17].

Inspired by the robust NMF (rNMF) [Zha+11] models from the audio literature, F  votte and Dobigeon [FD15] proposed a robust LMM (rLMM) that accounts for outliers in the dataset through an additive spatially indexed term. The rLMM model writes

$$\mathbf{y}_n = \sum_{k=1}^K a_{k,n} \mathbf{m}_k + \mathbf{f}_n, \quad (2.39)$$

where  $\mathbf{f}_n$  denotes the outlier term. A  $\ell_{2,1}$  norm regularizer is applied to induce sparsity in  $\mathbf{f}_n$ , since outliers are expected to be exceptions on the overall data.

## 2.7. Conclusion

This chapter showed the interest of blind source separation methods, which, under different denominations, are the key tool for analysing various datasets, ranging from audio recording to spectral imagery or functional imaging. In most of the cases, the aim of BSS is twofold: to provide a compact representation of data while providing physically meaningful factors.

Often appearing as factor analysis or matrix factorization in the dynamic PET literature, it has become a valuable tool for the extraction of TACs representative of body tissues. Many priors previously introduced by the PET community as constraints or penalizations are also explored throughout this thesis.

For hyperspectral imagery applications, BSS was formulated as unmixing and introduced many concepts that were essential to the development of this thesis. Among them is spectral variability that can be generalized as endmember or factor variability so as to fit in other contexts. A drawback from all variability models is the several constraints and penalizations applied on the parameters associated with variability that have to be carefully chosen so as to limit variation overfitting. In this chapter, factor variability was presented for hyperspectral imagery applications. However, it may come at hand in other domains when the signal is not expected to follow a linear mixing process. For each application, additional *a priori* information may be needed in order to adapt the model accordingly.

In the following chapters, the methods and techniques developed with the use of the concepts herein presented will be detailed.

## Part II.

# Development of algorithms for dynamic PET images unmixing



# Unmixing dynamic PET images with variable specific binding kinetics

The publications related to this chapter are [[Cav+17b](#); [Cav+17a](#); [Cav+18b](#)]

## Contents

3.1	Introduction . . . . .	<b>59</b>
3.2	Variability on specific binding kinetics . . . . .	<b>61</b>
3.3	Method . . . . .	<b>62</b>
3.3.1	Specific binding linear mixing model (SLMM) . . . . .	62
3.3.2	Problem formulation . . . . .	66
	Factor proportion penalization . . . . .	66
	Factor penalization . . . . .	68
	Variability penalization . . . . .	68
3.4	Algorithm implementation . . . . .	<b>68</b>
3.4.1	PALM: general principle . . . . .	69
3.4.2	Optimization with respect to $\mathbf{M}$ . . . . .	70
3.4.3	Optimization with respect to $\mathbf{A}$ . . . . .	71
3.4.4	Optimization with respect to $\mathbf{B}$ . . . . .	72
3.5	Evaluation on Synthetic Data . . . . .	<b>73</b>
3.5.1	Synthetic data generation . . . . .	73
3.5.2	Compared methods . . . . .	77
3.5.3	Hyperparameter influence . . . . .	79
3.5.4	Results . . . . .	79
3.5.5	Impact of the deconvolution . . . . .	83
3.6	Evaluation on Real Data . . . . .	<b>86</b>
3.6.1	PET data acquisition . . . . .	86
3.6.2	Results . . . . .	87
3.7	Discussion . . . . .	<b>94</b>
3.7.1	Performance of the method . . . . .	94
3.7.2	Flexibility of the method . . . . .	95
3.8	Conclusion . . . . .	<b>96</b>

## 3.1. Introduction

As described in Chapter 1, the analysis of dynamic PET images, in particular the quantification of the kinetic properties of the tracer, requires the extraction of tissue time-activity-curves (TACs) in order to estimate the parameters from compartmental modelling [[Inn+07](#)]. Section 2.3 summarized several blind source separation

(BSS) methods that have been applied to estimate these elementary TACs and their corresponding proportions from dynamic PET images [Bar80; CBD84; Wu+95; SDG00; Lee+01b].

The approach proposed in this chapter follows the same line as NMF or nonnegative FADS. It aims at decomposing each PET voxel TAC into a weighted combination of pure physiological factors, representing the elementary TACs associated with the different tissues present within the voxel. This factor modelling is enriched with a sum-to-one constraint to the factor proportions, so that they can be interpreted as tissue percentages within each voxel. In particular, this additional constraint explicitly solves the scaling ambiguity inherent to any NMF models, which has proven to increase robustness as well as interpretability. As detailed in Section 2.4, this BSS technique, referred to as *unmixing* or *spectral mixture analysis*, originates from the geoscience and remote sensing literature [Bio+12] and has proven its interest in other applicative contexts, such as microscopy [Hua+11] and genetics [DB12].

However, factor TACs to be recovered cannot always be assumed to have constant kinetic patterns, as implicitly considered in conventional methods. Considering both the 2-tissue and reference compartment models introduced in Chapter 1, the assumption of constant kinetic patterns seems appropriate for the blood compartment as well as non-specific binding tissues, since they present some homogeneity besides some perfusion difference (e.g. white matter versus gray matter). Therefore, their contribution to the voxel TAC should be fairly proportional to the fraction of this type of tissue in the voxel. However, things get different regarding the specific binding class, as the TAC associated with this tissue is nonlinearly dependent on both the perfusion and the concentration of the radiotracer target. The spatial variation in target concentration is in part governed by differences in the  $k_3$  and  $k_4$  kinetic parameters, which nonlinearly modify the shape of the TAC characterizing this particular class.

The main motivation of this chapter is to propose a more accurate description of the tissues and kinetics composing the voxels in dynamic PET images, in particular for those affected by specific binding. To this end, this work proposes to explicitly model the nonlinear variability inherent to the TAC corresponding to specific binding, by allowing the corresponding factor to vary spatially. This variation is approximated by a linear expansion over the atoms of a dictionary, which have been learned beforehand by conducting a principal component analysis on a learning dataset.

The sequel of this chapter is organized as follows. Section 3.2 provides the physical motivation of this work. The proposed mixing-based analysis model is described in Section 3.3. Section 3.4 presents the corresponding unmixing algorithm able to recover the factors, their corresponding proportions in each voxel and the variability maps. Simulation results obtained with synthetic data and experimental results on real data are reported in Sections 3.5 and 3.6, respectively. Section 3.7 discuss the significance of the results and Section 3.8 concludes the chapter.



### 3.2. Variability on specific binding kinetics

In this work, we raise the hypothesis that TACs cannot be assumed to be driven by constant kinetic parameters over time, as implicitly considered in general factor analysis methods from the dynamic PET literature seen in Section 2.3. Indeed, depending on the concentration of the biomarker, they may suffer from fluctuations in the exchange rate of tracer between the free compartment and a specifically bound ligand compartment in high-uptake region (see Fig. 1.12), which induces inaccuracies on compartment modelling [Gun+97][Inn+07]. For instance, Houston et al. [HS97] studied the performance of factor analysis on renal dynamic images and arrived to the conclusion that they work well when the compartments are homogeneous and non-homogeneous without pathology. However, the presence of an abnormality in the tissues lowers the performance of factor analysis. Muzi et al. [Muz+05] discussed the accuracy of parameter estimates for tumor regions and underlined high errors for the parameters related to specific binding, namely 26% for  $k_3$  and 49% for  $k_4$ . These results were further confirmed by Schiepers et al. [Sch+07]. More specifically, they studied the kinetics of lesioned regions that were tumor and treatment change predominant, showing that variations on  $k_3$  and  $k_4$  may allow for differentiation. Bai et al. [BBC13] further discussed nonuniformity in intratumoral uptake and its impact on predicting treatment response and tumor aggressiveness. Indeed, intratumoral spatial heterogeneity may indicate differences on malignant potential. In this context, a big challenge for precision medicine is the rigorous detection of regions with primary lesion or metastasis as sequencing a portion of the tumor may miss therapeutically relevant information [Sub16]. Eary et al. [Ear+08] showed that spatial heterogeneity can be used to predict tumor biological aggressiveness while Yu et al. [Yu+09] found that abnormal nodes were more heterogeneous than normal tissues in PET images. In stroke neuroinflammation, some regions may also be more or less affected by inflammation or lack of oxygen. To illustrate the hypothesis, Fig. 3.1 depicts some samples of the TACs belonging to the high-uptake tissue of 10 different patients that were manually labelled by an expert based on a magnetic resonance imaging (MRI) acquisition. The real images from which the TACs were extracted were produced from the [18F]-DPA-714 injection in each patient and acquired in 3D mode using an Ingenuity TOF Camera from Philips Medical Systems. The dynamic emission scan consisted of 31 frames with a total scan duration of 59 minutes ( $6 \times 10$ ,  $8 \times 30$ ,  $4 \times 60$ ,  $5 \times 120$ ,  $8 \times 300$  seconds). The presented TACs were normalized with the highest intensity of its corresponding image.

In those images, at least 6 patients show a significant variation between the specific binding TACs in both shape and area under the curve (AUC). The two patients in the last column have suffered a stroke while the others are healthy subjects. Indeed, stroke patients show great variability, but some of the normal subjects as well. Nonetheless, this fluctuation phenomenon has not been taken into account by the decomposition models from the literature. In the attempt of modelling this variability neglected in the dynamic PET domain, this work is inspired by solutions from the hyperspectral unmixing domain, detailed in Section 2.6.

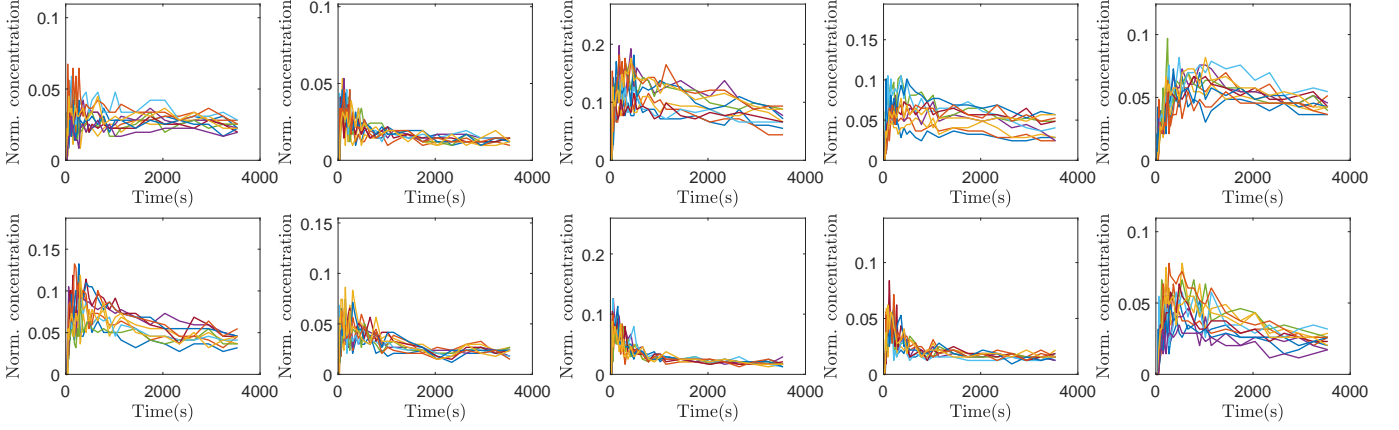


Figure 3.1.: Samples of TACs inside the high-uptake region (thalamus for healthy subjects and thalamus plus stroke for unhealthy subjects) of 10 real images of different patients, as delimited by a specialist.

### 3.3. Method

#### 3.3.1. Specific binding linear mixing model (SLMM)

Consider  $N$  voxels of a 3D dynamic PET image acquired at  $L$  successive time-frames. First, we omit the spatial blurring induced by the point spread function (PSF) of the instrument and any measurement noise. The TAC in the  $n^{th}$  voxel ( $n \in \{1, \dots, N\}$ ) over the  $L$  time-frames is denoted  $\mathbf{x}_n = [x_{1,n}, \dots, x_{L,n}]^T$ . Akin to various BSS techniques introduced in Chapter 2 and following the linear mixing model (LMM) for instance advocated in the PET literature by [Bar80], each TAC  $\mathbf{x}_n$  is assumed to be a linear combination of  $K$  *elementary factors*  $\mathbf{m}_k$

$$\mathbf{x}_n = \sum_{k=1}^K \mathbf{m}_k a_{k,n} \quad (3.1)$$

where  $\mathbf{m}_k = [m_{1,k}, \dots, m_{L,k}]^T$  denotes the pure TAC of the  $k^{th}$  tissue type and  $a_{k,n}$  is the factor proportion of the  $k^{th}$  tissue in the  $n^{th}$  voxel. The factors  $\mathbf{m}_k$  ( $k = 1, \dots, K$ ) correspond to the kinetics of the radiotracer in a particular type of tissue in which they are supposed spatially homogeneous. For instance, the experiments conducted in this work and described in Sections 3.5 and 3.6 consider 3 types of tissues that fall into this category: the blood, the non-specific gray matter and the white matter.

Additional constraints regarding these sets of variables are assumed. First, since the elementary TACs are expected to be nonnegative, the factors are constrained as

$$m_{l,k} \geq 0, \quad \forall l, k. \quad (3.2)$$

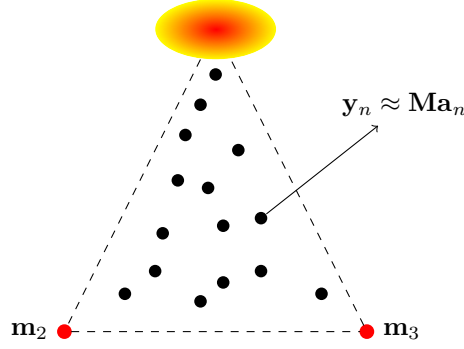


Figure 3.2.: Simplex with one varying factor.

Moreover, nonnegativity and sum-to-one constraints are assumed for all the factor proportions ( $n = 1, \dots, N$ )

$$\forall k \in \{1, \dots, K\}, a_{k,n} \geq 0 \quad \text{and} \quad \sum_{k=1}^K a_{k,n} = 1. \quad (3.3)$$

For a given voxel indexed by  $n$ , this sum-to-one constraint (3.3) enforces the mixing coefficients  $a_{k,n}$  ( $k = 1, \dots, K$ ) to be interpreted as concentrations. As discussed in Section 2.4, all factor proportion vectors  $\mathbf{a}_n$  ( $n = 1, \dots, N$ ) lie inside the unit  $(K - 1)$ -simplex. Similarly, the TAC  $\mathbf{x}_n$  belongs to the convex set whose vertices are the columns of matrix  $\mathbf{M} = [\mathbf{m}_1, \dots, \mathbf{m}_K]$  containing the factors, represented by a  $(K - 1)$ -simplex in  $\mathbb{R}^L$  [Bio+12].

More importantly, when factors are affected by possibly nonlinear and spatially varying fluctuations within the image, the conventional NMF-like linear mixing model (3.1) no longer provides a sufficient description of data. Therefore, as detailed in Section 2.6, factor variability has received increased interest in the hyperspectral imagery literature over recent years as it allows changes on lightening and the environment to be taken into account [ZH14; HDT15]. The perturbed LMM (PLMM) proposed in [TDT16a] and detailed in Section 2.6.3 further addresses this problem. In the dynamic PET image framework, factor variability is expected to mainly affect the TAC associated with specific binding, denoted  $\mathbf{m}_1$ , while the possible variabilities in the TACs  $\mathbf{m}_k$  ( $k \in \{2, \dots, K\}$ ) related to tissues devoid of a specifically bound compartment are supposed weaker and neglected in this study. Fig. 3.2 illustrates this idea with a simplex defined by three factors, where only one is allowed to vary. Since this so-called specific binding factor (SBF) is assumed to vary spatially, it will be spatially indexed. Thus, adapting the PLMM approach to our problem, the SBF in a given voxel will be modelled as a spatially-variant additive perturbation affecting a nominal and common SBF  $\bar{\mathbf{m}}_1$ :

$$\mathbf{m}_{1,n} = \bar{\mathbf{m}}_1 + \delta\mathbf{m}_{1,n}, \quad (3.4)$$

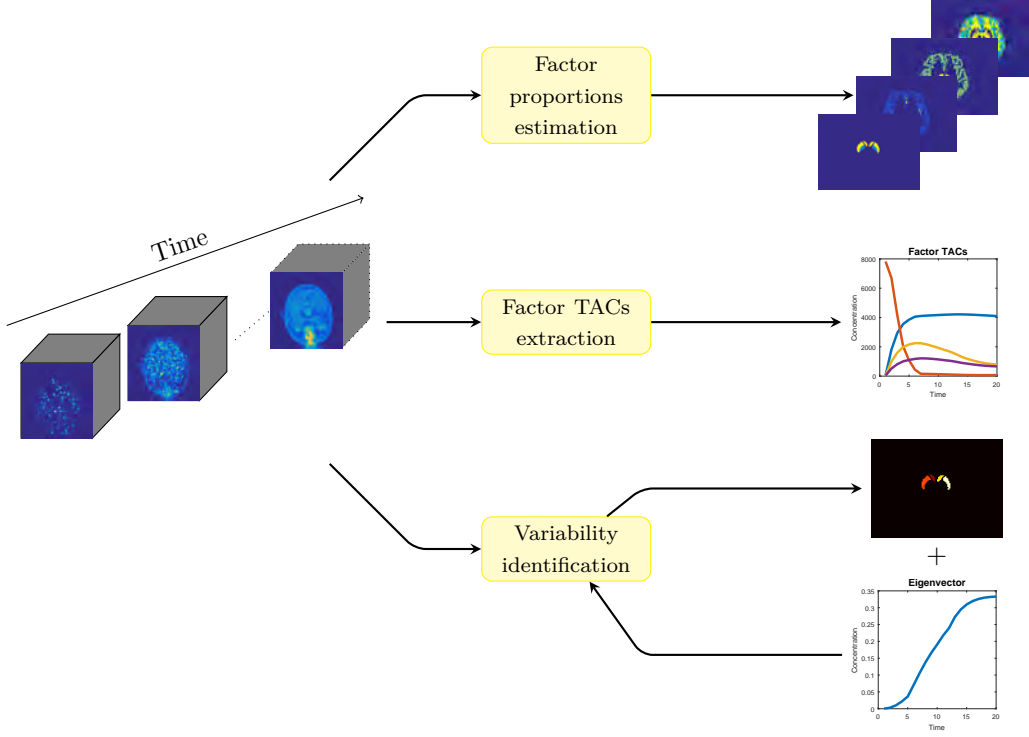


Figure 3.3.: Graphical representation of SLMM.

where the additive term  $\delta \mathbf{m}_{1,n}$  describes its spatial variability over the image. However, recovering the spatial fluctuation  $\delta \mathbf{m}_{1,n}$  in each image voxel is a high-dimensional problem. To reduce this dimensionality, the variations will be assumed to lie inside a subspace of small dimension  $N_v \ll L$ . As a consequence, similarly to the strategy followed by Park et al. [PDH14], the additive terms  $\delta \mathbf{m}_{1,n}$  ( $n \in \{1, \dots, N\}$ ) are supposed to be approximated by the linear expansion

$$\delta \mathbf{m}_{1,n} = \sum_{i=1}^{N_v} b_{i,n} \mathbf{v}_i, \quad (3.5)$$

where the  $N_v$  variability basis elements  $\mathbf{v}_1, \dots, \mathbf{v}_{N_v}$  can be chosen beforehand, e.g., by conducting a PCA on a learning set composed of simulated or measured SBFs (see Section 3.5.1 for further details on the dictionary generation). The PCA aims at extracting the main variability patterns, while allowing for dimension reduction. Thus, the set of coefficients  $\{b_{1,n}, \dots, b_{N_v,n}\}$  quantify the amount of variability in the  $n^{th}$  voxel.

Combining the linear mixing model (3.1), the perturbation model (3.4) and its linear expansion (3.5), the voxel TACs are described according to the following so-called specific binding linear mixing model (SLMM)

$$\mathbf{x}_n = a_{1,n} \left( \bar{\mathbf{m}}_1 + \sum_{i=1}^{N_v} b_{i,n} \mathbf{v}_i \right) + \sum_{k=2}^K a_{k,n} \mathbf{m}_k. \quad (3.6)$$

To be fully comprehensive and motivated by the findings of [Hen+14], this work also proposes to explicitly model the PET scan point spread function (PSF), combining a deconvolution step jointly with parameter

estimation. Therefore, the need to explicitly model the PSF and, further on, perform a joint PSF deconvolution. We will denote by  $\mathbf{H}$  the linear operator that computes the 3D convolution by some known and spatially invariant PSF. In brain imaging using a clinical PET scanner, it is a widely admitted approximation, since the degradation of the scanner resolution mainly affects the borders of the field-of-view [RQS13; Meh+17]. This deconvolution step relies on the assumption that the blurring matrix  $\mathbf{H} \in \mathbb{R}^{N \times N}$  is a block circulant matrix with circulant blocks (BCCB), which corresponds to convolve the image with an isotrope filter using cyclic convolution boundaries. Finally, the  $L \times N$  matrix  $\mathbf{Y} = [\mathbf{y}_1, \dots, \mathbf{y}_N]$  of the TACs associated with the image voxels can be written

$$\mathbf{Y} = \mathbf{M}\mathbf{A}\mathbf{H} + \underbrace{[\mathbf{E}_1 \mathbf{A} \circ \mathbf{V}\mathbf{B}]}_{\Delta} \mathbf{H} + \mathbf{R} \quad (3.7)$$

where  $\mathbf{M} = [\mathbf{m}_1, \dots, \mathbf{m}_K]$  is a  $L \times K$  matrix containing the factor TACs,  $\mathbf{A} = [\mathbf{a}_1, \dots, \mathbf{a}_n]$  is a  $K \times N$  matrix composed of the factor proportion vectors, “ $\circ$ ” is the Hadamard point-wise product,  $\mathbf{E}_1$  is the matrix  $[\mathbf{1}_{L,1} \mathbf{0}_{L,K-1}]$ ,  $\mathbf{V} = [\mathbf{v}_1, \dots, \mathbf{v}_{N_v}]$  is the  $L \times N_v$  matrix containing the basis elements used to expand the spatial variability of the SBF,  $\mathbf{B} = [\mathbf{b}_1, \dots, \mathbf{b}_n]$  is the  $N_v \times N$  matrix containing the intrinsic proportions, and  $\mathbf{R} = [\mathbf{r}_1, \dots, \mathbf{r}_N]^T$  is the  $L \times N$  matrix accounting for noise and mismodelling. Note that if  $\mathbf{B} = \mathbf{0}$  and  $\mathbf{H} = \mathbf{I}$ , the model in (3.7) reduces to the conventional linear mixing model generally assumed by factor model techniques like NMF and ICA. A graphical representation of this final model is shown in Fig. 3.3.

While the noise associated with the count rates is traditionally modelled by a Poisson distribution [SV82], postprocessing corrections and filtering operated by modern PET systems significantly alter the nature of the noise corrupting the final reconstructed images. Modelling the noise on this final data is a highly challenging task [WTB94]. However, as demonstrated by [Fes94], pre-corrected PET data can be sufficiently approximated by a Gaussian distribution, even though this is not an optimal assumption. As a consequence, in this work, the noise vectors  $\mathbf{r}_n = [r_{1,n}, \dots, r_{L,n}]$  ( $n \in \{1, \dots, N\}$ ) are assumed to be normally distributed. A more general setting will be considered in the next chapter by the use of the  $\beta$ -divergence. Moreover, without loss of generality, all vector components  $r_{\ell,n}$  ( $\ell = 1, \dots, L$  and  $n = 1, \dots, N$ ) will be assumed to be independent and identically distributed. This assumption seems to evade any spatial and temporal correlations that may characterize the noise generally affecting the reconstructed PET images [TS15]. However, the proposed model can be easily generalized to handle colored noise by weighting the model discrepancy measure, according to the noise covariance matrix, as done by [Fes94]. Alternatively, after diagonalizing the noise covariance matrix, the PET image to be analysed can undergo a conventional whitening pre-processing step [Thi+06; Bul+01; Tur+03] (see Appendix A.2 for further details on the whitening transform).

In addition to the nonnegativity constraints applied to the elementary factors (3.2) and factor proportions (3.3), the intrinsic variability proportion matrix  $\mathbf{B}$  is also assumed to be nonnegative, mainly to avoid spurious ambiguity, i.e.,

$$\mathbf{B} \succeq \mathbf{0}_{N_v, N}. \quad (3.8)$$

We accordingly fix the nominal SBF  $\bar{\mathbf{m}}_1$  with a robust estimation of the TAC chosen as a lower bounding signature of a set of previously generated or measured SBF TACs. This means that a negative bias on the SBF is artificially introduced to model the spatially-varying SBF TACs  $\mathbf{m}_{1,n}$  ( $n \in \{1, \dots, N\}$ ). This is alternatively compensated by a variability that is distorted by the same quantity but positively. This constraint is chosen to avoid a high correlation between the other factor TACs and  $\sum_{i=1}^{N_v} \mathbf{v}_i b_{i,n}$  when  $b_{i,n}$  is allowed to be negative. Capitalizing on this model, the unmixing-based analysis of dynamic PET images is formulated in the next paragraph.

### 3.3.2. Problem formulation

The SLMM (3.7) and constraints (3.2), (3.3) and (3.8) can be combined to formulate a constrained optimization problem. Fig. 3.4 provides an overall view of the optimization scheme. In order to estimate the matrices  $\mathbf{M}$ ,  $\mathbf{A}$ ,  $\mathbf{B}$ , a proper cost function is defined. The data-fitting term is defined as the Frobenius norm  $\|\cdot\|_F^2$  of the difference between the dynamic PET image  $\mathbf{Y}$  and the proposed data modelling  $\mathbf{MAH} + \Delta$ . This corresponds to the negative log-likelihood under the Gaussian noise assumption. Since the problem is ill-posed and non-convex, additional regularizers become essential. In this chapter, we propose to define penalization functions  $\Phi$ ,  $\Psi$  and  $\Omega$  to reflect the available *a priori* knowledge on  $\mathbf{M}$ ,  $\mathbf{A}$  and  $\mathbf{B}$ , respectively. The optimization problem is then defined as

$$(\mathbf{M}^*, \mathbf{A}^*, \mathbf{B}^*) \in \arg \min_{\mathbf{M}, \mathbf{A}, \mathbf{B}} \left\{ \mathcal{J}(\mathbf{M}, \mathbf{A}, \mathbf{B}) \text{ s.t. (3.2), (3.3), (3.8)} \right\} \quad (3.9)$$

with

$$\mathcal{J}(\mathbf{M}, \mathbf{A}, \mathbf{B}) = \frac{1}{2} \left\| \mathbf{Y} - \mathbf{MAH} - \left[ \mathbf{E}_1 \mathbf{A} \circ \mathbf{VB} \right] \mathbf{H} \right\|_F^2 + \alpha \Phi(\mathbf{A}) + \beta \Psi(\mathbf{M}) + \lambda \Omega(\mathbf{B}) \quad (3.10)$$

where the parameters  $\alpha$ ,  $\beta$  and  $\lambda$  control the trade-off between the data fitting term and the penalties  $\Phi(\mathbf{A})$ ,  $\Psi(\mathbf{M})$  and  $\Omega(\mathbf{B})$ , described hereafter.

#### Factor proportion penalization

The factor proportions representing the amount of different tissues are assumed to be spatially smooth, since neighbouring voxels may contain the same tissues. We thus penalize the energy of the spatial gradient

$$\Phi(\mathbf{A}) = \frac{1}{2} \|\mathbf{AS}\|_F^2, \quad (3.11)$$

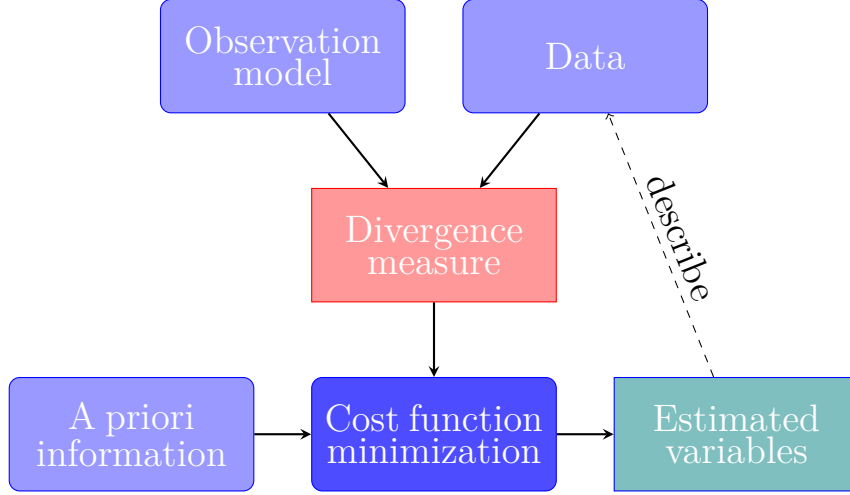


Figure 3.4.: Estimation scheme

where  $\mathbf{S}$  is the operator computing the first-order spatial finite differences. In our case, the considered PET image is of three dimensions, leading to the neighbourhood system depicted in Fig. (3.5). The first order finite differences in the three directions  $x, y$  and  $z$  are then defined for each pixel as

$$[\mathbf{AS}]_{x,y,z} = \begin{bmatrix} a_{x,y,z} - a_{x-1,y,z} \\ a_{x,y,z} - a_{x,y-1,z} \\ a_{x,y,z} - a_{x,y,z-1} \end{bmatrix}.$$

On the boundaries, finite differences are not taken into account. The transposed matrix  $\mathbf{S}^T$ , which will appear in gradient computation of the penalization, results also in a first-order finite difference calculus but in the other sense for each direction. Note also that the application of both  $\mathbf{S}$  and  $\mathbf{S}^T$  leads to a discrete 3D Laplacian.

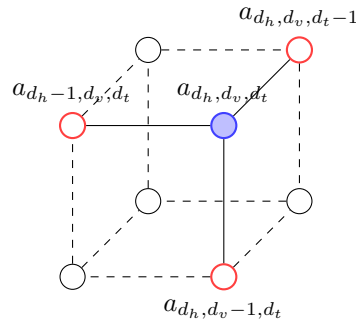


Figure 3.5.: Diagram of voxel neighbourhood structure for three dimensions, where the blue voxel is the one considered and the red ones are its direct neighbours.

### Factor penalization

The chosen factor penalization benefits from the availability of rough factor TACs estimates  $\mathbf{M}^0 = [\bar{\mathbf{m}}_1^0, \dots, \mathbf{m}_K^0]$ . Thus, we propose to enforce similarity (in terms of Euclidean distances) between these primary estimates and the factor TACs to be recovered

$$\Psi(\mathbf{M}) = \frac{1}{2} \|\mathbf{M} - \mathbf{M}^0\|_F^2. \quad (3.12)$$

Classical penalizations found in the hyperspectral literature consist of constraining the size of the simplex whose vertices are the factors. We also studied to consider a penalization based on the mutual distance between endmembers, defined as

$$\begin{aligned} \Psi(\mathbf{M}) &= \frac{1}{2} \sum_{i=1}^K \left( \sum_{\substack{k=1 \\ k \neq i}}^K \|\mathbf{m}_i - \mathbf{m}_k\|_2^2 \right) \\ &= \frac{1}{2} \sum_{k=1}^K \|\mathbf{M} \mathbf{G}_k\|_F^2 \end{aligned} \quad (3.13)$$

where

$$\mathbf{G}_k = -\mathbf{I}_K + \mathbf{e}_k \mathbf{1}_K^T \quad (3.14)$$

and  $\mathbf{e}_k$  denotes the canonical basis vector of  $\mathbb{R}^K$ . However, in dynamic PET imaging of the brain, the factors are highly correlated and promoting its approximation ended up by producing ambiguous results.

### Variability penalization

The SBF variability is expected to affect only a small number of voxels, those belonging to the region containing the SBF. As a consequence, we propose to enforce sparsity via the use of the  $\ell_{2,1}$ -norm, also known as the Group Lasso regularizer [YL06; Fer+17]

$$\Omega(\mathbf{B}) = \|\mathbf{B}\|_{2,1} = \sum_{n=1}^N \|\mathbf{b}_n\|_2, \quad (3.15)$$

where  $\|\cdot\|_{2,1}$  is the  $\ell_{2,1}$  norm. This penalty forces the columns  $\mathbf{b}_n$  to be 0 outside the high-uptake region, thus reducing overfitting.

## 3.4. Algorithm implementation

Given the nature of the optimization problem (3.9), which is genuinely nonconvex and nonsmooth, two strategies can be envisaged: gradient-descent-based and Lagrangian-computation-based. First, we studied the implementation of a Lagrangian-based algorithm based on a block coordinate descent alternating direction method of multipliers (ADMM). However, the resulting algorithm (see Appendix A.3) had a high computational cost with



several iterations within each variable loop. Thus, the adopted minimization strategy relies on the proximal alternating linearized minimization (PALM) scheme [BST13]. PALM is an iterative, gradient-based algorithm, which generalizes the Gauss-Seidel method. It consists in iterative proximal gradient steps with respect to  $\mathbf{A}$ ,  $\mathbf{M}$  and  $\mathbf{B}$  and ensures convergence to a local critical point  $\mathbf{A}^*$ ,  $\mathbf{M}^*$  and  $\mathbf{B}^*$ .

The principle of PALM is briefly recalled in the following section. Then it will be specifically instantiated for the unmixing-based kinetic component analysis considered in this chapter.

### 3.4.1. PALM: general principle

PALM is based on alternating partial gradient steps coupled with proximal mappings. For simplicity purposes, a nonconvex-nonsmooth problem composed of two blocks of variables  $x \in \mathbb{R}^n$  and  $y \in \mathbb{R}^m$  is considered

$$\min_{x,y} \Psi(x,y) := f(x) + g(y) + H(x,y),$$

where  $H(\cdot, \cdot)$  is a smooth and gradient-Lipschitz coupling function and the functions  $f$  and  $g$  are extended valued (i.e., allow constraints to be included). A classic approach to solve this problem is the Gauss-Seidel iteration scheme, also known as alternating minimization [Aus71]. A necessary assumption for this method to converge is that, in each iteration step, the minimum is uniquely attained [Pow73]. This strict convexity assumption can be removed by coupling the method with a proximal term [ABS13]. However, in the resultant method, only the convergence of the subsequences can be demonstrated [GS00]. To deal with nonconvex and nonsmooth settings, Bolte et al. [BST13] proposed an *approximation* of the proximal version of the Gauss-Seidel method via the *proximal linearization* of each subproblem. Thus, PALM consists in alternating minimization approach to the proximal forward backward algorithm, with the following minimal assumptions:

- (i)  $f : \mathbb{R}^n \rightarrow (-\infty, +\infty]$  and  $g : \mathbb{R}^m \rightarrow (-\infty, +\infty]$  are proper, semi-algebraic and lower semi-continuous functions, i.e.,  $\inf_{\mathbb{R}^n} f > -\infty$  and  $\inf_{\mathbb{R}^m} g > -\infty$ ;
- (ii) The objective function  $\Psi$  is also semi-algebraic, satisfies the Kurdyka-Lojasiewicz property and  $\inf_{\mathbb{R}^n \times \mathbb{R}^m} \Psi > -\infty$ ;
- (iii) with  $y$  fixed,  $H(x, y) : \mathbb{R}^n \times \mathbb{R}^m \rightarrow \mathbb{R}$  is a  $C_{L_1(y)}^{1,1}$  function, where the partial gradient  $\nabla_x H(x, y)$  is globally Lipschitz continuous with constant  $L_1(y)$

$$\|\nabla_x H(x_1, y) - \nabla_x H(x_2, y)\| \leq L_1(y) \|x_1 - x_2\|, \forall x_1, x_2 \in \mathbb{R}^n$$

and likewise for  $\nabla_y H(x, y)$ ;

(iv) for  $i = 1, 2$ , there are  $\lambda_i^-, \lambda_i^+ > 0$  such that

$$\inf\{L_1(y)^k : k \in \mathbb{N} \geq \lambda_1^-\} \text{ and } \inf\{L_2(x)^k : k \in \mathbb{N} \geq \lambda_2^-\}$$

$$\sup\{L_1(y)^k : k \in \mathbb{N} \leq \lambda_1^+\} \text{ and } \sup\{L_2(x)^k : k \in \mathbb{N} \leq \lambda_2^+\}$$

(v)  $\nabla H$  is Lipschitz continuous in bounded subsets.

The resultant algorithm, summarized in Algo. 2, is a maximization-minimization scheme with an uniform quadratic surrogate.

---

**Algorithm 2:** PALM: Proximal Alternating Linearized Minimization

---

**Initialization:**  $(x^0, y^0) \in \mathbb{R}^n \times \mathbb{R}^m$

**Input:** Algorithmic parameters  $\gamma_1 > 1$  and  $\gamma_2 > 1$

$k \leftarrow 0$

**for**  $k \geq 1$  **do**

Set  $c_k = \frac{L_x(y^k)}{\gamma}$

Compute  $x^{k+1} \in \text{prox}_{\frac{f}{c_k}} \left( x^k - \frac{1}{c_k} \nabla_x H(x^k, y^k) \right)$

Set  $d_k = \frac{L_y(x^{k+1})}{\gamma}$

Compute  $y^{k+1} \in \text{prox}_{\frac{g}{d_k}} \left( y^k - \frac{1}{d_k} \nabla_y H(x^{k+1}, y^k) \right)$

$k \leftarrow k + 1$

**Result:** A sequence  $\{(x^k, y^k)\}_{k \geq 0}$

---

Within this algorithmic scheme,  $\text{prox}_f$  denotes the proximal map associated to the function  $f$  defined as

$$\text{prox}_f(v) = \arg \min_x f(x) + \frac{1}{2} \|x - v\|_2^2,$$

$\gamma$  is a constant ensuring the convergence of the algorithm and may be fixed at, e.g., 0.99.

This general principle is applied to solve the unmixing problem. The resulting SLMM unmixing algorithm is sketched in Algo 3 whose main steps are described in the following paragraphs. The details are reported in Appendix A.1 for the sake of brevity.

### 3.4.2. Optimization with respect to $\mathbf{M}$

A direct application of the approach presented by [BST13] under the constraints defined by (3.2) leads to the following updating rule

$$\mathbf{M}^{k+1} = \mathcal{P}_+ \left( \mathbf{M}^k - \frac{1}{L_M^k} \nabla_{\mathbf{M}} \mathcal{J}(\mathbf{M}^k, \mathbf{A}^k, \mathbf{B}^k) \right) \quad (3.16)$$

**Algorithm 3:** SLMM unmixing: global algorithm

---

**Data:**  $\mathbf{Y}$   
**Input:**  $\mathbf{A}^0, \mathbf{M}^0, \mathbf{B}^0$   
1  $k \leftarrow 0$   
2 **while** *stopping criterion not satisfied* **do**  
3      $\mathbf{M}^{k+1} \leftarrow \mathcal{P}_+ \left( \mathbf{M}^k - \frac{\gamma}{L_M^k} \nabla_{\mathbf{M}} \mathcal{J}(\mathbf{M}^k, \mathbf{A}^k, \mathbf{B}^k) \right)$   
4      $\mathbf{A}^{k+1} \leftarrow \mathcal{P}_{\mathcal{A}_R} \left( \mathbf{A}^k - \frac{\gamma}{L_A^k} \nabla_{\mathbf{A}} \mathcal{J}(\mathbf{M}^{k+1}, \mathbf{A}^k, \mathbf{B}^k) \right)$   
5      $\mathbf{B}^{k+1} \leftarrow$   
6          $\text{prox}_{\frac{\lambda}{L_B^k} \|\cdot\|_1} \left( \mathcal{P}_+ \left( \mathbf{B}^k - \frac{\gamma}{L_B^k} \nabla_{\mathbf{B}} \mathcal{J}(\mathbf{M}^{k+1}, \mathbf{A}^{k+1}, \mathbf{B}^k) \right) \right)$   
6      $k \leftarrow k + 1$   
7  $\mathbf{A} \leftarrow \mathbf{A}^{k+1}$   
8  $\mathbf{M} \leftarrow \mathbf{M}^{k+1}$   
9  $\mathbf{B} \leftarrow \mathbf{B}^{k+1}$   
**Result:**  $\mathbf{A}, \mathbf{M}, \mathbf{B}$

---

where  $\mathcal{P}_+(\cdot)$  is the projector onto the nonnegative set  $\{\mathbf{X} | \mathbf{X} \succeq \mathbf{0}_{L,R}\}$  and the required gradient writes<sup>1</sup>

$$\nabla_{\mathbf{M}} \mathcal{J}(\mathbf{M}, \mathbf{A}, \mathbf{B}) = ((\mathbf{E}_1 \mathbf{A} \circ \mathbf{V} \mathbf{B}) \mathbf{H} - \mathbf{Y}) \mathbf{H}^T \mathbf{A}^T + \mathbf{M}(\mathbf{A} \mathbf{H} \mathbf{H}^T \mathbf{A}^T) + \beta(\mathbf{M} - \mathbf{M}^0). \quad (3.17)$$

Moreover,  $L_M^k$  is a bound on the Lipschitz constant of  $\nabla_{\mathbf{M}} \mathcal{J}(\mathbf{M}^k, \mathbf{A}^{k+1}, \mathbf{B}^k)$ , defined as

$$L_M(\mathbf{A}) = \left\| \mathbf{A} \mathbf{H} \mathbf{H}^T \mathbf{A}^T \right\| + \beta, \quad (3.18)$$

where the spectral norm  $\|\mathbf{X}\| = \sigma_{\max}(\mathbf{X})$  is the largest singular value of matrix  $\mathbf{X}$ . The BCCB deconvolution matrix can be decomposed as  $\mathbf{H} = \mathbf{F}^H \mathbf{\Lambda} \mathbf{F}$ , where  $\mathbf{F}$  and  $\mathbf{F}^H$  are associated with the Fourier and inverse Fourier transforms (satisfying  $\mathbf{F} \mathbf{F}^H = \mathbf{F}^H \mathbf{F} = \mathbf{I}_N$ ) and  $\mathbf{\Lambda} = \text{diag}\{\mathbf{F} \mathbf{h}\}$  is a diagonal matrix of eigenvalues whose diagonal elements are the Fourier coefficients of the first column of matrix  $\mathbf{H}$ , namely  $\mathbf{h}$ . Therefore  $\|\mathbf{H}\| \leq \|\mathbf{F}^H\| \|\mathbf{\Lambda}\| \|\mathbf{F}\| = \|\mathbf{\Lambda}\| = \max\{\mathbf{F} \mathbf{h}\}$ . The kernel that generates the operator  $\mathbf{H}$  can be decomposed as three one-dimensional filters. The Lipschitz bound corresponding to  $\mathbf{H}$  is then computed as the product of the norms of these one-dimensional filters.

### 3.4.3. Optimization with respect to $\mathbf{A}$

Similarly to paragraph 3.4.2, the factor proportion update is defined as the following

$$\mathbf{A}^{k+1} = \mathcal{P}_{\mathcal{A}_R} \left( \mathbf{A}^k - \frac{1}{L_A^k} \nabla_{\mathbf{A}} \mathcal{J}(\mathbf{M}^{k+1}, \mathbf{A}^k, \mathbf{B}^k) \right), \quad (3.19)$$

---

<sup>1</sup>Note that the iteration index has been omitted in the following definitions of the gradients to lighten the notations.

where  $\mathcal{P}_{\mathcal{A}_R}(\cdot)$  is the projection on the set  $\mathcal{A}_R$  defined by the factor proportion constraints (3.3), which can be computed with efficient algorithms, see, e.g., the work of [Con15]. The gradient writes

$$\nabla_{\mathbf{A}} \mathcal{J}(\mathbf{M}, \mathbf{A}, \mathbf{B}) = -\mathbf{M}^T \mathbf{D}_A - \mathbf{E}_1^T (\mathbf{D}_A \circ (\mathbf{V}\mathbf{B})) + \alpha \mathbf{A} \mathbf{S} \mathbf{S}^T$$

with  $\mathbf{D}_A = (\mathbf{Y} - \mathbf{M}\mathbf{A}\mathbf{H} - (\mathbf{E}_1 \mathbf{A} \circ \mathbf{V}\mathbf{B})\mathbf{H})\mathbf{H}^T$ .

Moreover,  $L_A^k$  is the Lipschitz constant of  $\nabla_{\mathbf{A}} \mathcal{J}(\mathbf{M}^k, \mathbf{A}^k, \mathbf{B}^k)$ .

$$L_A(\mathbf{M}, \mathbf{B}) = \|\mathbf{H}\|^2 \left( \|\mathbf{E}_1\| \|\mathbf{V}\mathbf{B}\| (2\|\mathbf{M}\|_\infty + \|\mathbf{E}_1\| \|\mathbf{V}\mathbf{B}\|_\infty) \right) + \|\mathbf{H}\|^2 \|\mathbf{M}^T \mathbf{M}\| + \alpha \|\mathbf{S} \mathbf{S}^T\|, \quad (3.20)$$

where  $\|\mathbf{X}\|_\infty = \max_{1 \leq i \leq m} \sum_{j=1}^n |x_{ij}|$  is the maximum absolute row sum norm. As in [Jen+12], we will consider  $\|\mathbf{S} \mathbf{S}^T\| \leq 12$ . This result is a generalization of the proof presented in [Dah+09].

#### 3.4.4. Optimization with respect to $\mathbf{B}$

Finally, the updating rule for the variability coefficients can be written as

$$\mathbf{B}^{k+1} = \text{prox}_{\frac{\lambda}{L_B^k} \|\cdot\|_{2,1}} \left( \mathcal{P}_+ \left( \mathbf{B}^k - \frac{1}{L_B^k} \nabla_{\mathbf{B}} \mathcal{J}(\mathbf{M}^{k+1}, \mathbf{A}^{k+1}, \mathbf{B}^k) \right) \right),$$

where the proximal mapping operator is the group soft-thresholding operator

$$\text{prox}_{c\|\cdot\|_{2,1}}(\mathbf{U}) = \begin{cases} \left(1 - \frac{c}{\|\mathbf{u}_i\|_2}\right) \mathbf{u}_i & \text{if } \|\mathbf{u}_i\|_2 > c \\ 0 & \text{otherwise,} \end{cases} \quad (3.21)$$

with  $\mathbf{u}_i$  a column of matrix  $\mathbf{U}$ . Indeed, the proximal map of the sum of the nonnegative indicator function and the  $\ell_{2,1}$  norm is exactly the composition of the proximal maps of both individual functions, following the same principle showed by Bolte et al. [BST13]. The gradient writes

$$\nabla_{\mathbf{B}} \mathcal{J}(\mathbf{M}, \mathbf{A}, \mathbf{B}) = \mathbf{V}^T ((\mathbf{E}_1 \mathbf{A}) \circ (-\mathbf{Y} + \mathbf{M}\mathbf{A}\mathbf{H} + \Delta) \mathbf{H}^T).$$

Moreover,  $L_B^k$  is a bound of the Lipschitz constant of  $\nabla_{\mathbf{B}} \mathcal{J}(\mathbf{M}^{k+1}, \mathbf{A}^{k+1}, \mathbf{B}^k)$

$$L_B(\mathbf{A}) = \|\mathbf{E}_1 \mathbf{A}\|_\infty^2 \|\mathbf{V}\|^2 \|\mathbf{H}\|^2. \quad (3.22)$$

## 3.5. Evaluation on Synthetic Data

### 3.5.1. Synthetic data generation

To evaluate, analyse and tune the performance of algorithms, researchers need databases generated from fully controlled and acknowledged processes. In this scenario, two kinds of data can be considered: realistic synthetic images for which the ground truth is known and real images with no ground truth to compare. The ground truth regarding the actual tracer uptake and kinetics is never completely known for clinical PET studies. The collection of patient data can take months or even years before the dataset is large enough to yield sufficient statistics. Furthermore, studies with healthy volunteers are restricted due to the radiation dose associated with PET scans. To tackle this limitation, an object, called phantom, that is specially designed such as to respond to the system under study in a similar way as human tissues and organs, is often used. Even though phantom studies solve part of this problem, dynamic scans where the tracer kinetics is of interest are not available, even with state-of-the-art phantoms. Advanced as they may be, phantoms can never truly represent a real patient in a clinical situation.

This is where the role of simulations come in. All properties of the patient (phantom) and kinetics are known, and the degree of complexity and detail of the simulation can be chosen according to the specific aim of the study. Physical effects can be included or not depending on the focus of the investigation and the level of complexity. If needed, a large (even huge) number of simulations can be performed in a reasonable time [Häg14].

Thus, in this work, synthetic images are generated and studied in order to validate the methods presented in this manuscript. Images are constructed from the Zubal high resolution numerical phantom [Zub+94] with TACs generated from real PET images acquired with the Siemens HRRT and injected with  $^{11}\text{C}$ -PE2I. The original phantom data has size  $128 \times 128 \times 64$ , and was acquired at  $L = 20$  times of acquisition that range from 1 to 5 minutes with 60 minutes of acquisition in total. Its voxel size is of  $1.1 \times 1.1 \times 1.4 \text{ mm}^3$ . Its regions-of-interest are segmented with a corresponding MRI to provide averaged TACs for each different tissue of the brain. This supervised segmentation neglects any labelled molecule concentration differences due to the variability on the specific binding region and describes the entire region by a single averaged TAC. TACs corresponding to each segmented region are then averaged. This high-resolution numerical phantom is presented in Fig. 3.6. To illustrate the accuracy of our algorithm, a synthetic data for which the ground truth of the main parameters of interest (i.e., factor TACs and factor proportion maps) is known is then constructed from this realistic phantom. The overall generation process is presented in Fig. 3.7 and described in what follows:

- The dynamic PET phantom showed in Fig. 3.6 has been first linearly unmixed using the N-FINDR [Win99] and SUnSAL [BF10] algorithms to select the ground-truth non-specific factor TACs  $\mathbf{m}_2, \dots, \mathbf{m}_K$

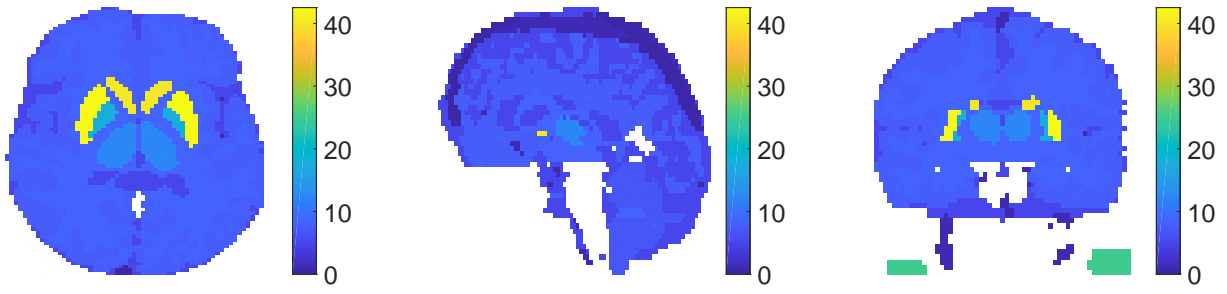


Figure 3.6.: 15<sup>th</sup> time-frame of the dynamic PET phantom: from left to right, transversal, sagittal and coronal views.

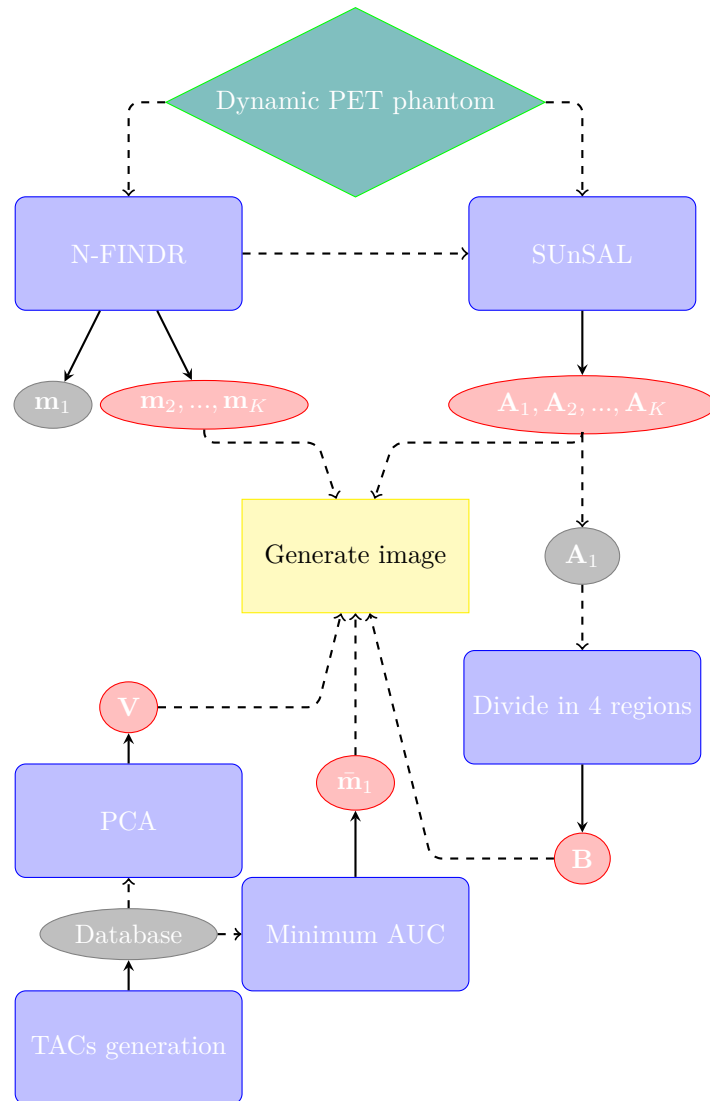


Figure 3.7.: Synthetic image generation scheme. The red ellipses constitute the ground truth data used for quantitative assessment.

and factor proportions  $\mathbf{a}_1, \dots, \mathbf{a}_N$ , respectively. As in [Boe+08; Yaq+12], we consider  $K = 4$  pure TACs representative of the brain, which is the organ of interest in the present work: specific gray matter, pure blood or veins, pure white matter and non-specific gray matter. These factor TACs and corresponding factor proportion maps are depicted in Fig. 3.8.

- A large database of SBF TACs has been generated with a 2-tissue compartmental model [PMS86] by randomly varying the  $k_3$  parameter (representing the specific binding rate of the radiotracer in the tissue). The generation function of the TAC in the  $n^{th}$  pixel  $\mathbf{x}_n$  is based on the 2-tissue compartment model presented in Section 1.6.2. After generation, a PCA is conducted on this dataset, and an analysis of the eigenvalues leads to the choice of a unique variability basis element  $\mathbf{V} = \mathbf{v}_1$  (i.e.,  $N_v = 1$ ), depicted in Fig. 3.9 (left).
- The nominal SBF TAC  $\bar{\mathbf{m}}_1$  is then chosen as the TAC of minimum AUC among all the TACs of this database. This TAC is depicted in Fig. 3.9 (right, red curve).
- The 1<sup>st</sup> row of the factor proportion matrix  $\mathbf{A}$ , namely  $\mathbf{A}_1 \triangleq [a_{1,1}, \dots, a_{1,N}]$  is designed to locate the region associated with specific binding. Then, the  $N_v \times N$  matrix  $\mathbf{B} = [b_1, \dots, b_N]$ , showed in Fig. 3.10 mapping the SBF variability in each voxel is artificially generated. The high-uptake region is divided into 4 subregions with non-zero coefficients  $b_n$ , as shown in Fig. 3.10, while these coefficients are set to  $b_n = 0$  outside the region affected with SBF. In each of these subregions, the non-zero coefficients  $b_n$  are drawn according to Gaussian distributions with a particular mean value and small variances. The spatially-varying SBFs in each region are then generated according to the model in (3.5) and (3.4). Some resulting typical SBF TACs are shown in Fig. 3.9.

After the synthetic phantom process, a PSF defined as a space-invariant and isotropic Gaussian filter with FWHM= 4.4mm is applied to the output image. This is a strong approximation. However, as the degradation of the scanner resolution mainly affects the borders of the field-of-view [RQS13; Meh+17], this is a frequent approximation in brain imaging using a clinical PET scanner, since the brain is centered and more far from the FOV than in images of other parts of the body. Moreover, the idea here is to apply the same PSF for the generation and analysis processes. Finally the measurements are corrupted by a zero-mean white Gaussian noise with a signal-to-noise ratio  $\text{SNR} = 15\text{dB}$ , in agreement with the preliminary study conducted on the realistic replicas of [Stu+15] (presented in Section 4.3.1), which shows that the SNR ranges from approximately 10dB on the earlier frames to 20dB on the latter ones. The resulting image is shown in Fig. 3.11. Simulations are conducted in 20 different realizations of the noise to get reliable performance measures.

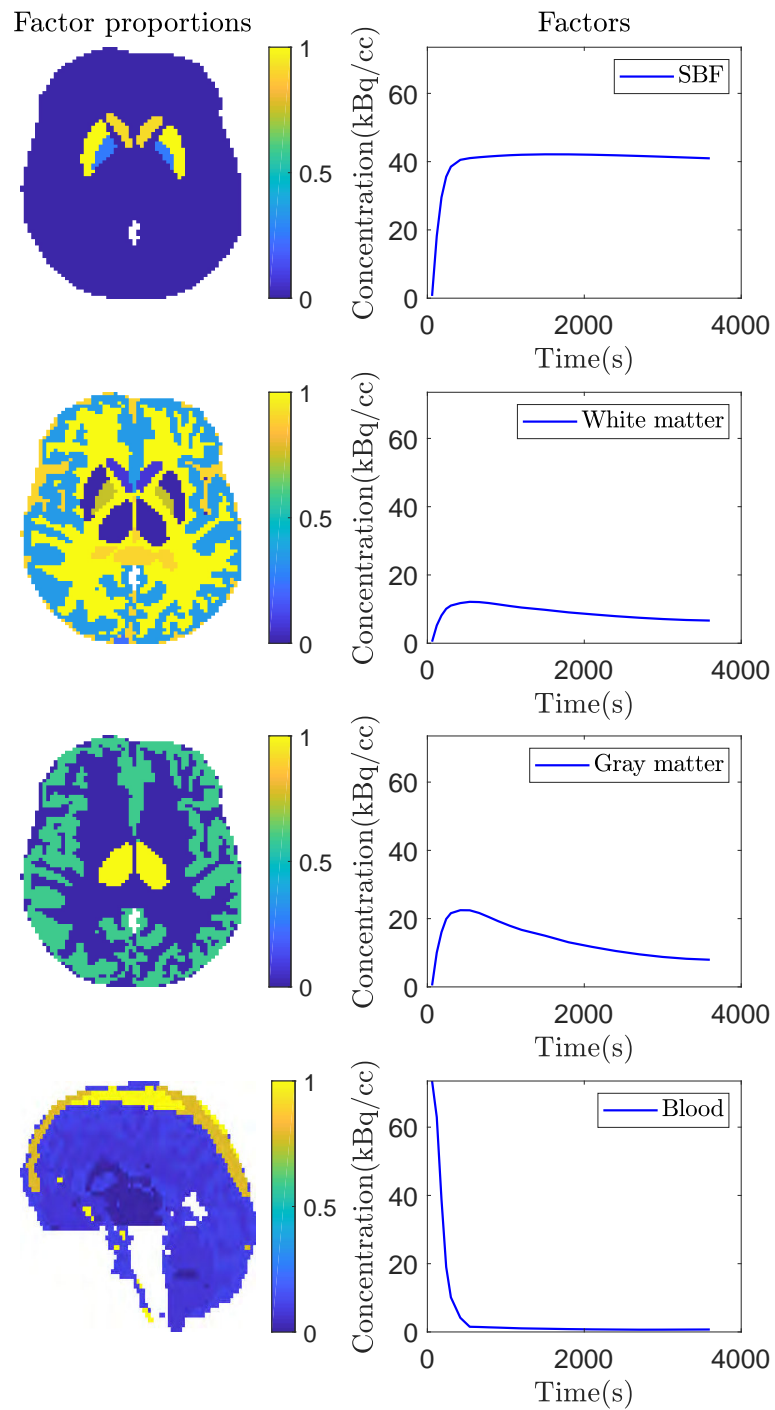


Figure 3.8.: Ground truth of factors (right) and corresponding proportions(left), extracted from SUNSAL/N-findr



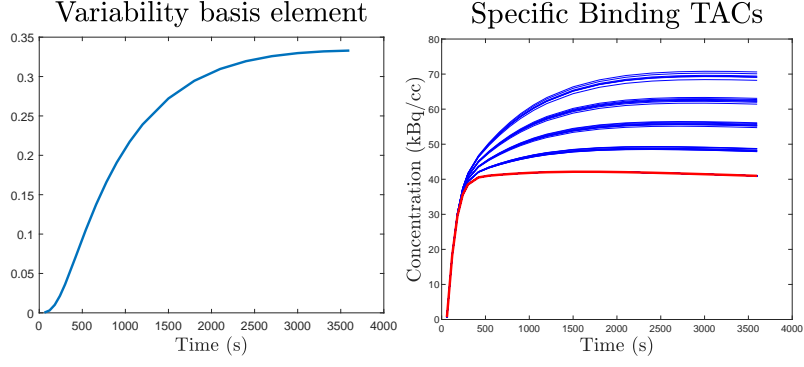


Figure 3.9.: Left: variability basis element  $\mathbf{v}_1$  identified by PCA. Right: generated SBFs (blue) and the nominal SBF signature (red).

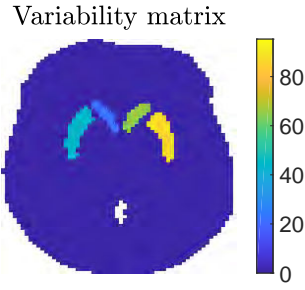


Figure 3.10.: Variability matrix  $\mathbf{B}$  randomly generated.

### 3.5.2. Compared methods

The results of the proposed algorithm are compared to those obtained with several classical linear unmixing methods and other BSS techniques presented in Sections 2.2.2 and 2.4. The methods are recalled below with their most relevant implementation details.

**NMF (no variability)** The NMF algorithm herein applied is based on multiplicative update rules using the Euclidean distance as the cost function [LS00]. The stopping criterion is set to  $10^{-3}$ . To obtain a fair comparison mitigating scale ambiguity inherent to matrix factorization-like problems, results provided by the

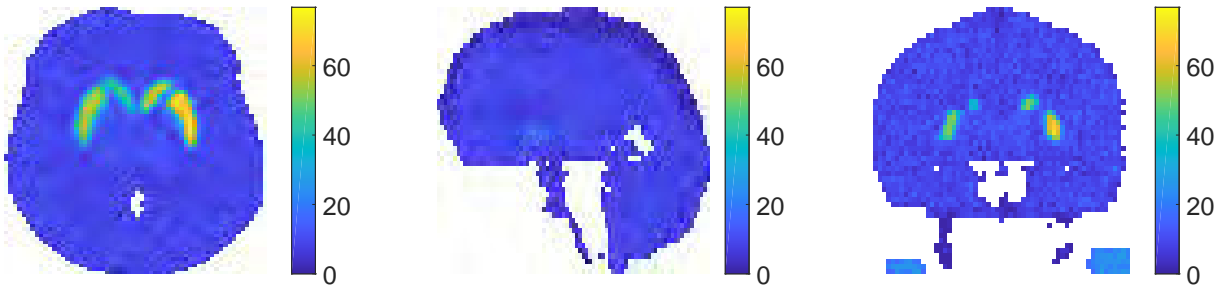


Figure 3.11.: 15<sup>th</sup> time-frame of 3D-generated image with PSF and a 15dB noise: from left to right, transversal, sagittal and coronal planes.

NMF have been normalized by the maximum value for the abundance, i.e.,

$$\hat{\mathbf{A}}_k \leftarrow \frac{\hat{\mathbf{A}}_k}{\|\hat{\mathbf{A}}_k\|_\infty} \quad \hat{\mathbf{m}}_k \leftarrow \hat{\mathbf{m}}_k \|\hat{\mathbf{A}}_k\|_\infty \quad (3.23)$$

where  $\hat{\mathbf{A}}_k$  denotes the  $k^{th}$  row of the estimated factor proportion matrix  $\hat{\mathbf{A}}$ .

**VCA (no variability)** The factor TACs are first extracted using the vertex component analysis (VCA) which requires pure voxels to be present in the analysed images [ND05b]. The factor proportions are subsequently estimated by sparse unmixing by variable splitting and augmented Lagrangian (SUnSAL) [BF10].

**LMM (no variability)** To appreciate the interest of explicitly modelling the spatial variability of the SBF, a depreciated version of the proposed SLMM algorithm is considered. More precisely, it uses the LMM (3.1) without allowing the SBF  $\mathbf{m}_{1,n}$  to be spatially varying. The stopping criterion, defined as  $\varepsilon$ , is set to  $10^{-3}$ . The values of the regularization parameter are reported in Table 3.1.

**SLMM (proposed approach)** As detailed in Section 3.3.1, matrix  $\mathbf{B}$  is constrained to be nonnegative to increase accuracy. Consequently, the nominal SBF TAC  $\bar{\mathbf{m}}_1$  is initialized as the TAC with the minimum AUC learned from the generated database to ensure a positive  $\mathbf{B}$ . The regularization parameters have been tuned to the values reported in Table 3.1. As for the other approaches, the stopping criterion is set to  $10^{-3}$ .

Since the addressed problem is non-convex, these algorithms require an appropriate initialization. In this work, the factor TACs have been initialized as the outputs  $\mathbf{M}^0$  of a K-means clustering conducted on the PET image. These K-means TACs estimates are also considered for performance comparison.

Table 3.1.: factor proportion, factor and variability penalization hyperparameters for LMM and SLMM with SNR= 15dB

	LMM	SLMM
$\alpha$	0.010	0.010
$\beta$	0.010	0.010
$\lambda$	-	0.020
$\varepsilon$	0.001	0.001

The performance of the algorithms is assessed by computing the normalized mean square error (NMSE) for each variable

$$\text{NMSE}(\hat{\boldsymbol{\theta}}) = \frac{\|\hat{\boldsymbol{\theta}} - \boldsymbol{\theta}\|_F^2}{\|\boldsymbol{\theta}\|_F^2} \quad (3.24)$$

where  $\hat{\boldsymbol{\theta}}$  denotes the estimated variable and  $\boldsymbol{\theta}$  the corresponding ground truth. The NMSE has been computed for the following variables: the factor proportions  $\mathbf{A}_1$  corresponding to the high-uptake region, the remaining factor proportions  $\mathbf{A}_{2:K}$ , the SBFs affected by the variability  $\tilde{\mathbf{M}}_1 \triangleq [\mathbf{m}_{1,1}, \dots, \mathbf{m}_{1,N}]$ , the non-specific factor TACs  $\mathbf{M}_{2:K} \triangleq [\mathbf{m}_2, \dots, \mathbf{m}_K]$  and finally the internal variability matrix  $\mathbf{B}$ .

### 3.5.3. Hyperparameter influence

Considering the significant number of hyperparameters to be tuned in both LMM and SLMM approaches (i.e.,  $\alpha$ ,  $\beta$ ,  $\lambda$ ), a full sensitivity analysis is a challenging task, which is further complexified by the non-convex nature of the problem. To alleviate this issue, each parameter has been individually adjusted while the others have been set to zero. Several simulations empirically showed that the result is not too sensitive to the choice of parameters. The parameters have been tuned such that the total percentage of their corresponding term in the overall objective function does not surpass 25% of the total value of the function. Given the high level of noise corrupting the PET images, the hyperparameter  $\alpha$  associated with the factor proportions has been set so as to reduce the noise impact while avoiding too much smoothing. The factor TAC penalization hyperparameter  $\beta$  results from a trade-off between the quality of the initial factor TAC estimates  $\mathbf{M}^0$  and the flexibility required by PALM to reach more accurate estimates. Finally the variability penalization  $\lambda$  has been tuned to achieve a compromise between the risks of capturing noise into the variability term (i.e., overfitting) and of losing information. While there are more automatized ways to choose the hyperparameter values (e.g., using cross-validation, grid search, random search and Bayesian estimation), these hyperparameter choices have seemed to be sufficient to assess the performance of the proposed method. The hyperparameter values used in LMM and SLMM are finally reported in Table 3.1.

### 3.5.4. Results

The factor proportion maps recovered by the compared algorithms are shown in Fig. 3.12. Each column corresponds to a specific factor: SBF, white matter, non-specific gray matter, blood (from left to right, respectively). The six rows contain the factor proportion maps of the ground truth, and those estimated by K-means, NMF, VCA, LMM and the proposed SLMM (from top to bottom, respectively). A visual comparison suggests that the factor proportion maps obtained with LMM and SLMM are more consistent with the expected localization of each factor in the brain than VCA. Meanwhile, they are less noisy than the maps obtained by NMF. The estimated LMM and SLMM proportions maps are closer to the ground truth than VCA and NMF, particularly in the region affected by specific binding, as quantitatively shown in Table 3.2. It can also be observed that the factor proportion maps obtained with the proposed SLMM approach present a higher contrast compared to LMM and other approaches, especially in the high-uptake region.

The maps of SLMM are also sharper compared to LMM. Additionally, it is also possible to see that NMF results for white matter are sharper but also noisier than both LMM and SLMM approaches. However, for the specific gray matter, both LMM and SLMM approaches show sharper estimated factor proportion maps. Note that the sharpness of the factor proportions is not necessarily a good criterion of comparison. Indeed, factor analysis-based methods do expect to recover smooth maps that take into account the spilling part of partial

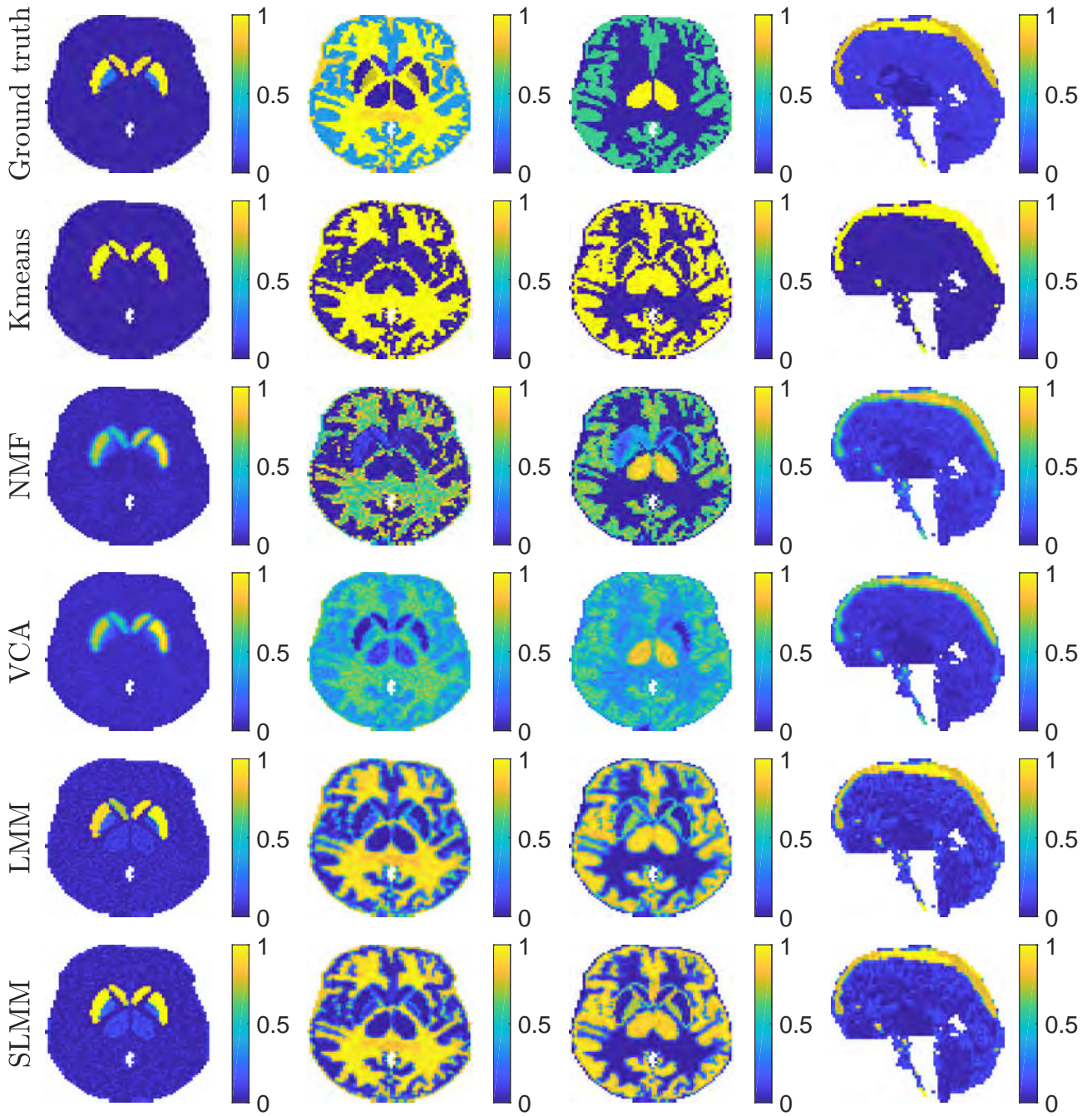


Figure 3.12.: Factor proportion maps of the 15<sup>th</sup> time-frame obtained for SNR=15dB corresponding to the specific gray matter, white matter, gray matter and blood, from left to right. The first 3 columns show a transaxial view while the last one shows a sagittal view. All images are in the same scale  $[0, 1]$ .

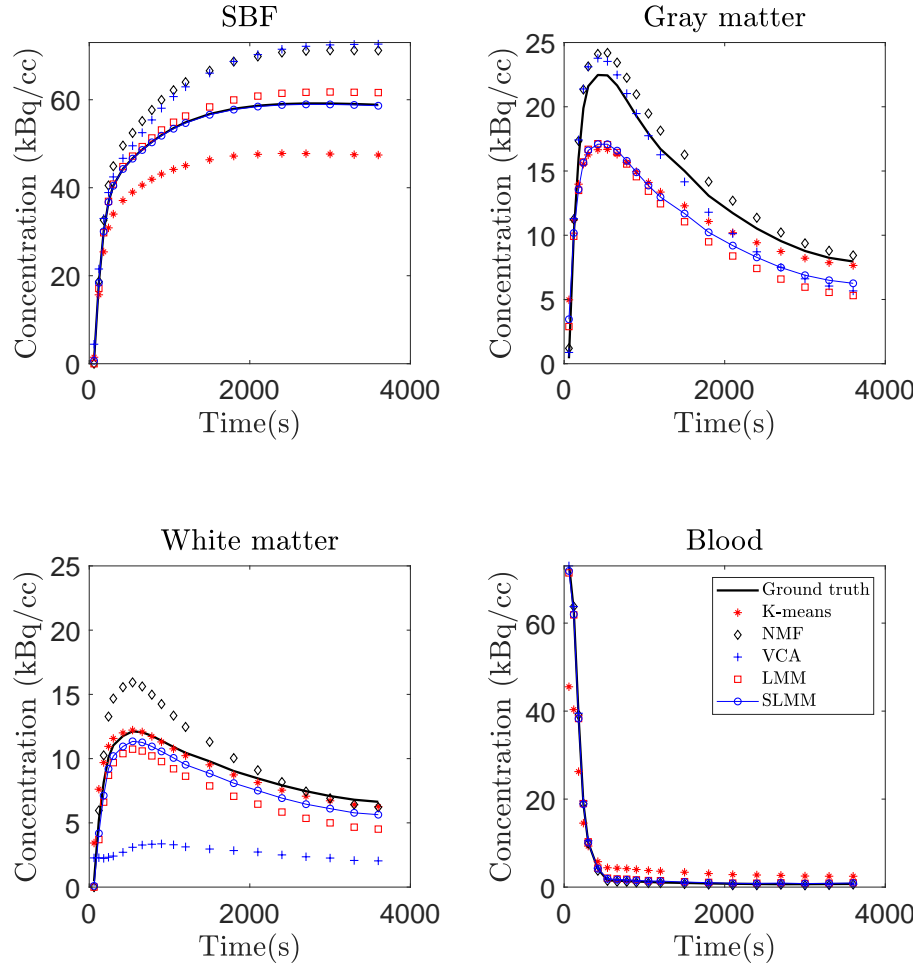


Figure 3.13.: TACs obtained for SNR = 15dB. For the proposed SLMM algorithm, the represented SBF TAC corresponds to the empirical mean of the estimated spatially varying SBFs  $\mathbf{m}_{1,1}, \dots, \mathbf{m}_{1,N}$ .

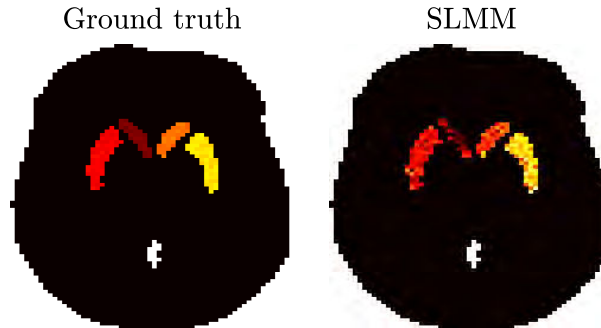


Figure 3.14.: Ground-truth (left) and estimated (right) SBF variability.

Table 3.2.: Normalized Mean Square Errors of the estimated variables  $\mathbf{A}_1$ ,  $\mathbf{A}_{2:K}$ ,  $\tilde{\mathbf{M}}^1$ ,  $\mathbf{M}^{2:K}$  and  $\mathbf{B}$  for K-means, VCA, NMF, LMM and SLMM

	$\mathbf{A}_1$	$\mathbf{A}_{2:K}$	$\tilde{\mathbf{M}}^1$	$\mathbf{M}^{2:K}$	$\mathbf{B}$
K-means	0.567 $\pm 4.3 \times 10^{-4}$	0.669 $\pm 2.2 \times 10^{-3}$	0.120 $\pm 1.5 \times 10^{-4}$	0.442 $\pm 6.1 \times 10^{-2}$	-
VCA	0.547 $\pm 6.7 \times 10^{-4}$	0.481 $\pm 1.8 \times 10^{-3}$	0.517 $\pm 9.3 \times 10^{-5}$	0.248 $\pm 1.3 \times 10^{-3}$	-
NMF	0.512 $\pm 1.0 \times 10^{-6}$	0.558 $\pm 3.8 \times 10^{-5}$	0.517 $\pm 4.5 \times 10^{-5}$	0.133 $\pm 1.5 \times 10^{-4}$	-
LMM	0.437 $\pm 3.8 \times 10^{-6}$	<b>0.473</b> $\pm 4.3 \times 10^{-8}$	0.349 $\pm 6.0 \times 10^{-7}$	0.148 $\pm 1.5 \times 10^{-6}$	-
SLMM	<b>0.359</b> $\pm 1.3 \times 10^{-5}$	0.495 $\pm 3.1 \times 10^{-5}$	<b>0.009</b> $\pm 3.0 \times 10^{-8}$	<b>0.128</b> $\pm 9.8 \times 10^{-7}$	0.259 $\pm 2.3 \times 10^{-5}$

volume effect, which is not considered within deconvolution. The aim of unmixing is not hard-clustering or classification.

The corresponding estimated factor TACs are shown in Fig. 3.13 where, for comparison purposes, the SBF depicted for SLMM is the empirical average over the whole set of spatially varying SBFs, as it is also the case for the SBF ground truth TACs. The best estimate of the SBF TAC seems to be obtained by the proposed SLMM approach, for which the TAC has been precisely recovered, as opposed to K-means, VCA and NMF. K-means provide the best estimate of the white matter TAC, closely followed by SLMM while NMF highly overestimates it. The best estimate of the non specific gray matter TAC is obtained by VCA and NMF, even though it is slightly overestimated. It can be observed that SLMM and LMM underestimate this factor TAC, which has been compensated with higher values in the corresponding factor proportion map. The factor TAC associated with blood is correctly estimated by all methods.

Table 3.2 presents the NMSE over the 20 realizations of the noise for all algorithms and variables of interest. These quantitative results confirm the preliminary findings drawn from the visual inspection of Fig. 3.12 and 3.13. The proposed method outperforms all the others for the estimation of  $\tilde{\mathbf{M}}_1$ ,  $\mathbf{M}^{2:K}$  and  $\mathbf{a}_1$ . In particular, SLMM provides a very precise estimation of the mean SBF TAC with an NMSE of 0.9%. In Fig. 3.13, the mean of the estimated SBF TACs  $\mathbf{m}_{1,1}, \dots, \mathbf{m}_{1,N}$  is very close to the ground truth for LMM and SLMM but the individual errors computed for each voxel demonstrate better performance obtained by SLMM. It also shows better results than K-means and NMF for  $\mathbf{A}_{2:K}$ , even though it is less effective but still competitive when compared to LMM and VCA. Moreover, Kmeans and VCA results present a higher variance, as seen in Table 3.2.

Taking into account the SBF variability allows the estimation of  $\mathbf{A}_1$  to be improved up to 35%. Fig. 3.14 compares the actual variability factor proportions and those estimated by the proposed SLMM. This figure shows that the estimated non-zeros coefficients are correctly localized in the 4 subregions characterized by some SBF variability. These non-zero values seem to be affected by some estimation inaccuracies, mainly due to the



	No deconvolution	Wiener pre-deconvolution	Joint deconvolution
$\alpha$	0.010	0.010	0.010
$\beta$	0.010	0.010	0.010
$\lambda$	0.020	0.020	0.020
$\varepsilon$	0.001	0.001	0.001

Table 3.3.: Factor proportion, factor and variability penalization parameters for SLMM with no deconvolution, wiener pre-deconvolution and joint deconvolution with SNR = 15dB.

	No deconvolution	Wiener pre-deconvolution	Joint deconvolution
$\mathbf{a}_1$	0.525	0.923	<b>0.382</b>
$\mathbf{A}_{2:K}$	<b>0.482</b>	0.553	<b>0.482</b>
$\tilde{\mathbf{M}}^1$	0.013	0.032	<b>0.009</b>
$\mathbf{M}^{2:K}$	0.220	0.270	<b>0.174</b>
$\mathbf{B}$	0.346	0.844	<b>0.248</b>

Table 3.4.: NMSE of estimated parameters for SLMM with no deconvolution, with Wiener pre-deconvolution and with joint deconvolution for SNR=15dB

deconvolution. However, the estimation error still stays close to 25%.

### 3.5.5. Impact of the deconvolution

PSF modelling has proven its interest within reconstruction [Kar+15] since it reduces the partial volume effect and enhances contrast. Similarly, conducting deconvolution and unmixing jointly has been shown to provide more reliable unmixing results [Hen+14]. To further demonstrate the interest of joint deconvolution, SLMM was applied in three different frameworks:

- SLMM without deconvolution;
- SLMM with a Wiener-based pre-deconvolution;
- SLMM within deconvolution (our original model).

The results from these simulations with a synthetic image are presented in the following.

Table 3.3 shows the parameters applied in each simulation while Table 3.4 shows the NMSE computed for each variable in each simulation. Visual comparison suggests that the error is the smallest for all variables with joint deconvolution. As expected, the Wiener pre-deconvolution increases the statistical noise, while no deconvolution presents a highly smoothed result. These results are enforced by Figs. 3.15, 3.16 and 3.17. Moreover, in the regular LMM, the factor proportions are directly affected by the PSF effect, providing smooth boundaries in between regions. However, our model contains two spatial maps related to the SBF that can be affected by the PSF: the corresponding factor proportion and the internal variability map. This may produce ambiguous results, since we cannot know which one will be affected by the boundary smoothness. This is why we chose to implement a joint deconvolution step in our model.

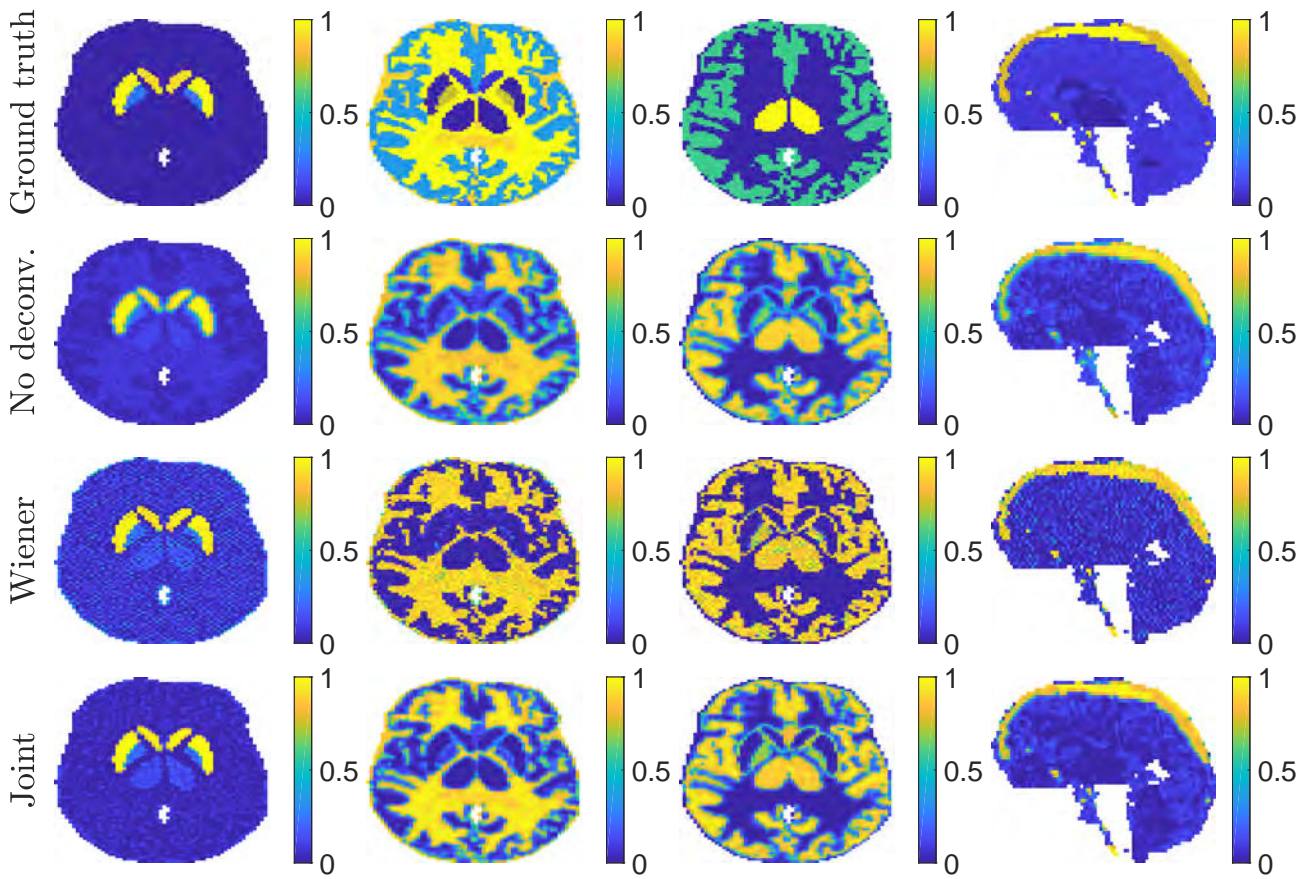


Figure 3.15.: Factor proportion maps of the 15<sup>th</sup> time-frame obtained for SNR=15dB corresponding to the specific gray matter, white matter, gray matter and blood, from left to right. The first 3 columns show a transaxial view while the last one shows a sagittal view.



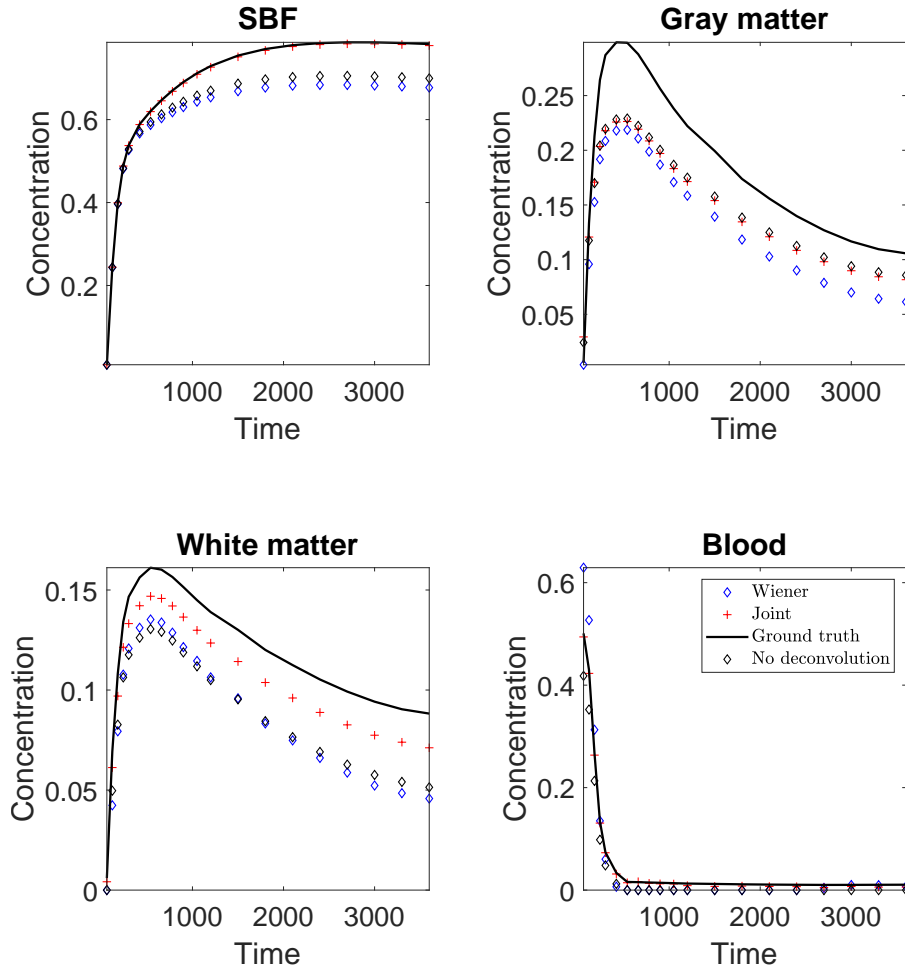


Figure 3.16.: TACs obtained for SNR=15dB. For the proposed SLMM algorithm, the represented SBF corresponds to the empirical mean of the estimated spatially varying SBFs  $\mathbf{m}_{1,1}, \dots, \mathbf{m}_{1,N}$ .

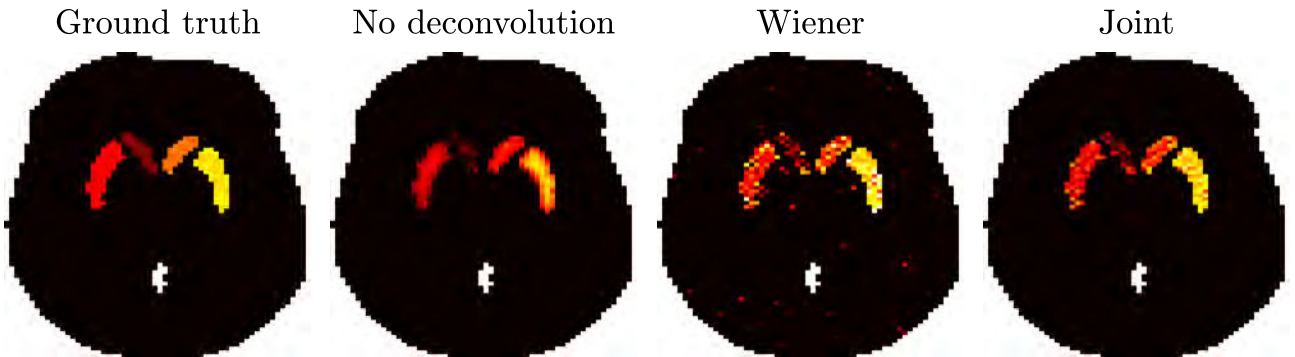


Figure 3.17.: Ground-truth (left) and estimated (right) SBF variability.

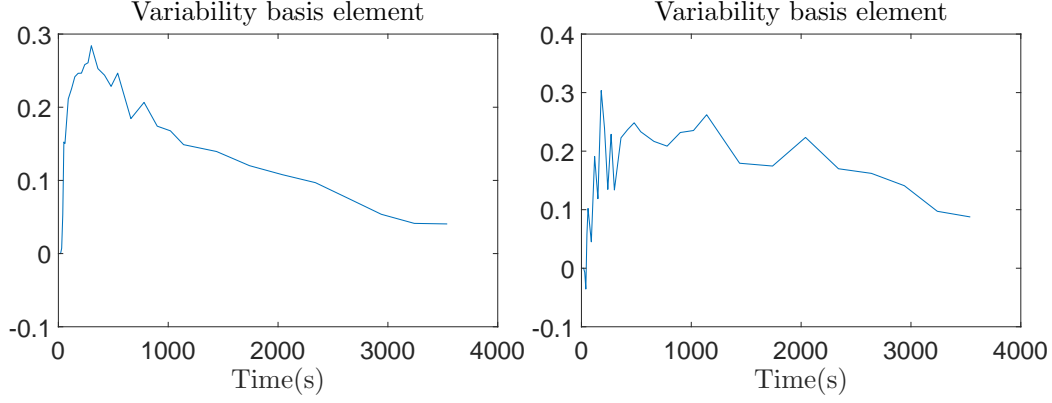


Figure 3.18.: Variability basis elements of first subject (left) and second subject (right)

## 3.6. Evaluation on Real Data

### 3.6.1. PET data acquisition

To assess the behaviour of the proposed approach when analysing real dynamic PET images, the different methods have been applied to two dynamic PET images of stroke subjects injected with [18F]DPA-714. Cerebral stroke is a severe and frequently occurring condition. While different mechanisms are involved in the stroke pathogenesis, there is an increasing evidence that inflammation, mainly involving the microglial and the immune system cells, account for its pathogenic progression. The [18F]DPA-714 is a ligand of the 18-kDa translocator protein (TSPO) for in vivo imaging, which is a biomarker of neuroinflammation. The subjects were examined using an Ingenuity TOF Camera from Philips Medical Systems, seven days after the stroke.

The PET acquisitions were reconstructed into a  $128 \times 128 \times 90$ -volume with  $L = 31$  time-frames. The PET scan images acquisition times ranged from 10 seconds to 5 minutes over a 59 minutes period. The voxel size was of  $2 \times 2 \times 2 \text{ mm}^3$ . As for the experiments conducted on simulated data, once again as in [Boe+08; Yaq+12], the voxel TACs have been assumed to be mixtures of  $K = 4$  types of elementary TAC: specific binding associated with inflammation, blood, the non-specific gray and white matters. For the first subject, the K-means method was applied to the images to mask the cerebrospinal fluid and to initialize NMF, LMM and SLMM algorithms. For the second subject, SVCA was applied to obtain the initialization of factors and factor proportions. A ground truth of the high-uptake tissue was manually labeled by an expert based on a magnetic resonance imaging (MRI) acquisition. The stroke region was segmented on this registered MRI image to define a set of voxels used to learn the variability descriptors  $\mathbf{V}$  by PCA with  $N_v = 1$ . Fig. 3.18 presents the final variability basis elements for the two subjects. The nominal SBF is fixed as the empirical average of the corresponding TACs with AUC comprised between the 5<sup>th</sup> and 10<sup>th</sup> percentile. The choice to use the average of a percentile instead of the minimum AUC TAC is motivated by the fact that, in this case, the learning set is corrupted by noise and partial volume effects. The algorithm parameters are set to  $\alpha = 0$ ,  $\beta = 0.1$  and  $\lambda = 0.5$ .

### 3.6.2. Results

Figure 3.19 depicts the factor proportion maps estimated by the compared methods. The corresponding estimated factor TACs are shown in Fig. 3.20. The LMM and SLMM algorithms estimate four distinct TACs associated with different tissues, as expected. In Fig. 3.19, a remarkable result is the factor proportion maps for the blood. The sagittal view represented in the last row is in the exact center of the brain. Both NMF and SLMM recover factor proportion maps that are in very good agreement with the superior sagittal sinus vein that passes on the higher part of the brain. On the contrary, VCA estimates two factors that seem to be mixtures of the vein TACs and other region TACs.

Fig. 3.21 depicts three different views of the stroke area identified by the expert on MRI acquisition (1<sup>st</sup> row), the estimated specific gray matter factor proportions (2<sup>nd</sup>-6<sup>th</sup> rows) and the estimated corresponding variability (7<sup>th</sup> row). All methods seem to correctly recover the main localization of the stroke area. However, the proposed SLMM approach identifies a significantly larger area. This result seems to be in better agreement with the stroke area identified in the MRI acquisition of the same patient. Moreover, the specific gray matter factor proportion maps estimated by SLMM and K-means show high values in the thalamus, which is a region known to present specific binding of [18F]DPA-714. It is possible to note an interesting improvement of the final SLMM estimate when compared to its K-means initialization. This demonstrates that the method converges to an estimation of the specifically bound gray matter that is more accurate with the proposed model.

Fig. 3.22 depicts the factor proportions of the second stroke subject. While SVCA seems to provide a good approximation of both white and gray matter, VCA is completely unable to unmix the two tissues. NMF increases the intensity of the gray matter regions, but seems to mix up the white matter with the blood factor proportion. Both LMM and SLMM better maintain and improve the regions found with SVCA for white and gray matter tissues. However, the intensity of the gray matter proportion is greater in SLMM while LMM presents some gray matter regions as high-uptake tissues. This visual comparison on factor proportions is further confirmed by the analysis of factors in Fig. 3.23. For the blood factor, while SVCA, LMM and SLMM present a peak in the initial frames, as expected from an input function, both VCA and NMF show completely different shapes. LMM and SLMM show the lower white matter factor, apart from VCA that presents a completely unexpected shape. The gray and white matter TACs from NMF are very near each other, as well as for SVCA. LMM and SLMM show more distinguishable white and gray matter factor TACs. As we can see in Fig. 3.24, the stroke region is more accurately detected by LMM and SLMM. LMM shows a larger area, but also present other non-affected gray matter tissues with high intensities. On the other hand, SLMM, even though not completely identifying the extremities of the affected regions, is more accurate in specifying the stroke region, with no “false alarm” intensities in terms of visual interpretability, i.e., no intensities higher than 50% for non-stroke or thalamus regions.

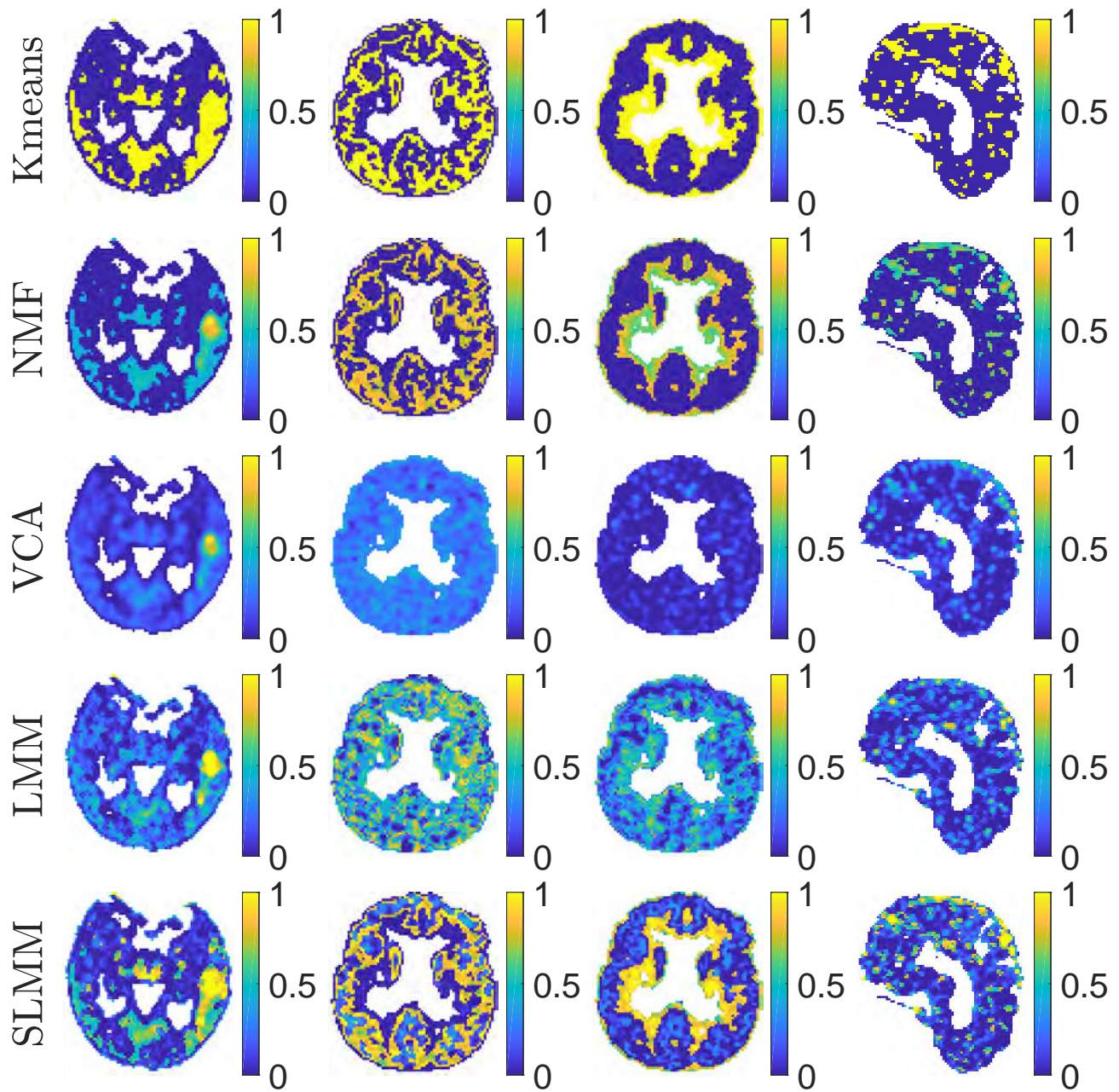


Figure 3.19.: Factor proportion maps of the first stroke subject. The first 3 columns show a transaxial view while the last one shows a sagittal view. From left to right: the specific gray matter, white matter, non-specific gray matter and blood.

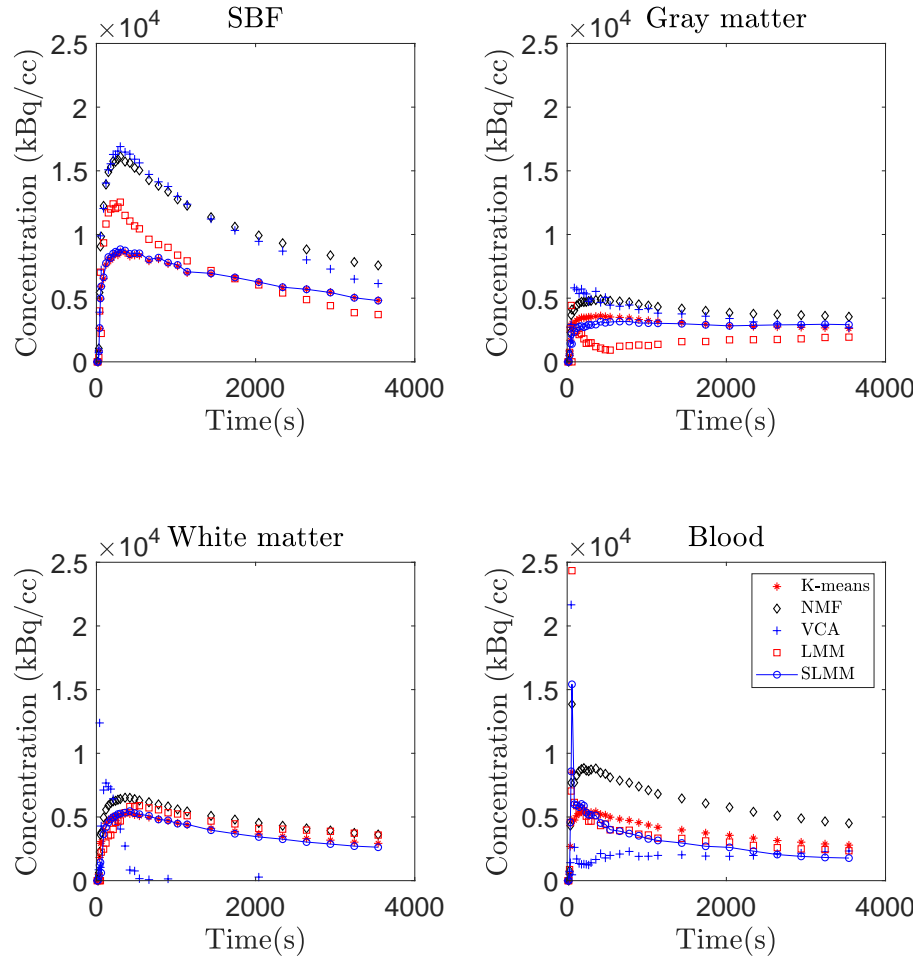


Figure 3.20.: TACs obtained by estimation from the first subject image.



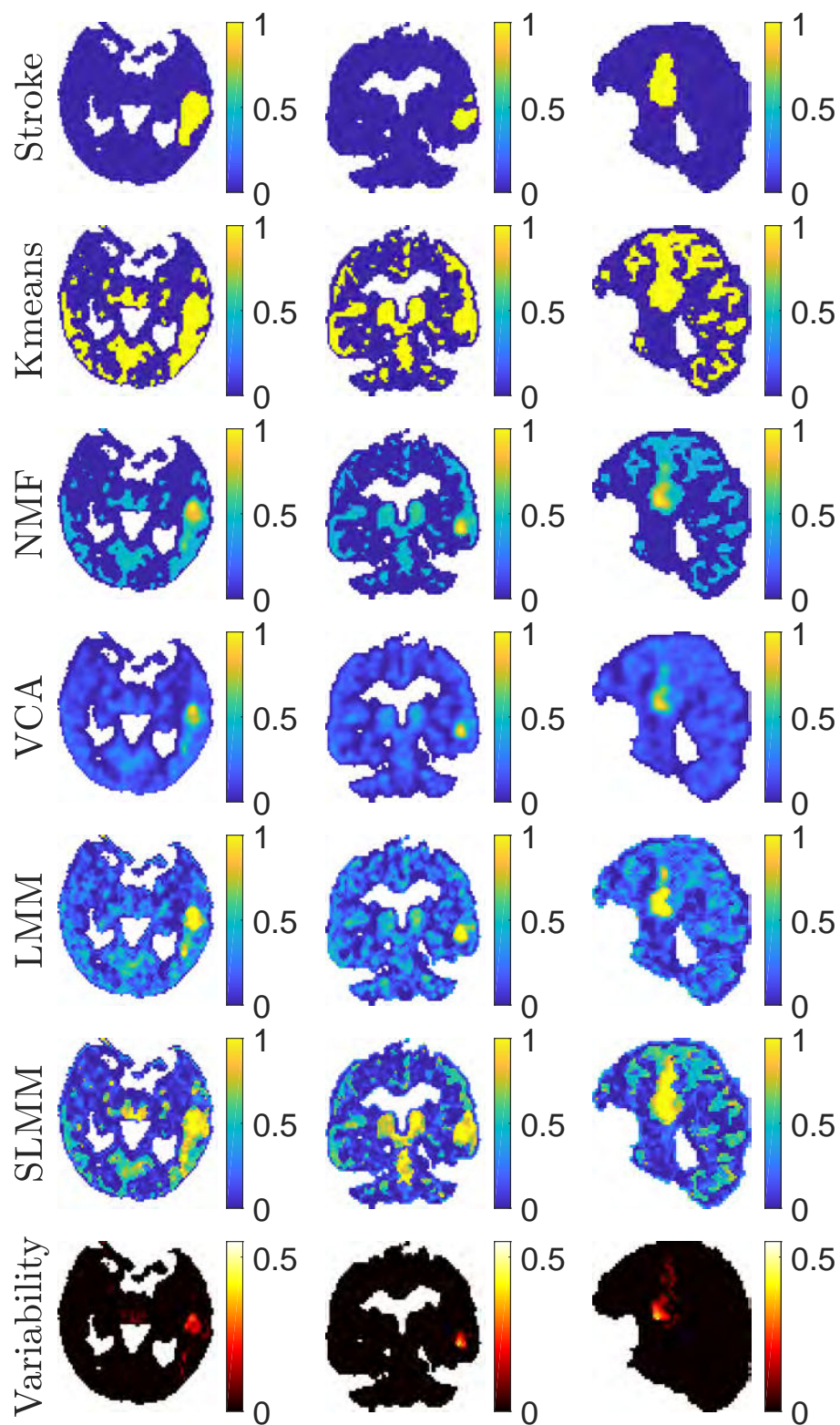


Figure 3.21.: From top to bottom: MRI ground-truth of the stroke area for the first stroke subject, SBF coefficient maps estimated by K-means, NMF, VCA, LMM, SLMM and SBF variability estimated by SLMM.

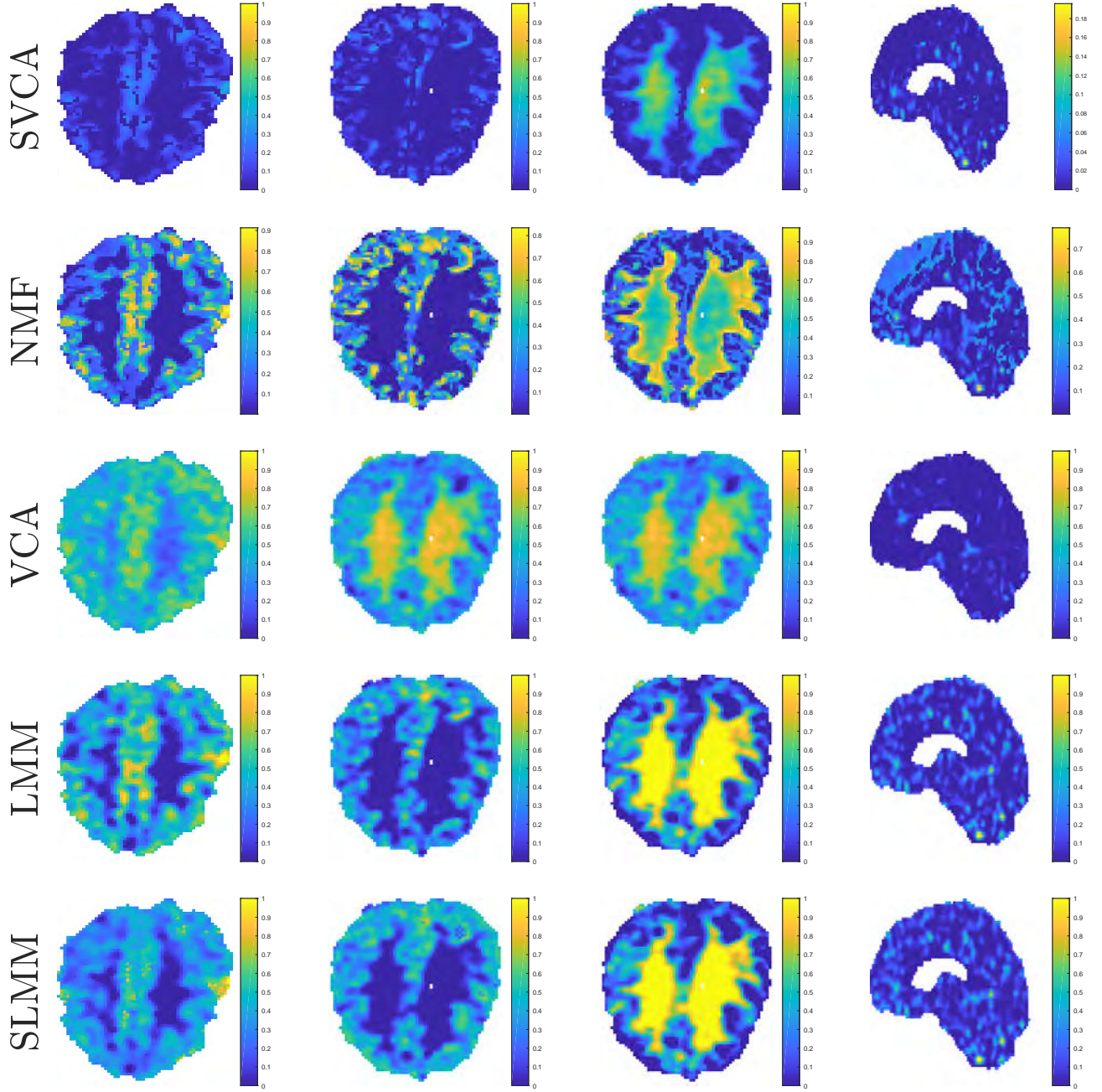


Figure 3.22.: Factor proportion maps of the second stroke subject. The first 3 columns show a transaxial view while the last one shows a sagittal view. From left to right: the specific gray matter, white matter, non-specific gray matter and blood.

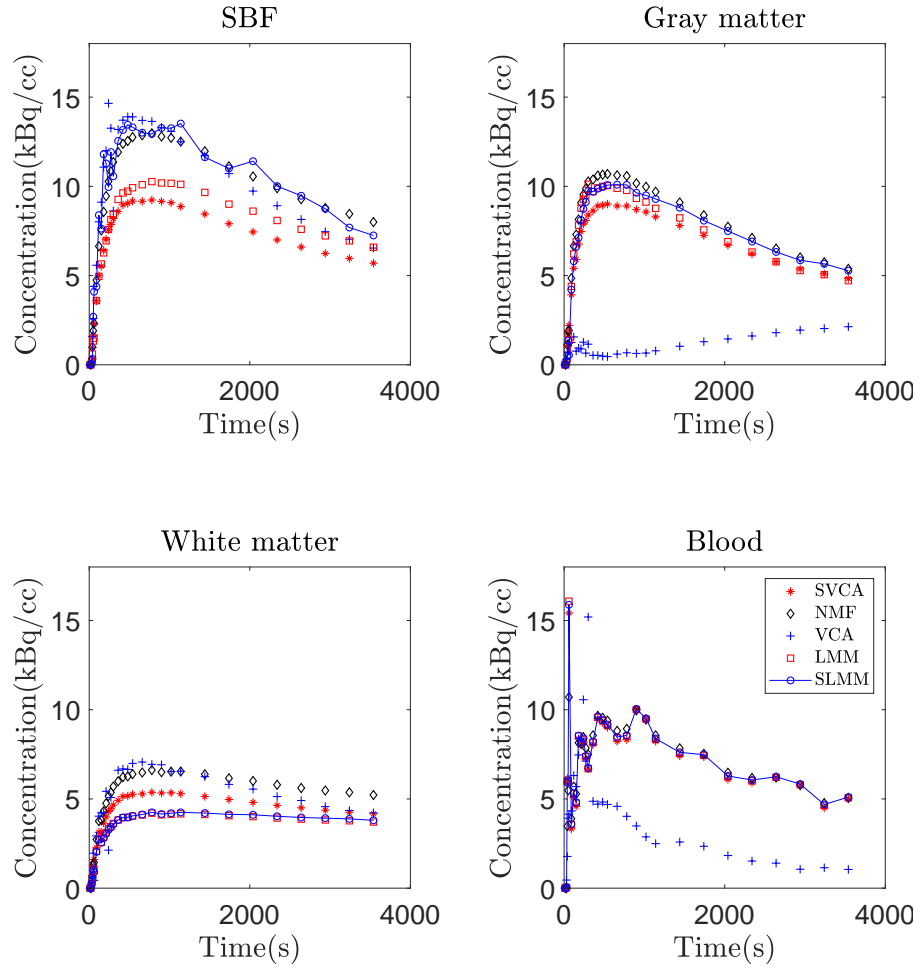


Figure 3.23.: TACs obtained by estimation from the second stroke subject image.



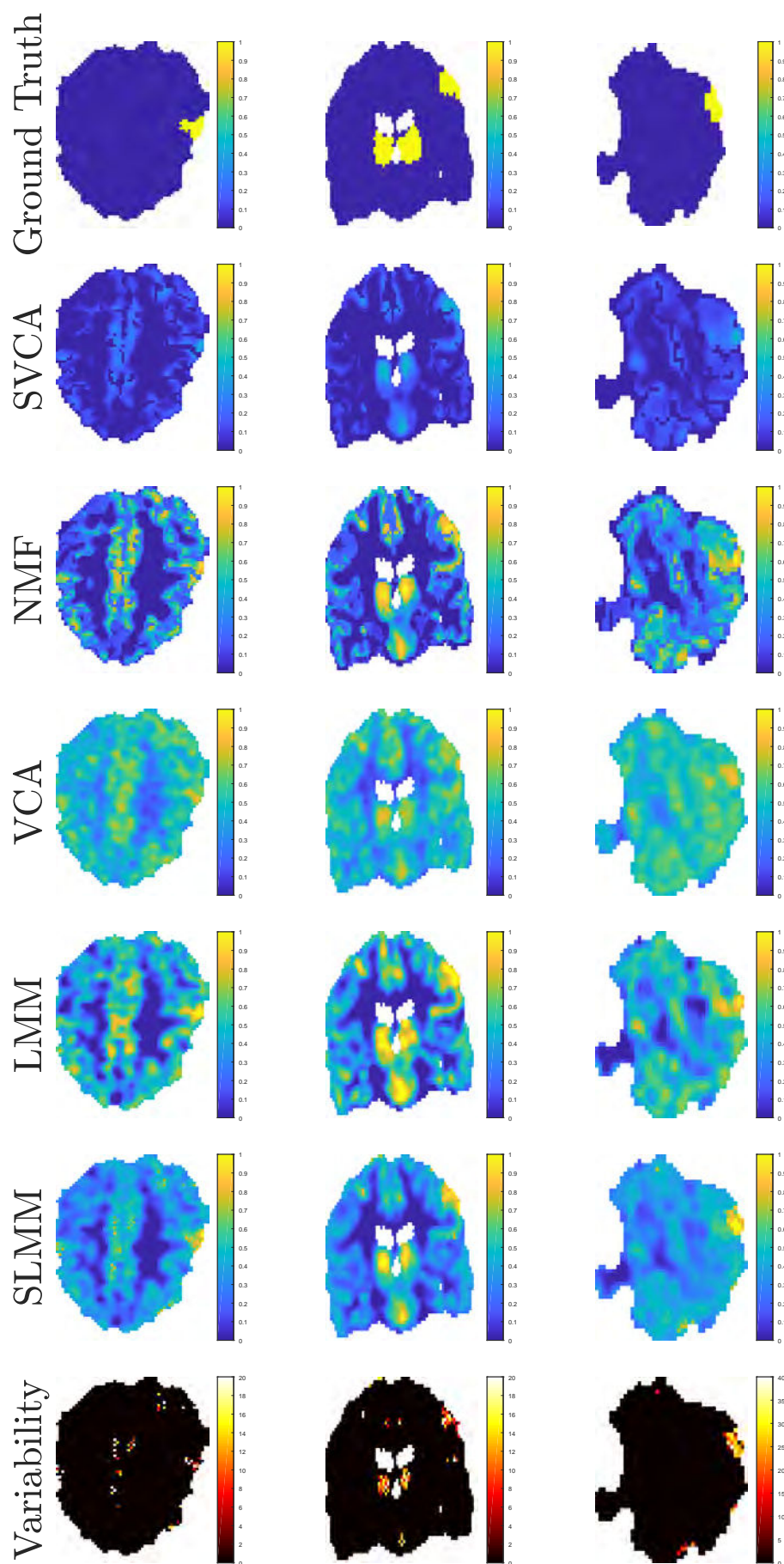


Figure 3.24.: From top to bottom: MRI ground-truth of the stroke area for the second stroke subject, SBF coefficient maps estimated by K-means, NMF, VCA, LMM, SLMM and SBF variability estimated by SLMM.

## 3.7. Discussion

### 3.7.1. Performance of the method

This chapter proposes a novel unmixing method, called SLMM, that takes into account the spatial variability of high-uptake tissues by modelling the SBF with an additional degree of freedom at each pixel. It also introduces a simplified version of this model with no variability, which consists of a regularized and constrained unmixing algorithm, herein named LMM.

For the cases studied in this chapter, SLMM and LMM always provide physically interpretable results, though not always the best, on the estimation of non-specific binding tissues. In Fig. 3.13 from synthetic data, we can see that both algorithms provide very accurate results for the white matter and blood factors. However, they provide the worst results for the gray matter factor, along with K-means, when compared with VCA and NMF. This results from the poor initialization of LMM and SLMM by the K-means outputs that are further propagated through the iterations by the factor regularization. A better initialization for the gray matter would provide better results. On the other hand, it is also the accurate initialization provided by K-means for the white matter that allows LMM and SLMM to present good results for this factor in comparison with the other algorithms. Both VCA and NMF show a very low performance for this factor TAC, in opposition to its good estimation of the gray matter TAC. As the gray and white matter TACs are highly correlated, it is natural to expect ambiguity on their results and therefore, a good performance on one of them may lower the performance on the other. Concerning the blood factor, both LMM and SLMM are able to overcome the poor K-means initialization and show a very accurate performance, along with VCA and NMF. In real data, while VCA is completely unable to differentiate tissues and LMM gets far away from the K-means initialization, both NMF and SLMM maintain the initialization structure for the non-specific binding tissues with some additional artifacts on the SLMM result due to deconvolution, as seen in Fig. 3.19. Moreover, the noisy artifacts produced by LMM and SLMM in real simulations are mainly due to the deconvolution step that has been included into the method. Note that the other methods (K-means, NMF and VCA) do not take into account this blurring effect. However, since the convolution by the PSF is known to affect accurate estimations of the factors and proportion maps, obtaining smoother (i.e., less noisy) maps does not mean better results.

Concerning high-uptake tissues, SLMM performs better than LMM and all the other algorithms for both the SBF and its associated proportion, as seen in Fig. 3.12, showing the interest of explicitly modelling the variability. Indeed, the variability proportion map computed by SLMM, depicted in Fig. 3.14 for synthetic simulations, not only delineates the specific binding region, but also is able to differentiate the intensity of high-uptake. This accurate estimation can be expected to characterize tissues differently affected by a tumor (some in early stages of metastasis and others already aggressively affected) or, in the case of stroke, to detect regions more or less affected by lack of oxygen or inflammation. When inspecting the experimental results

obtained on the real datasets in Figs. 3.21 and 3.24, the factor proportion related to specific binding seems to be estimated with a visually higher precision by the proposed model than the others. SLMM provides sharper and more accurate maps, characterized by a larger area with high uptake, as in the MRI ground-truth. The proposed technique seems to detect this meticulous difference, which are until now neglected in state-of-the-art computer-aided PET analysis.

### 3.7.2. Flexibility of the method

The method is an unsupervised approach and is easily adaptable to other contexts. In this work, two radiotracers for microglial activation were studied. Synthetic images were based on a phantom that presented the kinetics of the  $[^{11}\text{C}]\text{-PE2I}$  radioligand, while real images were acquired from  $[^{18}\text{F}]\text{DPA-714}$  injection. Besides these two tracers, the algorithm may be adapted to any tracer and any subject. To be transposed to another setting, the method only requires:

- (i) as in all factor analysis techniques, the number of expected kinetic classes in a ROI;
- (ii) an initial guess of the factors and proportions;
- (iii) a dictionary with the specific binding variability pattern, that can be learned as long as TACs containing specific binding kinetics can be identified.

Thus, changes in perfusion along patients and scans do not affect the performance of the method, since both (ii) and (iii) are subject and scan-dependent, i.e., are provided for each subject and scan. What indeed affects the performance of the method is rather the quality of (ii) and (iii) previous estimations. In this work, the initial guess (ii) was provided by K-means, however, the choice of the initialization can be adapted to the available data (e.g. an MRI scan of each subject, pre-defined population-based classes or atlas-based segmentations, SVCA results). The specific binding TACs needed in (iii) were identified by visual inspection of the real image, a procedure that can generally be repeated in any case, as long as some high-uptake voxels can be identified. A thresholding can also be used to identify these TACs, e.g., the 10% maximum AUC voxels in the last frames, or some atlas if high specific binding regions are known, e.g. the thalamus for  $[^{18}\text{F}]\text{DPA-714}$ .

Note however that we also have a high number of priors that may need to be adapted to each new scenario, even though their *a priori* assumptions are often very generic. The factor proportion penalization, related to the homogeneity of neighbouring regions in the image, is a quite general prior for all biomedical image processing applications. The factors prior is related to the reliability of initialization. It further intensifies the dependency of the LMM and SLMM solutions on a good initialization of factors, but also allows to benefit from a previous knowledge on the pattern of the factors, e.g., the kinetics of the tracer. Finally, the prior of the variability related to specific binding induces sparsity, i.e., assumes that only a few voxels in the image are impacted

by specific binding. The [11C]-PE2I is expected to mainly specifically bind in the striatum, so, in this case, sparsity is an adequate assumption. On the other hand, the [18F]DPA-714 targets microglial activation and therefore neuroinflammation in the brain, which can potentially affect a greater part of the image, in opposition to the sparsity assumption. Nevertheless, in our specific case of stroke patients, neuroinflammation was mainly expected in the stroke area and the thalamus, which represent a very small part of the brain, therefore this assumption was still adequate. Depending on the application, the intensity of the expected sparsity may be easily regulated by its corresponding weight (as for the other penalties), i.e., if specific binding is expected in a greater part of the image, we may reduce the level of the sparsity penalty or even set it to zero. So it is also quite adaptable. However, this highlights a drawback of our method that is the high number of hyperparameters to be tuned. The use of automatic estimation strategies within the algorithms should be envisaged in future developments.

### 3.8. Conclusion

This chapter introduced a new model to conduct factor analysis of dynamic PET images. It relied on the unmixing concept accounting for specific binding TACs variation. The method was based on the hypothesis that the variations within the SBF can be described by a small number of basis elements and their corresponding proportions per voxel. The resulting optimization problem was extremely non-convex with highly correlated factors and variability basis elements, which led to a high number of spurious local optima for the cost function. However, the experiments conducted on synthetic data showed that the proposed method succeeded in estimating this variability, which improved the estimation of the specific binding factor and the corresponding proportions. For the other quantities of interest, the proposed approach compared favourably with state-of-the-art unmixing techniques. The proposed approach has many potential applications in dynamic PET imaging. It could be used for the segmentation of a region-of-interest, classification of the voxels, creation of subject-specific kinetic reference regions or even simultaneous filtering and partial volume correction.

# Factor analysis of dynamic PET images: beyond Gaussian noise

The publication related to this chapter is [\[Cav+18a\]](#)

## Contents

4.1	Introduction . . . . .	98
4.2	Factor analysis techniques . . . . .	99
4.3	Divergence measure . . . . .	100
4.3.1	Noise in PET images . . . . .	100
4.3.2	The $\beta$ -divergence . . . . .	105
4.4	Block-coordinate descent algorithm . . . . .	106
4.4.1	Majorization-minimization algorithm . . . . .	109
4.4.2	Update of the factor TACs $\mathbf{M}$ . . . . .	110
4.4.3	Update of the factor proportions $\mathbf{A}$ . . . . .	111
4.4.4	Update of the internal variability $\mathbf{B}$ . . . . .	113
4.5	Experiments with synthetic data . . . . .	115
4.5.1	Synthetic data generation . . . . .	115
	Phantom I generation . . . . .	115
	Phantom II generation . . . . .	115
	Dynamic PET image simulation . . . . .	115
4.5.2	Compared methods . . . . .	116
	Phantom I . . . . .	116
	Phantom II . . . . .	117
4.5.3	Performance measures . . . . .	117
	Phantom I . . . . .	117
	Phantom II . . . . .	117
4.5.4	Results on Phantom I . . . . .	118
	$\beta$ -NMF results . . . . .	118
	$\beta$ -LMM results . . . . .	119
4.5.5	Results on Phantom II . . . . .	119
4.6	Experiments with real data . . . . .	129
4.6.1	Real data acquisition . . . . .	129
4.6.2	Results . . . . .	129
4.7	Conclusion . . . . .	131

## 4.1. Introduction

The previous chapter presented a model that handles the variations in perfusion and labelled molecule concentration affecting the TACs from specific binding tissues. As in several other methods from the dynamic PET literature, the data-fitting term in the previous method relies on the Frobenius norm that results from the assumption that the dynamic PET noise and the model approximation errors follow Gaussian distributions. However, this is a strong simplification of the underlying statistics of PET images. To overcome this limitation, [Ben+93] proposed a statistical model, demonstrating that accounting for Poisson noise instead of Gaussian noise was especially important in low count settings. Other works applied nonnegative matrix factorization (NMF) techniques, allowing the Kullback-Leibler (KL) divergence to be used, which is more appropriate for data corrupted by Poisson noise [Lee+01b; Pad+12; Sch13]. NMF with multiplicative updates is the approach generally employed since the algorithm is simple and there are fewer parameters to adjust than in FADS.

Nevertheless, even though the positron decay process can be described by a Poisson distribution [SV82], the actual noise in reconstructed PET images is not expected to be simply described by Poisson nor Gaussian distributions, as discussed in Section 1.5.2. Several acquisition characteristics, such as the detector system and electronic components, as well as post-processing corrections for scatter and attenuation, significantly alter the initial Poissonian statistics of the count-rates [Alp+82; Raz+05]. Considering the difficulties in characterizing the noise properties in PET images, many works have assumed the data to be corrupted by a Gaussian noise [Fes94; CHB97; Kam09]. Under some approximations, Barret et al. [BWT94; WTB94] have found the noise distribution on emission tomography (and images reconstructed with the EM algorithm in general) as being rather close to log-normal than normal statistics. Hybrid distributions, such as Poisson-Gaussian [MOM00] and Poisson-Gamma [Ira+11], have been also proposed in an attempt to take into account various phenomena occurring in the data. The work of Teymurazyan et al. [Tey+12] tried to determine the statistical properties of data reconstructed by filtered-back projection (FBP) and iterative expectation maximization (EM) algorithms. While FBP reconstructed images were sufficiently described by a normal distribution, the Gamma statistics were a better fit for EM reconstructions. The recent work of Mou et al. [MHO17] further studied the Gamma behaviour that can be found in PET reconstructed data.

While these works mainly put the emphasis on the noise model, we decide to investigate the impact of the divergence measure to be used for factor analysis of dynamic PET images. To this end, our study applies a popular and quite general loss function in NMF, namely the  $\beta$ -divergence [Bas+98; FI11]. The  $\beta$ -divergence is a family of divergences parametrized by a unique scalar parameter  $\beta \in [0, 2]$ . In particular, it has the great advantage of generalizing conventional loss functions such as the least-square, KL and Itakura-Saito divergences, respectively corresponding to Gaussian, Poisson and Gamma distributions.

The current chapter will empirically study the influence of  $\beta$  on the factor estimation for three different

methods. First, the standard  $\beta$ -NMF algorithm is applied. Then, an approach that includes a normalization of the factor proportions (herein called  $\beta$ -LMM) and previously considered in [EK04], is used to provide factors with a physical meaning. Finally, the  $\beta$ -divergence is also used to generalize the previous model introduced in Chapter 3, yielding an algorithm that we herein refer to as  $\beta$ -SLMM. Simulations are conducted on two different sets of synthetic data based on realistic count-rates and one real image of a patient's brain.

This chapter is organized as follows. The considered factor analysis models are described in Section 4.2. Section 4.3 presents the  $\beta$ -divergence as a measure of similarity. Section 4.4 discusses the corresponding factor analysis algorithms. Simulation results obtained with synthetic data are reported in Section 4.5. Experimental results on real data are provided in Section 4.6, and Section 4.7 concludes the chapter.

## 4.2. Factor analysis techniques

In this chapter, we apply three factor analysis models discussed in the previous chapters: nonnegative matrix factorization (NMF), linear mixing model (LMM) and specific binding LMM (SLMM). To this end, we recall the notations already provided in chapter 2, where  $\mathbf{Y}$  is the  $L \times N$  observation matrix that can be approximated by an estimated image  $\mathbf{X}(\boldsymbol{\theta})$  according to a factorization model described by  $P$  physically interpretable variables  $\boldsymbol{\theta} = [\theta_1, \dots, \theta_P]$ :

$$\mathbf{Y} \approx \mathbf{X}(\boldsymbol{\theta}). \quad (4.1)$$

The observation image is affected by a noise whose distribution characterization is a highly challenging task, as previously explained. For this reason, for the sake of generality, the description in (4.1) makes use of an approximation symbol  $\approx$  that generalizes the relation between the factor-dependent estimated image  $\mathbf{X}(\boldsymbol{\theta})$  and the observed data  $\mathbf{Y}$ . As in chapter 2, we formulate the optimization problem as the estimation of the parameter vector  $\boldsymbol{\theta}$  assumed to belong to a set denoted  $\mathcal{C}$  with possible complementary penalizations  $R(\boldsymbol{\theta})$ . It is mathematically described as

$$\hat{\boldsymbol{\theta}} \in \arg \min_{\boldsymbol{\theta} \in \mathcal{C}} \left\{ \mathcal{D}(\mathbf{Y}|\mathbf{X}(\boldsymbol{\theta})) + R(\boldsymbol{\theta}) \right\}, \quad (4.2)$$

where  $\mathcal{D}(\cdot|\cdot)$  is a measure of dissimilarity between the observed PET image  $\mathbf{Y}$  and the proposed model. The choice of this dissimilarity measure will be discussed in Section 4.3.

Table 4.1 summarizes the three factor analysis techniques - NMF, LMM and SLMM - presented in this chapter under (4.2) formulation. For both NMF and LMM,  $\mathbf{M} = [\mathbf{m}_1, \dots, \mathbf{m}_K]$  is a  $L \times K$  matrix of factors and  $\mathbf{A} = [\mathbf{A}_1, \dots, \mathbf{A}_N]$  is a  $K \times N$  matrix containing the factor coefficients. To produce a low-rank approximation of the matrix  $\mathbf{X}$ , we choose  $K \ll L, N$ .

For SLMM,  $\mathbf{M} = [\bar{\mathbf{m}}_1, \dots, \mathbf{m}_K]$  where  $\bar{\mathbf{m}}_1$  is the nominal specific binding factor. Moreover, “ $\circ$ ” is the Hadamard point-wise product,  $\mathbf{E}_1$  is the matrix  $[\mathbf{1}_{L,1} \mathbf{0}_{L,K-1}]$ ,  $\mathbf{V} = [\mathbf{v}_1, \dots, \mathbf{v}_{N_v}]$  is the  $L \times N_v$  matrix composed

of the basis elements used to describe the variability of the specific binding factor (SBF) with  $N_v \ll L$ , and  $\mathbf{B} = [\mathbf{b}_1, \dots, \mathbf{b}_n]$  is the  $N_v \times N$  matrix composed of internal variability proportions. Differently from the optimization problem described in Chapter 3, here we will discard the factors and factor proportions penalization and only keep the variability sparsity penalization for simplification purposes. The final SLMM cost function writes

$$\mathcal{J}(\mathbf{M}, \mathbf{A}, \mathbf{B}) = \mathcal{D}(\mathbf{Y} | \underbrace{\mathbf{M}\mathbf{A} + [\mathbf{E}_1 \mathbf{A} \circ \mathbf{V}\mathbf{B}]}_{\Delta}) + \lambda \varphi \|\mathbf{B}\|_{2,1}, \quad (4.3)$$

where the trade-off between the data fitting term and the penalty  $\|\mathbf{B}\|_{2,1}$  is controlled by the parameter  $\lambda$  and also depends on the dispersion parameter  $\varphi$  that is related to the noise distribution and will be further detailed in Section 4.3.1.

Table 4.1.: Summary of NMF, LMM and SLMM under (4.2)

	$\boldsymbol{\theta}$	$\mathbf{X}(\boldsymbol{\theta})$	$\mathcal{C}$	$R(\boldsymbol{\theta})$
NMF	$\{\mathbf{M}, \mathbf{A}\}$	$\mathbf{X} = \mathbf{M}\mathbf{A}$	$\mathbf{A} \succeq \mathbf{0}_{K,N}$ $\mathbf{M} \succeq \mathbf{0}_{L,K}$	-
LMM	$\{\mathbf{M}, \mathbf{A}\}$	$\mathbf{X} = \mathbf{M}\mathbf{A}$	$\mathbf{A} \succeq \mathbf{0}_{K,N}$ $\mathbf{M} \succeq \mathbf{0}_{L,K}$ $\mathbf{A}^T \mathbf{1}_K = \mathbf{1}_N$	-
SLMM	$\{\mathbf{M}, \mathbf{A}, \mathbf{B}\}$	$\mathbf{X} = \mathbf{M}\mathbf{A} + [\mathbf{E}_1 \mathbf{A} \circ \mathbf{V}\mathbf{B}]$	$\mathbf{A} \succeq \mathbf{0}_{K,N}$ $\mathbf{M} \succeq \mathbf{0}_{L,K}$ $\mathbf{B} \succeq \mathbf{0}_{N_v,N}$ $\mathbf{A}^T \mathbf{1}_K = \mathbf{1}_N$	$\ \mathbf{B}\ _{2,1} = \sum_{n=1}^N \ \mathbf{b}_n\ _2$

### 4.3. Divergence measure

When analyzing PET data, most studies in the literature have considered the Euclidean distance or the Kullback-Leibler divergence as the loss function  $\mathcal{D}(\cdot|\cdot)$  to be used in the inverse problem (4.1). These choices are intrinsically related to the assumptions of Gaussian and Poissonian noise, respectively, as detailed in the next paragraphs. However, as previously discussed, the noise encountered in PET data is altered by several external circumstances and parameters, even though the initial count-rates are known to follow a Poisson distribution. Hence, to provide a generalization of these PET noise models, this work proposes to resort to the  $\beta$ -divergence as the dissimilarity measure underlying the approximation in (4.1).

#### 4.3.1. Noise in PET images

Before introducing the solution proposed in this chapter to deal with the unknown nature of the noise in PET images, we present a study conducted on 64 samples simulated with the realistic count-rates process posteriorly detailed in Section 4.5.1, with 6 reconstruction iterations. Each sample is a 4D image (3D+time) of size



$128 \times 128 \times 64 \times 20$ . This study further explains the noise and effects discussed in Section 1.5.2. There are many ways to study the noise, such as through the calculus of pixel normalized standard deviation [Paj+98]; the study of the histogram of the region of interest in order to characterize the noise probability density function; the evaluation of differences between the histogram of a population from a reference distribution with graphical methods such as Quantile-Quantile (Q-Q) plots; the use of skewness (third standardized moment) and kurtosis (fourth standardized moment) [Tey+12]; and finally the analysis of the spatial variance in the region-of-interest (ROI) [RT13]. In this section, we will limit ourselves to the study of spatial variation and estimation of the noise distribution with the histogram.

First, we present pixel variance, covariance and mean over time inside a ROI containing high-uptake tissue of size  $20 \times 20 \times 10$  pixels. As previously discussed, the varying durations of frames, among other factors, change the noise levels from frame to frame [CQ10]. On Fig. 4.1, the variation seems to be directly proportional to the signal power, since the earlier frames of a typical dynamic PET acquisition are expected to have fewer photon counts and be more heavily corrupted by noise than the latter ones. This is also seen in Fig. 4.2, since the time bins of the earlier parts of the scan are kept short to capture the fast kinetics right after tracer injection [DLL13]. From Fig. 4.2, we also verify that the SNR is always around 12dB, in a range between 8dB and 15dB.

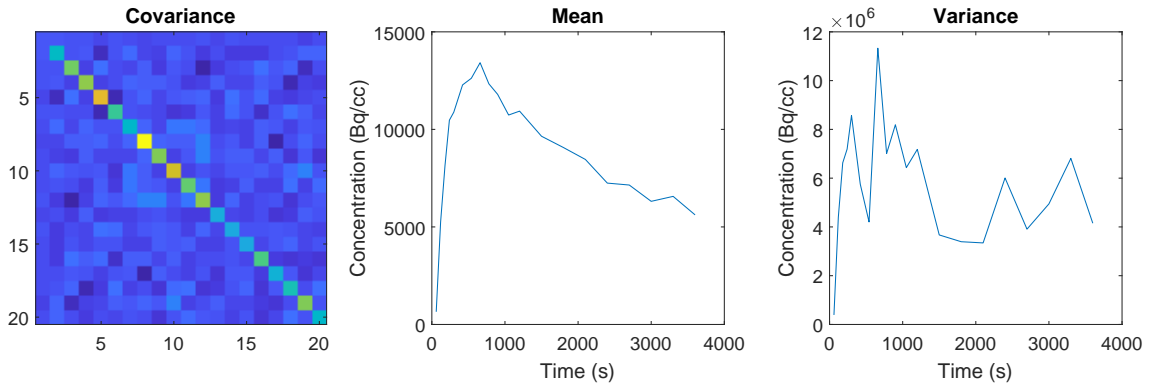


Figure 4.1.: Empirical covariance, mean and variance of a randomly chosen region.

A second study is conducted to investigate the distribution of the noise. It consisted in a comparison of the histogram with three distributions, particularly Poisson, Gaussian and Gamma distributions, whose parameters are estimated by computing their maximum likelihood estimators (MLE). Acknowledging that the noise changes with time, we compare the histogram in six different time frames (1, 4, 7, 10, 13, 16) and four different pixels over the 64 samples.

Computing the MLE related to a given noise distribution consists in minimizing the partial derivative of the negative log-likelihood of this distribution with respect to the parameter we want to estimate. In the following, the MLE of the parameters for the three distributions will be provided.

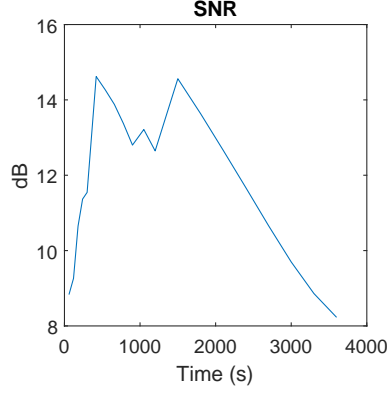


Figure 4.2.: Empirical SNR for each frame of time (in dB)

- **MLE for the Gaussian distribution:** Considering an observation  $y$  corrupted by an additive white Gaussian noise  $n$  affecting a signal  $x$ , i.e.  $y = x + n$  with  $n \sim \mathcal{N}(0, \sigma^2)$ , the probability density function that describes the data distribution writes

$$p(y|x, \sigma^2) = \frac{1}{\sqrt{2\pi\sigma^2}} \exp\left(-\frac{1}{2} \frac{(y-x)^2}{\sigma^2}\right) \quad (4.4)$$

and its negative log likelihood is

$$-\log(p(y|x, \sigma^2)) = \frac{1}{2\sigma^2}(y-x)^2 + \text{cte.} \quad (4.5)$$

As the noise mean is zero, the mean of the observations is the signal  $x$ . Moreover, the variance  $\sigma^2$  that describes this Gaussian distribution is estimated from  $P$  samples as:

$$\hat{\sigma}^2 = \frac{1}{P} \sum_{j=1}^P (y_j - x). \quad (4.6)$$

- **MLE for the Gamma distribution:** Considering a multiplicative Gamma noise, i.e.  $y = xn$  with  $n \sim \mathcal{G}(\eta, \eta)$  and  $\mathbb{E}[n] = 1$ , the Gamma distribution describing the noise  $n$  is given by

$$p(n|\eta, \eta) = \frac{\eta^\eta n^{\eta-1} e^{-\eta n}}{\Gamma(\eta)}. \quad (4.7)$$

The negative log likelihood for the data  $y$  writes:

$$\begin{aligned}
 -\log(p(y|x, \eta, \eta)) &= -\log p(n|\eta, \eta)/x \\
 &= -\log \frac{1}{x} \frac{\eta^\eta \left(\frac{y}{x}\right)^{\eta-1} e^{-\eta \left(\frac{y}{x}\right)}}{\Gamma(\eta)} \\
 &= \eta \left(\frac{y}{x} - \log \left(\frac{y}{x}\right)\right) + \text{cte.}
 \end{aligned} \tag{4.8}$$

From the minimization of negative log likelihood of the Gamma distribution regarding  $\eta$ , the MLE  $\hat{\eta}$  is

$$P(\log \hat{\eta} - \frac{\partial}{\partial \eta} \log \Gamma(\hat{\eta}) + \frac{1}{P} \sum_{j=1}^P \log y_j) = 0. \tag{4.9}$$

As there is no closed-form solution for  $\hat{\eta}$ , a numerical iterative solution, such as the Newton-Raphson technique or the fixed-point method, must be applied [KR09].

- **MLE for the Poisson distribution:** A Poisson distribution is described by the following discrete probability

$$p(y|x) = \frac{x^y e^{-x}}{y!} \tag{4.10}$$

and the negative log-likelihood is

$$-\log(p(y|x)) = -y \log x + x + \text{cte.} \tag{4.11}$$

The MLE for the Poisson parameter simply gives  $\mathbb{E}[y] = x$ . However, the images herein studied do not follow a standard Poisson distribution. The generation process of the count-rates  $y$  can be approximated with scaled Poisson random variables, i.e.,  $y = \gamma v$  and  $v \sim \mathcal{P}(\frac{x}{\gamma})$ .

The mean of variable  $y$  may be written as

$$\mathbb{E}[y] = \gamma \mathbb{E}[v] = x, \tag{4.12}$$

while the variance is

$$\text{var}[y] = \gamma^2 \text{var}[v] = \gamma x. \tag{4.13}$$

Thus, to obtain a rough estimation of the scaling constant  $\gamma$  for each studied frame, we simply compute

$$\gamma = \frac{\text{var}[y]}{\mathbb{E}[y]}. \tag{4.14}$$

Note that scaled Poisson random variables do not follow a Poisson distribution.

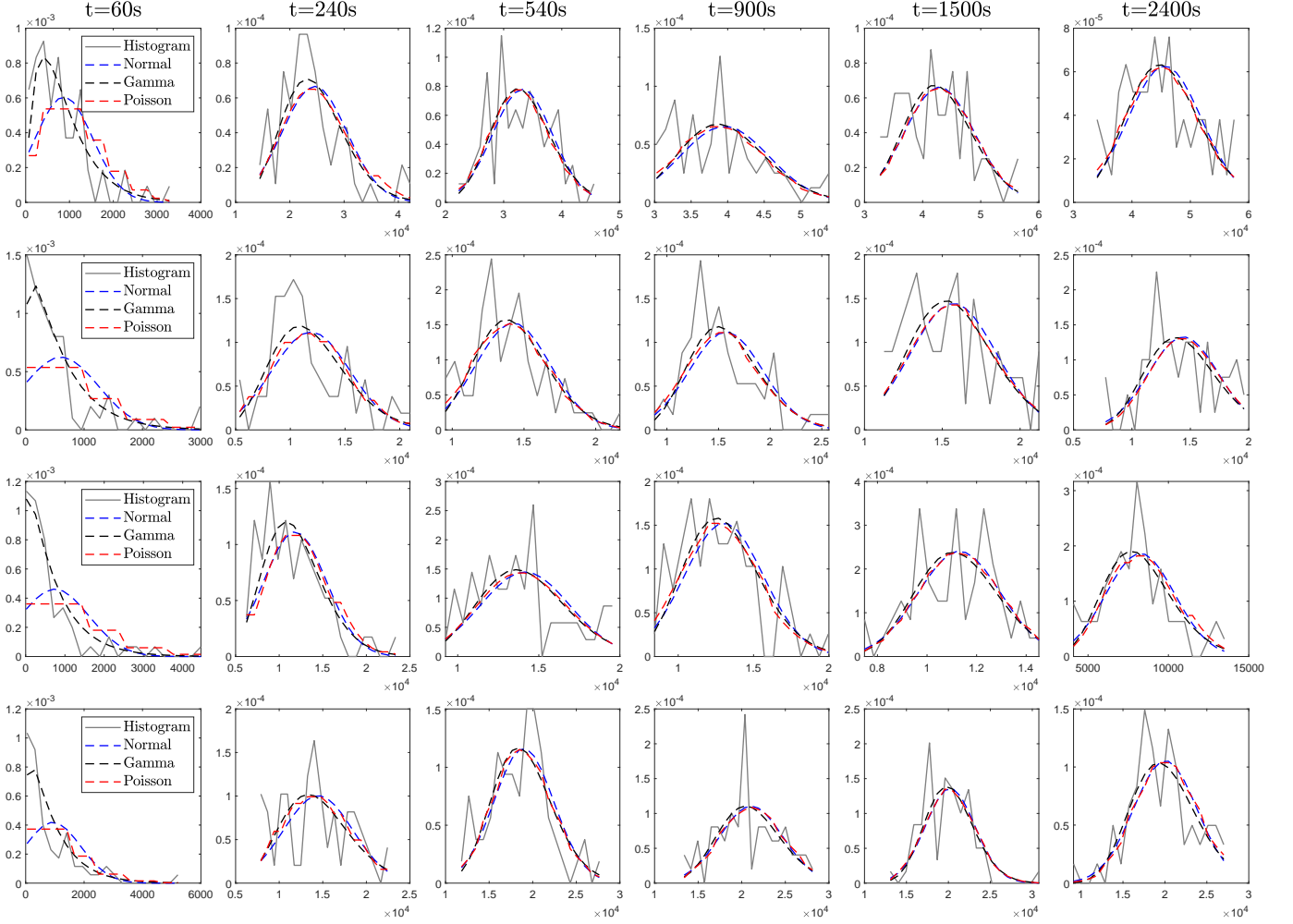


Figure 4.3.: Histogram study in 4 different regions of the image and 4 different time frames

Fig. 4.3 shows the empirical histograms as well as the corresponding theoretical probability density functions (i.e., whose parameters are the MLEs) obtained from the 64 samples of each pixel. Visual comparison suggests that in the earlier frames the noise distribution is close to the Gamma distribution, gradually acquiring a more Poisson-like shape until it is no longer visually recognizable which distribution fits the best. Note that for sufficiently large values of the mean, the Poisson distribution can be approximated by a Gaussian distribution with equal mean and variance. This may also explain why they are so close in latter frames, where the tracer concentration in tissues is generally higher.

### 4.3.2. The $\beta$ -divergence

The  $\beta$ -divergence first appeared in the works of Basu et al. [Bas+98] and Eguchi and Kano [EK01]. Since then, it has been intensively used, with noticeable successes in the audio literature for music transcription and separation [OP08; FCC09; FBD09]. More precisely, the  $\beta$ -divergence applied to two matrices  $\mathbf{Y}$  and  $\mathbf{X}$  follows the component-wise separability property

$$\mathcal{D}_\beta(\mathbf{Y}|\mathbf{X}) = \sum_{\ell=1}^L \sum_{n=1}^N d_\beta(y_{\ell,n}|x_{\ell,n}) \quad (4.15)$$

and is defined, for  $\beta \in (0, 2)$ , as

$$d_\beta(y|x) = \frac{1}{\beta(\beta-1)}(y^\beta + (\beta-1)x^\beta - \beta yx^{\beta-1}) \quad (4.16)$$

with

$$d'_\beta(y|x) = x^{(\beta-2)}(x-y), \quad (4.17)$$

$$d''_\beta(y|x) = x^{(\beta-3)}[(\beta-1)x - (\beta-2)y]. \quad (4.18)$$

The limit cases for the  $\beta$ -divergence are the following

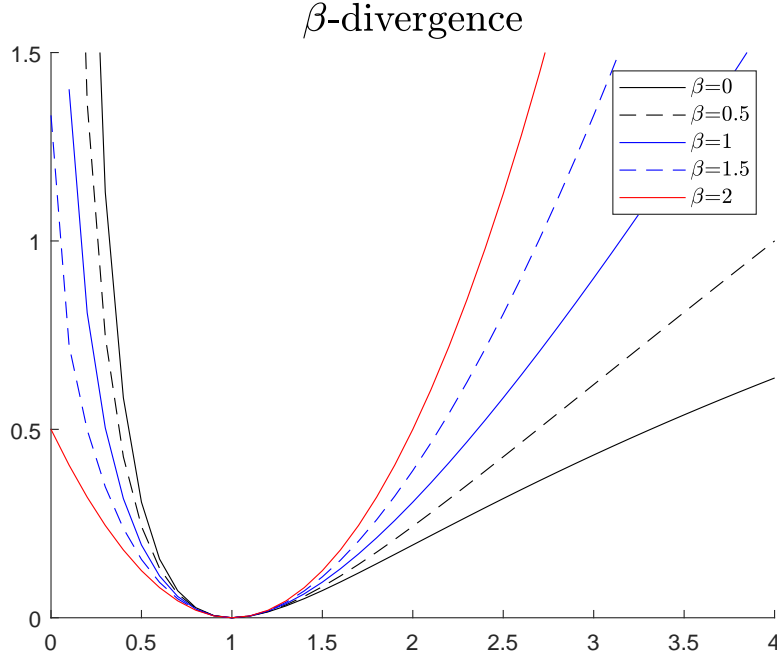
$$d_\beta(y|x) = \begin{cases} \frac{1}{2}(y^2 + x^2 - 2yx) & \beta = 2, \\ y \log \frac{y}{x} - y + x & \beta = 1, \\ \frac{y}{x} - \log \frac{y}{x} - 1 & \beta = 0. \end{cases} \quad (4.19)$$

Note that the cases  $\beta = 1$  and  $\beta = 2$  lead to the Kullback-Leibler divergence and the squared Euclidean distance, respectively, already discussed above, while  $\beta = 0$  leads to the Itakura-Saito divergence. To illustrate this family, Fig. 4.4 compares the loss functions  $d(y=1|x)$  as functions of  $x$  for various values of  $\beta$ . A comprehensive presentation of the  $\beta$ -divergence is available at [CA10].

Among its interesting properties, the  $\beta$ -divergence can be related to a wide family of distributions, namely the Tweedie distributions, via its corresponding density  $p(y|x)$  following

$$-\log p(y|x) = \varphi^{-1} d_\beta(y|x) + \text{const.} \quad (4.20)$$

where  $\varphi$  is the dispersion parameter that is related to the variance of the distribution. In particular, the Tweedie distributions encompass a large class of popular distributions, including the Gaussian  $y \sim \mathcal{N}(x, \sigma^2)$ , Poissonian  $y \sim \mathcal{P}(x)$  and Gamma  $y \sim \mathcal{G}(\eta, \eta/x)$  observation noises studied in Section 4.3.1. As we can see from (4.5), the

Figure 4.4.:  $\beta$ -divergence  $d_\beta(y=1|x)$  as a function of  $x$ .

Gaussian distribution corresponds to the Euclidian distance with dispersion parameter  $\varphi = \sigma^2$ . For Poisson, the corresponding divergence in (4.11) is the Kullback-Leibler and the dispersion parameter is  $1^1$ . The Gamma distribution corresponds to the Itakura Saito divergence, as proved in (4.8), with  $\varphi = \text{var}$ , where  $\text{var} = \frac{1}{\eta}$ .

To summarize, choosing the  $\beta$ -divergence as the loss function in (4.2) allows the approximation (4.1) to stand for a wide range of noise models. As a consequence, thanks to its genericity, the  $\beta$ -divergence seems to be relevant and flexible tool to conduct factor analysis when the PET noise is difficult to be characterized.

## 4.4. Block-coordinate descent algorithm

The non-convex minimization problem stated in (5.12) is solved through a block-coordinate descent (BCD) algorithm. For each factor analysis model discussed in Section 4.2, the corresponding algorithm iteratively updates a latent variable  $\theta_i$  while all the others are kept fixed, allowing for convergence towards a local solution. The definition of these blocks naturally arises according to the considered latent factor model. The method detailed hereafter resorts to multiplicative update rules, i.e., consists in multiplying the current variable values by nonnegative terms, thus preserving the nonnegativity constraint along the iterations. To avoid undesirable solutions, given the non-convexity of the problem, the algorithms require proper initialization.

The algorithm and corresponding updates used for  $\beta$ -NMF have been introduced in [FI11] and are recalled in Algo. 4. The present chapter focuses on the SLMM model, that turns into LMM when fixing  $\mathbf{B} = \mathbf{0}$ .

<sup>1</sup>For scaled Poisson variables,  $\varphi = \frac{\text{var}[y]}{\mathbb{E}[y]}$ .

The updates are derived following the strategy proposed in [FD15], while some heuristic rules are inspired by [FBD09]. The principles of these updates are briefly recalled in paragraph 4.4.1 and particularly instantiated for the considered SLMM-based factor model in paragraphs 4.4.2–4.4.4. The resulting  $\beta$ -LMM and  $\beta$ -SLMM algorithms are summarized in Algos. 5 and 6, respectively. In Algos. 4, 5 and 6, all multiplications (identified by the  $\circ$  symbol), divisions and exponentiations are entry-wise operations,  $\mathbf{1}_{K,L}$  denote a  $K \times L$  matrix of ones and  $\mathbf{\Gamma}_{\mathbf{B}} \triangleq \text{diag}[\|\mathbf{b}_1\|_1, \dots, \|\mathbf{b}_1\|_N]^{-1}$ .

---

**Algorithm 4:**  $\beta$ -NMF unmixing

---

**Data:**  $\mathbf{Y}$   
**Input:**  $\mathbf{A}^0, \mathbf{M}^0$

```

1  $k \leftarrow 0$ 
2  $\mathbf{A} \leftarrow \mathbf{A}^0$ 
3  $\mathbf{M} \leftarrow \mathbf{M}^0$ 
4  $\tilde{\mathbf{X}} \leftarrow \mathbf{M}\mathbf{A}$ 
5 while stopping criterion not satisfied do
6   % Update factor TACs
7    $\mathbf{M} \leftarrow \mathbf{M} \circ \left[ \frac{(\mathbf{Y} \circ \tilde{\mathbf{X}}^{\beta-2}) \mathbf{A}^T}{\tilde{\mathbf{X}}^{\beta-1} \mathbf{A}^T} \right]$ 
8    $\tilde{\mathbf{X}} \leftarrow \mathbf{M}\mathbf{A}$ 
9   % Update factor proportions
10   $\mathbf{A} \leftarrow \mathbf{A} \circ \left[ \frac{\mathbf{M}^T (\mathbf{Y} \circ \tilde{\mathbf{X}}^{\beta-2})}{\mathbf{M}^T \tilde{\mathbf{X}}^{\beta-1}} \right]$ 
11   $k \leftarrow k + 1$ 
12   $\tilde{\mathbf{X}} \leftarrow \mathbf{M}\mathbf{A}$ 
Result:  $\mathbf{A}, \mathbf{M}$ 

```

---



---

**Algorithm 5:**  $\beta$ -LMM unmixing

---

**Data:**  $\mathbf{Y}$   
**Input:**  $\mathbf{A}^0, \mathbf{M}^0$

```

1  $k \leftarrow 0$ 
2  $\mathbf{A} \leftarrow \mathbf{A}^0$ 
3  $\mathbf{M} \leftarrow \mathbf{M}^0$ 
4  $\tilde{\mathbf{X}} \leftarrow \mathbf{M}\mathbf{A}$ 
5 while stopping criterion not satisfied do
6   % Update factor TACs
7    $\mathbf{M} \leftarrow \mathbf{M} \circ \left[ \frac{(\mathbf{Y} \circ \tilde{\mathbf{X}}^{\beta-2}) \mathbf{A}^T}{\tilde{\mathbf{X}}^{\beta-1} \mathbf{A}^T} \right]$ 
8    $\tilde{\mathbf{X}} \leftarrow \mathbf{M}\mathbf{A}$ 
9   % Update factor proportions
10   $\mathbf{A} \leftarrow \mathbf{A} \circ \left[ \frac{\mathbf{M}^T (\mathbf{Y} \circ \tilde{\mathbf{X}}^{\beta-2}) + \mathbf{1}_{K-1,L} \tilde{\mathbf{X}}^\beta}{\mathbf{M}^T \tilde{\mathbf{X}}^{\beta-1} + \mathbf{1}_{K-1,L} (\mathbf{Y} \circ \tilde{\mathbf{X}}^{\beta-1})} \right]$ 
11   $k \leftarrow k + 1$ 
12   $\tilde{\mathbf{X}} \leftarrow \mathbf{M}\mathbf{A}$ 
Result:  $\mathbf{A}, \mathbf{M}$ 

```

---

**Algorithm 6:**  $\beta$ -SLMM unmixing**Data:**  $\mathbf{Y}$ **Input:**  $\mathbf{A}^0, \mathbf{M}^0, \mathbf{B}^0, \lambda$ 


---

```

1  $k \leftarrow 0$ 
2  $\mathbf{A} \leftarrow \mathbf{A}^0$ 
3  $\mathbf{M} \leftarrow \mathbf{M}^0$ 
4  $\mathbf{B} \leftarrow \mathbf{B}^0$ 
5  $\tilde{\mathbf{X}} \leftarrow \mathbf{MA} + [\mathbf{E}_1 \mathbf{A} \circ \mathbf{VB}]$ 
6 while stopping criterion not satisfied do
7   % Update variability matrix
       $\mathbf{B} \leftarrow \mathbf{B} \circ \left[ \frac{\mathbf{1}_{N_v}^T \mathbf{A}_{1,:} \circ (\mathbf{V}^T (\mathbf{Y} \circ \tilde{\mathbf{X}}^{\beta-2}))}{\mathbf{1}_{N_v}^T \mathbf{A}_{1,:} \circ (\mathbf{V}^T \tilde{\mathbf{X}}^{\beta-1}) + \lambda \mathbf{B}^k \Gamma_{\mathbf{B}}} \right]^{\frac{1}{3-\beta}}$ 
8    $\tilde{\mathbf{X}} \leftarrow \mathbf{MA} + [\mathbf{E}_1 \mathbf{A} \circ \mathbf{VB}]$ 
9   % Update factor TACs
       $\mathbf{M}_{2:K} \leftarrow \mathbf{M}_{2:K} \circ \left[ \frac{(\mathbf{Y} \circ \tilde{\mathbf{X}}^{\beta-2}) \mathbf{A}_{2:K}^T}{\tilde{\mathbf{X}}^{\beta-1} \mathbf{A}_{2:K}^T} \right]$ 
10   $\tilde{\mathbf{X}} \leftarrow \mathbf{MA} + [\mathbf{E}_1 \mathbf{A} \circ \mathbf{VB}]$ 
11  % Update SBF factor proportion
       $\mathbf{A}_1 \leftarrow \mathbf{A}_1 \circ \left[ \frac{\mathbf{1}_L^T ((\mathbf{M}_1 \mathbf{1}_N^T + \mathbf{VB}) \circ (\mathbf{Y} \circ \tilde{\mathbf{X}}^{\beta-2}) + \tilde{\mathbf{X}}^\beta)}{\mathbf{1}_L^T ((\mathbf{M}_1 \mathbf{1}_N^T + \mathbf{VB}) \circ \tilde{\mathbf{X}}^{\beta-1} + \mathbf{Y} \circ \tilde{\mathbf{X}}^{\beta-1})} \right]$ 
12  % Update other factor proportions
       $\mathbf{A}_{2:K} \leftarrow \mathbf{A}_{2:K} \circ \left[ \frac{\mathbf{M}_{2:K}^T (\mathbf{Y} \circ \tilde{\mathbf{X}}^{\beta-2}) + \mathbf{1}_{K-1,L} \tilde{\mathbf{X}}^\beta}{\mathbf{M}_{2:K}^T \tilde{\mathbf{X}}^{\beta-1} + \mathbf{1}_{K-1,L} (\mathbf{Y} \circ \tilde{\mathbf{X}}^{\beta-1})} \right]$ 
13   $k \leftarrow k + 1$ 
14   $\tilde{\mathbf{X}} \leftarrow \mathbf{MA} + [\mathbf{E}_1 \mathbf{A} \circ \mathbf{VB}]$ 

```

---

**Result:**  $\mathbf{A}, \mathbf{M}, \mathbf{B}$

---



#### 4.4.1. Majorization-minimization algorithm

Majorization-minimization (MM) algorithms consist in finding a surrogate function that majorizes the original objective function and then computing its minimum. MM algorithms used to solve NMF problems are based on gradient-descent updates, whose step-size is specifically chosen to provide multiplicative updates [CZA06]. The algorithm iteratively updates each variable  $\theta_i$  given all the other variables  $\theta_{j \neq i}$ . Hence, the subproblems can be written

$$\min_{\theta_i} \mathcal{J}(\theta_i) = \mathcal{D}(\mathbf{Y}|\mathbf{X}(\boldsymbol{\theta})) + R(\theta_i) \text{ s.t. } \theta_i \in \mathcal{C}. \quad (4.21)$$

By denoting  $\tilde{\theta}_i$  the state of the latent variable  $\theta_i$  at the current iteration, we first define an auxiliary function  $G(\theta_i|\tilde{\theta}_i)$  that majorizes  $\mathcal{J}(\theta_i)$ , i.e.,  $G(\theta_i|\tilde{\theta}_i) \geq \mathcal{J}(\theta_i)$ , and is tight at  $\tilde{\theta}_i$ , i.e.  $G(\tilde{\theta}_i|\tilde{\theta}_i) = \mathcal{J}(\tilde{\theta}_i)$ . The optimization problem (4.21) is then replaced by the minimization of the auxiliary function. Setting the associated gradient to zero generally leads to multiplicative updates of the form [FI11]

$$\theta_i = \tilde{\theta}_i \left[ \frac{N(\tilde{\theta}_i)}{D(\tilde{\theta}_i)} \right]^{\gamma(\beta)}, \quad (4.22)$$

where the functions  $N(\cdot)$  and  $D(\cdot)$  are problem-dependent and  $\gamma(\beta)$  is  $\frac{1}{2-\beta}$  for  $\beta < 1$ , 1 for  $\beta \in [1, 2]$  and  $\frac{1}{\beta-1}$  for  $\beta > 2$ .

A heuristic alternative to this algorithm was provided in [FBD09]. It consists in decomposing the gradient w.r.t. the variable  $\tilde{\theta}_i$  as the difference between two nonnegative functions [FI11]:

$$\nabla_{\theta_i} \mathcal{J}(\tilde{\theta}_i) = \nabla_{\tilde{\theta}_i}^+ \mathcal{J}(\tilde{\theta}_i) - \nabla_{\tilde{\theta}_i}^- \mathcal{J}(\tilde{\theta}_i) \quad (4.23)$$

and the multiplicative updates of [CZA06; FBD09] can be heuristically written as in (4.22) with

$$N(\tilde{\theta}_i) = \nabla_{\tilde{\theta}_i}^- \mathcal{J}(\tilde{\theta}_i), \quad (4.24)$$

$$D(\tilde{\theta}_i) = \nabla_{\tilde{\theta}_i}^+ \mathcal{J}(\tilde{\theta}_i). \quad (4.25)$$

Kompass [Kom07] proved the monotonicity of the corresponding algorithm with the  $\beta$ -divergence for the interval  $\beta \in (1, 2)$ . Note however, that monotonicity does not imply convergence while not being a strict requirement. Nonetheless, despite the lack of theoretical guarantees, in practice, the multiplicative algorithm based on these updates has shown to provide a decreasing cost function at each iteration, even when  $\beta$  does not belong to  $(1, 2)$ , as already pointed out in [FI11].

#### 4.4.2. Update of the factor TACs $\mathbf{M}$

According to the optimization framework described above, given the current values  $\mathbf{A}$  and  $\mathbf{B}$  of the abundance matrix and the internal proportions updating, the factor matrix  $\mathbf{M}$  can be formulated as the minimization sub-problem

$$\min_{\mathbf{M}} \mathcal{J}(\mathbf{M}) = \mathcal{D}(\mathbf{Y}|\mathbf{M}\mathbf{A} + \Delta) \text{ s.t. } \mathbf{M} \succeq \mathbf{0}_{L,K}. \quad (4.26)$$

As in [FD15], the objective function  $\mathcal{J}(\mathbf{M})$  can be majorized for  $\beta \in [1, 2]$  using Jensen's inequality:

$$\begin{aligned} \mathcal{J}(\mathbf{M}) &= \sum_{ln} d(y_{ln} | \sum_k m_{lk} a_{kn} + \delta_{ln}) \\ &= \sum_{ln} d(y_{ln} | \sum_k \frac{\tilde{t}_{lkn}}{\tilde{t}_{l(K+1)n}} m_{lk} a_{kn} + \frac{\tilde{t}_{l(K+1)n}}{\tilde{t}_{l(K+1)n}} \delta_{ln}) \\ &\leq \sum_{ln} \left[ \sum_k \tilde{t}_{lkn} d(y_{ln} | \frac{m_{lk} a_{kn}}{\tilde{t}_{lkn}}) + \tilde{t}_{l(K+1)n} d(y_{ln} | \frac{\delta_{ln}}{\tilde{t}_{l(K+1)n}}) \right] \text{ [Jensen's inequality]} \end{aligned} \quad (4.27)$$

with

$$\begin{aligned} \tilde{t}_{lkn} &= \frac{\tilde{m}_{lk} a_{kn}}{\tilde{x}_{ln}} \\ \tilde{t}_{l(K+1)n} &= \frac{\delta_{ln}}{\tilde{x}_{ln}}. \end{aligned} \quad (4.28)$$

Hence

$$\begin{aligned} \mathcal{J}(\mathbf{M}) &\leq \sum_{ln} \left[ \sum_k \frac{\tilde{m}_{lk} a_{kn}}{\tilde{x}_{ln}} d(y_{ln} | \frac{\tilde{x}_{ln} m_{lk}}{\tilde{m}_{lk}}) + \frac{\delta_{ln}}{\tilde{x}_{ln}} d(y_{ln} | \tilde{x}_{ln}) \right] \\ &= G(\mathbf{M}|\tilde{\mathbf{M}}), \end{aligned} \quad (4.29)$$

where  $\tilde{x}_{kn} = \sum_k \tilde{m}_{lk} a_{kn} + \delta_{ln}$  is the current state of the model-based reconstructed data. The auxiliary function  $G(\mathbf{M}|\tilde{\mathbf{M}})$  majorizes the divergence of the sum by the sum of the divergences, allowing the optimization of  $\mathbf{M}$  to be conducted element-by-element. The gradient w.r.t. the variable  $m_{lk}$  writes

$$\nabla_{m_{lk}} G(\mathbf{M}|\tilde{\mathbf{M}}) = \sum_n a_{kn} \tilde{x}_{ln}^{\beta-1} \left( \frac{m_{lk}}{\tilde{m}_{lk}} \right)^{\beta-1} - \sum_n a_{kn} y_{ln} \tilde{x}_{ln}^{\beta-2} \left( \frac{m_{lk}}{\tilde{m}_{lk}} \right)^{\beta-2}. \quad (4.30)$$

Thus, minimizing  $G(\mathbf{M}|\tilde{\mathbf{M}})$  w.r.t.  $\mathbf{M}$  leads to the following element-wise update

$$m_{lk} = \tilde{m}_{lk} \left[ \frac{\sum_n a_{kn} y_{ln} \tilde{x}_{ln}^{\beta-2}}{\sum_n a_{kn} \tilde{x}_{ln}^{\beta-1}} \right]^{\gamma(\beta)}. \quad (4.31)$$

The update is the same for all three algorithms  $\beta$ -NMF,  $\beta$ -LMM and  $\beta$ -SLMM.

### 4.4.3. Update of the factor proportions $\mathbf{A}$

Given the current values  $\mathbf{M}$  and  $\mathbf{B}$  of the factor matrix and internal propositions, the update rule for  $\mathbf{A}$  is obtained by solving

$$\min_{\mathbf{A}} \mathcal{J}(\mathbf{A}) = \mathcal{D}(\mathbf{Y}|\mathbf{M}\mathbf{A} + [\mathbf{E}_1 \mathbf{A} \circ \mathbf{W}]) \text{ s.t. } \mathbf{A} \succeq \mathbf{0}_{K,N}, \mathbf{A}^T \mathbf{1}_K = \mathbf{1}_N, \quad (4.32)$$

with  $\mathbf{W} = \mathbf{V}\mathbf{B}$ . The sum-to-one constraint (2.13) could be handled within gradient descent methods by introducing Lagrange multipliers that would further lead to projection onto the corresponding simplex [Con15]. However, incorporating this constraint into a MM formulation is not straightforward. On the other hand, normalizing the factor proportions at each iteration seems sufficient to produce a similar effect. To this end, this work proposes to resort to a change of variable that demonstrated its interest in previous works [EK04; FD15]. More precisely, the factor proportions matrix  $\mathbf{A}$  can be expressed thanks to an auxiliary matrix  $\mathbf{U}$ , such that

$$a_{kn} = \frac{u_{kn}}{\sum_j u_{jn}}, \quad (4.33)$$

which explicitly ensures the sum-to-one constraint (2.13). The new optimization problem is then

$$\min_{\mathbf{U}} \mathcal{J}(\mathbf{U}) \text{ s.t. } \mathbf{U} \succeq \mathbf{0}_{K,N}, \quad (4.34)$$

with

$$\begin{aligned} \mathcal{J}(\mathbf{U}) &= \mathcal{D}(\mathbf{Y}|\mathbf{M} \left[ \frac{\mathbf{u}_1}{\|\mathbf{u}_1\|_1}, \dots, \frac{\mathbf{u}_N}{\|\mathbf{u}_N\|_1} \right] + [\mathbf{E}_1 \left[ \frac{u_{11}}{\|\mathbf{u}_1\|_1}, \dots, \frac{u_{1N}}{\|\mathbf{u}_N\|_1} \right] \circ \mathbf{W}]) \\ &= \sum_{ln} d(y_{ln}) \left[ \frac{u_{1n}}{\|\mathbf{u}_n\|_1} \right] w_{ln} + \sum_k m_{lk} \left[ \frac{u_{kn}}{\|\mathbf{u}_n\|_1} \right]. \end{aligned} \quad (4.35)$$

However, contrary to the strategy followed in paragraph 4.4.2, majorizing  $\mathcal{J}(\mathbf{U})$  does not lead to an auxiliary function easy to minimize. Conversely, as motivated in paragraph 4.4.1, one proposes to resort to the heuristic MM by using the multiplicative updates (4.22) combined with (4.24) and (4.25). The gradient of  $\mathcal{J}(\mathbf{U})$  can be expressed as

$$\nabla_{u_{kn}} \mathcal{J}(\mathbf{U}) = \nabla_{u_{kn}}^+ \mathcal{J}(\mathbf{U}) - \nabla_{u_{kn}}^- \mathcal{J}(\mathbf{U}) \quad (4.36)$$

The heuristic algorithm simply writes

$$u_{kn} = \tilde{u}_{kn} \left( \frac{\nabla_{u_{kn}}^- \mathcal{J}(\mathbf{U})}{\nabla_{u_{kn}}^+ \mathcal{J}(\mathbf{U})} \right) \quad (4.37)$$

The updates are also different for  $k = 1$  and  $k \neq 1$ . For  $k \neq 1$ , the gradient writes

$$\begin{aligned}\nabla_{u_{kn}} \mathcal{J}(\mathbf{U}) &= \sum_l \left( \frac{m_{lk}}{\|\mathbf{u}_n\|_1} - \frac{\tilde{x}_{ln}}{\|\mathbf{u}_n\|_1} \right) \left( \tilde{x}_{ln}^{\beta-1} - \tilde{x}_{ln}^{\beta-2} y_{ln} \right) \\ &= \underbrace{\frac{1}{\|\mathbf{u}_n\|_1} \sum_l \left( m_{lk} \tilde{x}_{ln}^{\beta-1} + y_{ln} \tilde{x}_{ln}^{\beta-1} \right)}_{\nabla_{u_{kn}}^+ \mathcal{J}(\mathbf{U})} - \underbrace{\frac{1}{\|\mathbf{u}_n\|_1} \sum_l \left( \tilde{x}_{ln}^\beta + m_{lk} y_{ln} \tilde{x}_{ln}^{\beta-2} \right)}_{\nabla_{u_{kn}}^- \mathcal{J}(\mathbf{U})}\end{aligned}\quad (4.38)$$

with  $\tilde{x}_{ln} = \sum_k m_{lk} \tilde{a}_{kn} + \tilde{a}_{1n} w_{ln}$  being the pixel value reconstructed with the previous factor proportion value  $\tilde{a}_{kn}$ , leading the following update

$$u_{kn} = \tilde{u}_{kn} \left[ \frac{\sum_l (\tilde{x}_{ln}^\beta + m_{lk} y_{ln} \tilde{x}_{ln}^{\beta-2})}{\sum_l (m_{lk} \tilde{x}_{ln}^{\beta-1} + y_{ln} \tilde{x}_{ln}^{\beta-1})} \right]^{\gamma(\beta)}. \quad (4.39)$$

This is the same update as for all the factor proportions in the  $\beta$ -LMM algorithm.

Meanwhile, the gradient for  $k = 1$  writes

$$\begin{aligned}\nabla_{u_{1n}} \mathcal{J}(\mathbf{U}) &= \sum_l \left( \frac{m_{l1} + w_{ln}}{\|\mathbf{u}_n\|_1} - \frac{\tilde{x}_{ln}}{\|\mathbf{u}_n\|_1} \right) \left( \tilde{x}_{ln}^{\beta-1} - \tilde{x}_{ln}^{\beta-2} y_{ln} \right) \\ &= \underbrace{\frac{1}{\|\mathbf{u}_n\|_1} \sum_l \left( (m_{l1} + w_{ln}) \tilde{x}_{ln}^{\beta-1} + y_{ln} \tilde{x}_{ln}^{\beta-1} \right)}_{\nabla_{u_{kn}}^+ \mathcal{J}(\mathbf{U})} - \underbrace{\frac{1}{\|\mathbf{u}_n\|_1} \sum_l \left( \tilde{x}_{ln}^\beta + (m_{l1} + w_{ln}) \tilde{x}_{ln}^{\beta-2} y_{ln} \right)}_{\nabla_{u_{kn}}^- \mathcal{J}(\mathbf{U})}\end{aligned}\quad (4.40)$$

and the respective update rule when  $\beta < 1$  is then

$$u_{1n} = \tilde{u}_{1n} \left[ \frac{\sum_l (\tilde{x}_{ln}^\beta + (m_{l1} + w_{ln}) \tilde{x}_{ln}^{\beta-2} y_{ln})}{\sum_l ((m_{l1} + w_{ln}) \tilde{x}_{ln}^{\beta-1} + y_{ln} \tilde{x}_{ln}^{\beta-1})} \right]^{\gamma(\beta)}. \quad (4.41)$$

To summarize, we can write

$$u_{kn} = \tilde{u}_{kn} v_{kn}^{\gamma(\beta)}$$

with

$$v_{kn} = \begin{cases} \frac{\sum_l (\tilde{x}_{ln}^\beta + (m_{l1} + w_{ln}) \tilde{x}_{ln}^{\beta-2} y_{ln})}{\sum_l ((m_{l1} + w_{ln}) \tilde{x}_{ln}^{\beta-1} + y_{ln} \tilde{x}_{ln}^{\beta-1})}, & \text{if } k = 1; \\ \frac{\sum_l (\tilde{x}_{ln}^\beta + m_{lk} y_{ln} \tilde{x}_{ln}^{\beta-2})}{\sum_l (m_{lk} \tilde{x}_{ln}^{\beta-1} + y_{ln} \tilde{x}_{ln}^{\beta-1})}, & \text{otherwise.} \end{cases}$$

Finally, the update for  $\beta$ -NMF writes

$$v_{kn} = \frac{\sum_l m_{lk} y_{ln} \tilde{x}_{ln}^{\beta-2}}{\sum_l m_{lk} \tilde{x}_{ln}^{\beta-1}}, \quad \forall k.$$

#### 4.4.4. Update of the internal variability $\mathbf{B}$

Given the current states  $\mathbf{M}$  and  $\mathbf{A}$  of the factor matrix and factor proportions, respectively, updating  $\mathbf{B}$  consists in solving

$$\min_{\mathbf{B}} \mathcal{J}(\mathbf{B}) = \mathcal{D}(\mathbf{Y}|\mathbf{MA} + [\mathbf{E}_1\mathbf{A} \circ \mathbf{VB}]) + \lambda\varphi\|\mathbf{B}\|_{2,1} \text{ s.t. } \mathbf{B} \succeq \mathbf{0}_{N_v, N}, \quad (4.42)$$

Denoting by  $\tilde{\mathbf{B}}$  the current state of  $\mathbf{B}$ , the model-based reconstructed data using the current estimates is defined by  $\tilde{x}_{ln} = s_{ln} + a_{1n} \sum_i v_{li} \tilde{b}_{in}$  with  $s_{ln} = \sum_k m_{lk} a_{kn}$ .

Assuming  $\beta \in [1, 2]$ , and defining

$$\tilde{t}_{lin} = \begin{cases} \frac{s_{ln}}{\tilde{x}_{ln}} & \text{if } i = N_v + 1 \\ \frac{a_{1n} v_{li} \tilde{b}_{in}}{\tilde{x}_{ln}} & \text{otherwise,} \end{cases} \quad (4.43)$$

so that  $\sum_i^{N_v+1} t_{lkp} = 1$ , we use Jensen's inequality as follows.

$$\begin{aligned} \mathcal{D}(\mathbf{Y}|\mathbf{S} + [\mathbf{E}_1\mathbf{A} \circ \mathbf{VB}]) &= \sum_{ln} d\left(y_{ln} \middle| \underbrace{\sum_k m_{lk} a_{kn}}_{s_{ln}} + \sum_i a_{1n} v_{li} b_{in}\right) \\ &= \sum_{ln} d\left(y_{ln} \middle| \frac{\tilde{t}_{l(N_v+1)n}}{\tilde{t}_{l(N_v+1)n}} s_{ln} + \sum_i \frac{\tilde{t}_{lin}}{\tilde{t}_{lin}} a_{1n} v_{li} b_{in}\right) \\ &\leq \sum_{ln} \left[ \frac{s_{ln}}{\tilde{x}_{ln}} d(y_{ln}|\tilde{x}_{ln}) + \sum_i \frac{a_{1n} v_{li} \tilde{b}_{in}}{\tilde{x}_{ln}} d\left(y_{ln} \middle| \frac{\tilde{x}_{ln} b_{in}}{\tilde{b}_{in}}\right) \right] \\ &= F(\mathbf{B}|\tilde{\mathbf{B}}). \end{aligned} \quad (4.44)$$

The data fitting term is then majorized as

$$\mathcal{D}(\mathbf{Y}|\mathbf{S} + [\mathbf{E}_1\mathbf{A} \circ \mathbf{VB}]) \leq \underbrace{\sum_{ln} \left[ \frac{s_{ln}}{\tilde{x}_{ln}} d(y_{ln}|\tilde{x}_{ln}) + \sum_i \frac{a_{1n} v_{li} \tilde{b}_{in}}{\tilde{x}_{ln}} d\left(y_{ln} \middle| \frac{\tilde{x}_{ln} b_{in}}{\tilde{b}_{in}}\right) \right]}_{F(\mathbf{B}|\tilde{\mathbf{B}})}.$$

The auxiliary function associated with  $\mathcal{J}(\mathbf{B})$  can be decomposed as  $G(\mathbf{B}|\tilde{\mathbf{B}}) = F(\mathbf{B}|\tilde{\mathbf{B}}) + \lambda\varphi\|\mathbf{B}\|_{2,1}$ . However, minimizing this auxiliary function w.r.t.  $\mathbf{B}$  is not straightforward. Hence, as in [FD15], the regularization  $\|\mathbf{B}\|_{2,1}$  is majorized, benefiting from the concavity of the square-root function as showed in [TF13]

$$\left(\frac{b_{in}}{\tilde{b}_{in}}\right) - 1 \leq \frac{1}{2} \left[ \left(\frac{b_{in}}{\tilde{b}_{in}}\right)^2 - 1 \right], \quad (4.45)$$

leading to

$$\|\mathbf{B}\|_{2,1} \leq \underbrace{\frac{1}{2} \sum_n \left( \frac{\|\mathbf{b}_n\|_2^2}{\|\tilde{\mathbf{b}}_n\|_2} + \|\tilde{\mathbf{b}}_n\|_2 \right)}_{H(\mathbf{B}|\tilde{\mathbf{B}})}. \quad (4.46)$$

The gradient of  $H(\mathbf{B}|\tilde{\mathbf{B}})$  is

$$\nabla_{b_{in}} H(\mathbf{B}|\tilde{\mathbf{B}}) = \frac{b_{in}}{\|\tilde{\mathbf{b}}_n\|_2}. \quad (4.47)$$

If the extra majorization in (4.46) is only applied to  $H(\mathbf{B}|\tilde{\mathbf{B}})$ , minimizing  $G(\mathbf{B}|\tilde{\mathbf{B}})$  w.r.t.  $\mathbf{B}$  becomes a very difficult task. Thus, to match the quadratic upper bound of the penalty function, we further majorize the linear term  $b_{in}$ , as in [TF13]. For  $\beta \leq 2$ , we have

$$\frac{1}{\beta} \left[ \left( \frac{b_{in}}{\tilde{b}_{in}} \right)^\beta - 1 \right] \leq \frac{1}{2} \left[ \left( \frac{b_{in}}{\tilde{b}_{in}} \right)^2 - 1 \right]. \quad (4.48)$$

By replacing only the first term of the following divergence

$$d(y_{ln} | \frac{\tilde{x}_{ln} b_{in}}{\tilde{b}_{in}}) = \frac{1}{\beta} \left( \tilde{x}_{ln} \frac{b_{in}}{\tilde{b}_{in}} \right)^\beta - \frac{y_{ln}}{\beta - 1} \left( \tilde{x}_{ln} \frac{b_{in}}{\tilde{b}_{in}} \right)^{\beta-1} + \frac{y_{ln}^\beta}{\beta(\beta - 1)} \quad (4.49)$$

with (4.48), we will have

$$\hat{d}(y_{ln} | \frac{\tilde{x}_{ln} b_{in}}{\tilde{b}_{in}}) = \tilde{x}_{ln}^\beta \left[ \frac{1}{2} \left( \frac{b_{in}}{\tilde{b}_{in}} \right)^2 + cte \right] - \frac{y_{ln}}{\beta - 1} \left( \tilde{x}_{ln} \frac{b_{in}}{\tilde{b}_{in}} \right)^{\beta-1} + \frac{y_{ln}^\beta}{\beta(\beta - 1)}. \quad (4.50)$$

This leads to the following gradient for  $\hat{F}(\mathbf{B}|\tilde{\mathbf{B}})$

$$\nabla_{b_{in}} \hat{F}(\mathbf{B}|\tilde{\mathbf{B}}) = a_{1n} \sum_l v_{li} \left( \frac{b_{in}}{\tilde{b}_{in}} - \frac{y_{ln} \tilde{b}_{in}}{\tilde{x}_{ln} b_{in}} \right). \quad (4.51)$$

By minimizing  $G(\mathbf{B}|\tilde{\mathbf{B}})$ , the following update is obtained:

$$b_{in} = \tilde{b}_{in} \left( \frac{a_{1n} \sum_l v_{li} y_{ln} \tilde{x}_{ln}^{\beta-2}}{a_{1n} \sum_l v_{li} \tilde{x}_{ln}^{\beta-1} + \lambda \varphi \frac{\tilde{b}_{in}}{\|\tilde{\mathbf{b}}_n\|_2}} \right)^{\frac{1}{3-\beta}}. \quad (4.52)$$

All the above results are also valid for the interval  $\beta \in [0, 1)$ , as shown in [FI11], using the heuristic approach previously presented. Practical simulations showed that when  $\beta \in [1, 2]$ , ignoring the exponent  $\frac{1}{3-\beta}$  increases the speed of convergence [FI11].

## 4.5. Experiments with synthetic data

### 4.5.1. Synthetic data generation

Simulations are conducted on synthetic images with realistic count-rate properties [Stu+15]. These images have been generated from the Zubal high resolution numerical phantom [Zub+94] with values derived from real PET images acquired with the Siemens HRRT using the  $^{11}\text{C}$ -PE2I radioligand. The original phantom data is of size  $256 \times 256 \times 128$  with a voxel size of  $1.1 \times 1.1 \times 1.4 \text{ mm}^3$ , and was acquired over  $L = 20$  frames of durations that range from 1 to 5 minutes for a 60 minutes total acquisition.

#### Phantom I generation

A clinical PET image with  $^{11}\text{C}$ -PE2I of a healthy control subject has been segmented into regions-of-interest using a corresponding magnetic resonance image. Then averaged TACs of each region have been extracted and set as the TAC of voxels in the corresponding phantom region. It is worth noting that this supervised segmentation neglects any labelled molecule concentration differences due to possible variability in the specific binding region. Thus, it describes each entire segmented region by a single averaged TAC. This phantom, referred to as Phantom I, has been used to evaluate the reconstruction error for different values of  $\beta$ .

#### Phantom II generation

To evaluate the impact of  $\beta$  on the factor analysis, the synthetic phantom generated with the process described in Section 3.5.1, herein referred to as Phantom II, is also used. The generation process is recalled in the following. Phantom I has been unmixed with the N-FINDR [Win99] to extract  $K = 4$  factors [Yaq+12] that correspond to the tissues of the brain: specific gray matter, blood or veins, white matter and non-specific gray matter. The corresponding ground truth factor proportions have been subsequently set as those estimated by SUNSAL [BF10]. Then, the SBF as well as the variability dictionary have been generated from a compartment model [PMS86], while the internal variability has been generated by dividing the region concerned by specific binding into 4 subregions with different mean variabilities. Phantom II has been finally obtained by mixing these ground truth components according to SLMM in Table 4.1.

#### Dynamic PET image simulation

The generation process that takes realistic count rates properties into consideration is detailed in [Stu+15]. To summarize, activity concentration images are first computed from the input phantom and TACs, applying the decay of the positron emitter with respect to the provided time frames. To mimic the partial volume effect, a stationary 4mm FWHM isotropic 3D Gaussian point spread function is applied, followed by a down-sampling to a  $128 \times 128 \times 64$  image matrix of  $2.2 \times 2.2 \times 2.8 \text{ mm}^3$  voxels. Data is then projected with respect to real

crystal positions of the Siemens Biograph TruePoint TrueV scanner, taking attenuation into account. A scatter distribution is computed from a radial convolution of this signal. A random distribution is computed from a fan-sum of the true-plus-scatter signal. Realistic scatter and random fractions are then used to scale all distributions and compute the prompt sinograms. Finally, Poisson noise is applied based on a realistic total number of counts for the complete acquisition. The standard ordered-subset expectation maximization (OSEM) algorithm with 16 subsets is used to reconstruct the data, along with the PSF used in the simulation process. Two images, referred to as *6it* (Fig. 4.5) and *50it* (Fig. 4.6), are considered for the analysis: the 6th iteration without post-smoothing, and the 50th iteration post-smoothed with the PSF [SC13]. A set of 64 independent samples of each phantom were generated to assess statistical consistency.

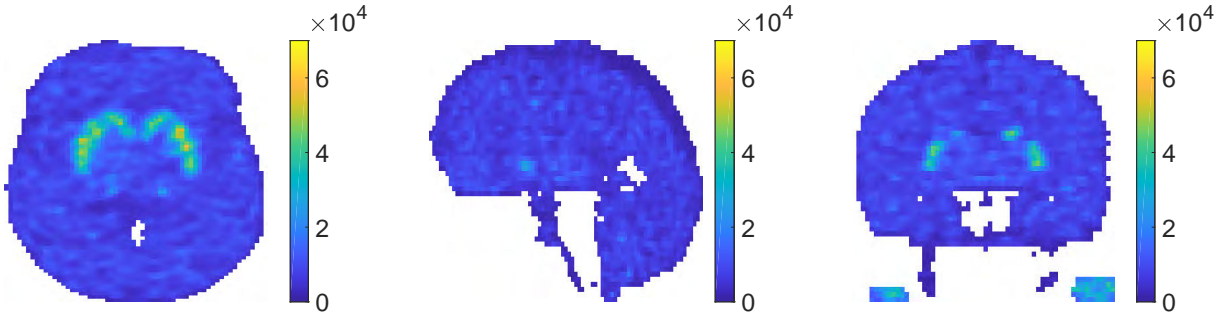


Figure 4.5.: 15<sup>th</sup> time-frame of 6it image: from left to right, transversal, sagittal and coronal planes.

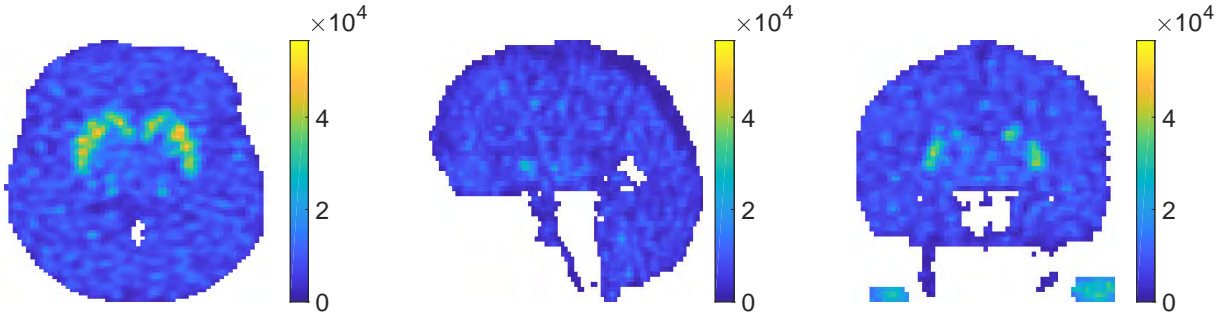


Figure 4.6.: 15<sup>th</sup> time-frame of 50it image: from left to right, transversal, sagittal and coronal planes.

### 4.5.2. Compared methods

#### Phantom I

The main objective when using Phantom I is to evaluate the influence of  $\beta$  on the factor modelling (i.e., by evaluating the reconstruction error) for images reconstructed with 6 and 50 iterations. It also provides a relevant comparison of the  $\beta$ -LMM and the regular  $\beta$ -NMF algorithms. Within this experimental setup,  $\beta$  ranges from 0 to 2.4 with a step size of 0.2. Factor TACs are initialized by vertex component analysis (VCA) [ND05b],



while the factor proportions are initialized either thanks to SUnSAL or randomly, depending on the considered setting (see paragraph 4.5.4). The stopping criterion  $\varepsilon$ , defined as the relative decrease of the cost function, is given in Table 4.2.

### Phantom II

For the sake of comparison, Phantom II will be analysed with both the  $\beta$ -SLMM algorithm and its simpler version,  $\beta$ -LMM, which does not take variability into account. The corresponding algorithms are applied for  $\beta \in \{0, 1, 2\}$  where factor TACs have been initialized with K-means, while factor proportions have been initialized either with SUnSAL or randomly, depending on the considered setting (see paragraph 4.5.5). The variability matrix  $\mathbf{B}$  is randomly initialized on both settings. The values for  $\varepsilon$  in Table 4.2 are also valid in this setting.

#### 4.5.3. Performance measures

##### Phantom I

In the first round of experiments, the reconstruction error is computed in terms of peak signal-to-noise ratio (PSNR)

$$\text{PSNR}(\hat{\mathbf{X}}) = 10 \log_{10} \frac{\max(\mathbf{X}^*)^2}{\|\hat{\mathbf{X}} - \mathbf{X}^*\|_F^2} \quad (4.53)$$

where  $\max(\mathbf{X}^*)$  is the maximum value of the ground-truth image  $\mathbf{X}^*$  and  $\hat{\mathbf{X}} \triangleq \mathbf{X}(\hat{\boldsymbol{\theta}})$  is the image recovered, according to the considered factor model (4.1) with the estimated latent variables  $\hat{\boldsymbol{\theta}}$ .

##### Phantom II

In addition to the PSNR, performances on Phantom II have been evaluated w.r.t. each latent variable by computing the normalized mean square error (NMSE):

$$\text{NMSE}(\hat{\theta}_i) = \frac{\|\hat{\theta}_i - \theta_i^*\|_F^2}{\|\theta_i^*\|_F^2}, \quad (4.54)$$

where  $\theta_i^*$  and  $\hat{\theta}_i$  are the actual and estimated latent variables, respectively. In particular, the NMSE has been computed for the following variables: the high-uptake factor proportions  $\mathbf{A}_1$ , the remaining factor proportions  $\mathbf{A}_{2:K}$ , the SBF TAC  $\tilde{\mathbf{M}}_1$ , the non-specific factor TACs  $\mathbf{M}_{2:K}$  and finally, when considering  $\beta$ -SLMM, the point-wise product of  $\mathbf{A}_1$  and the internal variability  $\mathbf{B}$ . The estimation performance of  $\mathbf{A}_1 \circ \mathbf{B}$  rather than  $\mathbf{B}$  is evaluated because the partial volume effect (due to the PSF) can be propagated either in variable  $\mathbf{A}_1$  or in  $\mathbf{B}$ .

#### 4.5.4. Results on Phantom I

In the first round of simulations,  $\beta$ -NMF and  $\beta$ -LMM algorithms are evaluated in terms of the reconstruction error (4.53) for several values of  $\beta$ . Two cases are considered. The first one assumes that the factor TACs previously estimated by VCA are fixed. Thus, the algorithm described in Section 4.4 only updates the factor proportions, within a convex optimization setting. In this case, the factor proportions have been randomly initialized. Within the second and non-convex setting, the algorithm estimates both factor TACs and proportions where the factor proportions have been initialized using SUnSAL.

##### $\beta$ -NMF results

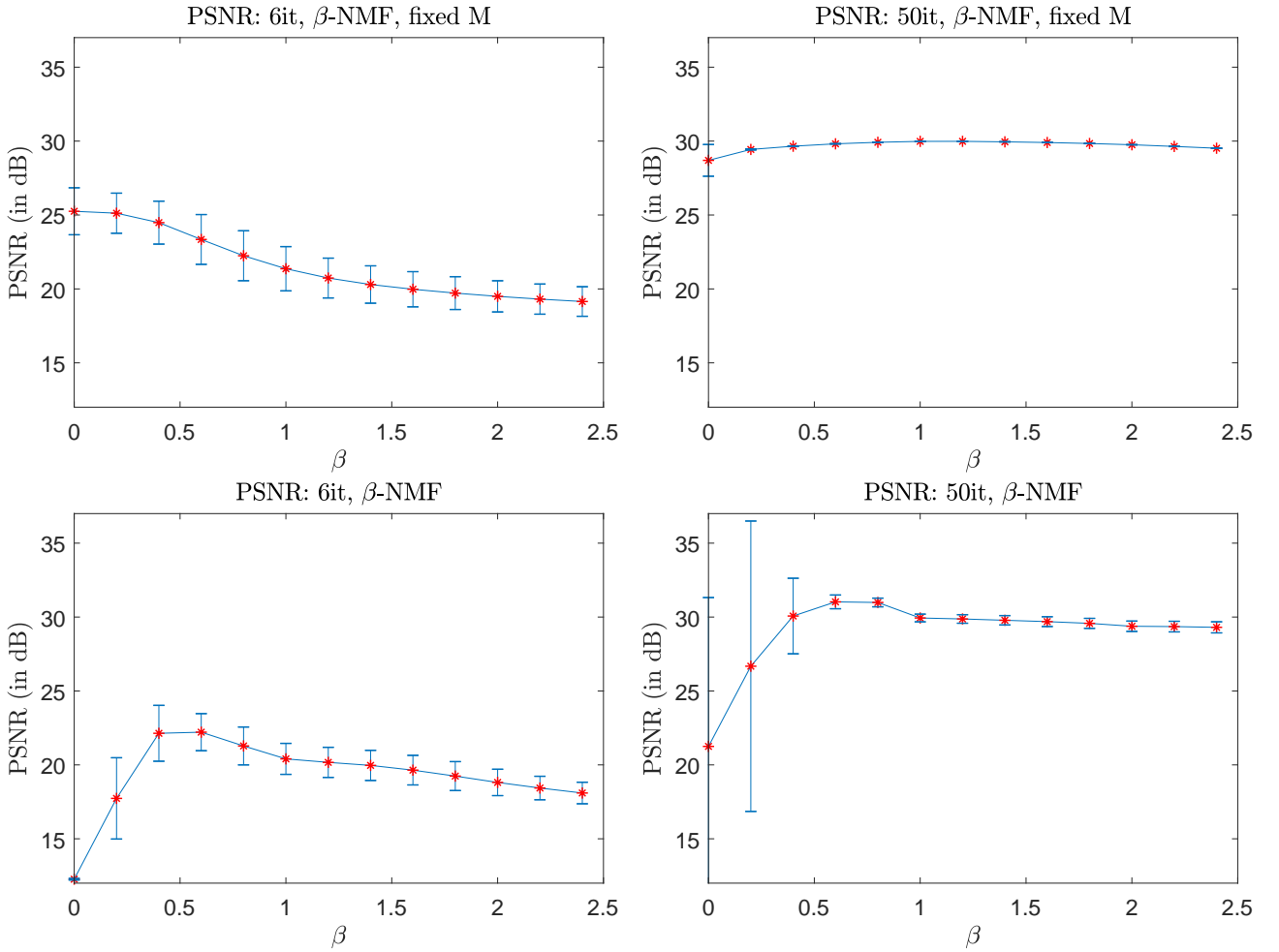


Figure 4.7.: PSNR mean and standard deviation obtained on the 6it (left) and 50it (right) images after factorization with  $\beta$ -NMF with fixed (top) and estimated (bottom) factor TACs over 64 samples.

Fig. 4.7 shows the PSNR mean and corresponding standard deviation obtained on the 6it and 50it images when analysed with  $\beta$ -NMF. The first line corresponds to the convex estimation setting (i.e., fixed factor TACs) while the non-convex framework (i.e., estimated factor TACs) is reported in the second line. The 6it images

show higher PSNRs for the values of  $\beta \in [0, 0.6]$  in both convex and non-convex settings. This result indicates a residual noise that is rather between Gamma and Poisson distributed, which is consistent with previous studies from the literature [Tey+12; MHO17]. The best performance PSNR = 25dB with fixed  $\mathbf{M}$  is reached for  $\beta = 0$ , which significantly outperforms the result obtained with the Euclidean divergence  $\beta = 2$  commonly adopted in the literature. Within a non-convex optimization setting, when estimating both factor TACs and proportions, the maximum PSNR = 22.2dB is obtained for  $\beta = 0.6$ , followed by  $\beta = 0.4$ . In this case, the difference between the greatest and smallest PSNRs is of almost 3.5 dB. As non-convex optimization problems are highly sensitive to the initialization, the convex frameworks shows a better mean performance for all values of  $\beta$ , as well as less variance among the different realizations.

The reconstruction of the 50it images is clearly less sensitive to the choice of the divergence. Yet, values  $\beta = 1$  and  $\beta = 0.5$  in the convex and non-convex settings, respectively, increase the reconstruction PSNR by about 1dB. This is consistent with prior knowledge about the noise statistics: whereas the nature of noise in the 50it image still presents a reminiscent Poissonian nature, its power is very low due to a higher level of filtering.

#### $\beta$ -LMM results

Fig. 4.8 shows the PSNR mean and standard deviation after factorization with  $\beta$ -LMM with fixed (top) and estimated (bottom) factor TACs. The results look similar as with the  $\beta$ -NMF: the factorization of the 6it image is optimal for a value of  $\beta$  around 0.5, which is in agreement with the expected Poisson-Gamma nature of the noise before post-filtering. Factor modelling with  $\beta = 0.5$  is about 5dB better than the one obtained from the usual Euclidean divergence relying on Gaussian noise ( $\beta = 2$ ). Again, the  $\beta$  parameter has less impact for the 50it image which has been strongly filtered, but the optimal  $\beta$  is still around 1. The results are also similar in the non-convex setting, but with expected lower performance.

For the 50it image, once again, it is possible to see a more Poisson-like distributed noise with a higher PSNR around 30dB with  $\beta = 1$ . In this setting, the difference between the highest PSNR and the lowest one for  $\beta = 0$  is of more than 3dB. The highest PSNR for the non-convex case is reached with  $\beta = 1$  and is of 32dB. The highest PSNR is 9dB greater than the lowest one obtained with  $\beta = 0$  when estimating both TAC factors and proportions. However, the difference between the PSNR reached with  $\beta = 1$  and  $\beta = 2$  is of less than 0.5dB. All remarks previously made for  $\beta$ -NMF in this case are confirmed by the results of  $\beta$ -LMM.

#### 4.5.5. Results on Phantom II

This paragraph discusses the results of  $\beta$ -SLMM obtained on Phantom II. This experiment considers both the reconstruction error (in terms of PSNR) and the estimation error for each latent variable (in terms of NMSE). The factorization with  $\beta$ -SLMM requires the tuning of parameter  $\lambda$ , which controls the sparsity of the internal variability. In this work, the value of this parameter has been empirically tuned to obtain the best possible

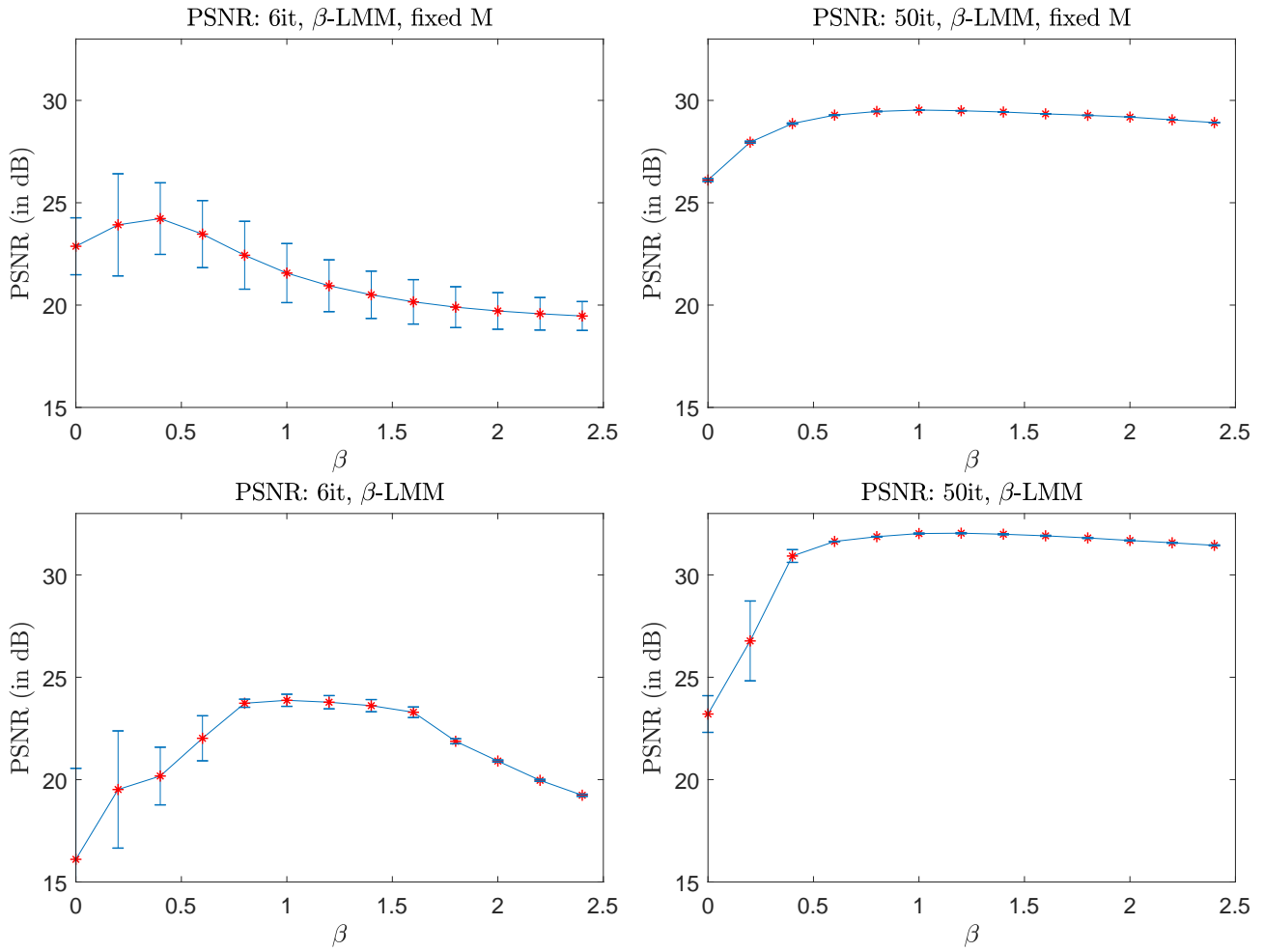


Figure 4.8.: PSNR mean and standard deviation obtained on the 6it (left) and 50it (right) images after factorization with  $\beta$ -LMM with fixed (top) and estimated (bottom) factor TACs over 64 samples.

Table 4.2.: Stopping criterion and variability penalization parameters

	$\lambda$			$\varepsilon$	
	$\beta=0$	$\beta=1$	$\beta=2$	$\mathbf{M}$ fixed	$\mathbf{M}$ estimated
6it	$1, 3 \cdot 10^{-4}$	$1, 3 \cdot 10^{-3}$	$3, 9 \cdot 10^{-3}$	$10^{-5}$	$10^{-4}$
50it	$6, 8 \cdot 10^{-5}$	$6, 8 \cdot 10^{-4}$	$2 \cdot 10^{-3}$	$10^{-5}$	$10^{-4}$

Table 4.3.: Mean NMSE of  $\mathbf{A}_1$ ,  $\mathbf{A}_{2:K}$  and  $\mathbf{A}_1 \circ \mathbf{B}$  and PSNR of reassembled images estimated by  $\beta$ -LMM and  $\beta$ -SLMM with fixed  $\mathbf{M}$  over the 64 samples, for different values of  $\beta$ .

	$\beta$	$\beta$ -LMM			$\beta$ -SLMM		
		0	1	2	0	1	2
6it	$\mathbf{A}_1$	0.500	0.497	<b>0.491</b>	0.273	<b>0.262</b>	0.274
	$\mathbf{A}_{2:K}$	0.304	<b>0.282</b>	0.290	0.292	<b>0.267</b>	0.276
	$\mathbf{A}_1 \circ \mathbf{B}$	-	-	-	<b>0.423</b>	0.439	0.492
	PSNR	28.325	<b>28.345</b>	28.224	<b>31.905</b>	31.693	29.825
50it	$\mathbf{A}_1$	<b>0.447</b>	0.453	0.452	0.209	<b>0.196</b>	0.204
	$\mathbf{A}_{2:K}$	0.262	<b>0.251</b>	0.268	0.255	<b>0.236</b>	0.258
	$\mathbf{A}_1 \circ \mathbf{B}$	-	-	-	<b>0.293</b>	0.305	0.371
	PSNR	31.992	<b>32.799</b>	32.180	34.556	<b>36.385</b>	35.178

result for the different values of  $\beta$  and for the two 6it and 50it images. Two settings have been considered. In the first one, the factor TACs are fixed to their ground-truth value. Thus, the algorithm described in Section 4.4 only updates the factor proportions and the internal variability  $\mathbf{B}$ . In this case, the factor proportions have been randomly initialized. In the second setting, the algorithm estimates the factor TACs and proportions, as well as the internal variability. In this setting, the factor proportions have been initialized using SUnSAL.

Table 4.2 reports the values of  $\lambda$  for each value of  $\beta$  and each image. The parameters are the same for fixed and estimated  $\mathbf{M}$ . Figs. 4.9 and 4.11 present the factor proportions resultant from  $\beta$ -SLMM with fixed  $\mathbf{M}$  for  $\beta = 0, 1, 2$  applied to a 6it and a 50it image, respectively. As we can see, with  $\mathbf{M}$  fixed on the ground-truth, it is natural to expect good and similar results for all tissues and blood. Moreover, 50it results seem noisier than 6it. Figs. 4.10 and 4.12 show the variability matrices estimated in the same simulations. A more attentive analysis shows that  $\beta = 0$  is able to recover more variability pixels with intensities that are nearer the ground-truth, while  $\beta = 2$  recovers the smallest variability area for both 6it and 50it images. These differences are, however, not easily perceivable. Table 4.3 presents the mean NMSE for  $\mathbf{A}_1$ ,  $\mathbf{A}_{2:K}$  and  $\mathbf{A}_1 \circ \mathbf{B}$  as well as the mean PSNR for the same simulations but considering all samples. Both 6it and 50it images present similar results, with the smallest NMSE of  $\mathbf{A}_1$  and  $\mathbf{A}_{2:K}$  obtained for  $\beta = 1$  and the best estimation performance of  $\mathbf{A}_1 \circ \mathbf{B}$  obtained for  $\beta = 0$ . Interestingly, even though the results for 50it seem noisier when looking at the corresponding factor proportion figure, the table of errors show that the factor proportions are better recovered in 50it than in 6it. The PSNR values show that, while 6it reaches its best performance for  $\beta = 0$  closely followed by  $\beta = 1$ , 50it achieves its highest PSNR for  $\beta = 1$ , followed by  $\beta = 2$ . This result confirms the previous results on phantom I, which exhibited a Poisson-Gamma noise distribution on the 6it image and a Poisson-Gaussian noise distribution on the 50it images.

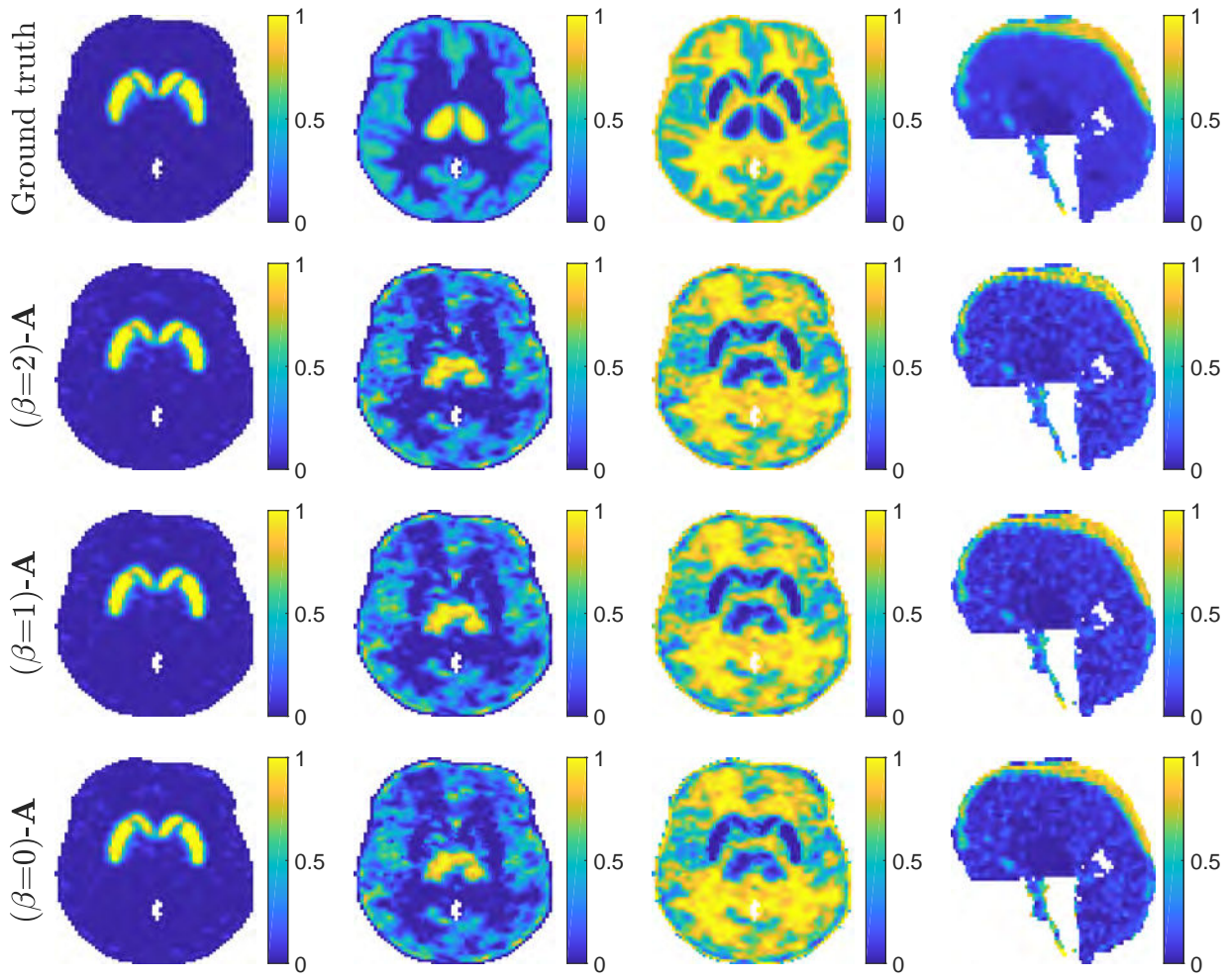


Figure 4.9.: From left do right: factor proportions from specific gray matter, non-specific gray matter, white matter and blood for one 6it sample, estimated with fixed  $\mathbf{M}$ .

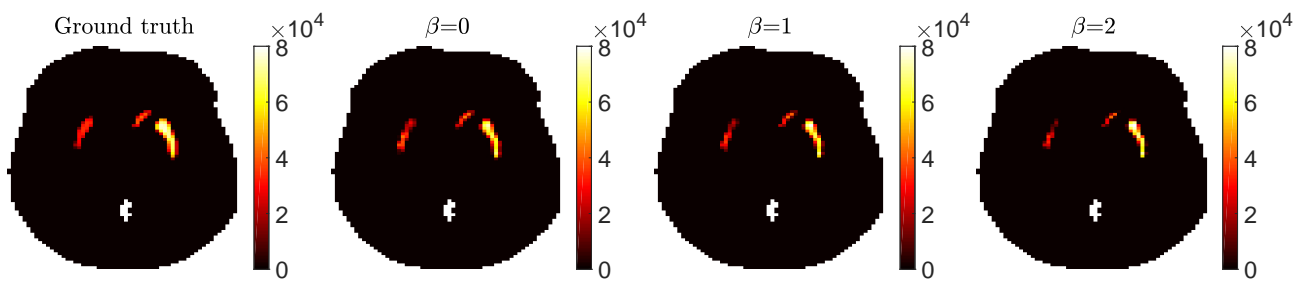


Figure 4.10.: Variability matrices estimated with fixed  $\mathbf{M}$  on a 6it sample.



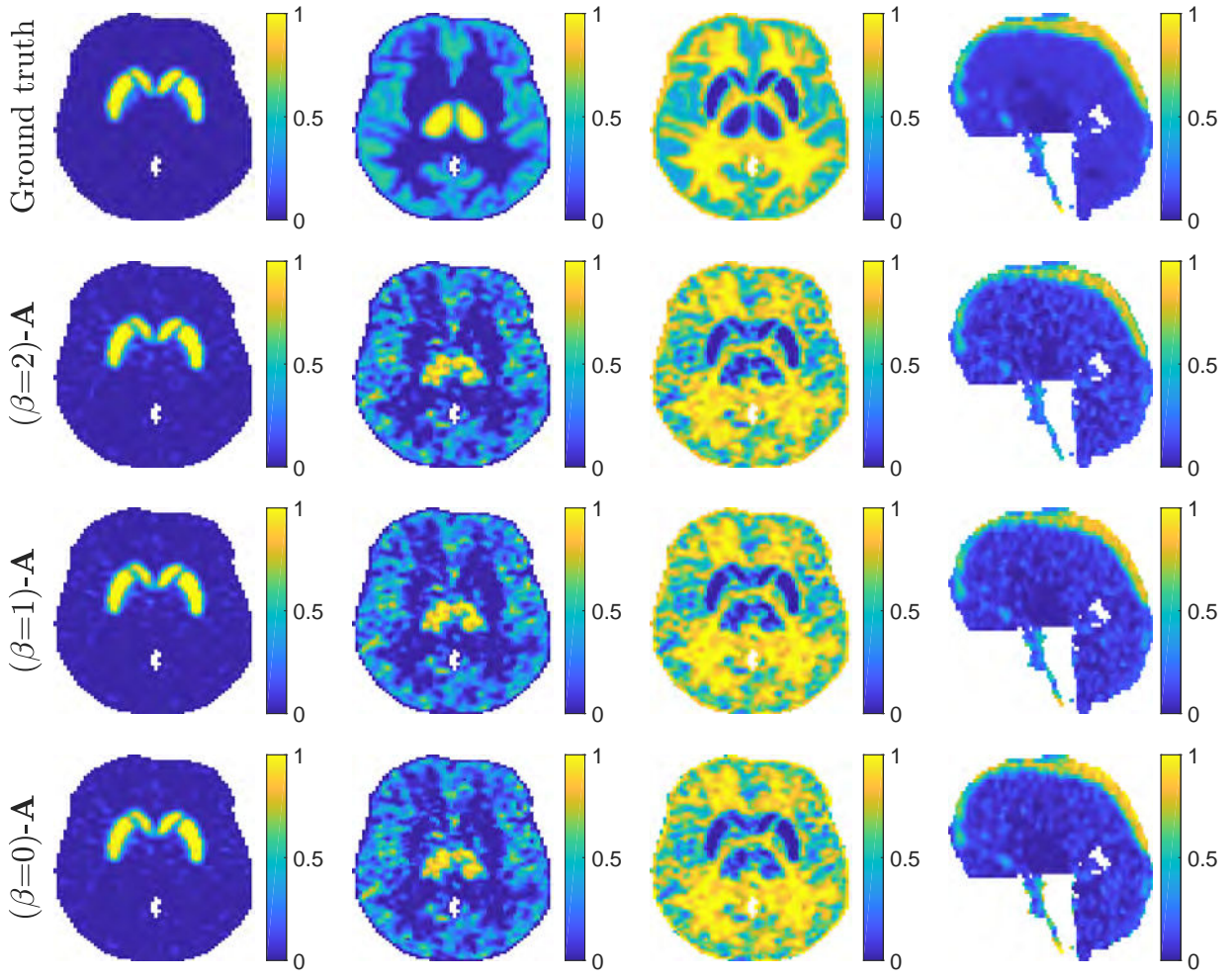


Figure 4.11.: From left do right: factor proportions from specific gray matter, non-specific gray matter, white matter and blood for one 50it sample, estimated with fixed  $\mathbf{M}$ .

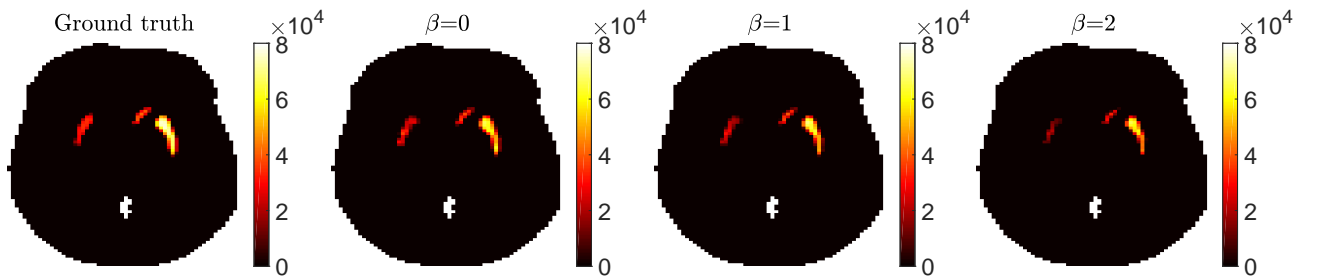


Figure 4.12.: Variability matrices estimated with fixed  $\mathbf{M}$  on a 50it sample.

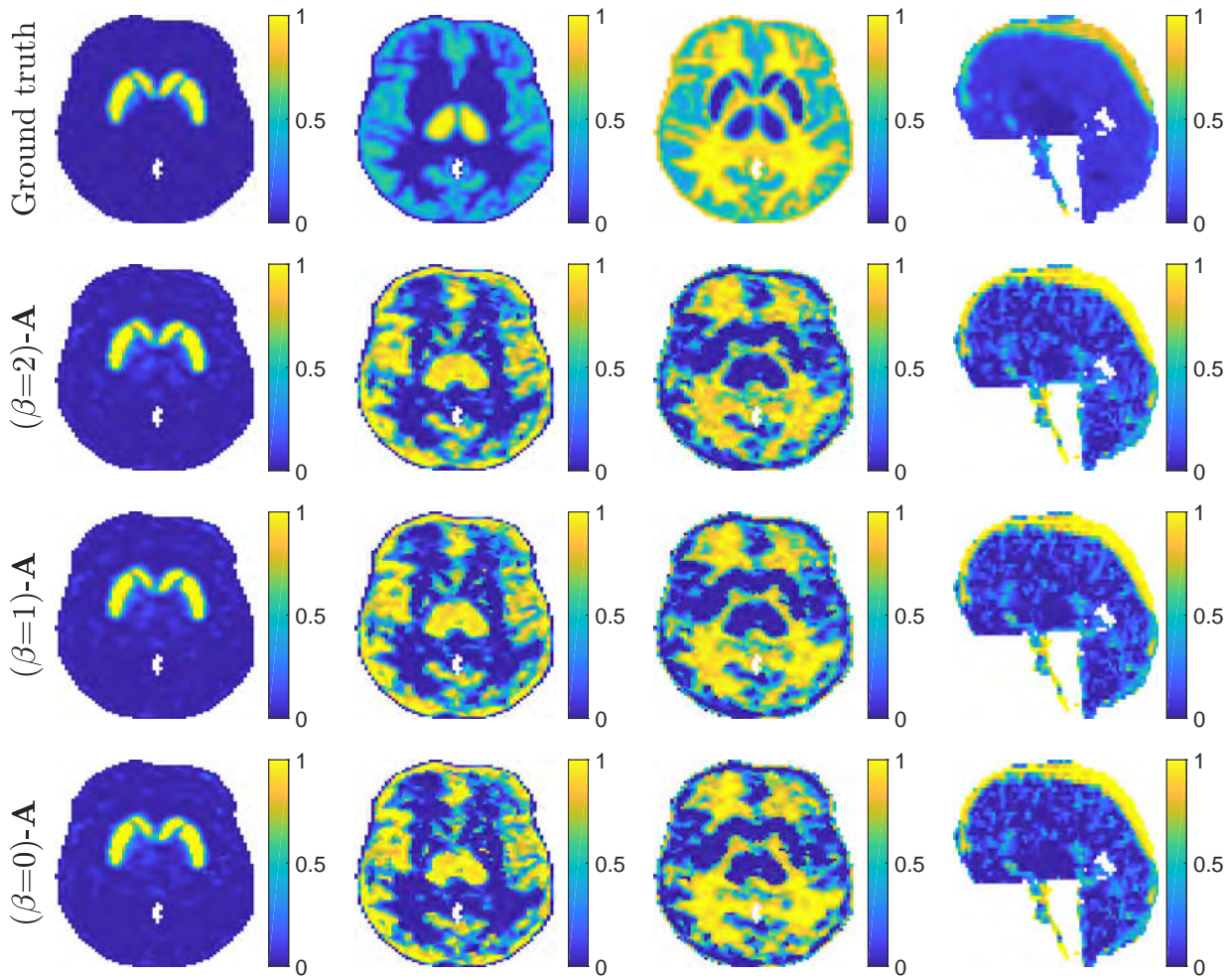


Figure 4.13.: From left do right: factor proportions from specific gray matter, non-specific gray matter, white matter and blood for one 6it sample.



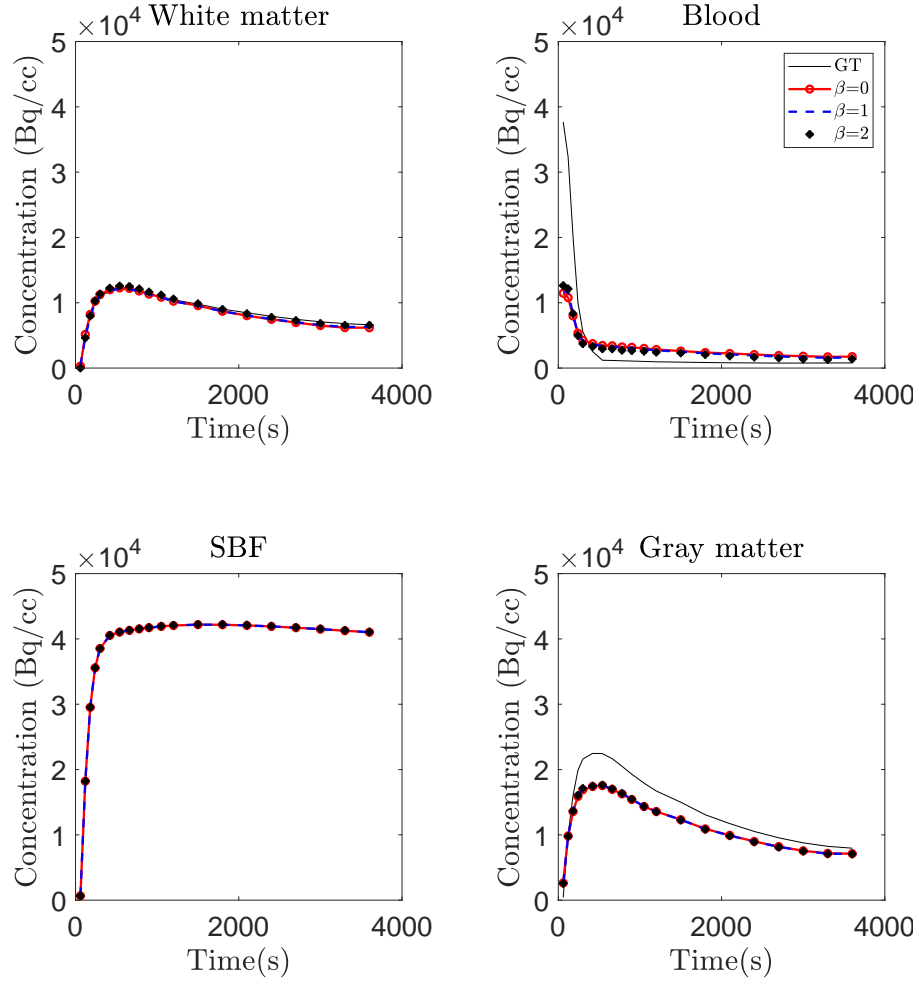


Figure 4.14.:  $\beta$ -SLMM TACs for  $\beta = 0, 1, 2$  corresponding to the specific binding factor, gray matter, white matter and blood for one 6it sample.

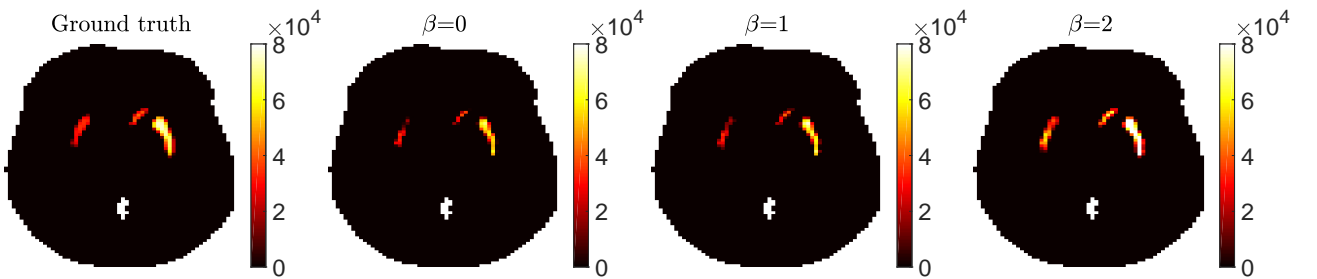


Figure 4.15.: Variability matrices estimated on a 6it sample.

Fig. 4.13 shows the factor proportions estimated from  $\beta$ -SLMM on a 6it image when all variables are estimated. The quality of this estimation is clearly lower than for the fixed  $\mathbf{M}$  framework. Moreover, the K-means clustering is used to provide the initialization. It induces a local minimum that becomes difficult to overcome due to the high non-convexity of this framework. In Fig. 4.14 we can see the corresponding factors estimated by the same simulation. While the estimated white matter is close to the ground-truth, the blood and gray matter TACs are very much different. The difference in the input function can be further explained by the lower intensities in the corresponding factor proportion ground-truth in Fig. 4.13, in opposition to high intensities for the same image in the estimated results. Finally, Fig. 4.15 shows the internal variability estimated in this framework. Once again, the variability of  $\beta = 0$  and  $\beta = 1$  are close to each other. However, this time,  $\beta = 1$  is able to recover a larger zone, almost matching the ground-truth. Although  $\beta = 2$  approximately finds the good localization of the variability, its intensities are very far away from the expected ones, showing the lower performance between the three values of  $\beta$ .

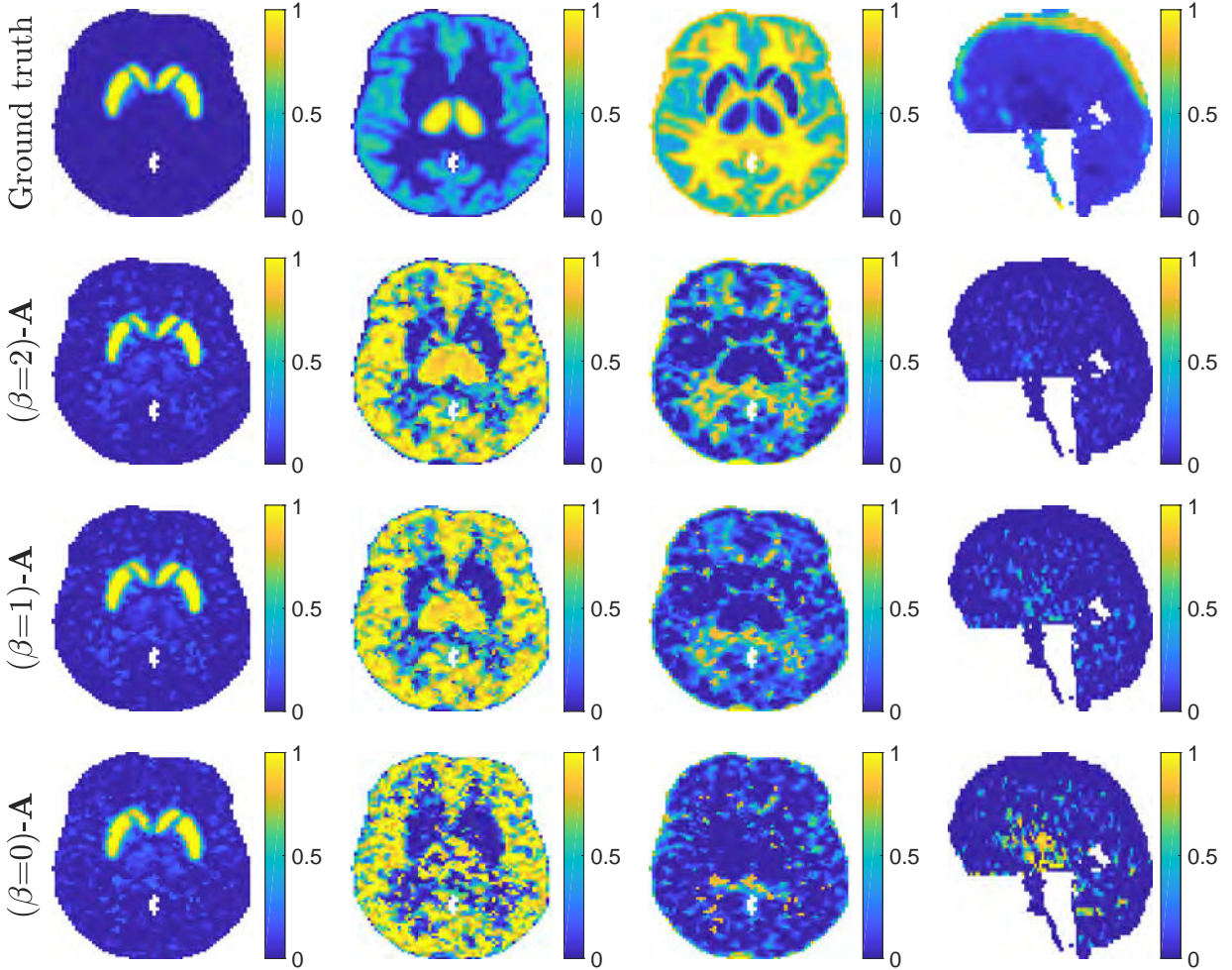


Figure 4.16.: From left do right: factor proportions from specific gray matter, non-specific gray matter, white matter and blood for one 50it sample.

Meanwhile, Fig. 4.16 shows the factor proportion results from  $\beta$ -SLMM applied to 50it when all variables are

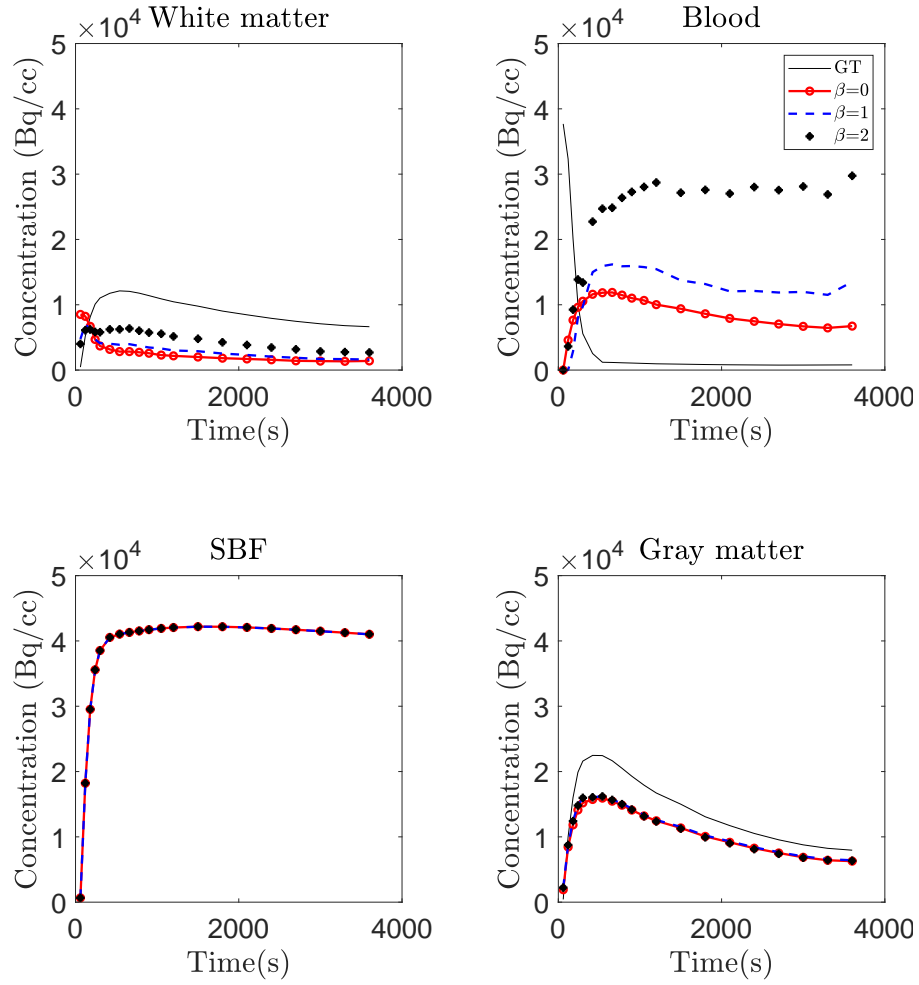


Figure 4.17.:  $\beta$ -SLMM TACs for  $\beta = 0, 1, 2$  corresponding to the specific binding factor, gray matter, white matter and blood for one 50it sample.

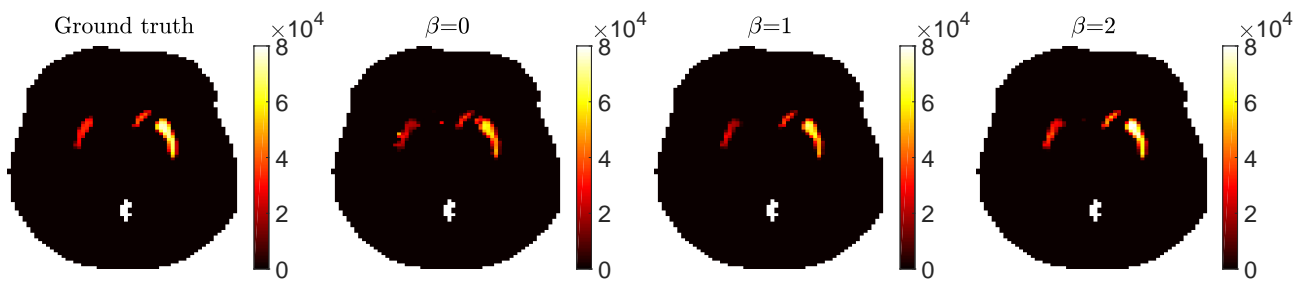


Figure 4.18.: Variability matrices estimated on a 50it sample.

Table 4.4.: Mean NMSE of  $\mathbf{A}_1$ ,  $\mathbf{A}_{2:K}$ ,  $\tilde{\mathbf{M}}^1$ ,  $\mathbf{M}^{2:K}$  and  $\mathbf{A}_1 \circ \mathbf{B}$  and PSNR of reassembled image estimated by  $\beta$ -LMM and  $\beta$ -SLMM with  $\mathbf{M}$  estimated over the 64 samples, for different values of  $\beta$ .

	$\beta$	$\beta$ -LMM			$\beta$ -SLMM		
		0	1	2	0	1	2
6it	$\mathbf{A}_1$	0.382	0.336	<b>0.327</b>	0.323	<b>0.311</b>	0.313
	$\mathbf{A}_{2:K}$	0.629	0.616	<b>0.608</b>	0.634	0.629	<b>0.628</b>
	$\tilde{\mathbf{M}}^1$	<b>0.300</b>	0.343	0.375	0.007	<b>0.006</b>	0.010
	$\mathbf{M}^{2:K}$	0.356	0.346	<b>0.306</b>	0.398	0.390	<b>0.380</b>
	$\mathbf{A}_1 \circ \mathbf{B}$	-	-	-	0.475	<b>0.450</b>	0.686
	PSNR	27.046	29.445	<b>30.231</b>	<b>31.301</b>	30.279	27.178
50it	$\mathbf{A}_1$	0.482	0.491	<b>0.472</b>	0.441	<b>0.423</b>	0.428
	$\mathbf{A}_{2:K}$	1.018	0.842	<b>0.799</b>	1.055	0.886	<b>0.808</b>
	$\tilde{\mathbf{M}}^1$	0.430	<b>0.294</b>	0.332	0.006	0.004	<b>0.003</b>
	$\mathbf{M}^{2:K}$	<b>0.716</b>	0.896	0.832	<b>0.707</b>	0.811	1.169
	$\mathbf{A}_1 \circ \mathbf{B}$	-	-	-	0.382	0.307	<b>0.223</b>
	PSNR	<b>31.302</b>	27.335	28.891	31.599	<b>31.775</b>	31.080

estimated. 50it images are very noisy even with the post-filtering, thus, the non-convexity of the model presents a very bad performance in this case. It is specially true for  $\beta = 0$  that clearly show the worst performance.  $\beta = 2$  seems to acquire the best estimation. In Fig. 4.17 we can see the corresponding factors estimated by the same simulation. The blood TAC is completely misestimated in all cases. It seems to be transferred into the white matter in the case  $\beta = 0$ . The white matter is also misestimated for all values of  $\beta$ . Even though the estimated gray matter TACs are far from the ground-truth, they show the most interpretable shape. Finally, 4.15 show the variability estimated in this framework. This time,  $\beta = 2$  shows the best estimation, while  $\beta = 0$  presents a low performance.

Table 4.4 shows the mean NMSE for  $\mathbf{A}_1$ ,  $\mathbf{A}_{2:K}$ ,  $\tilde{\mathbf{M}}^1$ ,  $\mathbf{M}^{2:K}$  and  $\mathbf{A}_1 \circ \mathbf{B}$  in the setting where  $\mathbf{M}$  is estimated with the other latent variables. Unlike the previous experiments, the results here are less clear since, depending on the variable, different values of  $\beta$  lead to the best results. This could be explained by the strong non-convexity of the problem, and possibly identifiability issues since 3 sets of latent variables need to be estimated. The results in Table 4.4 show that  $\beta$ -LMM with  $\beta = 2$  performs the best for the estimation of  $\mathbf{A}_{2:K}$  and  $\mathbf{M}_{2:K}$  in the 6it image, and for the estimation of  $\mathbf{A}_{2:K}$  in the 50it image. All variables related to specific binding, i.e.,  $\mathbf{A}_1$ ,  $\tilde{\mathbf{M}}^1$  and  $\mathbf{A}_1 \circ \mathbf{B}$ , are best estimated by  $\beta$ -SLMM with  $\beta = 1$ . For 50it, due to the high level of filtering along with the non-convexity of this setting, analysing the results is more difficult. It is, however, possible to state that a rather Poisson-Gaussian distributed noise yields the overall best mean NMSE of each variable.

Regarding the PSNRs, once again, the best PSNR on the 6it image is reached for  $\beta = 0$ , closely followed by  $\beta = 1$ . Conversely, on the 50it image, the best performance is reached for  $\beta = 1$ , then followed by  $\beta = 0$ . As also stated in the non-convex case of Phantom I, the initialization plays a relevant role when several sets of variables are to be estimated. This explains the differences found for the results with  $\mathbf{M}$  fixed and estimated. Indeed, the high non-convexity of the problem with estimated  $\mathbf{M}$  may sometimes alter the expected response.

## 4.6. Experiments with real data

### 4.6.1. Real data acquisition

A real dynamic PET image of a stroke subject injected with [18F]DPA-714 has been used to evaluate the behaviour of  $\beta$ -SLMM in a real setting. The image is the same as the first subject of Chapter 3. The [18F]DPA-714 is a ligand of the 18-kDa translocator protein (TSPO) and has shown its relevance as a biomarker of neuroinflammation [Cha+09]. The image of interest has been acquired seven days after the stroke with an Ingenuity TF64 Tomograph from Philips Medical Systems. The image has been reconstructed using the clinical reconstruction protocol used for this study. It consists of  $L = 31$  frames with durations that range from 10 seconds to 5 minutes over a total of 59 minutes. Each frame is composed of  $128 \times 128 \times 90$  voxels of size  $2 \times 2 \times 2$  mm<sup>3</sup>. Each voxel TAC is assumed to be a mixture of  $K = 4$  types of elementary TACs: specific binding associated with neuroinflammation, blood, non-specific gray matter and white matter. A supervised segmentation from a registered MRI image has provided a ground-truth of the stroke region, containing specific binding. The variability descriptors  $\mathbf{V}$  have been learned by PCA from this ground-truth. The cerebrospinal fluid has been segmented and masked as a 5th class of a K-means clustering that has also provided the initialization of the factors. Factor proportions have been initialized with the clustering labels found by K-means. For  $\beta$ -SLMM, the nominal SBF has been fixed as the empirical average of TACs from the stroke region with area-under-the-curve (AUC) between the 5th and 10th percentile. Note that the reconstruction settings typically used on the Ingenuity TF64 tomograph for this kind of imaging protocol produce PET images that are characterized by a relatively high level of smoothness, inducing spatial noise correlation.

### 4.6.2. Results

Figure 4.19 shows, from left to right, the factor proportions for gray matter, white matter and blood estimated by  $\beta$ -SLMM for  $\beta \in \{0, 1, 2\}$  where the stopping criterion  $\varepsilon$  was defined as  $5 \times 10^{-4}$  and the hyperparameter  $\lambda$  was set to 1. Visual analysis suggests that all the algorithms provide a good estimation of both gray and white matters. The results for  $\beta = 1$  and  $\beta = 2$  are very similar and it is difficult to state which one achieves the best performance. This is in agreement with the synthetic results previously presented, that showed very similar estimation errors in case of more post-reconstruction filtering. The result for  $\beta = 0$  is quite different from the others with more contrasted factor proportions. The sagittal view of the blood in the 3rd column has been taken from the center of the brain. The proposed approach correctly identifies the superior sagittal sinus vein of the brain for all tested  $\beta$  values. However, some clear differences can be observed and the blood is also more easily identified for  $\beta = 0$  than for the other values of  $\beta$ . Fig. 4.21 confirms these findings, showing TACs that are very similar for  $\beta \in \{1, 2\}$  while the TACs for  $\beta = 0$  are always a bit apart from the others. The expected initial pick characterizing the blood TAC is more easily identified with  $\beta = 1$  and  $\beta = 2$ . On the other hand,



for  $\beta = 0$  the TAC associated with the non-specific gray matter has a lower AUC than the two others, further differentiating from the specific binding TAC.

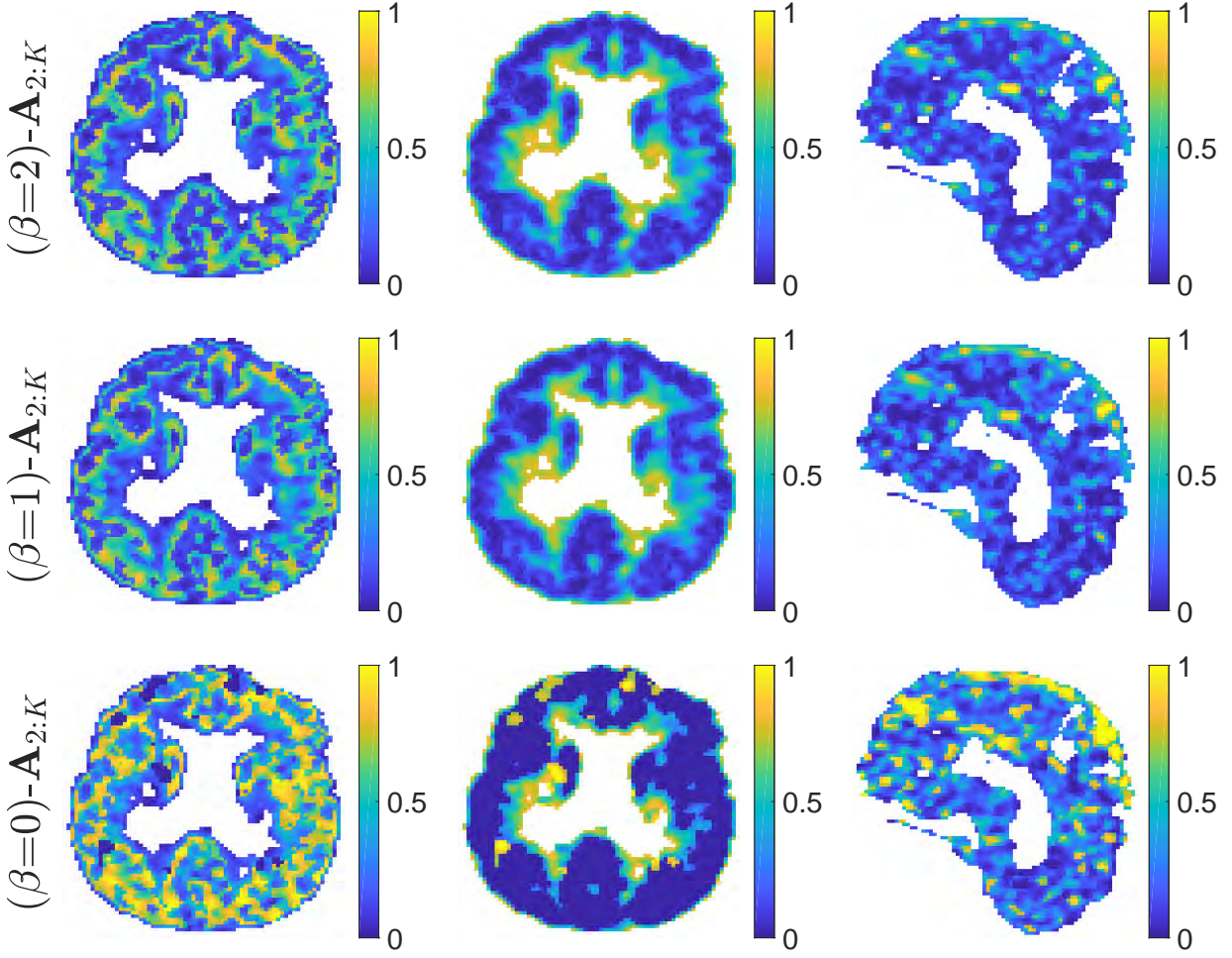


Figure 4.19.: From left do right: factor proportions from non-specific gray matter, white matter and blood obtained with  $\beta$ -SLMM for  $\beta = 0, 1, 2$ .

Fig. 4.20 shows a manual segmentation of the stroke zone along with the corresponding factor proportions and variability matrices estimated with SLMM. The results obtained with  $\beta = 0$  show a more correct identification of the stroke zone. Results with  $\beta = 1, 2$  are very similar, they better detect the thalamus, known for having higher binding of neuroinflammation. Nevertheless, they also contain the non-specific gray matter in the factor proportion related to specific binding. All values of  $\beta$  show variability matrices that are correctly located. Moreover, they present an expected magnitude around 30, as roughly estimated from the segmented stroke region. Besides, some differences may be highlighted in the variability matrix estimation. Indeed,  $\beta = 0$  shows a slightly weaker magnitude of the variability. However, it identifies some variability in a region not located by the others, as shown in the last row. As no variability is expected in this region, adjusting the sparsity parameter  $\lambda$  so as to make it disappear would also decrease the intensities of the variability matrix in the other regions and so the weaker result for  $\beta = 0$  is not due to a wrong parameter tuning. The results for  $\beta \in \{1, 2\}$

are very similar but  $\beta = 2$  shows a stronger intensity, while  $\beta = 1$  shows a more spread result, even presenting the influence of the thalamus in the  $2^{nd}$  row, similarly to  $\beta = 0$ .

## 4.7. Conclusion

This chapter studied the role of the data-fidelity term when conducting factor analysis of dynamic PET images. We focused on the beta-divergence, for which the NMF and LMM decompositions were already proposed in other applicative contexts. We introduced a new algorithm to conduct analysis, allowing for variable specific-binding factor, termed  $\beta$ -SLMM.

For all those three models, experimental results showed the interest of using the  $\beta$ -divergence in place of the standard least-square distance. The factor and proportion estimations were indeed more accurate when computed with a suitable value of  $\beta$ . The improvement was shown to be higher when the image had not suffered too strong post-processing corrections. The  $\beta$ -divergence thus appeared to be a general and flexible framework for analysing different kinds of dynamic PET images.

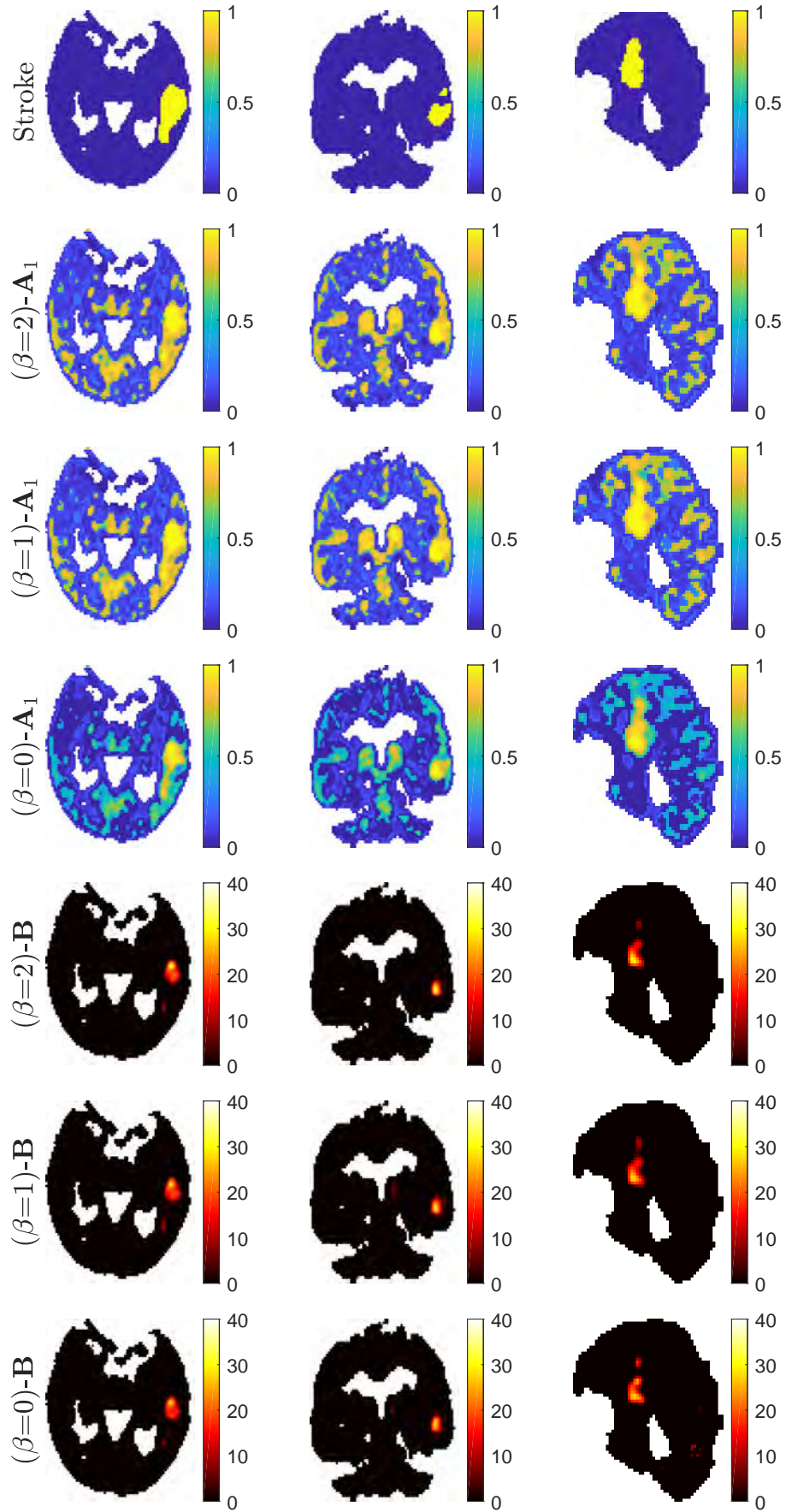


Figure 4.20.: From top to bottom: MRI ground truth of the stroke zone, factor proportions from specific gray matter and variability matrices obtained with  $\beta$ -SLMM for  $\beta = 0, 1, 2$ .



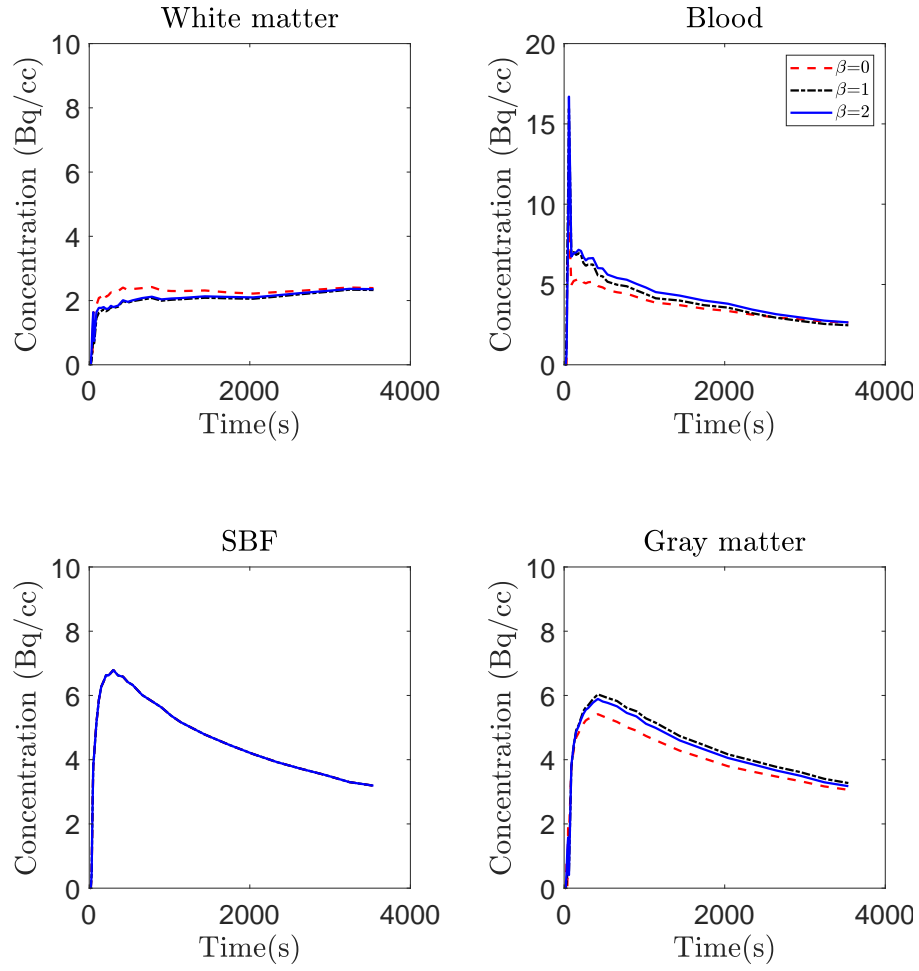


Figure 4.21.: TACs corresponding to the specific binding factor, gray matter, white matter and blood.



# Towards parametric nonlinear unmixing of dynamic PET images

## Contents

5.1	Introduction . . . . .	<b>135</b>
5.2	Proposed model . . . . .	<b>138</b>
5.3	Derivation of the objective function . . . . .	<b>139</b>
5.4	A PALM algorithm . . . . .	<b>140</b>
5.4.1	Optimization with respect to $\mathbf{M}$ . . . . .	140
5.4.2	Optimization with respect to $\mathbf{A}$ . . . . .	142
5.4.3	Optimization with respect to $\mathbf{B}_i$ . . . . .	142
5.4.4	Optimization with respect to $\alpha_{ki}$ . . . . .	143
5.5	Evaluation on synthetic data . . . . .	<b>143</b>
5.5.1	Synthetic data generation . . . . .	143
5.5.2	Compared methods . . . . .	147
	DEPICT . . . . .	148
	SLMM-unmixing . . . . .	148
	PNMM-unmixing (proposed approach) . . . . .	148
5.5.3	Results and discussion . . . . .	149
5.6	Evaluation on real data . . . . .	<b>153</b>
5.6.1	PET data settings . . . . .	153
5.6.2	Results and discussion . . . . .	153
5.7	Conclusion . . . . .	<b>155</b>

## 5.1. Introduction

Chapter 3 introduced a factor analysis model that handles nonlinearities in specific binding (SB) kinetics with a spatially indexed variability. The previous model tried to extract a factor for the blood input function, a factor for each non-specific binding (nSB) tissue of the region under study and assigned a factor for high-uptake tissues explicitly, in which the variability was applied. However, the kinetics of SB tissues are often related to that of nSB tissues, as shown by the reference tissue input models presented in Section 1.6.2. Moreover, when abnormalities are present, the kinetics of a tissue that is non-specific under healthy circumstances will be nonlinearly modified in the presence of the labelled molecule, though it is still the same tissue or organ.

Therefore, we decide to study SB as an instance of nSB kinetics. The main idea is to perform factor analysis on nSB tissues and blood while allowing for nonlinearities on each nSB tissue that will describe SB regions. Nonlinear unmixing is a wide branch of study in hyperspectral imaging [Dob+14b; Dob+14a]. As discussed in Section 2.5, a large family of nonlinear models can be described as

$$\mathbf{x}_n = \mathbf{M}\mathbf{a}_n + \boldsymbol{\mu}(\mathbf{M}, \mathbf{a}_n, \mathbf{b}_n), \quad (5.1)$$

where the observed pixel  $\mathbf{x}_n$  is composed by a linear contribution, as in LMM, and an additive nonlinear term  $\boldsymbol{\mu}(\cdot)$  that often depends on the factors matrix  $\mathbf{M}$ , the factor proportion coefficients  $\mathbf{a}_n$  and internal nonlinearities coefficients  $\mathbf{b}_n$  that adjust the amount of nonlinearity in each pixel.

Moreover, we want these nonlinearities to directly provide an interpretable result in terms of quantification, representing different levels of binding. To do so, we came across the parametric pharmacokinetic models [GGC01] discussed in Section 1.6.2. They are very useful in providing physiologically meaningful estimates on the analysis of PET data. Conventional methods used for kinetic parameter estimation often define a ROI and then perform estimation based on the ROI average [LH96; Ber+10]. These approaches neglect any spatial variations in the tracer kinetics within the ROI, e.g., due to partial volume effects and tissue heterogeneity. To avoid this homogeneous ROI assumption, some studies performed a voxel-by-voxel estimation of kinetic parameters and, in an attempt to overcome the low SNR, applied additional penalizations to stabilize the estimation [Kam+05; HZ98].

As presented in (1.13) from Section 1.6.2, Gunn et al. [Gun+02] use the following model to describe each target voxel TAC:

$$\mathbf{x}_n(\mathbf{b}_n, \boldsymbol{\alpha}) = \left( (1 + b_{0n})\delta(\mathbf{t}) + \sum_{i=1}^V b_{in}e^{-\alpha_i \mathbf{t}} \right) * \mathbf{m}_R, \quad (5.2)$$

where, as in Section 1.6.2,  $\mathbf{t} = [t_1, \dots, t_L]^T$  are the times of acquisition, which are previously known,  $*$  stands for temporal convolution,  $V$  is the number of compartments,  $\delta(\mathbf{t})$  is the impulse function and  $e^{\theta}$  is a point-wise exponentiation. Moreover,  $\mathbf{x}_n$  is the target tissue in the  $n^{th}$  voxel,  $\mathbf{m}_R$  is the reference tissue TAC chosen to describe the studied ROI and  $\mathbf{b}_n = [b_{1n}, \dots, b_{Vn}]$  and  $\boldsymbol{\alpha} = [\alpha_1, \dots, \alpha_V]$  describe the kinetics of the tracer. Recall that this formulation neglects the blood volume in both target and reference tissues. In [Gun+02], the basis functions defined by  $\boldsymbol{\alpha}$  are pre-calculated and an undetermined system of equations is defined to fit to the data with a technique named DEPICT. As this is an ill-posed problem, an additional sparsity penalization is imposed to the basis coefficients  $\mathbf{b}$ . This sparsity assumption is based on the fact that data are expected to be described by just a few compartments. Peng et al. [Pen+08] investigated the use of sparse Bayesian learning for parametric estimation further allowing the weights of the basis functions to be nonnegative to fit reference tissue models.

Nevertheless, these approaches still assume that there is only one kinetic process occurring per voxel, while, due to the low spatial resolution, the partial volume effect and biological heterogeneity, the resulting signal is often a mixture of multiple kinetic processes. This is also the rationale behind the factor analysis models presented in the previous chapters. To overcome this limitation, Lin et al. [Lin+14] proposed a two-stage algorithm that benefits from the prior information provided by parametric imaging models on the physics and physiology of metabolism while introducing partial volume with a linear combination of the different kinetics. The first step consists in a dictionary-based estimation of the nonlinear kinetics of each considered tissue and the second step computes the tissue fractions and the linear terms of the tissue kinetic models. The model in [Lin+14] considers that each image voxel is described by a linear mixing of  $K$  classes, including blood and assuming that the blood input function  $\mathbf{m}_K$  is known. Each tissue factor TAC  $\mathbf{m}_k(\boldsymbol{\kappa})$ , for  $k = 1, \dots, K - 1$  is described by a three-tissue compartment model [Hua+80] with kinetic parameters  $\boldsymbol{\kappa}$ . The final formulation for each voxel can be written as

$$\mathbf{x}_n = \sum_{k=1}^{K-1} a_{kn} \mathbf{m}_k(\boldsymbol{\kappa}) + a_{Kn} \mathbf{m}_K, \quad (5.3)$$

following both the nonnegative and sum-to-one constraints in (2.8) and (2.13). A similar approach is also proposed in [Che+11]. Based on the same idea, Klein et al. [Kle+10] tries to describe each factor TAC with an input function-based kinetic model and to jointly estimate this input function as well as the model parameters for each factor.

However, many experimental results indicate that the use of commonly accepted multi-compartment models often leads to considerably biased and high-variance estimates of the pharmacokinetics parameters, due to the high number of parameters to be estimated [PH01; Pad03; Buc02]. Moreover, they often oversimplify the kinetics of several tracers, especially when they present tissue heterogeneity [DeL+09]. As an attempt at providing a more accurate description of the kinetics of the tracer while benefiting from the physiological description of parametric imaging, the approach proposed in this chapter relies on a parametrically nonlinear factor analysis. Differently from [Lin+14], factor TACs from nSB tissues will be directly estimated in the model and, based on the data-driven reference input model presented in Chapter 1, will be used as reference tissue TACs for the recovery of the kinetic parameters from SB. The idea of linking factor analysis to compartmental modeling has already been investigated by some works from the PET literature. In particular, Nijran and Barber [NB85] proposed to constrain the space of possible solutions of factor analysis with the space of theoretical solutions given by compartmental models. Szabo et al. [Sza+93] used factor analysis to differentiate SB and nSB TACs and determine the number of compartments needed to model the kinetics of [11C] pyrilamine in the brain. El Fakhri et al. [El+05; El+09] used a previous factor analysis step to extract the input functions that were used to compute the TACs in each voxel with a two-compartment model. The work proposed in this Chapter goes one step further by jointly conducting factor and kinetic analysis.

This Chapter is organized as follows. The proposed analysis model is presented in Section 5.2. The optimization problem is formulated in Section 5.3. Section 5.4 presents the corresponding PALM algorithm. Synthetic simulations are presented in Section 5.5 and real image results are reported in Section 5.6. Section 5.7 concludes the chapter.

## 5.2. Proposed model

The model proposed in this chapter combines the model in (5.2) with the generalization of (5.3), yielding a parametrically nonlinear mixing model (PNMM)

$$\mathbf{x}_n = \sum_{k=1}^{K-1} a_{kn}(\mathbf{m}_k + \sum_{i=1}^V b_{kin} \mathbf{m}_k * e^{-\alpha_{ki}\mathbf{t}} + b_{k0n} \mathbf{m}_k) + a_{Kn} \mathbf{m}_K, \quad (5.4)$$

where  $b_{kin}$  receives an additional index  $k$  since we will consider one coefficient for each reference tissue TAC as well. This model is expected to be more robust than the previous ones, as it accounts for possible partial volume effects induced by mixing between tissues and blood, while benefiting from the physical considerations of parametric imaging. It also directly estimates the global kinetics of one tissue, thus not being completely dependent of kinetic parameters. This can offer a more precise quantification as it automatically analyses different nSB tissues separately. It may also allow the tissue affected by SB to be identified, through the computation of the binding potential (BP) within each nSB tissue.

In matrix form, we may write

$$\mathbf{Y} = \mathbf{M}\mathbf{A} + \sum_{i=0}^V \mathbf{Q}_i(\tilde{\mathbf{A}} \circ \mathbf{B}_i) + \mathbf{R} \quad (5.5)$$

where  $\mathbf{M}$  is a  $L \times K$  matrix containing the factor TACs,  $\mathbf{A}$  is a  $K \times N$  matrix composed of the factor proportion vectors  $\mathbf{a}_n = [a_{1,n}, \dots, a_{K,n}]^T$ , “ $\circ$ ” is the Hadamard point-wise product and  $\mathbf{R} = [\mathbf{r}_1, \dots, \mathbf{r}_N]^T$  is an  $L \times N$  matrix accounting for noise and mismodelling. Moreover, we define  $\tilde{\mathbf{A}} = [\mathbf{A}_1, \dots, \mathbf{A}_{K-1}]$ , i.e., eliminating the blood factor proportion and

$$\mathbf{Q}_i = \begin{bmatrix} \mathbf{m}_1 * e^{-\alpha_{1i}\mathbf{t}} & \dots & \mathbf{m}_{K-1} * e^{-\alpha_{(K-1)i}\mathbf{t}} \end{bmatrix}, \text{ for } i \in \{0, \dots, V\}. \quad (5.6)$$

Furthermore, as in [Che+11], we replace the convolution operator by a Toeplitz matrix of the vectors  $e^{-\alpha_{ki}\mathbf{t}}$ , i.e.,

$$\mathbf{E}_{ki} = T_p(e^{-\alpha_{ki}\mathbf{t}}), i \in \{0, \dots, V\} \quad (5.7)$$

where  $T_p$  is the operator that transforms a vector into a symmetric Toeplitz matrix whose dimensions are the

length of the vector. Thus, matrix  $\mathbf{Q}_i$  can be written as

$$\mathbf{Q}_i = \begin{bmatrix} \mathbf{E}_{1i}\mathbf{m}_1 & \cdots & \mathbf{E}_{(K-1)i}\mathbf{m}_{K-1} \end{bmatrix}, \text{ for } i \in \{0, \dots, V\}. \quad (5.8)$$

Note that  $\alpha_{k0} = 0 \ \forall k \in \{1, \dots, K-1\}$  and therefore  $\mathbf{E}_{k0} = \mathbf{I}_L$  and  $\mathbf{Q}_0 = [\mathbf{m}_1, \dots, \mathbf{m}_{K-1}]$ . Also, the matrices of internal coefficients related to the basis functions are given by

$$\mathbf{B}_i = \begin{bmatrix} b_{1i1} & b_{1i2} & \cdots & b_{1iN} \\ b_{2i1} & b_{2i2} & \cdots & b_{2iN} \\ \vdots & \vdots & \vdots & \vdots \\ b_{(K-1)i1} & b_{(K-1)i2} & \cdots & b_{(K-1)iN} \end{bmatrix}, \text{ for } i \in \{0, \dots, V\}, \quad (5.9)$$

with  $\underline{\mathbf{B}} = \{\mathbf{B}_0, \dots, \mathbf{B}_V\}$ .

Besides, additional constraints regarding these sets of parameters are assumed. As in the previous chapters, non-negativity (2.8) and sum-to-one (2.13) are assumed for the factors and corresponding proportions to reflect physical considerations.

As in [Gun+02], we define maximum and minimum values for the elements of the vector  $\boldsymbol{\alpha}_i = \begin{bmatrix} \alpha_{1i} & \cdots & \alpha_{(K-1)i} \end{bmatrix}$  to reduce the indeterminacy of the basis elements solution while allowing a suitable coverage of the kinetic spectrum. Thus, we define

$$\begin{aligned} \boldsymbol{\alpha}_i &\in \mathcal{R}, \quad \forall i \in \{1, \dots, V\}, \\ \mathcal{R} &= \{\mathbf{z} \in \mathbb{R}^{K-1} : \alpha_{i_{\min}} \preceq z_k \preceq \alpha_{i_{\max}}\}. \end{aligned} \quad (5.10)$$

The same choice is adopted for the internal weights as

$$\begin{aligned} \mathbf{B}_i &\in \mathcal{B}, \quad \forall i \in \{0, \dots, V\}, \\ \mathcal{B} &= \{\mathbf{z} \in \mathbb{R}^{(K-1) \times N} : b_{i_{\min}} \preceq z_{kn} \preceq b_{i_{\max}}\}. \end{aligned} \quad (5.11)$$

### 5.3. Derivation of the objective function

The PNMM (5.5) and constraints (2.8), (2.13), (5.10) and (5.11) are combined to formulate a constrained optimization problem. We thereby define a cost function to estimate the matrices  $\mathbf{M}$ ,  $\mathbf{A}$  and  $\boldsymbol{\alpha}$  and the set  $\underline{\mathbf{B}}$  containing the matrices  $\mathbf{B}_i$ . For simplification purposes, we consider the noise to be Gaussian and the data-fitting term is defined as the Frobenius norm  $\|\cdot\|_F^2$  of the difference between the dynamic PET image  $\mathbf{Y}$  and the proposed data modelling  $\mathbf{X}$ . This formulation could be generalized for other noise distributions with the  $\beta$ -divergence studied in the previous chapter. Since the problem is ill-posed and non-convex, additional regularizers become essential. In this chapter, we propose to define penalization functions  $\Phi$ ,  $\Psi$  and  $\Omega$  to reflect the available *a priori* knowledge on  $\mathbf{M}$ ,  $\mathbf{A}$  and  $\underline{\mathbf{B}}$ , respectively. The optimization problem is then defined as

$$(\mathbf{M}^*, \mathbf{A}^*, \underline{\mathbf{B}}^*, \boldsymbol{\alpha}^*) \in \arg \min_{\mathbf{M}, \mathbf{A}, \underline{\mathbf{B}}, \boldsymbol{\alpha}} \left\{ \mathcal{J}(\mathbf{M}, \mathbf{A}, \underline{\mathbf{B}}, \boldsymbol{\alpha}) \text{ s.t. (2.8), (2.13), (5.10), (5.11)} \right\} \quad (5.12)$$

with

$$\mathcal{J}(\mathbf{M}, \mathbf{A}, \underline{\mathbf{B}}, \boldsymbol{\alpha}) = \frac{1}{2} \left\| \mathbf{Y} - \mathbf{M}\mathbf{A} - \sum_{i=0} \mathbf{Q}_i(\tilde{\mathbf{A}} \circ \mathbf{B}_i) \right\|_F^2 + \eta \Phi(\mathbf{A}) + \beta \Psi(\mathbf{M}) + \lambda \Omega(\underline{\mathbf{B}}) \quad (5.13)$$

where the parameters  $\eta$ ,  $\beta$  and  $\lambda$  control the trade-off between the data fitting term and the penalties  $\Phi(\mathbf{A})$ ,  $\Psi(\mathbf{M})$  and  $\Omega(\underline{\mathbf{B}})$ . The factors and factor proportions penalizations are given by (3.12) and (3.11), respectively. The penalization function for the variable  $\underline{\mathbf{B}}$  is separable, leading to

$$\Omega(\underline{\mathbf{B}}) = \sum_{i=0}^V \Omega_i(\mathbf{B}_i), \quad (5.14)$$

with  $\Omega_i(\mathbf{B}_i)$  the spatial sparsity-inducing group lasso regularizer, as defined in (3.15).

## 5.4. A PALM algorithm

As in Chapter 3, our optimization problem (5.12) is nonconvex and nonsmooth. Therefore, we will apply the same minimization strategy detailed in Section 3.4. This means that we will iteratively update each variable  $\mathbf{A}$ ,  $\mathbf{M}$ ,  $\underline{\mathbf{B}}$  and  $\boldsymbol{\alpha}$  while all the others are fixed, finally converging to a local critical point  $\mathbf{A}^*$ ,  $\mathbf{M}^*$ ,  $\underline{\mathbf{B}}^*$  and  $\boldsymbol{\alpha}^*$ . The resulting unmixing algorithm, whose main steps are described in the following paragraphs, is summarized in Algo. 7.

### 5.4.1. Optimization with respect to $\mathbf{M}$

A direct application of [BST13] under the constraints defined by (3.2) leads to the following updating rule

$$\mathbf{M}^{h+1} = \mathcal{P}_+ \left( \mathbf{M}^h - \frac{\gamma}{L_M^h} \nabla_{\mathbf{M}} \mathcal{J}(\mathbf{M}^h, \mathbf{A}^h, \underline{\mathbf{B}}^h, \boldsymbol{\alpha}^h) \right) \quad (5.15)$$

where  $\mathcal{P}_+(\cdot)$  is the projector onto the nonnegative set  $\{\mathbf{X} | \mathbf{X} \succeq \mathbf{0}_{L,R}\}$ .

For  $k = (1, \dots, K-1)$ , the required gradient is written<sup>1</sup>

$$\begin{aligned} \nabla_{m_k} \mathcal{J}(\mathbf{m}_k, \mathbf{A}_k, \mathbf{W}_k, \mathbf{E}_k) &= -(\tilde{\mathbf{Y}} - \mathbf{m}_k \mathbf{A}_k) \mathbf{A}_k^T - \sum_{i=0}^V \mathbf{E}_{ki}^T \tilde{\mathbf{Y}} \mathbf{W}_{k,i}^T + \sum_{i=0}^V (\mathbf{E}_{ki} + \mathbf{E}_{ki}^T) \mathbf{m}_k \mathbf{W}_{k,i} \mathbf{A}_k^T \\ &\quad + \frac{1}{2} \sum_{i=0}^V \sum_{j=0}^V (\mathbf{E}_{ki}^T \mathbf{E}_{kj} + (\mathbf{E}_{ki}^T \mathbf{E}_{kj})^T) (\mathbf{m}_k \mathbf{W}_{k,j} \mathbf{W}_{k,i}^T) + \beta (\tilde{\mathbf{M}} - \tilde{\mathbf{M}}^0) \end{aligned} \quad (5.16)$$

<sup>1</sup>Note that the iteration index has been omitted in the following definitions of the gradients to lighten the notations.



**Algorithm 7:** PNMM unmixing: global algorithm

---

**Data:**  $\mathbf{Y}$   
**Input:**  $\mathbf{A}^0, \mathbf{M}^0, \underline{\mathbf{B}}^0, \boldsymbol{\alpha}^0$

```

1  $h \leftarrow 0$ 
2 while stopping criterion not satisfied do
3    $\mathbf{M}^{h+1} \leftarrow \mathcal{P}_+ \left( \mathbf{M}^h - \frac{\gamma}{L_M^h} \nabla_{\mathbf{M}} \mathcal{J}(\mathbf{M}^h, \mathbf{A}^h, \underline{\mathbf{B}}^h, \boldsymbol{\alpha}^h) \right)$ 
4    $\mathbf{A}^{h+1} \leftarrow \mathcal{P}_{\mathcal{A}_R} \left( \mathbf{A}^h - \frac{\gamma}{L_A^h} \nabla_{\mathbf{A}} \mathcal{J}(\mathbf{M}^{h+1}, \mathbf{A}^h, \underline{\mathbf{B}}^h, \boldsymbol{\alpha}^h) \right)$ 
5   for  $i \leftarrow 0$  to  $V$  do
6      $\mathbf{B}_i^{h+1} \leftarrow \text{prox}_{\frac{\lambda}{L_{B_i}^h} \|\cdot\|_1} \left( \mathcal{P}_{\mathcal{B}} \left( \mathbf{B}_i^h - \frac{\gamma}{L_{B_i}^h} \nabla_{\mathbf{B}_i} \mathcal{J}(\mathbf{M}^{h+1}, \mathbf{A}^{h+1}, \underline{\mathbf{B}}^h, \boldsymbol{\alpha}^h) \right) \right)$ 
7   for  $i \leftarrow 1$  to  $V$  do
8     for  $k \leftarrow 1$  to  $K$  do
9        $\alpha_{ki}^{h+1} \leftarrow \mathcal{P}_{\mathcal{R}} \left( \alpha_{ki}^h - \frac{\gamma}{L_{\alpha_{ki}}^h} \nabla_{\alpha_{ki}} \mathcal{J}(\mathbf{M}^{h+1}, \mathbf{A}^{h+1}, \underline{\mathbf{B}}^{h+1}, \boldsymbol{\alpha}^h) \right)$ 
10   $h \leftarrow h + 1$ 
11  $\mathbf{A} \leftarrow \mathbf{A}^{h+1}$ 
12  $\mathbf{M} \leftarrow \mathbf{M}^{h+1}$ 
13  $\underline{\mathbf{B}} \leftarrow \underline{\mathbf{B}}^{h+1}$ 
14  $\boldsymbol{\alpha} \leftarrow \boldsymbol{\alpha}^{h+1}$ 
Result:  $\mathbf{A}, \mathbf{M}, \underline{\mathbf{B}}, \boldsymbol{\alpha}$ 

```

---

with  $\tilde{\mathbf{Y}} = \mathbf{Y} - \sum_{j \neq k} (\mathbf{m}_j \mathbf{A}_j - \sum_{i=0}^V \mathbf{E}_{ji} \mathbf{m}_j \mathbf{W}_{ji})$  and  $\mathbf{W}_i = (\tilde{\mathbf{A}} \circ \mathbf{B}_i)$ . Moreover,  $L_{m_k}$  is a bound on the Lipschitz constant of  $\nabla_{\tilde{\mathbf{M}}} \mathcal{J}(\mathbf{m}_k, \mathbf{A}_k, \mathbf{W}_k, \mathbf{E}_k)$ , defined as

$$L_{m_k} = \|\mathbf{A}_k \mathbf{A}_k^T\| + \sum_{i=0}^V \|\mathbf{E}_{ki} + \mathbf{E}_{ki}^T\| \|\mathbf{W}_{k,i} \mathbf{A}_k^T\| + \sum_{i=0}^V \sum_{j=0}^V \|\mathbf{E}_{ki}^T \mathbf{E}_{kj}\| \|\mathbf{W}_{k,j} \mathbf{W}_{k,i}^T\| + \beta \quad (5.17)$$

where the spectral norm  $\|\mathbf{X}\| = \sigma_{\max}(\mathbf{X})$  is the largest singular value of  $\mathbf{X}$  and  $\|\mathbf{X}\|_{\infty} = \max_{1 \leq i \leq m} \sum_{j=1}^n |x_{ij}|$  is the sum of the absolute values of the matrix row entries. It is important to note that this value may be not optimal and a lower value can be found to accelerate the updates.

For  $k = K$ , the gradient writes

$$\nabla_{m_K} \mathcal{J}(\mathbf{m}_K, \mathbf{A}_K) = -(\tilde{\mathbf{Y}} - \mathbf{m}_K \mathbf{A}_K) \mathbf{A}_K^T + \beta(\mathbf{m}_K - \mathbf{m}_K^0)$$

with  $\tilde{\mathbf{Y}} = \mathbf{Y} - \tilde{\mathbf{M}} \tilde{\mathbf{A}} - \sum_{i=0}^V \mathbf{Q}_i (\tilde{\mathbf{A}} \circ \mathbf{B}_i)$ . The Lipschitz constant is

$$L_{m_K} = \|\mathbf{A}_K \mathbf{A}_K^T\| + \beta.$$

### 5.4.2. Optimization with respect to $\mathbf{A}$

Similarly to paragraph 5.4.1, the abundance update is defined as the following

$$\mathbf{A}^{h+1} = \mathcal{P}_{\mathcal{A}_R} \left( \mathbf{A}^h - \frac{\gamma}{L_A^h} \nabla_{\mathbf{A}} \mathcal{J}(\mathbf{M}^{h+1}, \mathbf{A}^h, \underline{\mathbf{B}}^h, \boldsymbol{\alpha}^h) \right), \quad (5.18)$$

where  $\mathcal{P}_{\mathcal{A}_R}(\cdot)$  is the projection on the set  $\mathcal{A}_R$  defined by the abundance constraints (3.3), which can be computed with efficient algorithms, see, e.g., [Con15].

For  $\tilde{\mathbf{A}}$ , the gradient can be computed as

$$\begin{aligned} \nabla_{\tilde{\mathbf{A}}} \mathcal{J}(\tilde{\mathbf{M}}, \tilde{\mathbf{A}}, \mathbf{Q}, \mathbf{B}) &= -\tilde{\mathbf{M}}^T (\tilde{\mathbf{Y}} - \tilde{\mathbf{M}}\tilde{\mathbf{A}} - \sum_{i=0}^V \mathbf{Q}_i(\tilde{\mathbf{A}} \circ \mathbf{B}_i)) \\ &\quad - \sum_{i=0}^V \left( (\mathbf{Q}_i^T (\tilde{\mathbf{Y}} - \tilde{\mathbf{M}}\tilde{\mathbf{A}} - \sum_{j=0}^V \mathbf{Q}_j(\tilde{\mathbf{A}} \circ \mathbf{B}_j))) \circ \mathbf{B}_i \right) + \eta \tilde{\mathbf{A}} \mathbf{S} \mathbf{S}^T \end{aligned} \quad (5.19)$$

with  $\tilde{\mathbf{Y}} = \mathbf{Y} - \mathbf{m}_K \mathbf{A}_K$  and  $\tilde{\mathbf{M}} = [\mathbf{m}_1, \dots, \mathbf{m}_{K-1}]$ . Moreover,  $L_{\tilde{\mathbf{A}}}$  is the Lipschitz constant of  $\nabla_{\tilde{\mathbf{A}}} \mathcal{J}(\tilde{\mathbf{M}}, \tilde{\mathbf{A}}, \mathbf{Q}, \mathbf{B})$

$$L_{\tilde{\mathbf{A}}} = \|\tilde{\mathbf{M}}^T \tilde{\mathbf{M}}\| + \sum_{i=0}^V \left( 2\|\tilde{\mathbf{M}}^T \mathbf{Q}_i\| \|\mathbf{B}_i\| + \|\mathbf{B}_i\| \sum_{j=0}^V \|\mathbf{Q}_i^T \mathbf{Q}_j\| \|\mathbf{B}_j\| \right) + \eta \|\mathbf{S} \mathbf{S}^T\|. \quad (5.20)$$

For  $\mathbf{A}_K$ , the gradient writes

$$\nabla_{\mathbf{A}_K} \mathcal{J}(\mathbf{m}_K, \mathbf{A}_K) = -\mathbf{m}_K^T (\tilde{\mathbf{Y}} - \mathbf{m}_K \mathbf{A}_K) + \eta \mathbf{A}_K \mathbf{S} \mathbf{S}^T$$

with  $\tilde{\mathbf{Y}} = \mathbf{Y} - \tilde{\mathbf{M}}\tilde{\mathbf{A}} - \sum_{i=0}^V \mathbf{Q}_i(\tilde{\mathbf{A}} \circ \mathbf{B}_i)$ . The Lipschitz constant is

$$L_{\mathbf{A}_K} = \|\mathbf{m}_K^T \mathbf{m}_K\| + \eta \|\mathbf{S} \mathbf{S}^T\|.$$

### 5.4.3. Optimization with respect to $\mathbf{B}_i$

The updating rule for the basis function coefficients, under the constraints defined by (5.11), can be written as

$$\mathbf{B}_i^{h+1} = \text{prox}_{\frac{\lambda}{L_{\mathbf{B}_i}^h} \|\cdot\|_1} \left( \mathcal{P}_{\mathcal{B}} \left( \mathbf{B}_i^h - \frac{\gamma}{L_{\mathbf{B}_i}^h} \nabla_{\mathbf{B}_i} \mathcal{J}(\mathbf{M}^{h+1}, \mathbf{A}^{h+1}, \underline{\mathbf{B}}^h, \boldsymbol{\alpha}^h) \right) \right),$$

where the proximal mapping operator is the group soft-thresholding operator defined in (3.21). Also,  $\mathcal{P}_{\mathcal{B}}$  is the projection into the set  $\mathcal{B}$  defined in (5.11). Indeed, the proximal map of the sum of an indicator function and the  $\ell_1$  norm is exactly the composition of the proximal maps of both individual functions, following the same

principle showed in [BST13]. The gradient writes

$$\nabla_{B_i} \mathcal{J}(\tilde{\mathbf{A}}, \mathbf{B}, \mathbf{Q}) = - \left( (\mathbf{Q}_i^T (\tilde{\mathbf{Y}} - \mathbf{Q}_i(\tilde{\mathbf{A}} \circ \mathbf{B}_i))) \circ \tilde{\mathbf{A}} \right) \quad (5.21)$$

with  $\tilde{\mathbf{Y}} = \mathbf{Y} - \mathbf{MA} - \sum_{j \neq i} \mathbf{Q}_j(\tilde{\mathbf{A}} \circ \mathbf{B}_j)$ . Moreover,  $L_{B_i}$  is the Lipschitz constant of  $\nabla_{B_i} \mathcal{J}(\tilde{\mathbf{A}}, \mathbf{B}, \mathbf{Q})$

$$L_{B_i} = \|\mathbf{Q}_i^T \mathbf{Q}_i\| \|\tilde{\mathbf{A}}\|^2. \quad (5.22)$$

#### 5.4.4. Optimization with respect to $\alpha_{ki}$

Finally, the updating rule for the basis function exponential coefficients, under the constraints in (5.10), is

$$\alpha_{ki}^{h+1} = \mathcal{P}_{\mathcal{R}} \left( \alpha_{ki}^h - \frac{\gamma}{L_{\alpha_{ki}}^h} \nabla_{\alpha_{ki}} \mathcal{J}(\mathbf{M}^{h+1}, \mathbf{A}^{h+1}, \mathbf{B}^{h+1}, \boldsymbol{\alpha}^h) \right). \quad (5.23)$$

Also,  $\mathcal{P}_{\mathcal{R}}$  is the projection into the set  $\mathcal{R}$  defined in (5.10). The gradient writes

$$\nabla_{\alpha_{ki}} \mathcal{J}(\alpha_{ki}) = \mathbf{W}_{k,i} (\tilde{\mathbf{Y}}^T (T_p(\mathbf{t}) \circ \mathbf{E}_{ki}) - \frac{1}{2} \mathbf{W}_{k,i}^T \mathbf{m}_k^T ((T_p(\mathbf{t}) \circ \mathbf{E}_{ki})^T \mathbf{E}_{ki} + \mathbf{E}_{ki}^T (T_p(\mathbf{t}) \circ \mathbf{E}_{ki}))) \mathbf{m}_k,$$

with  $\tilde{\mathbf{Y}} = \mathbf{Y} - \mathbf{MA} - \sum_{j \neq i} \mathbf{Q}_j \mathbf{W}_j - \sum_{u \neq k} \mathbf{E}_{ui} \mathbf{m}_u \mathbf{w}_{ui}$ . The Lipschitz constant is

$$L_{\alpha_{ki}} = \|\mathbf{W}_{k,i}\| \left( \left\| -\tilde{\mathbf{Y}}^T + \frac{1}{2} \mathbf{W}_{k,i}^T \mathbf{m}_k^T \mathbf{E}_{ki}^T \right\| + \frac{3}{2} \|\mathbf{W}_{k,i}^T \mathbf{m}_k^T\| \|\mathbf{E}_{ki}\| \right) \|\mathbf{E}_{ki}\| \|T_p(\mathbf{t})\|^2 \|\mathbf{m}_k\|. \quad (5.24)$$

## 5.5. Evaluation on synthetic data

### 5.5.1. Synthetic data generation

To illustrate the accuracy of our algorithm, experiments are conducted on synthetic data for which the ground truth of the main parameters of interest (i.e., factor TACs, factor proportion maps, internal coefficients maps and exponential coefficients) is known. Thus, experimentations are conducted on one  $128 \times 128 \times 64$  synthetic image acquired in  $L = 20$  times of acquisition ranging from 1 to 5 minutes in a total period of 60 minutes. In this image, each voxel is constructed as a combination of  $K = 3$  pure classes representative of the brain, which is the organ of interest in the present work: pure nSB gray matter, pure nSB white matter and pure blood or veins. Moreover, SB tissues are subjected to nonlinearities affecting the pure nSB tissues, although they do not represent new factors. As in Section 3.5.1, the image is generated from the Zubal high resolution dynamic PET numerical phantom with TACs generated from real PET images acquired with the Siemens HRRT and injected with  $^{11}\text{C}$ -PE2I. The overall generation process is presented in Fig. 5.1 and described in what follows:

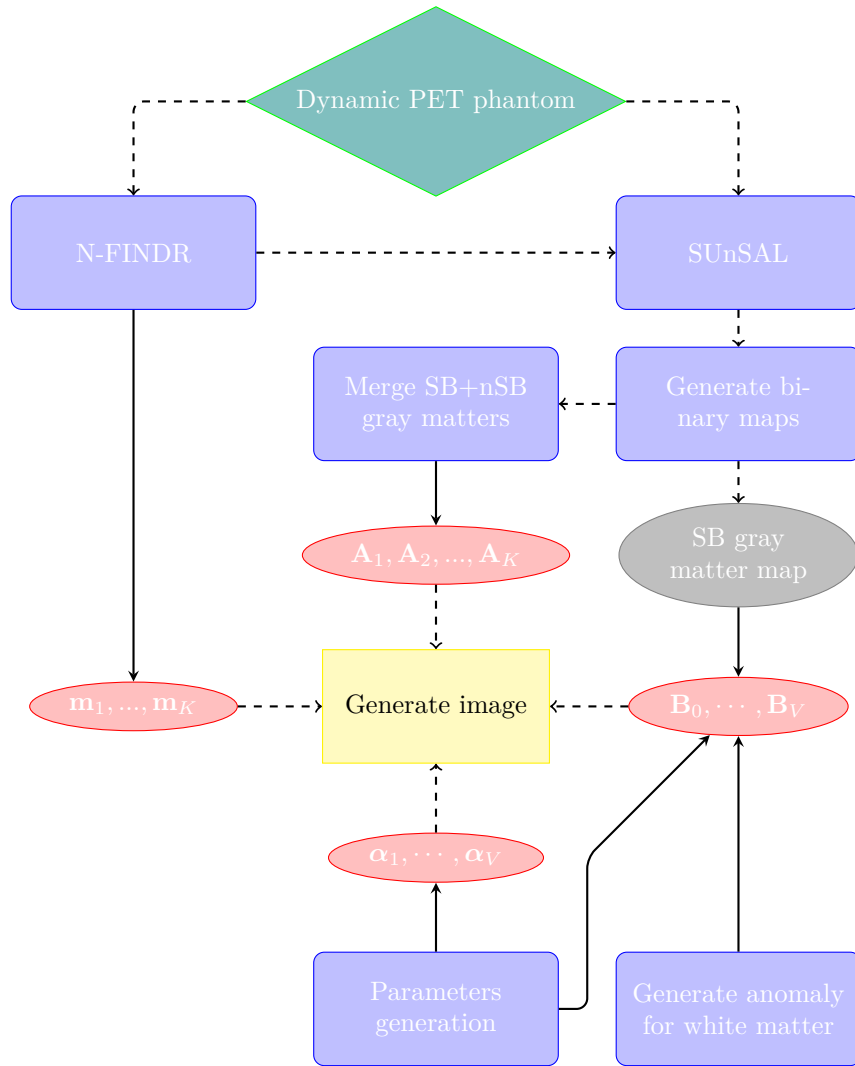


Figure 5.1.: Synthetic image generation scheme. The red ellipses constitute the ground truth data used for quantitative assessment.

- The dynamic PET phantom showed in Fig. 3.6 has been first linearly unmixed using the N-FINDR [Win99] and SUnSAL [BF10] algorithms with an initial number of classes of 4, accounting for SB and nSB gray matter, white matter and blood. The TAC factor for SB gray matter found by N-FINDR is discarded while the other factors are selected to constitute the ground-truth non-specific factor TACs  $\mathbf{m}_1, \dots, \mathbf{m}_K$ . The factor proportions found by SUnSAL are used to generate binary maps after a thresholding. Factors are shown in Fig. 5.2 (right).
- The binary maps of SB and nSB gray matter generated from the SUnSAL output are merged to yield a general gray matter factor proportion. The white matter and blood binary maps are directly used as factor proportions. All factor proportions are shown in Fig. 5.2 (left).

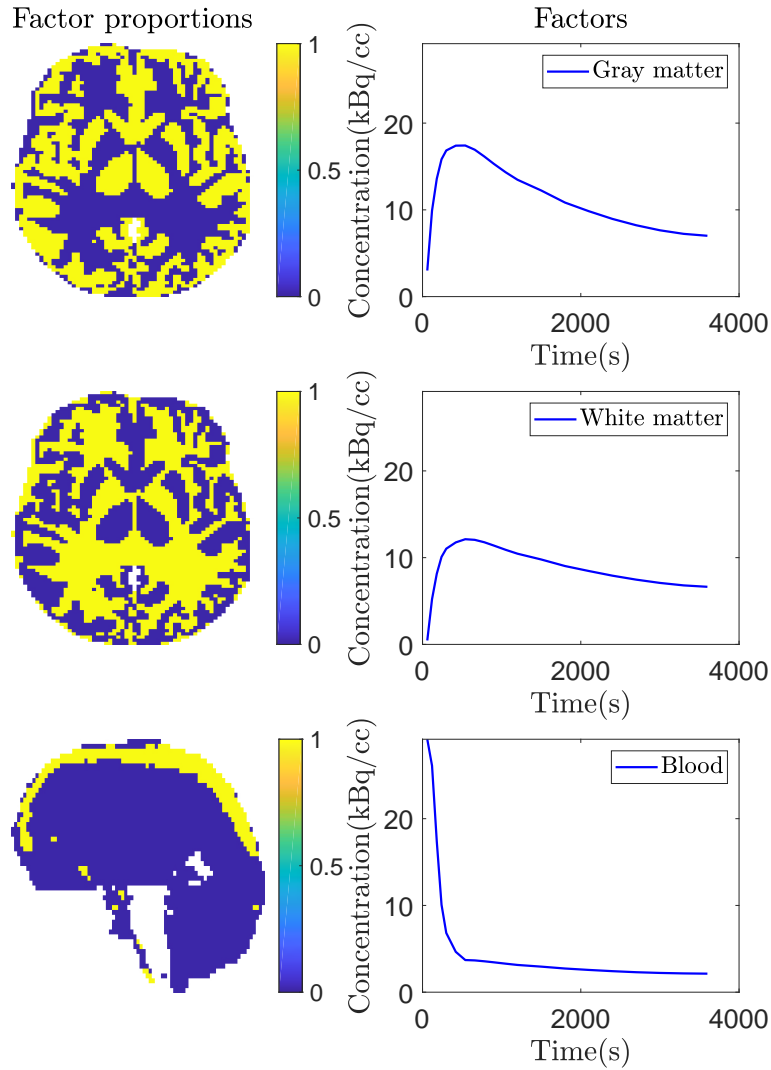


Figure 5.2.: Ground truth of factors (right) and corresponding proportions(left), extracted by SUnSAL/N-findr

- The SB gray matter binary map is used to provide the location of the weight coefficients of nonlinearity in

the gray matter. An anomaly binary map is generated inside the white matter factor proportion to provide the location of SB in white matter. Even though this is not necessarily a clinically relevant localization of the dopamine transporter, this area of SB in white matter is included for experimentation purposes.

- The weights and exponential coefficients describing the nonlinearities are generated from the two-tissue FRTM detailed in Section 1.6.2 and described by Eqs. (1.6) and (1.9). Moreover, two levels of binding are generated for each tissue by altering  $R_1$  and keeping the other parameters constant. For the SB gray matter, we used the following parameters:  $R_1 = [1, 1.7]$ ,  $k_2 = 0.2$ ,  $k_3 = 0.3$  and  $k_4 = 0.1$ . For the SB white matter, we use the following parameters:  $R_1 = [1, 1.6]$ ,  $k_2 = 0.2$ ,  $k_3 = 0.2$  and  $k_4 = 0.1$ . The choice of the two-tissue FRTM is based on a study by Pinborg et al. [Pin+02], that compared the one and two-tissue compartment models for human  $[^{11}C]$ -PE2I injection in SPECT data. The two-tissue compartment model presented a better performance. In the same line, DeLorenzo et al. [DeL+09] investigated the use of one- and two-tissue compartment models in several different ROIs of the brain, in particular the cerebellum. All the studied regions and their subregions fit better with the two-tissue compartment model.
- Parameter generation directly yields the exponential coefficients  $\alpha_1, \dots, \alpha_V$ , while the output of the weights is applied to the binary maps of SB previously defined for the gray and white matters accordingly to produce the final maps. BP maps w.r.t. the free fractions of the radioligand in tissue ( $f_T$ ), i.e.,  $\mathbf{BP} \cdot f_T$  computed with (1.14) are shown in Fig. 5.3 for the gray and white matters. The final TACs generated using these parameters are shown in red along with the elementary TACs in blue in Fig. 5.4.

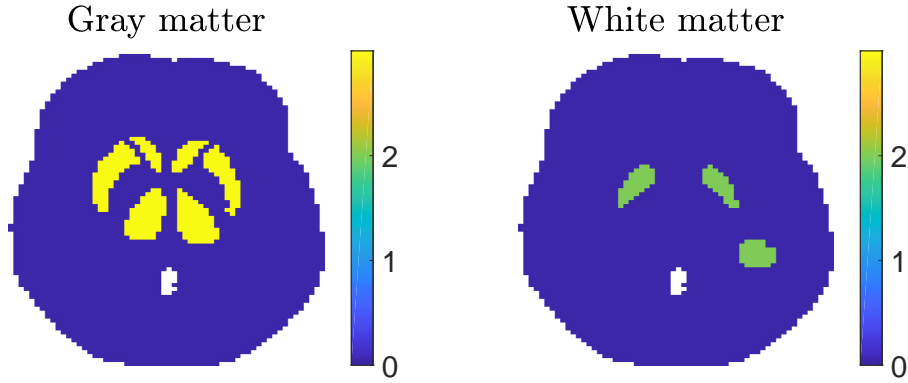


Figure 5.3.: Binding potential maps w.r.t. the free fraction of radioligand per tissue.

As in Chapter 3, after the phantom generation process, a PSF defined as a space-invariant and isotropic Gaussian filter with FWHM= 4.4mm is applied to the output image. Finally, as in [SDG00], the measurements are corrupted by a Gaussian noise whose variance is 25% of the pixel value. The resulting image is shown in Fig. 5.5. For fair comparison, the ground-truth for the factor proportions  $\mathbf{A}$  and the basis function coefficients  $\mathbf{B}$  corresponding to nonlinearities are computed by conducting the proposed algorithm with fixed factors and

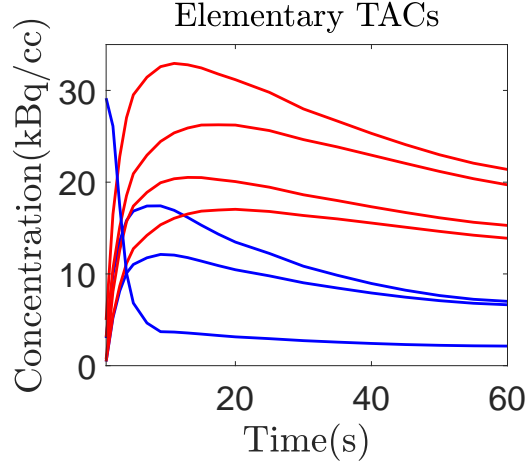
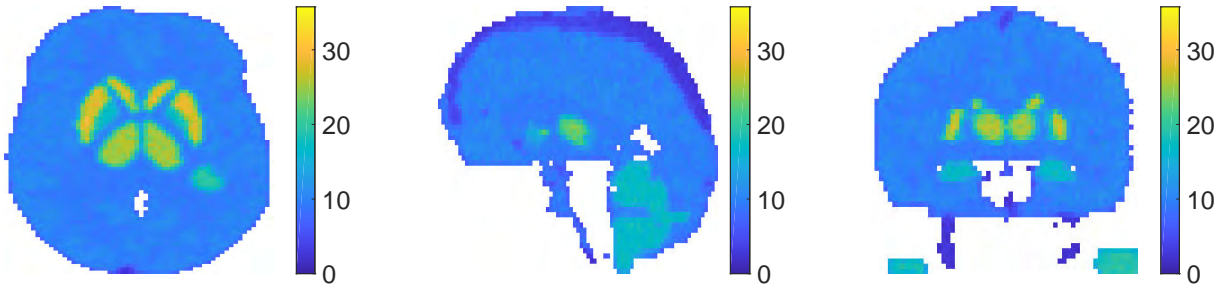


Figure 5.4.: Factors (blue) and TACs generated from the 2-tissue reference model.

	PNMM	SLMM
$\eta$	0.500	0.500
$\beta$	0.100	0.100
$\lambda$	0.500	0.500
$\varepsilon$	0.010	0.001

Table 5.1.: Parameters

exponential coefficients in an image with no noise affected by the PSF. This allows partial volume effect to be taken into account.

Figure 5.5.: 15<sup>th</sup> time frame of 3D-generated image with PSF and a 15dB noise: from left to right, transversal, sagittal and coronal planes.

### 5.5.2. Compared methods

The presented method is compared against the basis pursuit method in [Gun+02], referred to as DEPICT, and the SLMM-unmixing proposed in Chapter 3.

**DEPICT**

This method describes the data as

$$\mathbf{Y} = \mathbf{Q}\mathbf{B} + \mathbf{R}, \quad (5.25)$$

where, in this case,  $\mathbf{Q}$  is a  $L \times P$  matrix containing the  $P$  basis functions to be considered and  $\mathbf{B}$  is a  $P \times N$  matrix containing its corresponding coefficients. Including a sparsity regularization given by the  $\ell_{2,1}$  norm, the optimization problem to be solved is

$$(\mathbf{B}^*) \in \arg \min_{\mathbf{B}} \left\{ \frac{1}{2} \|\mathbf{Y} - \mathbf{Q}\mathbf{B}\|_F^2 + \lambda \|\mathbf{B}\|_{2,1} \right\}. \quad (5.26)$$

In this work, DEPICT is implemented with proximal gradient steps for comparison purposes. As in [Gun+02], the basis pursuit denoising approach is implemented with 30 basis functions logarithmically spaced between 0.03 and  $6 \text{ min}^{-1}$  and an additional basis function to represent the offset. The number of basis functions is fixed to 31 as a trade-off between precision and computation time. For comparison purposes, DEPICT is conducted with two different reference TACs: first the gray, then the white matter factors that are extracted as described in the following.

**SLMM-unmixing**

To appreciate the interest of extracting a physically interpretable quantity, the proposed algorithm is also compared with the previous method presented in Chapter 3. The penalizations chosen for  $\mathbf{M}$  and  $\mathbf{A}$  are the same, as the one for matrix  $\mathbf{B}$  from SLMM and the set of matrices  $\underline{\mathbf{B}}$  from PNMM. Thus, we consider the same regularization parameters (see Table 5.1) to allow fair comparison. The stopping criterion  $\varepsilon$  is set to  $10^{-3}$ . The variability dictionary is learned from a predefined high-uptake region of the image, comprising both SB gray and white matters. Factors and their corresponding proportions are initialized as described in the next paragraph for SLMM. Matrix  $\mathbf{B}$  is initialized with zeros and we allow the method to run 50 iterations with fixed  $\mathbf{M}$  so as to improve the initializations of  $\mathbf{A}$  and  $\mathbf{B}$ , while preventing factors from merging.

**PNMM-unmixing (proposed approach)**

Factor proportions for our method are initialized with the binary maps coming from the generation process. In a real image, this is equivalent to using an MRI segmentation to produce the maps of tissues. Regarding the initialization of the factors, the TACs from each tissue are organized from the lower area-under the curve (AUC) TAC to the higher. The first 10% AUC TACs are discarded and we average the TACs whose AUC are the 10% to 20% lowest ones. Then, the basis functions and their corresponding coefficients are computed with an instance of our algorithm, where factors and proportion maps are not updated. As in [Gun+02], the



exponential coefficients for our method will be limited with  $\alpha_{\min} = d_c$ , where  $d_c$  is the decay constant for  $[^{11}C]$  and  $d_c = 0.034 \text{ min}^{-1}$  and  $\alpha_{\max} = 6 \text{ min}^{-1}$ . Limits are also imposed for the nonlinearity coefficients. We know that  $b_{0n} = R_{1n} - 1$  cannot be nonnegative in SB tissues when nSB tissue are used as a reference. Moreover, the maximum value of  $R_{1n}$  is generally not greater than 1.7. Thus, we choose  $b_{0\min} = 0$  and  $b_{0\max} = 0.7$ . The limits for the nonlinearity coefficients can be chosen by analyzing the relations of the known kinetic parameters of the tracer under study and the weights defined by Eq. (1.9). In our study, we found to be sufficient to choose  $b_{1\min} = -0.2$ ,  $b_{1\max} = 0$ ,  $b_{2\min} = 0$  and  $b_{2\max} = 0.15$ . Table 5.1 presents the regularization parameters used.

As in Chapter 3, the performance of the method is measured by the NMSE defined by (3.24).

### 5.5.3. Results and discussion

Fig. 5.6 shows, from top to bottom: the ground-truth factor proportion, the initial segmentation and the final SLMM and PNMM results. The first column shows the gray matter, the second column shows the white matter and the third column presents the blood factor proportion. We can clearly see that both SLMM and PNMM techniques are able to include the partial volume effect into the factor proportions, as expected. Note that the SB gray and white matters have disappeared from the corresponding SLMM factor proportion, since the algorithm deals with nSB and SB as different tissues. Moreover, in Fig. 5.7 showing the corresponding factors, visual comparison suggests that PNMM improves the initial factor estimation with final global TACs that are very near the ground-truth. The SLMM result is a bit far from the ground-truth, since this simulation corresponds to a situation that is distinct from the initial assumptions of SLMM. These results are further confirmed by the quantitative evaluation of Table 5.2 that shows the NMSE of the variables of interest as chosen during the initialization and after conducting SLMM and PNMM unmixing. The SLMM result for  $\mathbf{A}$  is not entirely negative, as it is a characteristic of the algorithm to identify the SB regions with an exclusive factor. The PNMM results for both  $\mathbf{A}$  and  $\mathbf{M}$  are remarkably improved. This seems to be an interesting outcome, since it suggests that PNMM is able to improve the results with this initialization setting that can be easily replicated in real image applications.

Fig. 5.8 shows the binding potential w.r.t. the free fractions in tissue  $\mathbf{BP}.f_T$  for the gray matter (left) and white matter (right). The first two rows present the ground-truth and initial  $\mathbf{BP}.f_T$  and the last row presents the PNMM estimation of  $\mathbf{BP}.f_T$  in the PNMM formulation, where there are two  $\mathbf{BP}.f_T$  to be estimated in the same setting: one for the gray matter ( $\mathbf{BP}.f_G$ ) and one for the white matter ( $\mathbf{BP}.f_W$ ). It is hard to determine by visual comparison whether the binding potential is improved from initialization by the PNMM-unmixing. Table 5.2 presents the quantitative results of the NMSE for the matrix  $\mathbf{R}_1$  that corresponds to the value of  $\mathbf{R}_{1n} = 1 + \mathbf{b}_{0n}$  for each voxel, where  $\mathbf{b}_{0n}$  includes the coefficient for both non-specific tissues, and the NMSE for the matrix  $\mathbf{BP}.f_T$  with the binding potential in each voxel for each tissue. Quantitative results suggest that  $\mathbf{BP}.f_T$  is better estimated by conducting the whole PNMM-unmixing, which would be natural since the

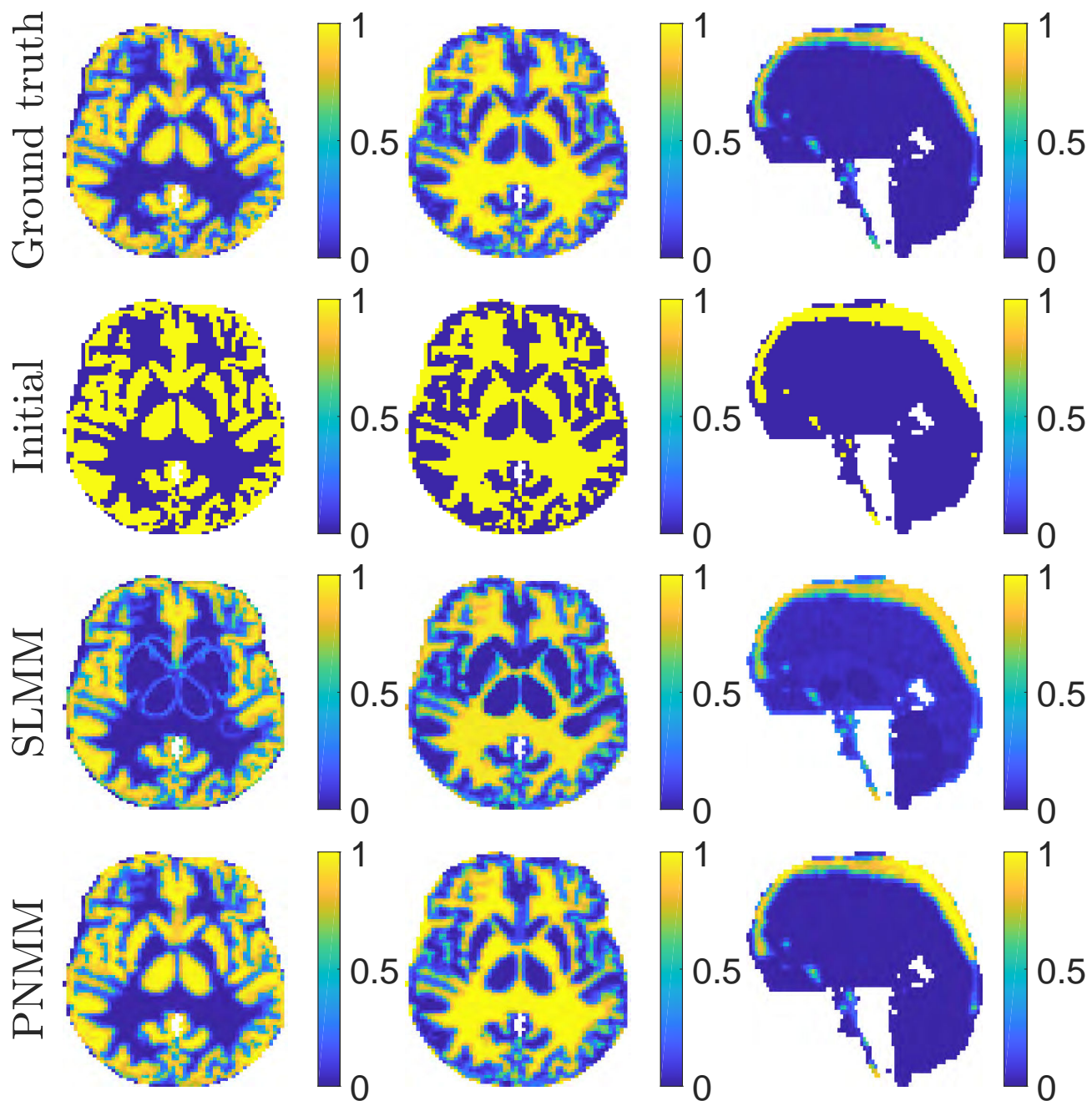


Figure 5.6.: Factor proportion maps obtained from the synthetic image corresponding to the gray matter, white matter and blood, from left to right. The first 2 columns show a transaxial view while the last one shows a sagittal view. All images are in the same scale  $[0, 1]$ .

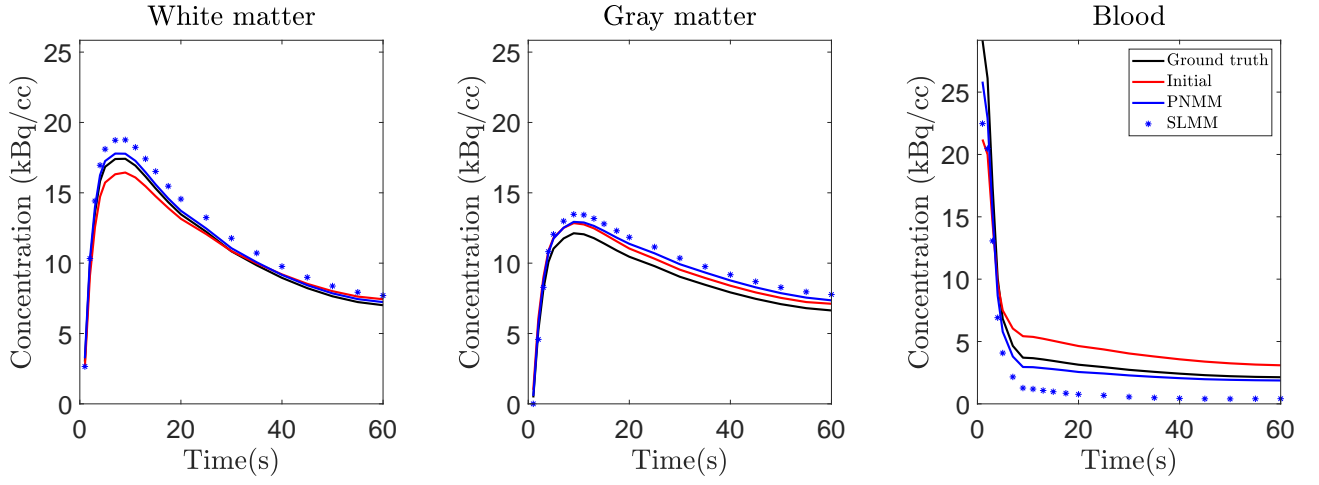
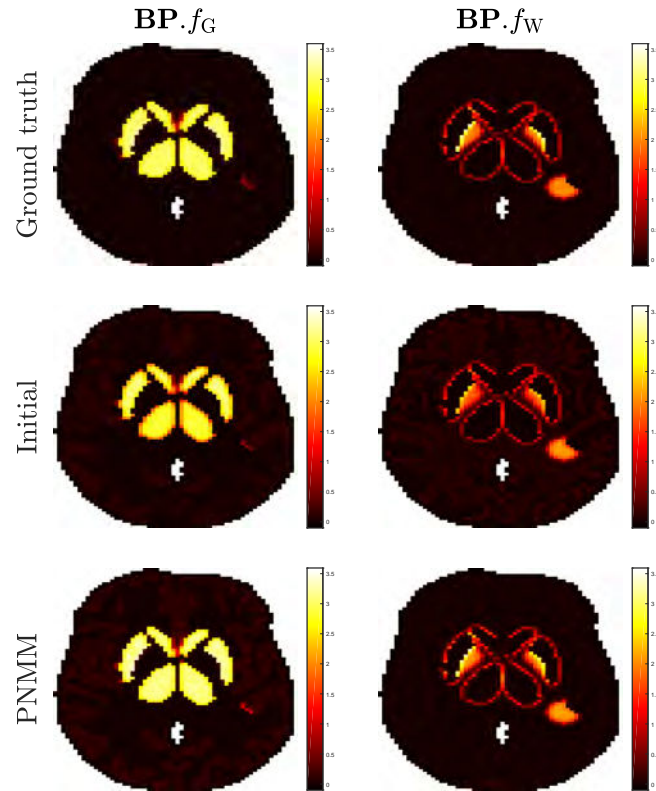


Figure 5.7.: Factor TACs estimated from the synthetic image

Figure 5.8.: From top to bottom: ground-truth, initial and PNMM estimations of  $BP.f_T$ . The first column corresponds to the gray matter and the second to the white matter. Note that for DEPICT  $BP.f_T$  was estimated for the whole image using the respective tissue TAC as reference.

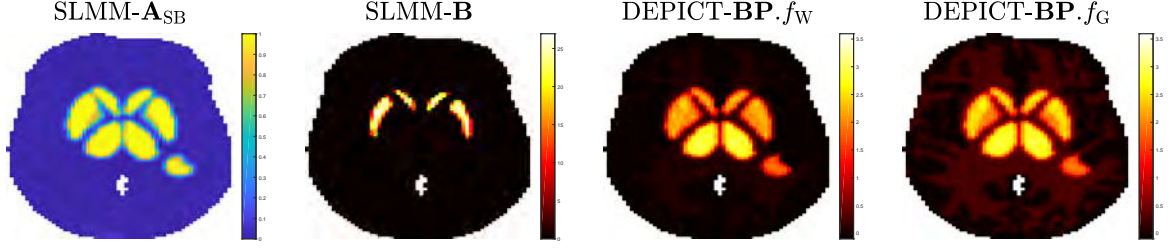


Figure 5.9.: From left to right: SLMM factor proportion related to the SBF, SLMM variability result and DEPICT  $BP.f_T$  estimation using the white and gray matters as reference TACs, respectively.

	Initial	PNMM	SLMM
<b>A</b>	0.279	0.049	0.339
<b>M</b>	0.147	0.082	0.181
<b>R<sub>1</sub></b>	0.946	0.303	-
<b>BP.f<sub>T</sub></b>	0.182	0.123	-

Table 5.2.: NMSE of **A**, **M** and **BP** as chosen in initialization and after conducting PNMM-unmixing

estimations of the factors and factor proportions are also improved. Moreover, the ratio of delivery of the tracer **R<sub>1</sub>** seems to show a much greater improvement.

Fig. 5.9 reports, from left to right, the SLMM results for the factor proportion and the internal variability and the DEPICT results taking the white matter as reference TAC (3<sup>rd</sup> column) and the gray matter as reference TAC (4<sup>th</sup> column). SLMM results are not equivalent to the binding potential or any other physical quantity of clinical use. Still, it is possible to see that SB tissues have been identified and the missing regions from gray and white matter factor proportions of Fig. 5.6 are relocated in the SB factor proportion. The evaluation of **R<sub>1</sub>** and **BP.f<sub>T</sub>** is not done for the DEPICT result, since the ground-truths are not equivalent. Visual inspection suggests that DEPICT is able to correctly locate the specific binding tissues with similar intensities of **BP.f<sub>T</sub>**. The gray matter result presents some binding in the white matter tissue, showing the potential bias that could be expected when the whole image is represented by one reference TAC, while considering distinct reference TACs in distinct non-specific binding tissues is more accurate. Even though the overall result may often be sufficient for clinical applications, given the challenge of interpreting dynamic PET images, they seem to be less accurate than the method herein proposed, in terms of both BP intensities and location. Moreover, DEPICT does not allow the user to differentiate the tissue that is affected, for instance, by an abnormality, while our method may provide this detailed information.

Note that if the factor proportions are initialized with an MRI segmentation and fixed, PNMM works as a “local reference model (LRM)”, where each non-specific tissue of the image is treated as a different region-of-interest (ROI) and is therefore allowed to have its own reference TAC. This is equivalent of conducting DEPICT in each segmented tissue, but allowing the global reference TAC to be improved in each step. This setting is also able to provide the tissues affected by specific binding but does not take into account the partial volume

effect.

## 5.6. Evaluation on real data

### 5.6.1. PET data settings

The different methods have been applied to one dynamic PET image acquired with an Ingenuity TOF Camera from Philips Medical Systems of a stroke subject injected with  $[^{18}\text{F}]\text{DPA-714}$ , seven days after the stroke. The image is the same as for Chapter 4. Recall that the PET acquisitions were reconstructed into a  $128 \times 128 \times 90$ -volume with  $L = 31$  time frames. The PET scan images acquisition times ranged from 10 seconds to 5 minutes over a 59 minutes period. The voxel size was of  $2 \times 2 \times 2 \text{ mm}^3$ .

Factor proportions are initialized with binary maps mainly constituted from a manually labelled MRI segmentation and improved with a K-means result for the voxels that were not labelled in the MRI segmentation. Factors are initialized as in the synthetic case.

The stroke region is segmented on this registered MRI image. It is used to define a set of voxels used to learn the variability descriptors  $\mathbf{V}$  by PCA with  $N_v = 1$  for SLMM-unmixing. The nominal SBF for SLMM is fixed as the empirical average of the corresponding TACs with AUC comprised between the 10<sup>th</sup> and 20<sup>th</sup> percentile. Matrix  $\mathbf{B}$  is initialized with zeros and, as before, we allow the method to run 50 iterations with fixed  $\mathbf{M}$ .

For PNMM, the basis functions and their corresponding coefficients are initialized as in the synthetic case, with an instance of our algorithm, where factors and proportion maps are not updated. The exponential coefficients are limited with  $\alpha_{\min} = 0.0063 \text{ min}^{-1}$  and  $\alpha_{\max} = 6 \text{ min}^{-1}$ . The nonlinearity coefficients are limited with  $b_{i_{\min}} = -1$  and  $b_{i_{\max}} = 1 \forall i$ .

### 5.6.2. Results and discussion

Fig. 5.10 presents, from top to bottom, the initial binary factor proportion map and the maps estimated by SLMM and PNMM. As before, both algorithms consider partial volume in their estimation. Fig. 5.11 shows the initial and estimated factor TACs. The initial gray and white matter factor TACs are very similar. The blood factors estimated by both SLMM and PNMM are very close, showing a high pick at the beginning and reducing its intensities in the other acquisition times. SLMM estimates gray and white matter TACs that are lower than initialization. This may be because the SBF, that is fixed, is very near the gray matter factor TAC, inducing the gray matter factor to be smaller. On the other hand, PNMM seems to be able to differentiate the gray and white matter factor TACs in both intensity and shape, showing a promising result.

Fig. 5.12 shows a 3D visualization of the results corresponding to the gray matter. From top to bottom, the stroke segmented with an MRI, the initial gray matter factor proportion  $\mathbf{A}_G$ , the PNMM gray matter factor



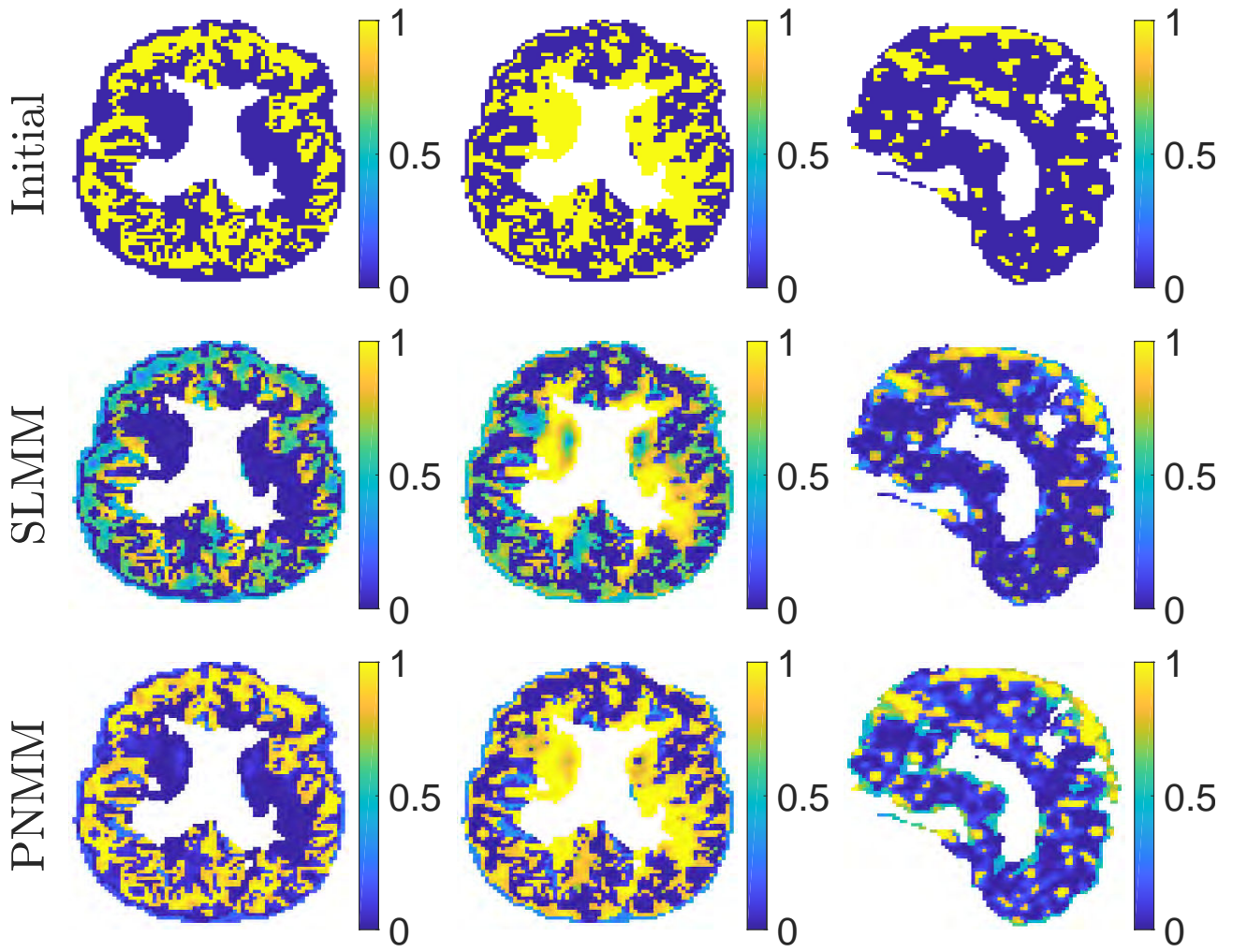


Figure 5.10.: Factor proportion maps obtained from the real image corresponding to the gray matter, white matter and blood, from left to right. The first 2 columns show a transaxial view while the last one shows a sagittal view. All images are in the same scale  $[0, 1]$ .

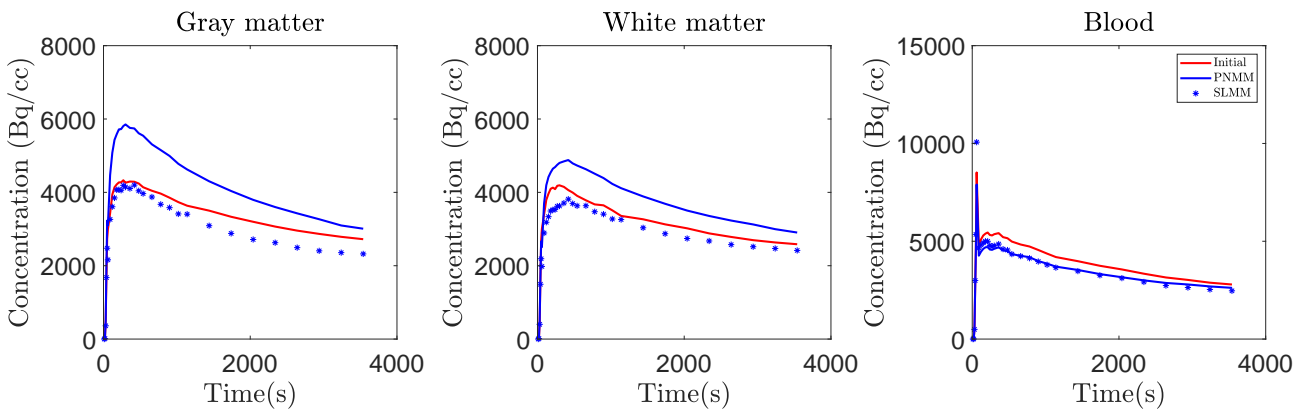


Figure 5.11.: Factor TACs estimated from the real image

proportion  $\mathbf{A}_G$ , the DEPICT  $\mathbf{BP}.f_G$  result using the initial gray matter TAC as reference and the PNMM  $\mathbf{BP}.f_G$  result corresponding to the gray matter. The factor proportions are presented together with this result, so the reader can see the difference between the DEPICT result and the PNMM result. While DEPICT provides the binding potential for the entire image, the PNMM result shows the SB gray matter voxels. This is a very particular outcome, that was previously shown to work in the synthetic case and that seems to be also useful in the real case, showing the potential interest of the method. Moreover, DEPICT presents other brain regions not expected to be affected by SB with a relevant binding potential, while PNMM is more visually accurate. Fig. 5.13 shows the corresponding results for the white matter, complementary of the results in Fig. 5.12 (except for DEPICT). From top to bottom, the stroke segmented with an MRI, the initial white matter factor proportion  $\mathbf{A}_W$ , the PNMM white matter factor proportion  $\mathbf{A}_W$ , the DEPICT  $\mathbf{BP}.f_W$  result using the initial white matter TAC as reference and the PNMM  $\mathbf{BP}.f_W$  result corresponding to the white matter. We can see that the SB regions missing in the PNMM binding potential for the gray matter can be found in this complementary result for the white matter. It is also interesting to note that the DEPICT result using the white matter TAC presents stronger intensities, which is natural since this TAC has lower AUC. These DEPICT results also reinforces our theory that using the same TAC of reference for the whole image may potentially bias the result. Finally, Fig. 5.14 shows the SLMM  $\mathbf{A}_{SB}$  factor proportion and internal variability  $\mathbf{B}$  results in this setting. While the  $\mathbf{A}_{SB}$  result presents a lot of nSB gray matter, it highlights a large area affected by SB, which is a relevant outcome. The variability  $\mathbf{B}$ , that has no physically meaningful unit, shows a small area of SB, which is complementary to the information brought with the corresponding factor proportion. Although the result is informative, it is not complete in terms of clinical assessment, in opposition to the other two methods studied.

## 5.7. Conclusion

This chapter presented a prospective work that combines nonlinear unmixing and parametric imaging to yield a clinically interpretable result for factor analysis. To this end, this work was based on reference tissue input models with reversible kinetics to produce a physically meaningful nonlinearity affecting the TACs of non-specific binding tissues. Moreover, it considered an aspect generally neglected in parametric imaging methods: the mixed kinetics that can be present in each voxel due to partial volume, PSF and biological heterogeneity. The resulting method looks promising, since it manages to recover the binding potential related to the different responses of the tissues to tracer kinetics on simulations. It also provides the tissue affected by abnormalities. The potential interest of this novel technique was evaluated on synthetic and real data. A deeper evaluation of the method with real images for which arterial sampling is available remains to be studied.

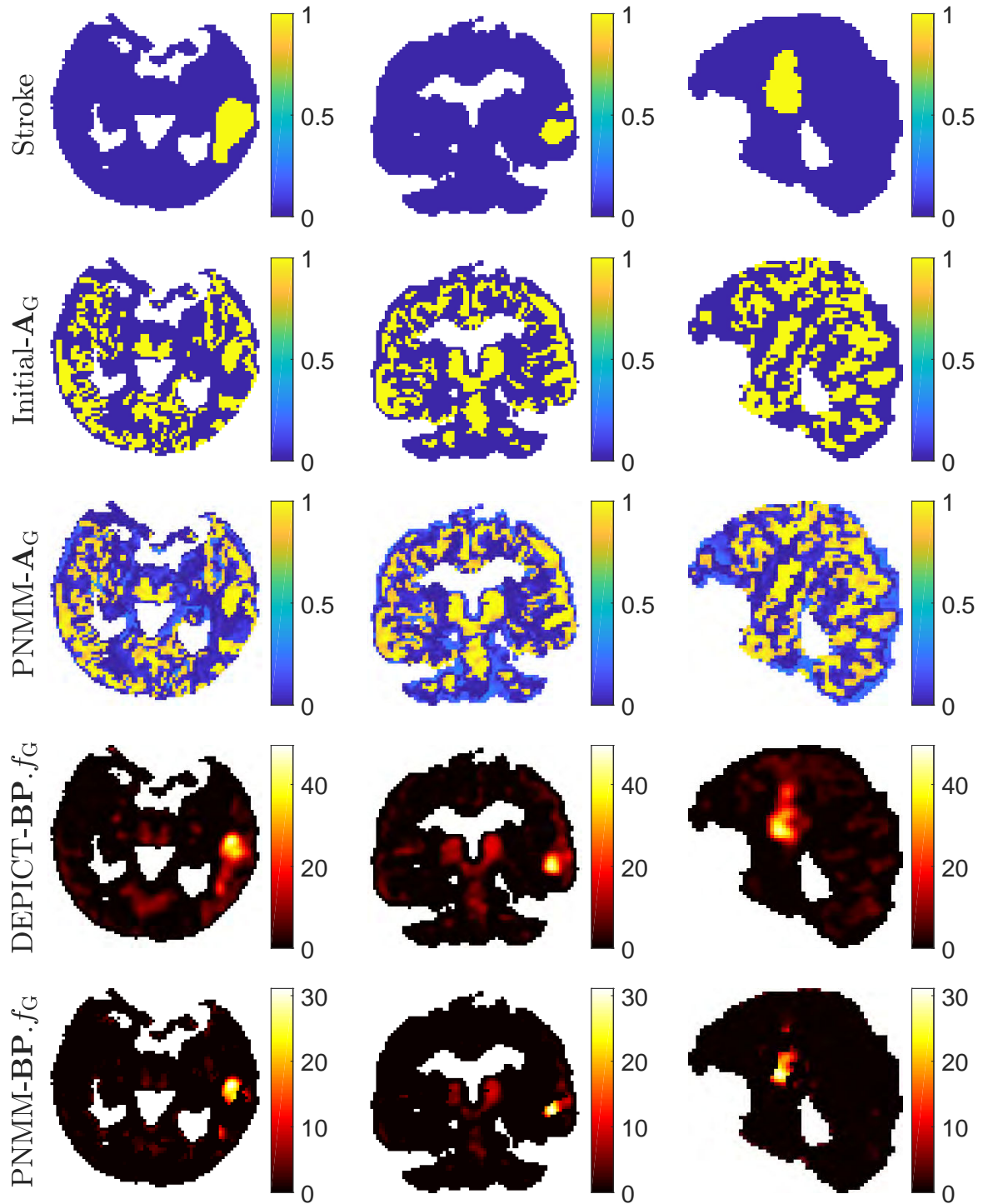


Figure 5.12.: From top to bottom: stroke region, initial gray matter factor proportion, gray matter factor proportion estimated by PNMM, DEPICT  $\mathbf{BP}.f_T$  using the gray matter TAC as reference and PNMM  $\mathbf{BP}.f_T$  for the gray matter.



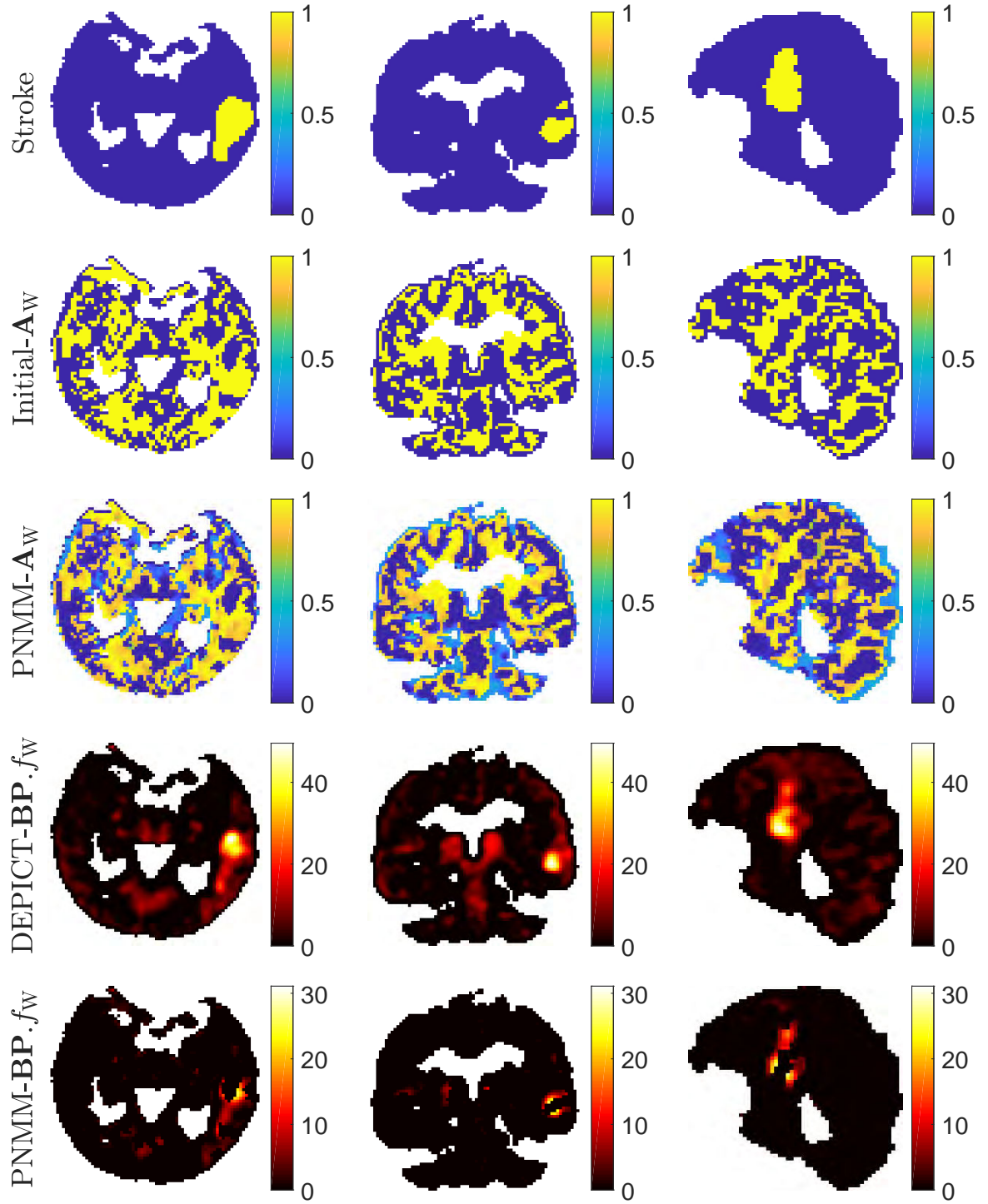


Figure 5.13.: From top to bottom: stroke region, initial white matter factor proportion, white matter factor proportion estimated by PNMM, DEPICT  $\mathbf{BP}.f_T$  using the white matter TAC as reference and PNMM  $\mathbf{BP}.f_T$  for the white matter.

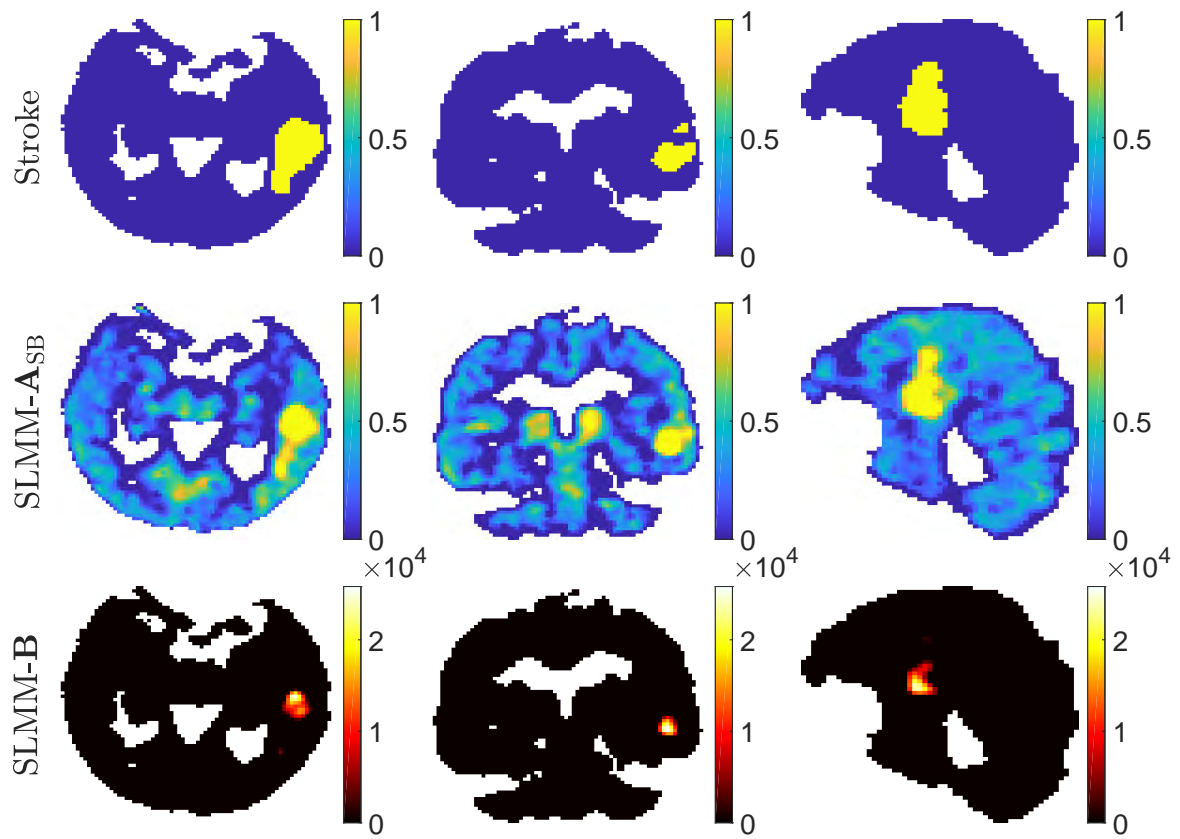


Figure 5.14.: From top to bottom: stroke region, SB factor proportion estimated by SLMM and interval variability estimated by SLMM.

# List of publications

## Submitted

- [Cav+18a] Y. C. Cavalcanti et al. “Factor analysis of dynamic PET images: beyond Gaussian noise”. Submitted. 2018 (cit. on p. 97).
- [Cav+18c] Y. C. Cavalcanti et al. “Unmixing dynamic PET images: combining spatial heterogeneity and non-Gaussian noise”. Submitted. 2018.

## International journals

- [Cav+18b] Y. C. Cavalcanti et al. “Unmixing dynamic PET images with variable specific binding kinetics”. In: *Med Imag. Anal.* 49 (2018), pp. 117–127. ISSN: 1361-8415. DOI: <https://doi.org/10.1016/j.media.2018.07.011>. URL: <http://www.sciencedirect.com/science/article/pii/S1361841518305541> (cit. on p. 59).

## International conferences

- [Cav+17b] Y. C. Cavalcanti et al. “Unmixing dynamic PET images with a PALM algorithm”. In: *Proc. European Signal Process. Conf. (EUSIPCO)*. Kos, Greece, Aug. 2017, pp. 425–429 (cit. on p. 59).

## National conferences

- [Cav+17a] Y. C. Cavalcanti et al. “Démélange d’images TEP dynamiques”. In: *Actes du XXVIème Colloque GRETSI sur le Traitement du Signal et des Images (GRETSI 2017)*. Juan-les-Pins, France, Sept. 2017, pp. 425–429 (cit. on p. 59).

## Technical report

- [Cav+17c] Y. C. Cavalcanti et al. *Unmixing dynamic PET images with variable specific binding kinetics – Supporting materials*. Tech. rep. France: University of Toulouse, IRIT/INP-ENSEEIH, July 2017.  
URL: [http://dobigeon.perso.enseeiht.fr/papers/Cavalcanti\\_TechReport\\_2017.pdf](http://dobigeon.perso.enseeiht.fr/papers/Cavalcanti_TechReport_2017.pdf).

# Conclusions and perspectives

## Context

Factor analysis is an efficient unsupervised learning technique to extract physically meaningful global patterns from multivariate data. In dynamic positron emission tomography, it has shown its value as a non-invasive tool to identify reference tissue global TACs and arterial plasma or blood input functions, that are generally required by quantification techniques based on kinetic parameter estimation. Conventional factor analysis techniques generally assume spatial homogeneity on the distribution of radiotracer concentration in each factor. However, variations on perfusion or labelled molecule concentration in high-uptake regions may alter the TAC pattern in each voxel. Moreover, general factor analysis techniques assume the noise distribution of data to follow a standard probability density function, such as Gaussian or Poisson. Even though the count-rates that constitute the elementary PET data present a Poissonian nature, the noise in the final signal is hard to characterize, due to the several effects that corrupt the initial signal in acquisition and reconstruction.

To address these issues, the present manuscript first investigated a new explicit mixture model to handle spatial specific binding variability on the corresponding factor TAC. Based on this model, a second approach generalized the optimization problem to deal with the undetermined nature of the PET image noise. Finally, a nonlinear unmixing model was also proposed to explicitly relate specific and non-specific binding tissues. The study conducted in this manuscript allowed the following conclusions to be drawn.

## Conclusions

**Part I** introduced the global context of this manuscript, which capitalizes on the hyperspectral unmixing literature to develop solutions for factor analysis in dynamic PET applications.

- **Chapter 1** discussed the properties that led PET imaging to become an ubiquitous tool for the diagnosis and treatment evaluation of several diseases. It also reviewed the main effects that deteriorate the quality of the final data, making PET image analysis a challenging task. This chapter then addressed the challenges of quantification that justify the need for a non-invasive estimation of global TACs, naturally leading to factor analysis solutions.

- **Chapter 2** summarized the key concepts of blind source separation applied to multi-band imaging. After briefly discussing the state-of-the-art non-parametric methods generally used in clinical research to conduct a non-invasive extraction of reference tissue TACs or blood input function, it introduced factor analysis as an unsupervised learning alternative. General solutions historically applied to handle the BSS problem were then discussed. In particular, a literature review on factor analysis in dynamic PET was presented. To provide the fundamental basis of the manuscript, this chapter also detailed hyperspectral unmixing with its nonlinear and spectral-variability instances.

**Part II** described our contributions to factor analysis techniques adapted to PET imaging, as detailed in the following.

- **Chapter 3** introduced an unmixing approach that explicitly models the spatial variability in high-uptake tissues, referred to as specific binding linear mixing model (SLMM). The variability was described by a dictionary of eigenvectors that have been previously learned with PCA and its corresponding map of coefficients. Due to the high number of variables to be estimated, we resorted to an algorithm that has proven convergence to a local optimum when the optimization problem is non-convex, namely proximal alternating linearized minimization (PALM). The results obtained on real data have notably exemplified the relevance of the proposed model to handle images presenting an abnormality. In practice, the proposed approach provided physically interpretable results on the estimation of non-specific binding tissues and an accurate estimation of specific binding ones. In particular, the high level of detail captured by the variability spatial map may improve diagnosis, since it may potentially describe different levels of abnormalities in the tissues. Moreover, as an unsupervised learning technique, the method has shown to be very flexible. To be transposed to another setting, it only required a previous knowledge on the number of expected kinetic classes in a ROI, an initial guess of the factors and proportions and TACs containing specific binding kinetics to conduct a dictionary learning for the variability.
- **Chapter 4** investigated the use of the  $\beta$ -divergence in PET imaging factor analysis. To this end, three algorithms were studied:  $\beta$ -NMF,  $\beta$ -LMM and  $\beta$ -SLMM. An algorithm based on multiplicative updates was derived for the SLMM model. Exhaustive simulations were conducted on two different phantoms using an analytical approach to generate the final synthetic image with realistic count-rates properties. The first phantom was used to evaluate the denoising potential of each value of  $\beta$  for images with different iterations and various levels of postfiltering. No variability was considered in this first framework. Results showed that changing the value of  $\beta$  can indeed alter the quality of the estimation and an optimal value can be found for different numbers of iterations. When a lot of postfiltering was applied, even though slight improvements can be made by tuning the value of  $\beta$ , it was less relevant. Raw data was then shown to benefit from the use of the  $\beta$ -divergence. The second phantom was used to evaluate the estimation

of variables in the framework where variability is taken into account, further validating the results found in the previous setting. Moreover, real data results were also evaluated on an image that was subjected to postfiltering. Visual inspection showed some differences between the results for different values of  $\beta$ , highlighting the relevance of considering the  $\beta$ -divergence for PET applications.

- **Chapter 5** illustrated the interest of combining factor analysis and parametric imaging in dynamic PET. In brain imaging, even though gray and white matter factor TACs are very correlated, they are not exactly the same. This is also true for different tissues and organs in other ROI of the body. Our method allowed high-uptake voxels located in different non-specific binding tissues to be described by different reference TACs. Moreover, it took into account the partial volume effect in neighboring classes that is neglected in most applications. Even though the final problem is extremely non-convex, results showed that the proposed method is able to improve the initial guess based on a previous segmentation and directly provides the binding potential w.r.t. the free fractions in tissue.

## Perspectives and future work

The present study has raised several research perspectives summarized in the following lines.

### Model developments

The SLMM considered in Chapter 3 provides a measure of specific binding through the variability spatial map. However, these internal coefficients are not directly associated to a physically interpretable quantities, as the volume of distribution or the binding potential. Chapter 5 presents a formulation that yields the measure of binding potential w.r.t. the free fractions in the tissue, which is inherent to reference tissue input models with reversible target tissue kinetics. Other models could be studied to generalize the method for other parametric imaging settings. As such, the design of physically inspired models can be further investigated to provide more informative results in the sense of clinical analysis.

Moreover, none of the models proposed in this manuscript consider the temporally varying statistical uncertainty of the measures. This deficiency could be corrected with a previous whitening step (see Appendix A.2), as discussed in Chapter 3, or by directly adding the inverse of the covariance matrix to the model, herein called  $\mathbf{W}$ , as in [Gun+02]. For the SLMM with no convolution operator, it yields

$$\mathbf{W}^{\frac{1}{2}} \mathbf{Y} \approx \mathbf{W}^{\frac{1}{2}} \mathbf{M} \mathbf{A} + \mathbf{W}^{\frac{1}{2}} \left[ \mathbf{E}_1 \mathbf{A} \circ \mathbf{V} \mathbf{B} \right].$$

With the same approach, the nonlinear model in Chapter 5 would become

$$\mathbf{W}^{\frac{1}{2}}\mathbf{Y} \approx \mathbf{W}^{\frac{1}{2}}\mathbf{M}\mathbf{A} + \mathbf{W}^{\frac{1}{2}}\sum_{i=0}^V \mathbf{Q}_i(\tilde{\mathbf{A}} \circ \mathbf{B}_i).$$

The PSF in Chapter 3 is approximated as a spatially invariant isotropic Gaussian filter, while the spatial resolution is non-stationary in the FOV [MAI12]. Even though we obtained good results for real data with this rough approximation, improvements can be made with a pre-estimation of the PSF [Ash+17; Ira+16] or even a joint estimation of the PSF within the model.

Furthermore, Chapters 4 and 5 do not include the convolutional operator introduced in Chapter 3 within the model because it would significantly increase the computational complexity of the resulting algorithms. In Chapter 4, the convolutional operator was also neglected because it complicated the computation of the update steps. However, this induces ambiguity between the results of the internal coefficients related to the variability or nonlinearity and the corresponding factor proportion. Considering the convolution operator into the formulation of Chapter 5 would yield

$$\mathbf{Y} \approx \mathbf{M}\mathbf{A}\mathbf{H} + \sum_{i=0}^V \mathbf{Q}_i(\tilde{\mathbf{A}} \circ \mathbf{B}_i)\mathbf{H}. \quad (5.27)$$

This issue can be further investigated in future developments with alternative algorithms or tools to include this deconvolution step, while maintaining a reasonable computational complexity.

## Computational aspects

**Hyperparameter selection.** The factor analysis problems formulated in Chapters 3 and 5 depend on several hyperparameters that have been empirically adjusted by testing several values on a predefined grid. In future works, the use of automatic estimation strategies within the algorithms developed in this manuscript could be envisaged. An alternative would be to apply approaches based on the Stein’s unbiased risk estimate [Ste81; Del+14]. The methods developed in [PBF15] could also be considered. They assign appropriate priors to the hyperparameters (which are generally gamma) and then estimate them along with the other parameters of interest. The final optimization problem is then minimized by an alternating optimization algorithm, such as block coordinate descent [Wri15]. Alternatively, a two-step strategy could be adopted, as in [Fre+17].

**Computational improvements.** To increase the computational speed of the methods, an accelerated PALM approach can be envisaged [LL15]. To this end, adaptive steps inspired by the method devised by Nesterov [Nes83] could be implemented, as done in [BT09b; BT09a]. Another approach to allow a more efficient estimation of the variance in terms of convergence speed would rely on variable metrics [CPR14; CPR16]. Moreover, the



most expensive step in terms of processing time is the convolution of Chapter 3 and it is particularly penalizing since it is done several times. This is why this step was discarded for the subsequent studies. A way to try to alleviate this issue would be to propose an efficient approach to compute these convolutions.

## Application-oriented developments

The  $\beta$ -divergence was applied in Chapter 4 into a factor analysis setting. Results showed that the quality of estimation can indeed be improved by tuning  $\beta$ . Several configuration parameters on reconstruction may alter the nature of the final noise, in particular the number of reconstruction iterations. This aspect should be further investigated by evaluating images with several different values of reconstruction iterations in order to find a general rule for tuning  $\beta$ . Distinct reconstruction algorithms will also produce dissimilar results and thus the study would have to be done for each setting. Moreover, this study opens the discussion on the application of the  $\beta$ -divergence in any optimization problems related to PET imaging. This means that an interesting perspective would be to apply this measure for different steps of the PET imaging pipeline. A potential direct application would be the derivation of a generic reconstruction algorithm.

Another aspect that could be investigated is the direct application of the methods developed in this manuscript into the sinogram domain. The idea would be to combine analysis along with reconstruction in the same problem formulation. This could be especially interesting since the nature of the noise in the count-rates is easier to recognize. On the other hand, the identification of tissues or high-uptake voxels for initialization would be a much more challenging task.

Moreover, future works should evaluate the impact of the method on clinical applications, in particular by conducting quantification with the use of non-anatomical reference curves to assess the performance of the method in comparison with standard techniques such as SVCA. Comparison of the performance of the proposed developments with state-of-the-art methods using similar priors should also be considered, as well as evaluation of the robustness and relevance of the proposed approaches on patient scans with a well-defined quantification output for which arterial sampling is available. The quality of segmentation based on the resulting spatial maps and the correction of partial volume effect also remains to be evaluated. In particular, the PNMM proposed in Chapter 5 should be validated with additional experiments on real images.



## Appendix to chapter 3

### A.1. Solutions to the optimization sub-problems

#### A.1.1. Resolution with respect to $\mathbf{A}$

Using the basic definition of a differentiable function

$$\left\langle \nabla_a f(A), h \right\rangle = f(A + U) - f(A) - o(\|U\|)$$

for

$$\mathcal{J}(\mathbf{A}) = \frac{1}{2} \|\mathbf{Y} - \mathbf{MAH} - (\mathbf{E}_1 \mathbf{A} \circ \mathbf{VB})\mathbf{H}\|_F^2$$

it yields

$$\begin{aligned} f(\mathbf{A} + \mathbf{U}) &= \underbrace{\frac{1}{2} \|\mathbf{Y} - \mathbf{MAH} - (\mathbf{E}_1 \mathbf{A} \circ \mathbf{VB})\mathbf{H}\|_F^2}_{\mathcal{J}(\mathbf{A})} - \left\langle \mathbf{Y} - \mathbf{MAH} - (\mathbf{E}_1 \mathbf{A} \circ \mathbf{VB})\mathbf{H} \mid \mathbf{MUH} + (\mathbf{E}_1 \mathbf{U} \circ \mathbf{VB})\mathbf{H} \right\rangle \\ &\quad + \underbrace{\frac{1}{2} \|\mathbf{MUH} + (\mathbf{E}_1 \mathbf{U} \circ \mathbf{VB})\mathbf{H}\|_F^2}_{o\|\mathbf{U}\|} \end{aligned}$$

so the trace becomes

$$Tr(\nabla_A \mathcal{J}(\mathbf{A})^T \mathbf{U}) = Tr(-\underbrace{(\mathbf{Y} - \mathbf{MAH} - (\mathbf{E}_1 \mathbf{A} \circ \mathbf{VB})\mathbf{H})}_{\mathbf{D}_A})^T (\mathbf{MUH} + (\mathbf{E}_1 \mathbf{U} \circ \mathbf{VB})\mathbf{H}))$$

knowing that

$$Tr(ABC) = Tr(BCA) = Tr(CAB)$$

$$Tr((A^T \circ B^T)C) = Tr(A^T (B \circ C))$$

then

$$Tr(\nabla_A \mathcal{J}(\mathbf{A})^T \mathbf{U}) = Tr(-\mathbf{HD}_A^T \mathbf{MU}) + Tr((-\mathbf{HD}_A^T \circ (\mathbf{VB})^T) \mathbf{E}_1 \mathbf{U})$$

and

$$\nabla_A \mathcal{J}(\mathbf{A}) = -\mathbf{M}^T \mathbf{D}_A \mathbf{H}^T - \mathbf{E}_1^T (\mathbf{D}_A \mathbf{H}^T \circ (\mathbf{V}\mathbf{B}))$$

The Lipschitz constant computation is based in the following inequalities:

$$\|AB\| \leq \|A\| \|B\|$$

$$\|AB\|_\phi \leq \|A\|_\infty \|B\|_\phi \text{ from Holder's inequality}$$

$$\|A \circ B\| \leq \|A\| \|B\| \text{ [Hua11]}$$

so the chosen value for the Lipschitz constant of the factor proportion is

$$L_A = \|\nabla_a^2 \mathcal{J}(\mathbf{A})\| = \|\mathbf{M}^T \mathbf{M}\| \|\mathbf{H}\|^2 + 2\|\mathbf{E}_1\| \|\mathbf{M}\| \|\mathbf{V}\mathbf{B}\| \|\mathbf{H}\|^2 + \|\mathbf{E}_1\|^2 \|\mathbf{V}\mathbf{B}\|^2 \|\mathbf{H}\|^2$$

### A.1.2. Resolution with respect to M

$$\|\mathbf{Y} - \mathbf{MAH} - \Delta\|_F^2 = \|\mathbf{Y}\|_F^2 - 2\langle \mathbf{Y} | \mathbf{MAH} + \Delta \rangle + \|\mathbf{MAH} + \Delta\|_F^2$$

The only terms depending on  $\mathbf{M}$  are

$$\|\mathbf{MAH}\|_F^2 + 2\langle \Delta - \mathbf{Y} | \mathbf{MAH} \rangle = Tr(\mathbf{AHH}^T \mathbf{A}^T \mathbf{M}^T \mathbf{M}) + 2Tr(\mathbf{MAH}(\Delta - \mathbf{Y})^T)$$

So

$$\nabla_M \mathcal{J}(\mathbf{M}) = \mathbf{MAHH}^T \mathbf{A}^T + \mathbf{AH}(\Delta - \mathbf{Y})^T$$

and the Lipschitz constant of the factors is

$$L_M = \|\nabla_M^2 \mathcal{J}(\mathbf{M})\| = \|\mathbf{AHH}^T \mathbf{A}^T\|$$

### A.1.3. Resolution with respect to B

For

$$\mathcal{J}(\mathbf{B}) = \frac{1}{2} \|\mathbf{Y} - \mathbf{MAH} - (\mathbf{E}_1 \mathbf{A} \circ \mathbf{V}\mathbf{B})\mathbf{H}\|_F^2$$

we will have

$$\mathcal{J}(\mathbf{B}+\mathbf{U}) = \underbrace{\frac{1}{2}\|\mathbf{Y} - \mathbf{MAH} - (\mathbf{E}_1\mathbf{A} \circ \mathbf{VB})\mathbf{H}\|_F^2}_{\mathcal{J}(\mathbf{B})} - \left\langle \mathbf{Y} - \mathbf{MAH} - (\mathbf{E}_1\mathbf{A} \circ \mathbf{VB})\mathbf{H} \mid (\mathbf{E}_1\mathbf{A} \circ \mathbf{VU})\mathbf{H} \right\rangle \underbrace{\frac{1}{2}\|(\mathbf{E}_1\mathbf{A} \circ \mathbf{VU})\mathbf{H}\|_F^2}_{o\|\mathbf{U}\|}$$

so the trace becomes

$$\begin{aligned} \text{Tr}(\nabla_B \mathcal{J}(\mathbf{B})^T \mathbf{U}) &= -\text{Tr}((\mathbf{Y} - \mathbf{MAH} - (\mathbf{E}_1\mathbf{A} \circ \mathbf{VB})\mathbf{H})^T ((\mathbf{E}_1\mathbf{A} \circ \mathbf{VU})\mathbf{H})) \\ &= -\text{Tr}(((\mathbf{H}(\mathbf{Y} - \mathbf{MAH} - (\mathbf{E}_1\mathbf{A} \circ \mathbf{VB})\mathbf{H})^T) \circ (\mathbf{E}_1\mathbf{A}))\mathbf{VU}) \end{aligned}$$

and

$$\nabla_B \mathcal{J}(\mathbf{B}) = V^T((\mathbf{E}_1\mathbf{A}) \circ (-\mathbf{Y} + \mathbf{MAH} + \Delta)\mathbf{H}^T)$$

The Lipchitz constant is

$$L_B = \|\nabla_B^2 \mathcal{J}(\mathbf{B})\| = \|\mathbf{E}_1\mathbf{A}\|_\infty^2 \|\mathbf{V}\|^2 \|\mathbf{H}\|^2 \quad (\text{A.1})$$

## A.2. The whitening transform

Whitening is a linear transformation that converts a multivariate Gaussian  $N$ -dimensional random vector  $\mathbf{Y}$  with positive definite covariance matrix  $\Sigma_Y$  and mean vector  $\mu_Y$  into a new random vector

$$\mathbf{I}_W = \mathbf{W}\mathbf{Y} \quad (\text{A.2})$$

whose covariance matrix  $\Sigma_I$  is an identity, i.e., the components of  $\mathbf{I}_W$  are uncorrelated and its variance equals to 1. The whitening matrix is denoted by  $\mathbf{W}$ .

The whitening procedure is a generalization of the standardization procedure, with which a decorrelation step is combined. These transformations are often associated to a mean-centering to ensure  $\mathbb{E}_I = 0$  but this step is not essential to acquire a white covariance matrix.

The first step on whitening is decorrelation of the vector components. The aim is to extract a diagonal covariance matrix. In order to do this, a first assumption is that  $\Sigma_Y$  is positive definite and that  $\mathbf{X}$  is zero-mean, what can be ensured with a previous step of subtracting the mean. Then we need the eigendecomposition of the covariance matrix which may be known or can be estimated from data. The covariance matrix writes

$$\Sigma_Y = \mathbb{E}[\mathbf{Y}\mathbf{Y}^T] = \Phi_Y \Lambda_Y \Phi_Y^{-1} = \Phi_Y \Lambda_Y^{\frac{1}{2}} \Lambda_Y^{\frac{1}{2}} \Phi_Y^{-1} \quad (\text{A.3})$$

where  $\Phi_Y$  is the matrix of eigenvectors  $\phi_i$  of  $\Sigma_Y$  and  $\Lambda_Y$  is the corresponding diagonal matrix of eigenvalues

$\lambda_i$ . Additionally, as the columns of  $\Phi$  are orthonormal

$$\Phi_Y^{-1} = \Phi_Y^T \quad (\text{A.4})$$

Let  $\mathbf{I}_D$  be a random vector with decorrelated multivariate Gaussian distribution defined as

$$\mathbf{I}_D = \mathbf{W}_D \mathbf{Y} \quad (\text{A.5})$$

where  $\mathbf{W}_D$  is the decorrelation transformation. The covariance matrix of  $\mathbf{I}_D$  can be approximated as

$$\mathbb{E}[\mathbf{I}_D \mathbf{I}_D^T] \simeq \frac{\mathbf{I}_D \mathbf{I}_D^T}{N} \quad (\text{A.6})$$

$$\simeq \frac{\mathbf{W}_D \mathbf{Y} \mathbf{Y}^T \mathbf{W}_D^T}{N} \quad (\text{A.7})$$

$$\simeq \mathbf{W}_D \mathbb{E}[\mathbf{Y} \mathbf{Y}^T] \mathbf{W}_D^T \quad (\text{A.8})$$

$$\simeq \mathbf{W}_D \Phi_Y \Lambda_Y \Phi_Y^T \mathbf{W}_D^T \quad (\text{A.9})$$

So we reach decorrelation by defining  $\mathbf{W}_D = \Phi_Y^T$ , and the covariance becomes

$$\mathbb{E}[\mathbf{I}_D \mathbf{I}_D^T] \simeq \Phi_Y^T \Phi_Y \Lambda_Y \Phi_Y^T \Phi_Y \quad (\text{A.10})$$

$$\simeq \Lambda_Y \quad (\text{A.11})$$

and the components of  $\mathbf{I}_D$  are uncorrelated since the covariance matrix is diagonal.

Then we proceed to standardization which is equivalent to scale the different components of the vector so that they have a unit variance. The aim is to turn the already diagonal covariance matrix into an identity. The whitened matrix is defined as

$$\mathbf{I}_W = \mathbf{W}_S \Phi_Y^T \mathbf{Y} \quad (\text{A.12})$$

where  $\mathbf{W}_S$  is the standardization operator. The diagonal matrix  $\Lambda_Y$  is symmetric and

$$\Lambda_Y^{-1} \Lambda_Y = \mathbf{I} \quad (\text{A.13})$$

Therefore, considering  $\mathbf{W}_S = \Lambda_Y^{-\frac{1}{2}}$  we will have the following covariance matrix

$$\mathbb{E}[\mathbf{I}_W \mathbf{I}_W^T] \simeq \frac{\mathbf{I}_W \mathbf{I}_W^T}{N} \quad (\text{A.14})$$

$$\simeq \Lambda_Y^{-\frac{1}{2}} \Phi_Y^T \Phi_Y \Lambda_Y \Phi_Y^T \Phi_Y \Lambda_Y^{-\frac{1}{2}} \quad (\text{A.15})$$

$$\simeq \Lambda_Y^{-\frac{1}{2}} \Lambda_Y \Lambda_Y^{-\frac{1}{2}} \quad (\text{A.16})$$

$$\simeq \Lambda_Y^{-\frac{1}{2}} \Lambda_Y^{\frac{1}{2}} \Lambda_Y^{\frac{1}{2}} \Lambda_Y^{-\frac{1}{2}} \quad (\text{A.17})$$

$$\simeq \mathbf{I} \quad (\text{A.18})$$

The total whitening matrix is  $\mathbf{W} = \Phi_Y^T \Lambda_Y^{-\frac{1}{2}}$

### A.2.1. Noise whitening

In dynamic PET, different frames of time presented different statistical noises. Therefore, we studied the application of noise whitening is an alternative for standardization of the frames. The total  $\mathbf{Y}$  signal writes

$$\mathbf{Y} = \mathbf{X} + \mathbf{N} \quad (\text{A.19})$$

The whitening matrix is considered

$$\mathbf{W} = \Phi_N^T \Lambda_N^{-\frac{1}{2}} \quad (\text{A.20})$$

where  $\Phi_N$  is the matrix of eigenvectors of the noise covariance matrix  $\Sigma_N$  and  $\Lambda_N$  is the corresponding diagonal matrix of eigenvalues. The whitened matrix is defined as

$$\mathbf{I}_W = \Phi_N^T \Lambda_N^{-\frac{1}{2}} (\mathbf{X} + \mathbf{N}) \quad (\text{A.21})$$

The covariance matrix of the original signal  $\mathbf{Y}$  is

$$\mathbb{E}[\mathbf{Y} \mathbf{Y}^T] = \mathbb{E}[\mathbf{X} \mathbf{X}^T] + \mathbb{E}[\mathbf{N} \mathbf{N}^T] \quad (\text{A.22})$$

and the covariance matrix of  $\mathbf{I}_W$  becomes

$$\mathbb{E}[\mathbf{I}_W \mathbf{I}_W^T] = \Phi_N^T \Lambda_N^{-\frac{1}{2}} \mathbb{E}[\mathbf{X} \mathbf{X}^T] \Lambda_N^{-\frac{1}{2}} \Phi_N + \Phi_N^T \Lambda_N^{-\frac{1}{2}} \mathbb{E}[\mathbf{N} \mathbf{N}^T] \Lambda_N^{-\frac{1}{2}} \Phi_N \quad (\text{A.23})$$

$$= \Phi_N^T \Lambda_N^{-\frac{1}{2}} \mathbb{E}[\mathbf{X} \mathbf{X}^T] \Lambda_N^{-\frac{1}{2}} \Phi_N + \mathbf{I} \quad (\text{A.24})$$

In this case, whitening distorts the covariance matrix of the signal in order to reduce the relevance of highly noised frames. In our case, this turns unmixing into a difficult task since the early frames are important to detect blood, the middle frames are extremely important to differentiate between white and gray matter and the latter frames hold information on the specific binding region and its variability. To simulate the validity of whitening before unmixing, we could synthetically induce extra noise in several different frame locations to subsequently whiten the data. In dynamic PET image, a previous whitening preprocessing step may not be ideal as, along with the noise, some of the true signal is also extracted from the highly noised frames.

### A.3. An ADMM approach

#### A.3.1. Problem formulation

Previous to our PALM approach, we studied to use an ADMM approach to solve the problem in Chapter 3. In this formulation, a depreciated version of SLMM (3.7) with no deconvolution step was combined to the constraints in (3.2) and (3.3). An appropriate cost function is required to estimate the parameters  $\mathbf{M}$ ,  $\mathbf{A}$ ,  $\mathbf{B}$ . Assuming the signal is corrupted by a zero-mean white Gaussian noise, we also define the data fitting term as the Frobenius norm of the difference between the acquisitions  $\mathbf{Y}$  and the reconstructed data  $\mathbf{MA} + \Delta$ . Since the problem is ill-posed, additional penalization terms are needed. In this formulation, we propose to define penalization functions  $\Phi$  and  $\Psi$  to reflect the available *a priori* knowledge on  $\mathbf{M}$  and  $\mathbf{A}$ . As a result, the optimization problem is expressed as

$$(\mathbf{M}^*, \mathbf{A}^*, \mathbf{B}^*) \in \arg \min_{\mathbf{M}, \mathbf{A}, \mathbf{B}} \left\{ \mathcal{J}(\mathbf{M}, \mathbf{A}, \mathbf{B}) \text{ s.t. (3.2) and (3.3)} \right\} \quad (\text{A.25})$$

with

$$\mathcal{J}(\mathbf{M}, \mathbf{A}, \mathbf{B}) = \frac{1}{2} \|\mathbf{Y} - \mathbf{MA} - \Delta\|_F^2 + \alpha \Phi(\mathbf{A}) + \gamma \Psi(\mathbf{M}) \quad (\text{A.26})$$

where the penalization parameters  $\alpha$  and  $\gamma$  control the trade-off between the data fitting term  $\|\mathbf{Y} - \mathbf{MA} - \Delta\|_F^2$  and the penalties  $\Phi(\mathbf{A})$  and  $\Psi(\mathbf{M})$ .

In addition, we assume that the penalization functions are separable, leading to

$$\Phi(\mathbf{A}) = \sum_{n=1}^N \phi(\mathbf{a}_n) \quad (\text{A.27})$$

$$\Psi(\mathbf{M}) = \sum_{l=1}^L \psi(\tilde{\mathbf{m}}_l) \quad (\text{A.28})$$

where  $\tilde{\mathbf{m}}_l$  denotes the  $l$ th row of  $\mathbf{M}$  and  $\phi$  and  $\psi$  are non-negative differentiable convex functions. The variability penalization of Chapter 3 is a nonsmooth function and could not be transposed to this setting.



### Abundance penalization

The abundance spatial smoothness penalization is expressed in matrix form as

$$\Phi(\mathbf{A}) = \frac{1}{2} \|\mathbf{A}\mathbf{H}\|_F^2 \quad (\text{A.29})$$

where  $\mathbf{H}$  is a matrix computing the differences between the abundances of a given pixel and those of its 4 nearest neighbors.

### Endmember penalization

Classical penalizations found in the literature consist of constraining the size of the simplex whose vertices are the endmember signatures. Under the pure pixel and linear mixture assumptions, the data points are enclosed in a  $(K-1)$ -simplex whose vertices are the endmembers. Let  $\mathbf{T}$  be the projection of  $\mathbf{M}$  on the space spanned by the  $K-1$  principal components of  $\mathbf{Y}$ . The expression of the volume of this subspace is

$$\mathcal{V}(\mathbf{T}) = \frac{1}{(K-1)!} \left| \det \begin{pmatrix} \mathbf{T} \\ \mathbf{1}_K^T \end{pmatrix} \right| \quad (\text{A.30})$$

To ensure the differentiability of the penalization with respect to  $\mathbf{T}$ , we propose to consider the following penalty

$$\Psi(\mathbf{M}) = \frac{1}{2} \mathcal{V}^2(\mathbf{T}) \quad (\text{A.31})$$

---

#### Algorithm 8: SLMM-unmixing: global algorithm

---

**Data:**  $\mathbf{Y}, \mathbf{A}^{(0)}, \mathbf{M}^{(0)}, \mathbf{B}^{(0)}$

**Result:**  $\mathbf{A}, \mathbf{M}, \mathbf{B}$

```

1 begin
2    $k \leftarrow 1$ 
3   while stopping criterium not satisfied do
4      $\mathbf{A}^{(k)} \leftarrow \arg \min_{\mathbf{A}} \mathcal{J}(\mathbf{M}^{(k-1)}, \mathbf{A}, \mathbf{B}^{(k-1)})$ 
5      $\mathbf{M}^{(k)} \leftarrow \arg \min_{\mathbf{M}} \mathcal{J}(\mathbf{M}, \mathbf{A}^{(k)}, \mathbf{B}^{(k-1)})$ 
6      $\mathbf{B}^{(k)} \leftarrow \arg \min_{\mathbf{B}} \mathcal{J}(\mathbf{M}^{(k)}, \mathbf{A}^{(k)}, \mathbf{B})$ 
7      $k \leftarrow k + 1$ 
8    $\mathbf{A} \leftarrow \mathbf{A}^{(k)}$ 
9    $\mathbf{M} \leftarrow \mathbf{M}^{(k)}$ 
10   $\mathbf{B} \leftarrow \mathbf{B}^{(k)}$ 

```

---

## A.4. An ADMM-based algorithm

### A.4.1. ADMM: general principle

Given  $f : \mathbb{R}^p \rightarrow \mathbb{R}^+$ ,  $g \in \mathbb{R}^m \rightarrow \mathbb{R}^+$ ,  $\mathbf{A} \in \mathbb{R}^{n \times p}$  and  $\mathbf{B} \in \mathbb{R}^{n \times m}$ , consider the general optimization problem

$$\begin{aligned} & \underset{x, z}{\text{minimize}} && f(x) + g(z) \\ & \text{subject to} && \mathbf{A}x + \mathbf{B}z = c \end{aligned} \tag{A.32}$$

The scaled augmented Lagrangian associated with this problem can be written

$$\mathcal{L}_\rho(\mathbf{x}, \mathbf{z}, \mathbf{u}) = f(\mathbf{x}) + g(\mathbf{z}) + \frac{\rho}{2} \|\mathbf{A}\mathbf{x} + \mathbf{B}\mathbf{z} - \mathbf{c} + \mathbf{u}\|_2^2$$

where  $\rho > 0$ . Denote as  $\mathbf{x}^{(k+1)}, \mathbf{z}^{(k+1)}$  and  $\mathbf{u}^{(k+1)}$  the primal variables and dual variable at iteration  $k+1$  of the algorithm, respectively

$$\begin{aligned} \mathbf{x}^{(k+1)} &\in \arg \min_{\mathbf{x}} \mathcal{L}_\rho(\mathbf{x}, \mathbf{z}^{(k)}, \mathbf{u}^{(k)}) \\ \mathbf{z}^{(k+1)} &\in \arg \min_{\mathbf{z}} \mathcal{L}_\rho(\mathbf{x}^{(k+1)}, \mathbf{z}, \mathbf{u}^{(k)}) \\ \mathbf{u}^{(k+1)} &= \mathbf{u}^{(k)} + \mathbf{A}\mathbf{x}^{(k+1)} + \mathbf{B}\mathbf{z}^{(k+1)} - \mathbf{c} \end{aligned}$$

The ADMM consists in successively minimizing  $\mathcal{L}_\rho$  with respect to  $\mathbf{x}, \mathbf{z}$  and  $\mathbf{u}$ . A classical stopping criterion involves the primal and dual residuals at iteration  $k+1$ : the procedure is iterated until

$$\|\mathbf{r}^{(k)}\|_2 \leq \varepsilon^{pri} \text{ and } \|\mathbf{s}^{(k)}\|_2 \leq \varepsilon^{dual} \tag{A.33}$$

where the primal and dual residuals at iteration  $k+1$  are respectively given by

$$\begin{aligned} \mathbf{r}^{(k+1)} &= \mathbf{A}\mathbf{x}^{(k+1)} + \mathbf{B}\mathbf{z}^{(k+1)} - \mathbf{c} \\ \mathbf{s}^{(k+1)} &= \rho \mathbf{A}^T \mathbf{B}(\mathbf{z}^{(k+1)} - \mathbf{z}^{(k)}) \end{aligned} \tag{A.34}$$

and

$$\begin{aligned} \varepsilon^{pri} &= \sqrt{p} \varepsilon^{abs} + \varepsilon^{rel} \max \left\{ \|\mathbf{A}\mathbf{x}^{(k)}\|_2^2, \|\mathbf{B}\mathbf{z}^{(k)}\|_2^2, \|\mathbf{c}\|_2^2 \right\} \\ \varepsilon^{dual} &= \sqrt{n} \varepsilon^{abs} + \varepsilon^{rel} \|\mathbf{A}^T \mathbf{y}^{(k)}\|_2^2 \end{aligned} \tag{A.35}$$

Finally, the parameter  $\rho$  can be adjusted using the rule

$$\rho^{(k+1)} = \begin{cases} \tau^{incr} \rho^{(k)} & \text{if } \|\mathbf{r}^{(k)}\|_2 > \mu \|\mathbf{s}^{(k)}\|_2 \\ \rho^{(k)} / \tau^{decr} & \text{if } \|\mathbf{s}^{(k)}\|_2 > \mu \|\mathbf{r}^{(k)}\|_2 \\ \rho^{(k)} & \text{otherwise} \end{cases} \quad (\text{A.36})$$

#### A.4.2. Optimization with respect to $\mathbf{A}$

Optimizing the cost function  $\mathcal{J}$  with respect to  $\mathbf{A}$  under the constraints (3.3) is equivalent to solving the following problems:

$$\mathbf{a}_n^* = \arg \min_{\mathbf{a}_n} \left\{ \frac{1}{2} \|\mathbf{y}_n - [\tilde{\mathbf{m}}_1, \dots, \tilde{\mathbf{m}}_j + \mathbf{v}_n \mathbf{B}_n, \dots, \tilde{\mathbf{m}}_k] \mathbf{a}_n\|_2^2 + \alpha \Phi(\mathbf{a}_n) \right\} \quad (\text{A.37})$$

s.t.  $\mathbf{a}_n \succeq \mathbf{0}_K, \mathbf{a}_n^T \mathbf{1}_K = 1$

After introducing the splitting variable  $\mathbf{w}_n^{(\mathbf{A})} \in \mathbb{R}^K$  for  $n = 1, \dots, N$  such that

$$\underbrace{\begin{pmatrix} \mathbf{I}_K \\ \mathbf{1}_K^T \end{pmatrix}}_{\mathbf{Q}} \mathbf{a}_n + \underbrace{\begin{pmatrix} -\mathbf{I}_K \\ \mathbf{0}_K^T \end{pmatrix}}_{\mathbf{R}} \mathbf{w}_n = \underbrace{\begin{pmatrix} \mathbf{0}_K \\ 1 \end{pmatrix}}_{\mathbf{s}} \quad (\text{A.38})$$

The resulting scaled augmented Lagrangian is expressed as

$$\begin{aligned} \mathcal{L}_{\mu_n^{(\mathbf{A})}}(\mathbf{a}_n, \mathbf{w}_n^{(\mathbf{A})}, \boldsymbol{\lambda}_n^{(\mathbf{A})}) &= \frac{1}{2} \|\mathbf{y}_n - [\tilde{\mathbf{m}}_1, \dots, \tilde{\mathbf{m}}_j + \mathbf{v}_n \mathbf{B}_n, \dots, \tilde{\mathbf{m}}_k] \mathbf{a}_n\|_2^2 + \frac{\mu_n^{(\mathbf{A})}}{2} \|\mathbf{Q} \mathbf{a}_n + \mathbf{R} \mathbf{w}_n^{(\mathbf{A})} - \mathbf{s} + \boldsymbol{\lambda}_n^{(\mathbf{A})}\|_2^2 \\ &\quad + \alpha \Phi(\mathbf{a}_n) + \mathcal{I}_{S_{K,1}^+}(\mathbf{w}_n^{(\mathbf{A})}) \end{aligned} \quad (\text{A.39})$$

---

**Algorithm 9:** ADMM optimization w.r.t.  $\mathbf{A}$ 


---

**Data:**  $\mathbf{Y}, \mathbf{A}^{(0)}, \mathbf{M}^{(0)}, \varepsilon_{pri}, \varepsilon_{dual}, \tau^{incr}, \tau^{decr}, \mu_n^{(\mathbf{A})^{(0)}}$

**Result:**  $\mathbf{A}$

---

```

1 begin
2   for  $n = 1$  to  $N$  do
3      $k \leftarrow 1$ 
4      $\boldsymbol{\lambda}_n^{(\mathbf{A})^{(0)}} = \mathbf{0}$ 
5      $\mathbf{w}_n^{(\mathbf{A})^{(0)}} = \mathbf{0}$ 
6     while stopping criterium not satisfied do
7        $\mathbf{a}_n^{(k)} \leftarrow \arg \min_{\mathbf{a}_n} \mathcal{L}_{\mu_n^{(\mathbf{A})^{(k-1)}}}(\mathbf{a}_n, \mathbf{w}_n^{(\mathbf{A})^{(k-1)}}, \boldsymbol{\lambda}_n^{(\mathbf{A})^{(k-1)}})$ 
8        $\mathbf{w}_n^{(\mathbf{A})^{(k)}} \leftarrow \arg \min_{\mathbf{w}_n^{(\mathbf{A})}} \mathcal{L}_{\mu_n^{(\mathbf{A})^{(k-1)}}}(\mathbf{a}_n^{(k)}, \mathbf{w}_n^{(\mathbf{A})}, \boldsymbol{\lambda}_n^{(\mathbf{A})^{(k-1)}})$ 
9        $\boldsymbol{\lambda}_n^{(\mathbf{A})^{(k)}} \leftarrow \boldsymbol{\lambda}_n^{(\mathbf{A})^{(k-1)}} + \mathbf{Q} \mathbf{a}_n^{(k)} + \mathbf{R} \mathbf{w}_n^{(\mathbf{A})^{(k)}} - \mathbf{s}$ 
10       $k \leftarrow k + 1$ 
11     $\mathbf{a}_n \leftarrow \mathbf{a}_n^{(k)}$ 

```

---

### A.4.3. Optimization with respect to $\mathbf{M}$

Optimizing the cost function  $\mathcal{J}$  with respect to  $\mathbf{M}$  under the constraints (3.3) is equivalent to solving the following problems:

$$\tilde{\mathbf{m}}_\ell^* = \arg \min_{\tilde{\mathbf{m}}_\ell^*} \left\{ \begin{array}{l} \frac{1}{2} \|\tilde{\mathbf{y}}_\ell - \tilde{\mathbf{m}}_\ell \mathbf{A} - \Delta_\ell\|_2^2 + \gamma \Psi(\tilde{\mathbf{m}}_\ell) \\ \text{s.t. } \tilde{\mathbf{m}}_\ell \succeq \mathbf{0}_K \text{ for } n = 1, \dots, N \end{array} \right\} \quad (\text{A.40})$$

After introducing the splitting variable  $\mathbf{W}_\ell^{(\mathbf{M})} \in \mathbb{R}^K$  for  $n = 1, \dots, N$  such that

$$\tilde{\mathbf{m}}_\ell - \mathbf{W}_\ell^{(\mathbf{M})} = \mathbf{0}_K \quad (\text{A.41})$$

The resulting scaled augmented Lagrangian is expressed as

$$\begin{aligned} \mathcal{L}_{\mu_\ell^{(\mathbf{M})}}(\tilde{\mathbf{m}}_\ell, \mathbf{W}_\ell^{(\mathbf{M})}, \Lambda_\ell^{(\mathbf{M})}) = & \frac{1}{2} \|\tilde{\mathbf{y}}_\ell - \tilde{\mathbf{m}}_\ell \mathbf{A} - \Delta_\ell\|_2^2 + \frac{\mu_\ell^{(\mathbf{M})}}{2} \|\tilde{\mathbf{m}}_\ell - \mathbf{W}_\ell^{(\mathbf{M})} + \Lambda_\ell^{(\mathbf{M})}\|_F^2 \\ & + \gamma \Psi(\tilde{\mathbf{m}}_\ell) + \mathcal{I}_{\mathcal{S}_{1,K}^+}(\mathbf{W}_\ell^{(\mathbf{M})}) \end{aligned} \quad (\text{A.42})$$

with  $\mu_\ell^{(\mathbf{M})} > 0$ .

---

**Algorithm 10:** ADMM optimization w.r.t.  $\mathbf{M}$ 


---

**Data:**  $\mathbf{Y}, \mathbf{A}^{(0)}, \mathbf{M}^{(0)}, \varepsilon_{pri}, \varepsilon_{dual}, \tau^{incr}, \tau^{decr}, \mu_\ell^{(\mathbf{M}^{(0)})}$

**Result:**  $\mathbf{M}$

```

1 begin
2   for  $l = 1$  to  $L$  do
3      $k \leftarrow 1$ 
4      $\Lambda_\ell^{(\mathbf{M})^{(0)}} = \mathbf{0}$ 
5      $\mathbf{W}_\ell^{(\mathbf{M})^{(0)}} = \mathbf{0}$ 
6     while stopping criterium not satisfied do
7        $\tilde{\mathbf{m}}_\ell^{(k)} \leftarrow \arg \min_{\tilde{\mathbf{m}}_\ell} \mathcal{L}_{\mu_\ell^{(\mathbf{M})^{(k-1)}}}(\tilde{\mathbf{m}}_\ell, \mathbf{W}_\ell^{(\mathbf{M})^{(k-1)}}, \Lambda_\ell^{(\mathbf{M})^{(k-1)}})$ 
8        $\mathbf{W}_\ell^{(\mathbf{M})^{(k)}} \leftarrow \arg \min_{\mathbf{W}_\ell^{(\mathbf{M})}} \mathcal{L}_{\mu_\ell^{(\mathbf{M})^{(k-1)}}}(\tilde{\mathbf{m}}_\ell^{(k)}, \mathbf{W}_\ell^{(\mathbf{M})}, \Lambda_\ell^{(\mathbf{M})^{(k-1)}})$ 
9        $\Lambda_\ell^{(\mathbf{M})^{(k)}} \leftarrow \Lambda_\ell^{(\mathbf{M})^{(k-1)}} + \tilde{\mathbf{m}}_\ell^{(k)} - \mathbf{W}_\ell^{(\mathbf{M})^{(k)}}$ 
10       $k \leftarrow k + 1$ 
11    $\tilde{\mathbf{m}}_\ell \leftarrow \tilde{\mathbf{m}}_\ell^{(k)}$ 

```

---

#### A.4.4. Optimization with respect to $\mathbf{B}$

The optimization w.r.t. variable  $\mathbf{B}$  is, in this setting, much more simple than the others since no constraints or penalizations are considered. It is equivalent to solving

$$\mathbf{b}_n^* = \arg \min_{\mathbf{B}_n} \left\{ \frac{1}{2} \|\mathbf{y}_n - \mathbf{M}\mathbf{a}_n - \mathbf{1}_{L \times 1} a_{jn} \mathbf{V}\mathbf{B}_n\|_2^2 \right\}. \quad (\text{A.43})$$

It directly gives

$$\mathbf{b}_n^* = \frac{\mathbf{V}^T \epsilon_p}{a_{jn} \mathbf{I}_{N_v}} \quad (\text{A.44})$$

#### A.4.5. Constraints and penalization terms

##### Abundance penalization: spatial smoothness

The abundance smoothness is expressed in matrix form as

$$\Phi(\mathbf{A}) = \frac{1}{2} \|\mathbf{A}\mathbf{H}\|_F^2$$

where  $\mathbf{H}$  denotes the matrix computing the differences between the abundances of a given pixel and the respective abundance of its 4 neighbors

$$\mathbf{H} = \begin{bmatrix} \mathbf{H}_{\leftarrow} & \mathbf{H}_{\rightarrow} & \mathbf{H}_{\uparrow} & \mathbf{H}_{\downarrow} \end{bmatrix} \in \mathbb{R}^{N \times 4N}$$

where  $N = W \times H$ ,  $W$  is the width and  $H$  is the height of the image matrix. For  $h = 1, \dots, H$ , we introduce

$$\mathbf{H}_h = \begin{pmatrix} 0 & -1 & 0 & \cdots & 0 \\ 0 & 1 & \ddots & \ddots & \vdots \\ \vdots & \ddots & \ddots & \ddots & 0 \\ \vdots & & \ddots & 1 & -1 \\ 0 & \cdots & \cdots & 0 & 1 \end{pmatrix} \in \mathbb{R}^{W \times W}$$

$$\tilde{\mathbf{H}}_h = \begin{pmatrix} 1 & 0 & \cdots & \cdots & 0 \\ -1 & 1 & \ddots & & \vdots \\ 0 & \ddots & \ddots & \ddots & \vdots \\ \vdots & \ddots & \ddots & 1 & 0 \\ 0 & \cdots & 0 & -1 & 0 \end{pmatrix} \in \mathbb{R}^{W \times W}$$

Hence

$$\mathbf{H}_{\leftarrow} = \text{Diag}(\mathbf{H}_1, \dots, \mathbf{H}_H) \text{ and } \mathbf{H}_{\rightarrow} = \text{Diag}(\tilde{\mathbf{H}}_1, \dots, \tilde{\mathbf{H}}_H)$$

In addition

$$\mathbf{H}_{\uparrow} = [\mathbf{0}_{N,W}, \mathbf{H}_{\uparrow}^1] \text{ and } \mathbf{H}_{\downarrow} = [\mathbf{H}_{\downarrow}^1, \mathbf{0}_{N,W}]$$

with

$$\tilde{\mathbf{H}}_{\uparrow}^1 = \begin{pmatrix} \begin{matrix} \uparrow \\ W \\ \downarrow \end{matrix} & \begin{pmatrix} -1 & 0 & \cdots & 0 \\ & \ddots & \ddots & \vdots \\ & 1 & & \ddots & 0 \\ & 0 & \ddots & & -1 \\ \begin{matrix} \uparrow \\ N-W \\ \downarrow \end{matrix} & \begin{pmatrix} \vdots & \ddots & \ddots \\ & 0 & \cdots & 0 & 1 \end{pmatrix} \end{pmatrix} \in \mathbb{R}^{N \times (N-W)}$$

$$\mathbf{H}_{\downarrow}^1 = \mathbf{H}_{\uparrow}^1$$

As we know:

$$\|\mathbf{A}\mathbf{H}\|_F^2 = \left( \sum_{k=0}^3 h_{n,n+kN}^2 \right) \|\mathbf{a}_n\|_2^2 + 2 \left( \sum_{\substack{i=1 \\ i \neq n}}^N \sum_{k=0}^3 h_{n,n+kN} h_{i,n+kN} \mathbf{a}_i^T \right) \mathbf{a}_n + \sum_{\substack{i=1 \\ i \neq n}}^N \sum_{\substack{j=1 \\ j \neq n}}^N h_{j,n+kN} h_{i,n+kN} \mathbf{a}_i^T \mathbf{a}_j^T$$

So the only terms in  $\frac{1}{2} \|\mathbf{A}\mathbf{H}\|_F^2$  related to  $\mathbf{a}_n$  are

$$\Phi(\mathbf{a}_n) = \underbrace{\frac{1}{2} \left( \sum_{k=0}^3 h_{n,n+kN}^2 \right) \|\mathbf{a}_n\|_2^2}_{cA_n} + \underbrace{\left( \sum_{\substack{i=1 \\ i \neq n}}^N \sum_{k=0}^3 h_{n,n+kN} h_{i,n+kN} \mathbf{a}_i^T \right) \mathbf{a}_n}_{c_n^T} \quad (\text{A.45})$$

## Endmember penalization

**Volume and endmember positivity constraint** The volume penalization is expressed using  $\mathbf{T}$ , hence the need to find a condition equivalent to the positivity of  $\mathbf{M}$ . We will first analyze the general expression of the volume penalization with respect to  $\tilde{\mathbf{t}}_{(k)}$ , and then give a condition on  $\mathbf{T}$  ensuring the positivity of  $\mathbf{M}$ .

- **Volume** The determinant of a matrix  $\mathbf{X} \in \mathbb{R}^{K \times K}$  can be developed along its  $i$ th row yielding:

$$\det(\mathbf{X}) = \sum_j (-1)^{i+j} x_{ij} \det(\mathbf{X}_{ij}) = \tilde{\mathbf{x}}_i \mathbf{f}_i$$

with

$$\mathbf{f}_i = [(-1)^{i+j} \det(\mathbf{X}_{ij})]_{j=1}^K \in \mathbb{R}^K$$

Consequently for  $k = 1, \dots, K - 1$

$$\det \begin{pmatrix} \mathbf{T} \\ \mathbf{1}_K^T \end{pmatrix} = \tilde{\mathbf{t}}_k \mathbf{f}_k \quad (\text{A.46})$$

Using previous developments

$$\Psi(\tilde{\mathbf{t}}_k) = \frac{1}{2(K-1)!^2} (\tilde{\mathbf{t}}_k \mathbf{f}_k)^2 \quad (\text{A.47})$$

- **Positivity constraint on  $\mathbf{M}$**  Using the following notation

$$\begin{aligned} \mathbf{Y} &= \mathbf{U} \mathbf{Y}_{proj} + \bar{\mathbf{Y}}_1, & \bar{\mathbf{Y}}_1 &= [\bar{\mathbf{y}} | \dots | \bar{\mathbf{y}}] \in \mathbb{R}^{L \times N} \\ \mathbf{M} &= \mathbf{U} \mathbf{T} + \bar{\mathbf{Y}}_2, & \bar{\mathbf{Y}}_2 &= [\bar{\mathbf{y}} | \dots | \bar{\mathbf{y}}] \in \mathbb{R}^{L \times K} \end{aligned}$$

where  $\bar{\mathbf{Y}}$  is the mean of  $\mathbf{Y}$ ,  $\bar{\mathbf{Y}}_1$  is this mean replied  $N$  times and  $\bar{\mathbf{Y}}_2$  is this mean replied  $K$  times. The same way  $\mathbf{T}$  is the projection of  $\mathbf{M}$  in the space spanned by the  $K-1$  principal components of  $\mathbf{Y}$ ,  $\mathbf{Y}_{proj}$  is the equivalent projection of  $\mathbf{Y}$ . Thus, one has

$$m_{\ell r} = \sum_j u_{\ell j} t_{jr} + \bar{y}_\ell = \sum_{j \neq k} u_{\ell j} t_{jr} + u_{\ell k} t_{kr} + \bar{y}_\ell$$

The positivity constraint for  $m_{\ell r}$  can then be expressed as

$$t_{kr} \geq - \frac{\bar{y}_\ell + \sum_{j \neq k} u_{\ell j} t_{jr}}{u_{\ell k}}$$

Introducing the two sets of integers

$$\begin{aligned} \mathcal{U}_k^+ &= \{\ell | u_{\ell k} > 0\} \\ \mathcal{U}_k^- &= \{\ell | u_{\ell k} < 0\} \end{aligned}$$

The previous equation implies that  $t_{kr} \in [t_{kr}^-, t_{kr}^+]$ , with

$$\begin{aligned} t_{kr}^- &= \max_{\ell \in \mathcal{U}_k^+} \left( - \frac{\bar{y}_\ell + \sum_{j \neq k} u_{\ell j} t_{jr}}{u_{\ell k}} \right) \\ t_{kr}^+ &= \min_{\ell \in \mathcal{U}_k^-} \left( - \frac{\bar{y}_\ell + \sum_{j \neq k} u_{\ell j} t_{jr}}{u_{\ell k}} \right) \end{aligned} \quad (\text{A.48})$$

We introduce the functions  $g_k$  defined by

$$\begin{aligned} g_k : \mathbb{R}^{1 \times K} &\rightarrow \mathbb{R}^{2 \times K} \\ \tilde{\mathbf{x}} &\mapsto \begin{bmatrix} \tilde{\mathbf{x}} - \tilde{t}_k^- \\ -\tilde{\mathbf{x}} + \tilde{t}_k^+ \end{bmatrix} \end{aligned} \quad (\text{A.49})$$

where

$$\tilde{\mathbf{t}}_k^+ = [t_{k1}^+, \dots, t_{kK}^+]$$

$$\tilde{\mathbf{t}}_k^- = [t_{k1}^-, \dots, t_{kK}^-]$$

Finally, the positivity constraint of the endmembers can be written

$$\begin{aligned} \tilde{\mathbf{m}}_\ell &\succeq \mathbf{0}_K^T & \forall \ell, \forall n \\ \Leftrightarrow g_k(\tilde{t}_k) &\succeq \mathbf{0}_{2,K} & \forall k = 1, \dots, K-1 \end{aligned} \tag{A.50}$$

#### A.4.6. Solutions to the optimization sub-problems

##### Resolution with respect to $\mathbf{A}$

The scaled augmented Lagrangian becomes

$$\begin{aligned} \mathcal{L}_{\mu_n^{(\mathbf{A})}}(\mathbf{a}_n, \mathbf{w}_n^{(\mathbf{A})}, \boldsymbol{\lambda}_n^{(\mathbf{A})}) &= \frac{1}{2} \|\mathbf{y}_n - [\tilde{\mathbf{m}}_1, \dots, \tilde{\mathbf{m}}_j + \mathbf{B}_n \mathbf{v}_n, \dots, \tilde{\mathbf{m}}_K] \mathbf{a}_n\|_2^2 + \frac{\mu_n^{(\mathbf{A})}}{2} \left\| \mathbf{Q} \mathbf{a}_n + \mathbf{R} \mathbf{w}_n^{(\mathbf{A})} - \mathbf{s} + \boldsymbol{\lambda}_n^{(\mathbf{A})} \right\|_2^2 \\ &\quad + \frac{\alpha}{2} (cA_n \|\mathbf{a}_n\|_2^2 + 2c_n^T \mathbf{a}_n) + \mathcal{I}_{\mathcal{S}_{K,1}^+}(\mathbf{w}_n^{(\mathbf{A})}) \end{aligned}$$

To find the optimum value of  $\mathbf{a}_n^*$ , we consider

$$\frac{\partial \mathcal{L}_{\mu_n^{(\mathbf{A})}}(\mathbf{a}_n, \mathbf{w}_n^{(\mathbf{A})}, \boldsymbol{\lambda}_n^{(\mathbf{A})})}{\partial \mathbf{a}_n} = 0$$

We will define

$$D_M = [\tilde{\mathbf{m}}_1, \dots, \tilde{\mathbf{m}}_j + \mathbf{B}_n \mathbf{v}_n, \dots, \tilde{\mathbf{m}}_{(K)}]$$

thus we have

$$\mathbf{a}_n^* = \left[ D_M^T D_M + \mu_n^{(\mathbf{A})} \mathbf{Q}^T \mathbf{Q} + \alpha c A_n \mathbf{I}_K \right]^{-1} \left[ D_M^T \mathbf{y}_n - \alpha c_n + \mu_n^{(\mathbf{A})} \mathbf{Q}^T (\mathbf{s} - \mathbf{R} \mathbf{w}_n^{(\mathbf{A})} - \boldsymbol{\lambda}_n^{(\mathbf{A})}) \right] \tag{A.51}$$

and

$$\mathbf{w}_n^{\mathbf{A}*} = \max(\mathbf{a}_n + \boldsymbol{\lambda}_{n,1:K}^{\mathbf{A}}, \mathbf{0}_K) \tag{A.52}$$

where  $\boldsymbol{\lambda}_{n,1:K}^{\mathbf{A}}$  is the vector composed of the  $K$  first elements of  $\boldsymbol{\lambda}_n^{\mathbf{A}}$  and the max must be understood as a term-wise operator. In the absence of any penalization, the solution is obtained by making  $\alpha = 0$  in the previous equations.



## Resolution with respect to $\mathbf{M}$

### Volume penalization

$$\begin{aligned}\|\mathbf{Y} - \mathbf{MA} - \Delta\|_F^2 &= \|\mathbf{U}(\mathbf{Y}_{\text{proj}} - \mathbf{TA}) - \Delta + \bar{\mathbf{Y}}_1 - \bar{\mathbf{Y}}_2\mathbf{A}\|_F^2 \\ &= \|\mathbf{U}(\mathbf{Y}_{\text{proj}} - \mathbf{TA}) - \Delta\|_F^2 + 2\left\langle \mathbf{U}(\mathbf{Y}_{\text{proj}} - \mathbf{TA}) - \Delta \middle| \bar{\mathbf{Y}}_1 - \bar{\mathbf{Y}}_2\mathbf{A} \right\rangle + \|\bar{\mathbf{Y}}_1 - \bar{\mathbf{Y}}_2\mathbf{A}\|_F^2\end{aligned}$$

The only terms depending on  $\mathbf{T}$  are

$$\|\mathbf{Y}_{\text{proj}} - \mathbf{TA}\|_F^2 + 2\left\langle \underbrace{\mathbf{U}(\Delta - \bar{\mathbf{Y}}_1 + \bar{\mathbf{Y}}_2\mathbf{A})}_{\mathbf{S}} \middle| \mathbf{TA} \right\rangle$$

with

$$\langle \mathbf{S} | \mathbf{TA} \rangle = \text{Tr}(\mathbf{S}^T \mathbf{TA}) = \sum_{n=1}^N \left( \sum_{j=1}^{K-1} s_{jn} \tilde{\mathbf{t}}_j \mathbf{a}_n \right)$$

For  $k = 1, \dots, K-1$ , the resulting sub-problems are

$$\tilde{\mathbf{t}}_k^* = \arg \min_{\tilde{\mathbf{t}}_k} \left\{ \begin{aligned} &\frac{1}{2} \|\tilde{\mathbf{y}}_k^{\text{proj}} - \tilde{\mathbf{t}}_k \mathbf{A}\|_2^2 + \sum_{n=1}^N (s_{kn} \tilde{\mathbf{t}}_k \mathbf{a}_n) \\ &+ \frac{\beta}{2(K-1)!^2} (\tilde{\mathbf{t}}_k \mathbf{f}_k)^2 \\ &\text{s.t. } g_k(\tilde{\mathbf{t}}_k) \succeq \mathbf{0}_{2,K} \end{aligned} \right\} \quad (\text{A.53})$$

Introduce the splitting variables  $\mathbf{W}_k^{(\mathbf{T})}$  such that

$$g_k(\tilde{\mathbf{t}}_k) = \mathbf{W}_k^{(\mathbf{T})} \quad \forall k = 1, \dots, K-1 \quad (\text{A.54})$$

The scaled augmented Lagrangian is

$$\mathcal{L}_{\mu_k^{(\mathbf{T})}}(\tilde{\mathbf{t}}_k, \mathbf{W}_k^{(\mathbf{T})}, \mathbf{\Lambda}_k^{(\mathbf{T})}) = \frac{1}{2} \|\tilde{\mathbf{y}}_k^{\text{proj}} - \tilde{\mathbf{t}}_k \mathbf{A}\|_2^2 + \sum_{n=1}^N (s_{kn} \tilde{\mathbf{t}}_k \mathbf{a}_n) + \frac{\beta}{2(K-1)!^2} (\tilde{\mathbf{t}}_k \mathbf{f}_k)^2 + \mathcal{I}_{S^+}(\mathbf{W}_k^{(\mathbf{T})}) + \frac{\mu_k^{(\mathbf{T})}}{2} \|g_k(\tilde{\mathbf{t}}_k) - \mathbf{W}_k^{(\mathbf{T})} + \mathbf{\Lambda}_k^{(\mathbf{T})}\|_F^2$$

To find the optimum value of  $\tilde{\mathbf{t}}_k^*$ , we consider

$$\frac{\partial \mathcal{L}_{\mu_k^{(\mathbf{T})}}(\tilde{\mathbf{t}}_k, \mathbf{W}_k^{(\mathbf{T})}, \mathbf{\Lambda}_k^{(\mathbf{T})})}{\partial \tilde{\mathbf{t}}_k} = 0$$

$$\begin{aligned}
 \tilde{\mathbf{t}}_k^* = & \left[ (\tilde{\mathbf{y}}_k^{proj} - \tilde{\mathbf{s}}_k) \mathbf{A}^T \right. \\
 & \left. + \mu_k^{(\mathbf{T})} (\tilde{\mathbf{t}}_k^- + \tilde{\mathbf{t}}_k^+ + [1 \ -1] (\mathbf{W}_k^{(\mathbf{T})} - \mathbf{\Lambda}_k^{(\mathbf{T})})) \right] \\
 & \left[ \mathbf{A}^T \mathbf{A} + \frac{\beta}{(K-1)!^2} \mathbf{f}_k \mathbf{f}_k^{(\mathbf{T})} + 2\mu_k^{(\mathbf{T})} \right]^{-1}
 \end{aligned} \tag{A.55}$$

and

$$\mathbf{W}_{k,p}^{(\mathbf{T})*} = \max \left( \left[ g_k(\tilde{\mathbf{t}}_k) + \mathbf{\Lambda}_k^{\mathbf{T}} \right], \mathbf{0}_2 \right) \tag{A.56}$$

**Resolution with respect to  $\mathbf{B}$**

$$\mathbf{b}_n^* = \arg \min_{\mathbf{b}_n} \left\{ \frac{1}{2} \left\| \underbrace{\mathbf{y}_n - \mathbf{M}\mathbf{A}}_{\epsilon_p} - a_{jn} \mathbf{b}_n \mathbf{V} \right\|_2^2 \right\} \tag{A.57}$$

And as eigenvalues  $\mathbf{V}$  are orthogonal

$$\mathbf{b}_n^* = \frac{\mathbf{V}^T \epsilon_p}{a_{jn} \mathbf{I}_{N_v}} \tag{A.58}$$

## Appendix to chapter 5

### B.1. Solutions to the optimization sub-problems

#### B.1.1. Resolution with respect to $\mathbf{m}_k$

For  $k = (1, \dots, K-1)$

The optimization problem becomes

$$\begin{aligned} \mathcal{J}(\mathbf{m}_k) &= \frac{1}{2} \left\| \tilde{\mathbf{Y}} - \mathbf{m}_k \mathbf{A}_k - \sum_{i=0}^V \mathbf{E}_{ki} \mathbf{m}_k \underbrace{(\mathbf{A}_k \circ \mathbf{B}_i)}_{\mathbf{W}_{k,i}} \right\|_F^2, \\ &= \frac{1}{2} \left\| \tilde{\mathbf{Y}} \right\|_F^2 - \underbrace{Tr \left( \tilde{\mathbf{Y}}^T (\mathbf{m}_k \mathbf{A}_k + \sum_{i=0}^V \mathbf{E}_{ki} \mathbf{m}_k \mathbf{W}_{k,i}) \right)}_{g(\mathbf{m}_k)} + \frac{1}{2} \underbrace{\left\| \mathbf{m}_k \mathbf{A}_k + \sum_{i=0}^V \mathbf{E}_{ki} \mathbf{m}_k \mathbf{W}_{k,i} \right\|_F^2}_{f(\mathbf{m}_k)} \end{aligned}$$

with  $\tilde{\mathbf{Y}} = \mathbf{Y} - \sum_{j \neq k} (\mathbf{m}_j \mathbf{A}_j - \sum_{i=0}^V \mathbf{E}_{ji} \mathbf{m}_j \mathbf{W}_{ji})$ . First, we compute the gradient of  $g(\mathbf{m}_k)$ , yielding

$$\nabla_{\mathbf{m}_k} g(\mathbf{m}_k) = \tilde{\mathbf{Y}} \mathbf{A}_k^T + \sum_{i=0}^V \mathbf{E}_{ki}^T \tilde{\mathbf{Y}} \mathbf{W}_{k,i}^T.$$

Then developing  $f(\mathbf{m}_k)$

$$\begin{aligned} f(\mathbf{m}_k) &= \left\| \mathbf{m}_k \mathbf{A}_k \right\|_F^2 + 2 Tr \left( (\mathbf{m}_k \mathbf{A}_k)^T \left( \sum_{i=0}^V \mathbf{E}_{ki} \mathbf{m}_k \mathbf{W}_{k,i} \right) \right) + \left\| \sum_{i=0}^V \mathbf{E}_{ki} \mathbf{m}_k \mathbf{W}_{k,i} \right\|_F^2 \\ &= \left\| \mathbf{m}_k \mathbf{A}_k \right\|_F^2 + 2 \sum_{i=0}^V Tr \left( (\mathbf{m}_k \mathbf{A}_k)^T (\mathbf{E}_{ki} \mathbf{m}_k \mathbf{W}_{k,i}) \right) + \sum_{i=0}^V Tr \left( (\mathbf{E}_{ki} \mathbf{m}_k \mathbf{W}_{k,i})^T \sum_{j=0}^V \mathbf{E}_{kj} \mathbf{m}_k \mathbf{W}_{k,j} \right) \\ &= \left\| \mathbf{m}_k \mathbf{A}_k \right\|_F^2 + 2 \sum_{i=0}^V Tr \left( (\mathbf{m}_k \mathbf{A}_k)^T (\mathbf{E}_{ki} \mathbf{m}_k \mathbf{W}_{k,i}) \right) + \sum_{i=0}^V \sum_{j=0}^V Tr \left( (\mathbf{E}_{ki} \mathbf{m}_k \mathbf{W}_{k,i})^T (\mathbf{E}_{kj} \mathbf{m}_k \mathbf{W}_{k,j}) \right). \end{aligned}$$

Its gradient is

$$\nabla_{m_k} f(\mathbf{m}_k) = 2\mathbf{m}_k \mathbf{A}_k \mathbf{A}_k^T + 2 \sum_{i=0}^V (\mathbf{E}_{ki} + \mathbf{E}_{ki}^T) \mathbf{m}_k \mathbf{W}_{k,i} \mathbf{A}_k^T + \sum_{i=0}^V \sum_{j=0}^V (\mathbf{E}_{ki}^T \mathbf{E}_{kj} + (\mathbf{E}_{ki}^T \mathbf{E}_{kj})^T) (\mathbf{m}_k \mathbf{W}_{k,j} \mathbf{W}_{k,i}^T).$$

It yields

$$\begin{aligned} \nabla_{m_k} \mathcal{J}(\mathbf{m}_k) = & -(\tilde{\mathbf{Y}} \mathbf{A}_k^T + \sum_{i=0}^V \mathbf{E}_{ki}^T \tilde{\mathbf{Y}} \mathbf{W}_{k,i}^T) + \mathbf{m}_k \mathbf{A}_k \mathbf{A}_k^T + \sum_{i=0}^V (\mathbf{E}_{ki} + \mathbf{E}_{ki}^T) \mathbf{m}_k \mathbf{W}_{k,i} \mathbf{A}_k^T \\ & + \frac{1}{2} \sum_{i=0}^V \sum_{j=0}^V (\mathbf{E}_{ki}^T \mathbf{E}_{kj} + (\mathbf{E}_{ki}^T \mathbf{E}_{kj})^T) (\mathbf{m}_k \mathbf{W}_{k,j} \mathbf{W}_{k,i}^T) \end{aligned}$$

The Lipschitz constant computation is based in the following inequalities:

$$\|AB\| \leq \|A\| \|B\|$$

$$\|AB\|_\phi \leq \|A\|_\infty \|B\|_\phi \text{ from Holder's inequality}$$

$$\|A \circ B\| \leq \|A\| \|B\| \text{ [Hua11]}$$

so the chosen value for the Lipschitz constant of the abundance is

$$L_{m_k} = \|\nabla_{m_k}^2 \mathcal{J}(\mathbf{m}_k)\| = \|\mathbf{A}_k \mathbf{A}_k^T\| + \sum_{i=0}^V \|\mathbf{E}_{ki} + \mathbf{E}_{ki}^T\| \|\mathbf{W}_{k,i} \mathbf{A}_k^T\| + \sum_{i=0}^V \sum_{j=0}^V \|\mathbf{E}_{ki}^T \mathbf{E}_{kj}\| \|\mathbf{W}_{k,j} \mathbf{W}_{k,i}^T\|$$

**For  $k = K$**

In this case, we will have

$$\mathcal{J}(\mathbf{m}_K) = \frac{1}{2} \|\tilde{\mathbf{Y}} - \mathbf{m}_K \mathbf{A}_K\|_F^2,$$

with  $\tilde{\mathbf{Y}} = \mathbf{Y} - \tilde{\mathbf{M}} \tilde{\mathbf{A}} - \sum_{i=0}^V \mathbf{Q}_i (\tilde{\mathbf{A}} \circ \mathbf{B}_i)$ , it yields

$$\nabla_{m_K} \mathcal{J}(\mathbf{m}_K) = -(\tilde{\mathbf{Y}} - \mathbf{m}_K \mathbf{A}_K) \mathbf{A}_K^T.$$

The Lipschitz constant is

$$L_{m_K} = \|\nabla_{m_K}^2 \mathcal{J}(\mathbf{m}_K)\| = \|\mathbf{A}_K \mathbf{A}_K^T\|.$$

### B.1.2. Resolution with respect to $\tilde{\mathbf{A}}$

Using the definition of differentiable function

$$\langle \nabla_A \mathcal{J}(A), h \rangle = \mathcal{J}(A + U) - \mathcal{J}(A) - o(\|U\|)$$

for

$$\mathcal{J}(\tilde{\mathbf{A}}) = \frac{1}{2} \|\tilde{\mathbf{Y}} - \tilde{\mathbf{M}}\tilde{\mathbf{A}} - \sum_{i=0}^V \mathbf{Q}_i(\tilde{\mathbf{A}} \circ \mathbf{B}_i)\|_F^2,$$

with  $\tilde{\mathbf{Y}} = \mathbf{Y} - \mathbf{m}_K \mathbf{A}_K$ , it yields

$$\begin{aligned} \mathcal{J}(\tilde{\mathbf{A}} + \mathbf{U}) &= \underbrace{\frac{1}{2} \|\tilde{\mathbf{Y}} - \tilde{\mathbf{M}}\tilde{\mathbf{A}} - \sum_{i=0}^V \mathbf{Q}_i(\tilde{\mathbf{A}} \circ \mathbf{B}_i)\|_F^2}_{\mathcal{J}(\tilde{\mathbf{A}})} - \left\langle \tilde{\mathbf{Y}} - \tilde{\mathbf{M}}\tilde{\mathbf{A}} - \sum_{i=0}^V \mathbf{Q}_i(\tilde{\mathbf{A}} \circ \mathbf{B}_i) | \tilde{\mathbf{M}}\mathbf{U} + \sum_{i=0}^V \mathbf{Q}_i(\mathbf{U} \circ \mathbf{B}_i) \right\rangle \\ &\quad - \underbrace{\frac{1}{2} \|\tilde{\mathbf{M}}\mathbf{U} - \sum_{i=0}^V \mathbf{Q}_i(\mathbf{U} \circ \mathbf{B}_i)\|_F^2}_{o(\|\mathbf{U}\|)} \end{aligned}$$

so the trace becomes

$$Tr(\nabla_{\tilde{\mathbf{A}}} \mathcal{J}(\tilde{\mathbf{A}})^T \mathbf{U}) = Tr\left( - \underbrace{(\tilde{\mathbf{Y}} - \tilde{\mathbf{M}}\tilde{\mathbf{A}} - \sum_{i=0}^V \mathbf{Q}_i(\tilde{\mathbf{A}} \circ \mathbf{B}_i))^T}_{\mathbf{D}_{\tilde{\mathbf{A}}}} \tilde{\mathbf{M}}\mathbf{U} + \sum_{i=0}^V \mathbf{Q}_i(\mathbf{U} \circ \mathbf{B}_i) \right)$$

knowing that

$$Tr(ABC) = Tr(BCA) = Tr(CAB)$$

$$Tr((A^T \circ B^T)C) = Tr(A^T(B \circ C))$$

then

$$Tr(\nabla_{\tilde{\mathbf{A}}} \mathcal{J}(\tilde{\mathbf{A}})^T \mathbf{U}) = Tr\left( - \mathbf{D}_{\tilde{\mathbf{A}}}^T \tilde{\mathbf{M}}\mathbf{U} \right) + \sum_{i=0}^V Tr\left( - ((\mathbf{D}_{\tilde{\mathbf{A}}}^T \mathbf{Q}_i) \circ \mathbf{B}_i^T) \mathbf{U} \right)$$

and

$$\nabla_{\tilde{\mathbf{A}}} \mathcal{J}(\tilde{\mathbf{A}}) = -\tilde{\mathbf{M}}^T \mathbf{D}_{\tilde{\mathbf{A}}} - \sum_{i=0}^V \left( (\mathbf{Q}_i^T \mathbf{D}_{\tilde{\mathbf{A}}}) \circ \mathbf{B}_i \right)$$

The Lipschitz constant computation is based in the following inequalities:

$$\|AB\| \leq \|A\| \|B\|$$

$$\|AB\|_\phi \leq \|A\|_\infty \|B\|_\phi \text{ from Holder's inequality}$$

$$\|A \circ B\| \leq \|A\| \|B\| \text{ [Hua11]}$$

so the chosen value for the Lipschitz constant of the abundance is

$$L_{\tilde{A}} = \|\nabla_{\tilde{A}}^2 \mathcal{J}(\tilde{A})\| = \|\tilde{\mathbf{M}}^T \tilde{\mathbf{M}}\| + \sum_{i=0}^V \left( 2\|\tilde{\mathbf{M}}^T \mathbf{Q}_i\| \|\mathbf{B}_i\| + \|\mathbf{B}_i\| \sum_{j=0}^V \|\mathbf{Q}_i^T \mathbf{Q}_j\| \|\mathbf{B}_j\| \right)$$

### B.1.3. Resolution with respect to $\mathbf{A}_K$

The optimization problem is

$$\mathcal{J}(\mathbf{A}_K) = \frac{1}{2} \|\tilde{\mathbf{Y}} - \mathbf{m}_K \mathbf{A}_K\|_F^2,$$

with  $\tilde{\mathbf{Y}} = \tilde{\mathbf{Y}} - \tilde{\mathbf{M}}\tilde{\mathbf{A}} - \sum_{i=0}^V \mathbf{Q}_i(\tilde{\mathbf{A}} \circ \mathbf{B}_i)$ , it yields

$$\nabla_{\mathbf{A}_K} \mathcal{J}(\mathbf{A}_K) = -\mathbf{m}_K^T (\tilde{\mathbf{Y}} - \mathbf{m}_K \mathbf{A}_K).$$

The Lipschitz constant is

$$L_{\mathbf{A}_K} = \|\nabla_{\mathbf{A}_K}^2 \mathcal{J}(\mathbf{A}_K)\| = \|\mathbf{m}_K^T \mathbf{m}_K\|$$

### B.1.4. Resolution with respect to $\mathbf{B}_i$

For

$$\mathcal{J}(\mathbf{B}_i) = \frac{1}{2} \|\tilde{\mathbf{Y}} - \mathbf{Q}_i(\tilde{\mathbf{A}} \circ \mathbf{B}_i)\|_F^2$$

with  $\tilde{\mathbf{Y}} = \mathbf{Y} - \mathbf{M}\mathbf{A} - \sum_{j \neq i} \mathbf{Q}_j(\tilde{\mathbf{A}} \circ \mathbf{B}_j)$ , we will have

$$\mathcal{J}(\mathbf{B}_i + \mathbf{U}) = \underbrace{\frac{1}{2} \|\tilde{\mathbf{Y}} - \mathbf{Q}_i(\tilde{\mathbf{A}} \circ \mathbf{B}_i)\|_F^2}_{\mathcal{J}(\mathbf{B}_i)} - \left\langle \tilde{\mathbf{Y}} - \mathbf{Q}_i(\tilde{\mathbf{A}} \circ \mathbf{B}_i) \middle| \mathbf{Q}_i(\tilde{\mathbf{A}} \circ \mathbf{U}) \right\rangle \underbrace{\frac{1}{2} \|\mathbf{Q}_i(\tilde{\mathbf{A}} \circ \mathbf{U})\|_F^2}_{o\|\mathbf{U}\|}$$

so the trace becomes

$$\begin{aligned} \text{Tr}(\nabla_{\mathbf{B}_i} \mathcal{J}(\mathbf{B}_i)^T \mathbf{U}) &= -\text{Tr} \left( \underbrace{(\tilde{\mathbf{Y}} - \mathbf{Q}_i(\tilde{\mathbf{A}} \circ \mathbf{B}_i))}_{\mathbf{D}_{\mathbf{B}_i}}^T \mathbf{Q}_i(\tilde{\mathbf{A}} \circ \mathbf{U}) \right) \\ &= -\text{Tr} \left( ((\mathbf{D}_{\mathbf{B}_i}^T \mathbf{Q}_i) \circ \tilde{\mathbf{A}}^T) \mathbf{U} \right) \end{aligned}$$

and

$$\begin{aligned}\nabla_{B_i} \mathcal{J}(\mathbf{B}_i) &= - \left( (\mathbf{Q}_i^T (\tilde{\mathbf{Y}} - \mathbf{Q}_i(\tilde{\mathbf{A}} \circ \mathbf{B}_i))) \circ \tilde{\mathbf{A}} \right) \\ \nabla_{B_i} \mathcal{J}(\mathbf{B}_i) &= - \left( (\mathbf{Q}_i^T \mathbf{D}_{B_i}) \circ \tilde{\mathbf{A}} \right)\end{aligned}$$

Knowing that

$$\partial(\mathbf{X} \circ \mathbf{Z}) = \partial \mathbf{X} \circ \mathbf{Z} + \mathbf{X} \circ \partial \mathbf{Z}$$

The Lipschitz constant is

$$L_{B_i} = \|\nabla_{B_i}^2 \mathcal{J}(\mathbf{B}_i)\| = \|\mathbf{Q}_i^T \mathbf{Q}_i\| \|\tilde{\mathbf{A}}\|^2$$

### B.1.5. Resolution with respect to $\alpha_i$

Knowing that  $\boldsymbol{\alpha}_i = \begin{bmatrix} \alpha_{1i} & \alpha_{2i} & \cdots & \alpha_{(K-1)i} \end{bmatrix}$ , we will first derive a solution to the optimization of  $\alpha_{ki}$ .

$$\mathcal{J}(\alpha_{ki}) = \frac{1}{2} \|\tilde{\mathbf{Y}} - \mathbf{E}_{ki} \mathbf{m}_k \mathbf{W}_{k,i}\|_F^2,$$

with  $\tilde{\mathbf{Y}} = \mathbf{Y} - \mathbf{M}\mathbf{A} - \sum_{j \neq i} \mathbf{Q}_j \mathbf{W}_j - \sum_{u \neq k} \mathbf{E}_{ui} \mathbf{m}_u \mathbf{w}_{ui}$ , it yields

$$\mathcal{J}(\alpha_{ki}) = \frac{1}{2} \|\tilde{\mathbf{Y}}\|_F^2 - \left\langle \tilde{\mathbf{Y}} | \mathbf{E}_{ki} \mathbf{m}_k \mathbf{W}_{k,i} \right\rangle + \frac{1}{2} \|\mathbf{E}_{ki} \mathbf{m}_k \mathbf{W}_{k,i}\|_F^2.$$

From the definition of trace

$$\left\langle \tilde{\mathbf{Y}} | \mathbf{E}_{ki} \mathbf{m}_k \mathbf{W}_{k,i} \right\rangle = \text{Tr}(\tilde{\mathbf{Y}}^T \mathbf{E}_{ki} \mathbf{m}_k \mathbf{W}_{k,i}) = \sum_{n=1}^N w_{kn,i} \tilde{\mathbf{Y}}_n^T \mathbf{E}_{ki} \mathbf{m}_k$$

Its derivative with respect to  $\alpha_{ki}$  is

$$\frac{\partial \left\langle \tilde{\mathbf{Y}} | \mathbf{E}_{ki} \mathbf{m}_k \mathbf{W}_{k,i} \right\rangle}{\partial \alpha_{ki}} = - \sum_{n=1}^N w_{kn,i} \tilde{\mathbf{Y}}_n^T (T_p(\mathbf{t}) \circ \mathbf{E}_{ki}) \mathbf{m}_k$$

with the following property

$$\text{Tr}(\mathbf{a} \mathbf{b}^T) = \sum_{i=1}^n a_i b_i = \mathbf{a}^T \mathbf{b},$$

we can write

$$\frac{\partial \left\langle \tilde{\mathbf{Y}} | \mathbf{E}_{ki} \mathbf{m}_k \mathbf{W}_{k,i} \right\rangle}{\partial \alpha_{ki}} = - \mathbf{W}_{k,i} \tilde{\mathbf{Y}}^T (T_p(\mathbf{t}) \circ \mathbf{E}_{ki}) \mathbf{m}_k$$

Also, the Frobenius norm writes

$$\frac{1}{2}\|\mathbf{E}_{ki}\mathbf{m}_k\mathbf{W}_{k,i}\|_F^2 = \frac{1}{2}\text{Tr}(\mathbf{W}_{k,i}^T\mathbf{m}_k^T\mathbf{E}_{ki}^T\mathbf{E}_{ki}\mathbf{m}_k\mathbf{W}_{k,i}) = \frac{1}{2}\sum_{n=1}^N w_{kn,i}\mathbf{m}_k^T\mathbf{E}_{ki}^T\mathbf{E}_{ki}\mathbf{m}_k w_{kn,i}$$

Its derivative with respect to  $\alpha_{ki}$  is

$$\begin{aligned}\frac{\partial \frac{1}{2}\|\mathbf{E}_{ki}\mathbf{m}_k\mathbf{W}_{k,i}\|_F^2}{\partial \alpha_{ki}} &= -\frac{1}{2}\sum_{n=1}^N w_{kn,i}\mathbf{m}_k^T(T_p(\mathbf{t}) \circ \mathbf{E}_{ki})^T\mathbf{E}_{ki}\mathbf{m}_k w_{kn,i} - \frac{1}{2}\sum_{n=1}^N w_{kn,i}\mathbf{m}_k^T\mathbf{E}_{ki}^T(T_p(\mathbf{t}) \circ \mathbf{E}_{ki})\mathbf{m}_k w_{kn,i} \\ &= -\frac{1}{2}\sum_{n=1}^N w_{kn,i}\mathbf{m}_k^T((T_p(\mathbf{t}) \circ \mathbf{E}_{ki})^T\mathbf{E}_{ki} + \mathbf{E}_{ki}^T(T_p(\mathbf{t}) \circ \mathbf{E}_{ki}))\mathbf{m}_k w_{kn,i}\end{aligned}$$

Considering  $\text{Tr}((A^T \circ B^T)C) = \text{Tr}(A^T(B \circ C))$

$$\frac{\partial \frac{1}{2}\|\mathbf{E}_{ki}\mathbf{m}_k\mathbf{W}_{k,i}\|_F^2}{\partial \alpha_{ki}} = -\frac{1}{2}\mathbf{W}_{k,i}\mathbf{W}_{k,i}^T\mathbf{m}_k^T((T_p(\mathbf{t}) \circ \mathbf{E}_{ki})^T\mathbf{E}_{ki} + \mathbf{E}_{ki}^T(T_p(\mathbf{t}) \circ \mathbf{E}_{ki}))\mathbf{m}_k.$$

The gradient w.r.t.  $\alpha_{ki}$ , we can write

$$\begin{aligned}\nabla_{\alpha_{ki}}\mathcal{J}(\alpha_{ki}) &= \mathbf{W}_{k,i}\tilde{\mathbf{Y}}^T(T_p(\mathbf{t}) \circ \mathbf{E}_{ki})\mathbf{m}_k - \frac{1}{2}\mathbf{W}_{k,i}\mathbf{W}_{k,i}^T\mathbf{m}_k^T((T_p(\mathbf{t}) \circ \mathbf{E}_{ki})^T\mathbf{E}_{ki} + \mathbf{E}_{ki}^T(T_p(\mathbf{t}) \circ \mathbf{E}_{ki}))\mathbf{m}_k \\ &= \mathbf{W}_{k,i}(\tilde{\mathbf{Y}}^T(T_p(\mathbf{t}) \circ \mathbf{E}_{ki}) - \frac{1}{2}\mathbf{W}_{k,i}^T\mathbf{m}_k^T((T_p(\mathbf{t}) \circ \mathbf{E}_{ki})^T\mathbf{E}_{ki} + \mathbf{E}_{ki}^T(T_p(\mathbf{t}) \circ \mathbf{E}_{ki})))\mathbf{m}_k\end{aligned}$$

The Lipschitz constant is

$$L_{\alpha_{ki}} = \|\nabla_{\alpha_{ki}}^2\mathcal{J}(\alpha_{ki})\| = \|\mathbf{W}_{k,i}\|\left(\|-\tilde{\mathbf{Y}}^T + \frac{1}{2}\mathbf{W}_{k,i}^T\mathbf{m}_k^T\mathbf{E}_{ki}^T\| + \frac{3}{2}\|\mathbf{W}_{k,i}^T\mathbf{m}_k^T\|\|\mathbf{E}_{ki}\|\right)\|\mathbf{E}_{ki}\|\|T_p(\mathbf{t})\|^2\|\mathbf{m}_k\|$$



# Bibliography

- [ABS13] H. Attouch, J. Bolte, and B. F. Svaiter. “Convergence of descent methods for semi-algebraic and tame problems: proximal algorithms, forward–backward splitting, and regularized Gauss–Seidel methods”. In: *Math. Program., Ser. B* 137.1-2 (2013), pp. 91–129 (cit. on p. 69).
- [ADT11] Y. Altmann, N. Dobigeon, and J.-Y. Tournet. “Bilinear models for nonlinear unmixing of hyperspectral images”. In: *Proc. IEEE GRSS Workshop Hyperspectral Image Signal Process.: Evolution in Remote Sens. (WHISPERS)*. Lisbon, Portugal, June 2011, pp. 1–4 (cit. on p. 50).
- [ADT13] Y. Altmann, N. Dobigeon, and J. Y. Tournet. “Nonlinearity Detection in Hyperspectral Images Using a Polynomial Post-Nonlinear Mixing Model”. In: *IEEE Trans. Image Process.* 22.4 (Apr. 2013), pp. 1267–1276 (cit. on p. 52).
- [Alp+82] N. M. Alpert et al. “Estimation of the Local Statistical Noise in Emission Computed Tomography”. In: *IEEE Trans. Med. Imag.* 1.2 (Oct. 1982), pp. 142–146 (cit. on p. 98).
- [Alt+11] Y. Altmann et al. “Supervised nonlinear spectral unmixing using a polynomial post nonlinear model for hyperspectral imagery”. In: *Proc. IEEE Int. Conf. Acoust., Speech, and Signal Processing (ICASSP)*. Prague, Czech Republic, May 2011 (cit. on pp. 50, 52).
- [Amm+14] R. Ammanouil et al. “Blind and Fully Constrained Unmixing of Hyperspectral Images”. In: *IEEE Trans. Image Process.* 23.12 (Dec. 2014), pp. 5510–5518 (cit. on p. 45).
- [Aro92] B. Arons. “A Review of The Cocktail Party Effect”. In: *J. Amer. Voi. In./Out. Soc.* 12 (1992), pp. 35–50 (cit. on p. 35).
- [Ash+17] S. Ashrafinia et al. “Generalized PSF modeling for optimized quantitation in PET imaging”. In: *Phys. Med. Bio.* 62.12 (2017), p. 5149 (cit. on p. 164).
- [Ash+96] J. Ashburner et al. “A Cluster Analysis Approach for the Characterization of Dynamic PET Data”. In: Academic Press, 1996. Chap. 59, pp. 301–306 (cit. on p. 34).
- [Aus71] A. Auslender. “Méthodes numériques pour la décomposition et la minimisation de fonctions non différentiables”. In: *Numerische Mathematik* 18.3 (1971), pp. 213–223 (cit. on p. 69).

- [Bac+12] F. Bach et al. “Optimization with sparsity-inducing penalties”. In: *Foun. Tre. Mach. Lear.* 4.1 (2012), pp. 1–106 (cit. on p. 40).
- [Bar80] D. C. Barber. “The use of principal components in the quantitative analysis of gamma camera dynamic studies”. In: *Phys. Med. Bio.* 25.2 (1980), pp. 283–292 (cit. on pp. 1, 35, 41, 46, 60, 62).
- [Bas+98] A. Basu et al. “Robust and Efficient Estimation by Minimising a Density Power Divergence”. In: *Biometrika* 85.3 (1998), pp. 549–559 (cit. on pp. 98, 105).
- [Baz+80] J. Bazin et al. “Factor analysis of dynamic scintigraphic data as a modelling method. An application to the detection of metastases”. In: *Information processing in medical imaging* (1980), pp. 345–366 (cit. on p. 42).
- [BBC13] B. Bai, J. Bading, and P. S. Conti. “Tumor Quantification in Clinical Positron Emission Tomography”. In: *Theranostics* 3.10 (2013), pp. 787–801 (cit. on p. 61).
- [Ben+93] H. Benali et al. “A statistical model for the determination of the optimal metric in factor analysis of medical image sequences (FAMIS)”. In: *Phys. Med. Bio.* 38 (1993), pp. 1065–1080 (cit. on pp. 42, 98).
- [Ben+94] H. Benali et al. “Foundations of factor analysis of medical image sequences: a unified approach and some practical implications”. In: *Image and Vision Computing* 12.6 (1994). Information processing in medical imaging, pp. 375–385 (cit. on p. 42).
- [Ber+10] V. Berti et al. “Brain metabolic correlates of dopaminergic degeneration in de novo idiopathic Parkinson’s disease”. In: *European Journal of Nuclear Medicine and Molecular Imaging* 37.3 (Mar. 2010), pp. 537–544 (cit. on p. 136).
- [BF10] J. M. Bioucas-Dias and M. A. T. Figueiredo. “Alternating Direction Algorithms for Constrained Sparse Regression: Application to Hyperspectral Unmixing”. In: *Proc. IEEE GRSS Workshop Hyperspectral Image Signal Process.: Evolution in Remote Sens. (WHISPERS)*. 2010 (cit. on pp. 48, 53, 73, 78, 115, 145).
- [Bio+12] J. M. Bioucas-Dias et al. “Hyperspectral Unmixing Overview: Geometrical, Statistical, and Sparse Regression-Based Approaches”. In: *IEEE J. Sel. Topics Appl. Earth Observ. in Remote Sens.* 5.2 (Apr. 2012), pp. 354–379 (cit. on pp. 2, 33, 37, 45, 60, 63).
- [Bis06] C. M. Bishop. *Pattern Recognition and Machine Learning (Information Science and Statistics)*. Secaucus, NJ, USA: Springer-Verlag New York, Inc., 2006 (cit. on p. 38).
- [BLL01] R. Boellaard, A. van Lingen, and A. A. Lammertsma. “Experimental and Clinical Evaluation of Iterative Reconstruction (OSEM) in Dynamic PET: Quantitative Characteristics and Effects on Kinetic Modeling”. In: *J. Nuc. Med.* 42.5 (2001), pp. 808–817 (cit. on p. 22).

- [Blo+89] G. Blomqvist et al. “Dynamic models for reversible ligand binding”. In: *Positron emission tomography in clinical research and clinical diagnosis: tracer modelling and radioreceptors*. 1989 (cit. on pp. 24, 26, 34).
- [BN08] J. M. Bioucas-Dias and J. M. Nascimento. “Hyperspectral subspace identification”. In: *IEEE Trans. Geosci. Remote Sens.* 46.8 (2008), pp. 2435–2445 (cit. on p. 45).
- [Boe+08] R. Boellaard et al. “Performance of a modified supervised cluster algorithm for extracting reference region input functions from (R)-[11C]PK11195 brain PET studies”. In: Oct. 2008, pp. 5400–5402 (cit. on pp. 35, 75, 86).
- [Boy+11] S. Boyd et al. “Distributed optimization and statistical learning via the alternating direction method of multipliers”. In: *Foun. Tre. Mach. Lear.* 3.1 (2011), pp. 1–122 (cit. on p. 48).
- [Bra+03] J. Brankov et al. “Segmentation of Dynamic PET or fMRI Images Based on a Similarity Metric”. In: *IEEE Trans. Nucl. Sci.* 50.5 (Oct. 2003), pp. 1410–1414 (cit. on p. 34).
- [BSK07] B. Bodvarsson, L. K. H. C. Svarer, and G. Knudsen. “NMF ON POSITRON EMISSION TOMOGRAPHY”. In: *Proc. IEEE Int. Conf. Acoust., Speech, and Signal Processing (ICASSP)*. Vol. I. 2007, pp. 309–312 (cit. on p. 43).
- [BST13] J. Bolte, S. Sabach, and M. Teboulle. “Proximal alternating linearized minimization for nonconvex and nonsmooth problems”. In: *Math. Program., Ser. B* 146.1-2 (July 2013), pp. 459–494 (cit. on pp. 3, 69, 70, 72, 140, 143).
- [BT09a] A. Beck and M. Teboulle. “A fast Iterative Shrinkage-Thresholding Algorithm with application to wavelet-based image deblurring”. In: *Proc. IEEE Int. Conf. Acoust., Speech, and Signal Processing (ICASSP)*. Apr. 2009, pp. 693–696 (cit. on p. 164).
- [BT09b] A. Beck and M. Teboulle. “Fast Gradient-Based Algorithms for Constrained Total Variation Image Denoising and Deblurring Problems”. In: *IEEE Trans. Image Process.* 18.11 (Nov. 2009), pp. 2419–2434 (cit. on p. 164).
- [Buc02] D. L. Buckley. “Uncertainty in the analysis of tracer kinetics using dynamic contrast-enhanced T1-weighted MRI”. In: *Magnetic Resonance in Medicine: An Official Journal of the International Society for Magnetic Resonance in Medicine* 47.3 (2002), pp. 601–606 (cit. on p. 137).
- [Bul+01] E. Bullmore et al. “Colored Noise and Computational Inference in Neurophysiological (fMRI) Time Series Analysis: Resampling Methods in Time and Wavelet Domains”. In: *Human Brain Mapping* 12 (2001), pp. 61–78 (cit. on p. 65).
- [Buv+93] J. Buvat et al. “Target apex-seeking in factor analysis of medical image sequences”. In: *Phys. Med. Bio.* 38.1 (1993), p. 123 (cit. on p. 41).

- [Buv07] I. Buvat. “Quantification in emission tomography: Challenges, solutions, and performance”. In: *Nuclear Instruments and Methods in Physics Research Section A: Accelerators, Spectrometers, Detectors and Associated Equipment* 571.1 (2007), pp. 10–13 (cit. on pp. 1, 23).
- [BWT94] H. H. Barrett, D. W. Wilson, and B. M. W. Tsui. “Noise properties of the EM algorithm. I. Theory”. In: *Phys. Med. Bio.* 39.5 (1994), p. 833 (cit. on p. 98).
- [CA10] A. Cichocki and S.-i. Amari. “Families of Alpha- Beta- and Gamma- Divergences: Flexible and Robust Measures of Similarities”. In: *Entropy* 12.6 (2010), pp. 1532–1568 (cit. on p. 105).
- [Can+11] K. Canham et al. “Spatially adaptive hyperspectral unmixing”. In: *IEEE Trans. Geosci. Remote Sens.* 49.11 (2011), pp. 4248–4262 (cit. on p. 53).
- [Cau86] H. Caussinus. “Models and uses of principal component analysis”. In: *Multidimensional data analysis* 86 (1986), pp. 149–170 (cit. on p. 42).
- [Cav+17a] Y. C. Cavalcanti et al. “Démélange d’images TEP dynamiques”. In: *Actes du XXVIème Colloque GRETSI sur le Traitement du Signal et des Images (GRETSI 2017)*. Juan-les-Pins, France, Sept. 2017, pp. 425–429 (cit. on p. 59).
- [Cav+17b] Y. C. Cavalcanti et al. “Unmixing dynamic PET images with a PALM algorithm”. In: *Proc. European Signal Process. Conf. (EUSIPCO)*. Kos, Greece, Aug. 2017, pp. 425–429 (cit. on p. 59).
- [Cav+17c] Y. C. Cavalcanti et al. *Unmixing dynamic PET images with variable specific binding kinetics – Supporting materials*. Tech. rep. France: University of Toulouse, IRIT/INP-ENSEEIH, July 2017. URL: [http://dobigeon.perso.enseeiht.fr/papers/Cavalcanti\\_TechReport\\_2017.pdf](http://dobigeon.perso.enseeiht.fr/papers/Cavalcanti_TechReport_2017.pdf).
- [Cav+18a] Y. C. Cavalcanti et al. “Factor analysis of dynamic PET images: beyond Gaussian noise”. Submitted. 2018 (cit. on p. 97).
- [Cav+18b] Y. C. Cavalcanti et al. “Unmixing dynamic PET images with variable specific binding kinetics”. In: *Med Imag. Anal.* 49 (2018), pp. 117–127. ISSN: 1361-8415. DOI: <https://doi.org/10.1016/j.media.2018.07.011>. URL: <http://www.sciencedirect.com/science/article/pii/S1361841518305541> (cit. on p. 59).
- [Cav+18c] Y. C. Cavalcanti et al. “Unmixing dynamic PET images: combining spatial heterogeneity and non-Gaussian noise”. Submitted. 2018.
- [CBD84] F. Cavaillolles, J. P. Bazin, and R. Di Paola. “Factor analysis in gated cardiac studies”. In: *J. Nuc. Med.* 25 (1984), pp. 1067–1079 (cit. on pp. 1, 35, 41, 60).
- [CC97] S. Choi and A. Cichocki. “Adaptive blind separation of speech signals: Cocktail party problem”. In: *International Conference on Speech Processing*. 1997, pp. 617–622 (cit. on p. 37).

- [Cha+09] F. Chauveau et al. “Comparative evaluation of the translocator protein radioligands 11C-DPA-713, 18F-DPA-714, and 11C-PK11195 in a rat model of acute neuroinflammation”. In: *J. Nuc. Med.* 50.3 (2009), pp. 468–476 (cit. on p. 129).
- [Cha+11] T.-H. Chan et al. “A Simplex Volume Maximization Framework for Hyperspectral Endmember Extraction”. In: *IEEE Trans. Geosci. Remote Sens.* 49.11 (Nov. 2011), pp. 4177–4193 (cit. on p. 46).
- [CHB97] P. G. Coxson, R. H. Huesman, and L. Borland. “Consequences of Using a Simplified Kinetic Model for Dynamic PET Data”. In: *J. Nuc. Med.* 38.4 (1997), pp. 660–667 (cit. on pp. 22, 98).
- [Che+07] K. Chen et al. “Characterization of the image-derived carotid artery input function using independent component analysis for the quantitation of [18F] fluorodeoxyglucose positron emission tomography images”. In: *Phys. Med. Bio.* 52 (2007), pp. 7055–7071 (cit. on p. 43).
- [Che+11] L. Chen et al. “Tissue-Specific Compartmental Analysis for Dynamic Contrast-Enhanced MR Imaging of Complex Tumors”. In: *IEEE Trans. Med. Imag.* 30.12 (Dec. 2011), pp. 2044–2058 (cit. on pp. 137, 138).
- [CJ93] V. J. Cunningham and T. Jones. “Spectral Analysis of Dynamic PET Studies”. In: *J. Cer. Blo. Fl. Met.* 13.1 (1993), pp. 15–23 (cit. on p. 28).
- [Com94] P. Comon. “Independent component analysis, a new concept?” In: *Signal Process.* 36.3 (1994), pp. 287–314 (cit. on p. 38).
- [Con15] L. Condat. “Fast projection onto the simplex and the  $l_1$ -ball”. In: *Math. Program., Ser. B* 158.1-2 (Sept. 2015), pp. 575–585 (cit. on pp. 4, 48, 72, 111, 142).
- [CPR14] E. Chouzenoux, J.-C. Pesquet, and A. Repetti. “Variable Metric Forward–Backward Algorithm for Minimizing the Sum of a Differentiable Function and a Convex Function”. In: *Journal of Optimization Theory and Applications* 162.1 (July 2014), pp. 107–132 (cit. on p. 164).
- [CPR16] E. Chouzenoux, J.-C. Pesquet, and A. Repetti. “A block coordinate variable metric forward–backward algorithm”. In: *J. Glob. Optim* 66.3 (Nov. 2016), pp. 457–485 (cit. on p. 164).
- [CQ10] J. Cheng-Liao and J. Qi. “Segmentation of mouse dynamic PET images using a multiphase level set method”. In: *Phys. Med. Bio.* 55 (2010), pp. 6549–6569 (cit. on pp. 23, 34, 101).
- [Cra94] M. D. Craig. “Minimum-volume transforms for remotely sensed data”. In: *IEEE Trans. Geosci. Remote Sens.* 32.3 (1994), pp. 542–552 (cit. on p. 47).
- [CT03] E. Carlos and J.-i. Takada. “ICA based blind source separation applied to radio surveillance”. In: *IEICE transactions on communications* 86.12 (2003), pp. 3491–3497 (cit. on p. 37).

- [Cun+91] V. J. Cunningham et al. “Compartmental analysis of diprenorphine binding to opiate receptors in the rat in vivo and its comparison with equilibrium data in vitro”. In: *Journal of Cerebral Blood Flow & Metabolism* 11.1 (1991), pp. 1–9 (cit. on pp. 24, 26, 34).
- [CWT11] C.-l. Chang, C.-C. Wu, and C.-T. Tsai. “Random N-Finder (N-FINDR) Endmember Extraction Algorithms for Hyperspectral Imagery”. In: *IEEE Trans. Image Process.* 20.3 (Mar. 2011), pp. 641–656 (cit. on p. 46).
- [CZA06] A. Cichocki, R. Zdunek, and S.-i. Amari. “Csiszár’s Divergences for Non-negative Matrix Factorization: Family of New Algorithms”. In: *Independent Component Analysis and Blind Signal Separation: 6th International Conference, ICA 2006, Charleston, SC, USA, March 5-8, 2006. Proceedings.* Berlin, Heidelberg: Springer Berlin Heidelberg, 2006, pp. 32–39 (cit. on p. 109).
- [Dae+90] M. V. Daele et al. “Background correction in factor analysis of dynamic scintigraphic studies: necessity and implementation”. In: *Phys. Med. Bio.* 35.11 (1990), p. 1477. URL: <http://stacks.iop.org/0031-9155/35/i=11/a=004> (cit. on p. 41).
- [Dae+91] M. V. Daele et al. “A new vertex-finding algorithm for the oblique rotation step in factor analysis”. In: *Phys. Med. Bio.* 36.1 (1991), p. 77 (cit. on p. 42).
- [Dah+09] J. Dahl et al. “Algorithms and software for total variation image reconstruction via first-order methods”. In: *Numer. Algor.* 53.1 (July 2009), p. 67 (cit. on p. 72).
- [DB12] N. Dobigeon and N. Brun. “Spectral mixture analysis of EELS spectrum-images”. In: *Ultramicroscopy* 120 (Sept. 2012), pp. 25–34 (cit. on pp. 33, 37, 60).
- [DCJ16] L. Drumetz, J. Chanussot, and C. Jutten. “Variability of the endmembers in spectral unmixing: recent advances”. In: *Proc. IEEE GRSS Workshop Hyperspectral Image Signal Process.: Evolution in Remote Sens. (WHISPERS)*. 2016, pp. 1–5 (cit. on p. 52).
- [DDV00] L. De Lathauwer, B. De Moor, and J. Vandewalle. “Fetal electrocardiogram extraction by blind source subspace separation”. In: *IEEE Trans. Biomed. Eng.* 47.5 (2000), pp. 567–572 (cit. on p. 37).
- [DeL+09] C. DeLorenzo et al. “Modeling considerations for in vivo quantification of the dopamine transporter using [11C] PE2I and positron emission tomography”. In: *J. Cer. Blo. Fl. Met.* 29.7 (2009), pp. 1332–1345 (cit. on pp. 137, 146).
- [Del+14] C.-A. Deledalle et al. “Stein Unbiased GrAdient estimator of the Risk (SUGAR) for multiple parameter selection”. In: *SIAM J. Imaging Sciences* 7.4 (2014), pp. 2448–2487 (cit. on p. 164).
- [DKS06] Q. Du, I. Kopriva, and H. H. Szu. “Independent-component analysis for hyperspectral remote sensing imagery classification”. In: *Opt. Eng.* 45.1 (2006), p. 017008 (cit. on p. 37).

- 
- [DLL13] J. Dutta, R. M. Leahy, and Q. Li. “Non-Local Means Denoising of Dynamic PET Images”. In: *PLoS ONE* 8.12 (Dec. 2013) (cit. on p. 101).
  - [Dob+09] N. Dobigeon et al. “Joint Bayesian Endmember Extraction and Linear Unmixing for Hyperspectral Imagery”. In: *IEEE Trans. Signal Process.* 57.11 (Nov. 2009), pp. 4355–4368 (cit. on pp. 2, 45, 49).
  - [Dob+14a] N. Dobigeon et al. “A comparison of nonlinear mixing models for vegetated areas using simulated and real hyperspectral data”. In: *IEEE J. Sel. Topics Appl. Earth Observ. in Remote Sens.* 7.6 (June 2014), pp. 1869–1878 (cit. on pp. 50, 136).
  - [Dob+14b] N. Dobigeon et al. “Nonlinear unmixing of hyperspectral images: Models and algorithms”. In: *IEEE Signal Process. Mag.* 31.1 (2014), pp. 82–94 (cit. on pp. 2, 49, 50, 136).
  - [Dru+16] L. Drumetz et al. “Blind Hyperspectral Unmixing Using an Extended Linear Mixing Model to Address Spectral Variability”. In: *IEEE Trans. Image Process.* 25.8 (Aug. 2016), pp. 3890–3905 (cit. on p. 55).
  - [DS04] D. Donoho and V. Stodden. “When Does Non-Negative Matrix Factorization Give a Correct Decomposition into Parts?” In: *Adv. in Neural Information Processing Systems*. 2004 (cit. on p. 40).
  - [DTS07] N. Dobigeon, J.-Y. Tourneret, and J. D. Scargle. “Joint segmentation of multivariate astronomical time series: Bayesian sampling with a hierarchical model”. In: *IEEE Trans. Signal Process.* 55.2 (2007), pp. 414–423 (cit. on p. 33).
  - [Du+14] X. Du et al. “Spatial and spectral unmixing using the beta compositional model”. In: *IEEE J. Sel. Topics Appl. Earth Observ. in Remote Sens.* 7.6 (2014), pp. 1994–2003 (cit. on p. 54).
  - [Ear+08] J. F. Eary et al. “Spatial Heterogeneity in Sarcoma 18F-FDG Uptake as a Predictor of Patient Outcome”. In: *J. Nuc. Med.* 49.12 (Dec. 2008), pp. 1973–1979 (cit. on p. 61).
  - [Ech+10] O. Eches et al. “Bayesian estimation of linear mixtures using the normal compositional model. Application to hyperspectral imagery”. In: *IEEE Trans. Image Process.* 19.6 (2010), pp. 1403–1413 (cit. on p. 54).
  - [EG14] O. Eches and M. Guillaume. “A Bilinear-Bilinear Nonnegative Matrix Factorization Method for Hyperspectral Unmixing”. In: *IEEE Geosci. Remote Sens. Lett.* 11.4 (Apr. 2014), pp. 778–782 (cit. on p. 50).
  - [EK01] S. Eguchi and Y. Kano. *Robustifying maximum likelihood estimation. Technical report*. Tech. rep. Institute of Statistical Mathematics, June 2001 (cit. on p. 105).
  - [EK04] J. Eggert and E. Korner. “Sparse coding and NMF”. In: *Proc. Int. Joint Conf. Neural Net. (IJCNN)*. Vol. 4. July 2004, pp. 2529–2533 (cit. on pp. 99, 111).

- [El +05] G. El Fakhri et al. “Quantitative Dynamic Cardiac  $^{82}\text{Rb}$  PET Using Generalized Factor and Compartment Analyses”. In: *J. Nuc. Med.* 46.8 (Aug. 2005), pp. 1264–1271 (cit. on pp. 43, 137).
- [El +06] G. El Fakhri et al. “Generalized five-dimensional dynamic and spectral factor analysis”. In: *Medical Physics* 33.4 (2006), pp. 1016–1024 (cit. on p. 43).
- [El +09] G. El Fakhri et al. “Reproducibility and Accuracy of Quantitative Myocardial Blood Flow Assessment with  $^{82}\text{Rb}$  PET: Comparison with  $^{13}\text{N}$ -Ammonia PET”. In: *J. Nuc. Med.* 50.7 (2009), pp. 1062–1071 (cit. on p. 137).
- [Fan+09] W. Fan et al. “Comparative study between a new nonlinear model and common linear model for analysing laboratory simulated-forest hyperspectral data”. In: *Int. J. Remote Sens.* 30.11 (2009), pp. 2951–2962 (cit. on p. 51).
- [Far+03] D. Farina et al. “Blind source separation of multiplicative mixtures of non-stationary surface EMG signals”. In: *19 Colloque sur le traitement du signal et des images, FRA, 2003*. GRETSI, Groupe d’Etudes du Traitement du Signal et des Images. 2003 (cit. on p. 37).
- [Far+04] D. Farina et al. “Blind separation of linear instantaneous mixtures of nonstationary surface myoelectric signals”. In: *IEEE Trans. Biomed. Eng.* 51.9 (2004), pp. 1555–1567 (cit. on p. 37).
- [FBD09] C. Févotte, N. Bertin, and J.-L. Durrieu. “Nonnegative Matrix Factorization with the Itakura-Saito Divergence: With Application to Music Analysis”. In: *Neural Comput.* 21.3 (2009), pp. 793–830 (cit. on pp. 105, 107, 109).
- [FCC09] D. FitzGerald, M. Cranitch, and E. Coyle. “On the use of the beta divergence for musical source separation”. In: *IET Irish Signals and Systems Conference (ISSC 2009)*. June 2009, pp. 1–6 (cit. on p. 105).
- [FD15] C. Févotte and N. Dobigeon. “Nonlinear Hyperspectral Unmixing With Robust Nonnegative Matrix Factorization”. In: *IEEE Trans. Image Process.* 24.12 (Dec. 2015), pp. 4810–4819 (cit. on pp. 2, 4, 55, 107, 110, 111, 113).
- [FDM17] M. Filippi, M. Desvignes, and E. Moisan. “Robust Unmixing of Dynamic Sequences Using Regions of Interest (RUDUR)”. In: *IEEE Trans. Med. Imag.* PP.99 (2017), pp. 1–1 (cit. on p. 44).
- [Fer+17] V. Ferraris et al. “Robust fusion of multi-band images with different spatial and spectral resolutions for change detection”. In: *IEEE Trans. Comput. Imag.* 3.2 (Apr. 2017), pp. 175–186 (cit. on p. 68).
- [Fer+ed] V. Ferraris et al. “Coupled dictionary learning for unsupervised change detection between multi-sensor remote sensing images”. In: (submitted). URL: <https://arxiv.org/abs/1807.08118/> (cit. on p. 38).



- [Fes94] J. A. Fessler. “Penalized Weighted Least-Squares Image Reconstruction for Positron Emission Tomography”. In: *IEEE Trans. Med. Imag.* 13.2 (June 1994), pp. 290–300 (cit. on pp. 22, 65, 98).
- [FI11] C. Févotte and J. Idier. “Algorithms for Nonnegative Matrix Factorization with the  $\beta$ -Divergence”. In: *Neural Comput.* 23.9 (2011), pp. 2421–2456 (cit. on pp. 2, 4, 98, 106, 109, 114).
- [Fre+17] J. Frecon et al. “Bayesian Selection for the  $\ell_2$ -Potts Model Regularization Parameter: 1-D Piecewise Constant Signal Denoising”. In: *IEEE Trans. Signal Process.* 65.19 (2017), pp. 5215–5224 (cit. on p. 164).
- [Fri98] K. J. Friston. “Modes or models: a critique on independent component analysis for fMRI”. In: *Trends in cognitive sciences* 2.10 (1998), pp. 373–375 (cit. on p. 39).
- [GGC01] R. N. Gunn, S. R. Gunn, and V. J. Cunningham. “Positron emission tomography compartmental models”. In: *J. Cer. Blo. Fl. Met.* 21.6 (2001), pp. 635–652 (cit. on pp. 4, 27–29, 34, 136).
- [Gje82] A. Gjedde. “Calculation of cerebral glucose phosphorylation from brain uptake of glucose analogs in vivo: a re-examination”. In: *Brain Research Reviews* 4.2 (1982), pp. 237–274 (cit. on p. 28).
- [Goe+13] M. A. Goenaga et al. “Unmixing analysis of a time series of Hyperion images over the Guánica dry forest in Puerto Rico”. In: *IEEE J. Sel. Topics Appl. Earth Observ. in Remote Sens.* 6.2 (2013), pp. 329–338 (cit. on p. 53).
- [GPH04] C. Gobinet, E. Perrin, and R. Huez. “Application of non-negative matrix factorization to fluorescence spectroscopy”. In: *Proc. European Signal Process. Conf. (EUSIPCO)*. 2004, pp. 1095–1098 (cit. on p. 37).
- [GS00] L. Grippo and M. Sciandrone. “On the convergence of the block nonlinear Gauss–Seidel method under convex constraints”. In: *Operations Research Letters* 26.3 (2000), pp. 127–136 (cit. on p. 69).
- [Gun+02] R. N. Gunn et al. “Positron Emission Tomography Compartmental Models: A Basis Pursuit Strategy for Kinetic Modeling”. In: *J. Cer. Blo. Fl. Met.* 22.12 (2002), pp. 1425–1439 (cit. on pp. 24, 29, 136, 139, 147, 148, 163).
- [Gun+97] R. N. Gunn et al. “Parametric Imaging of Ligand-Receptor Binding in PET Using a Simplified Reference Region Model”. In: *NeuroImage* 6 (1997), pp. 279–287 (cit. on pp. 24, 61).
- [Guo+03] H. Guo et al. “Clustering huge data sets for parametric PET imaging”. In: *Biosystems* 71.1-2 (Sept. 2003), pp. 81–92 (cit. on p. 34).
- [GW08] R. C. Gonzalez and R. E. Woods. *Digital Image Processing*. Pearson, 2008 (cit. on p. 21).
- [Häg14] I. Häggström. *Quantitative Methods for Tumor Imaging with Dynamic PET*. Department of Radiation Sciences and Radiation Physics, 2014 (cit. on p. 73).

- [Hal+11] A. Halimi et al. “Nonlinear Unmixing of Hyperspectral Images Using a Generalized Bilinear Model”. In: *IEEE Trans. Geosci. Remote Sens.* 49.11 (Nov. 2011), pp. 4153–4162 (cit. on p. 51).
- [Hap81] B. Hapke. “Bidirectional reflectance spectroscopy: 1. Theory”. In: *Journal of Geophysical Research: Solid Earth* 86.B4 (1981), pp. 3039–3054 (cit. on p. 55).
- [Hap93] B. Hapke. *Theory of reflectance and emittance spectroscopy*. Cambridge university press, 1993 (cit. on p. 55).
- [HBS16] I. Häggström, B. J. Beattie, and C. R. Schmidlein. “Dynamic PET simulator via tomographic emission projection for kinetic modeling and parametric image studies”. In: *Medical Physics* 43.6 (2016), pp. 3104–3116 (cit. on p. 26).
- [HC01] D. C. Heinz and Chein-I-Chang. “Fully constrained least squares linear spectral mixture analysis method for material quantification in hyperspectral imagery”. In: *IEEE Trans. Geosci. Remote Sens.* 39.3 (Mar. 2001), pp. 529–545 (cit. on p. 47).
- [HDT15] A. Halimi, N. Dobigeon, and J.-Y. Tourneret. “Unsupervised Unmixing of Hyperspectral Images Accounting for Endmember Variability”. In: *IEEE Trans. Image Process.* 24.12 (Dec. 2015), pp. 4904–4917 (cit. on pp. 2, 49, 53, 54, 63).
- [Hen+14] S. Henrot et al. “Does deblurring improve geometrical hyperspectral unmixing?” In: *IEEE Trans. Image Process.* 23.3 (2014), pp. 1169–1180 (cit. on pp. 64, 83).
- [Hey+16] R. Heylen et al. “Hyperspectral Unmixing With Endmember Variability via Alternating Angle Minimization”. In: *IEEE Trans. Geosci. Remote Sens.* 54.8 (Aug. 2016), pp. 4983–4993 (cit. on p. 53).
- [HJA85] J. Hérault, C. Jutten, and B. Ans. “Détection de grandeurs primitives dans un message composite par une architecture de calcul neuromimétique en apprentissage non supervisé”. In: *10 Colloque sur le traitement du signal et des images, FRA, 1985*. GRETSI, Groupe d’Etudes du Traitement du Signal et des Images. 1985 (cit. on pp. 1, 37).
- [HO00] A. Hyvärinen and E. Oja. “Independent Component Analysis: Algorithms and Applications”. In: (2000), pp. 411–430 (cit. on p. 39).
- [Hon+08] I. Hong et al. “Ultra Fast 4D PET Image Reconstruction with User-Definable Temporal Basis Functions”. In: 2008, pp. 5475–5478 (cit. on p. 23).
- [Hou84] A. S. Houston. “The effect of apex-finding errors on factor images obtained from factor analysis and oblique transformation (nuclear medicine)”. In: *Phys. Med. Bio.* 29.9 (1984), p. 1109 (cit. on p. 41).

- [Hou86] A. Houston. “The use of set theory and cluster analysis to investigate the constraint problem in factor analysis in dynamic structures (FADS)”. In: *Information Processing in Medical Imaging*. Springer. 1986, pp. 177–192 (cit. on p. 41).
- [Hoy04] P. O. Hoyer. “Non-negative matrix factorization with sparseness constraints”. In: *J. Mach. Learning Research* 5 (Dec. 2004), pp. 1457–1469 (cit. on p. 40).
- [HPG14] R. Heylen, M. Parente, and P. Gader. “A review of nonlinear hyperspectral unmixing methods”. In: *IEEE J. Sel. Topics Appl. Earth Observ. in Remote Sens.* 7.6 (2014), pp. 1844–1868 (cit. on p. 49).
- [HS97] A. S. Houston and W. F. D. Sampson. “A quantitative comparison of some FADS methods in renal dynamic studies using simulated and phantom data”. In: *Phys. Med. Bio.* 42.1 (1997), p. 199 (cit. on pp. 42, 61).
- [Hua+11] Y. Huang et al. “Temporal Dynamics of Host Molecular Responses Differentiate Symptomatic and Asymptomatic Influenza A Infection”. In: *PLoS Genetics* 8.7 (Aug. 2011) (cit. on p. 60).
- [Hua+80] S. C. Huang et al. “Noninvasive determination of local cerebral metabolic rate of glucose in man”. In: *American Journal of Physiology-Endocrinology and Metabolism* 238.1 (1980), E69–E82 (cit. on p. 137).
- [Hua11] Z. Huang. “On the spectral radius and the spectral norm of Hadamard products of nonnegative matrices”. In: *Linear Algebra and its Applications* 434.2 (Jan. 2011), pp. 457–462 (cit. on pp. 168, 184, 186).
- [Hum+92] S. P. Hume et al. “Quantitation of Carbon-11-labeled raclopride in rat striatum using positron emission tomography”. In: *Synapse* 12.1 (1992), pp. 47–54 (cit. on pp. 24, 34).
- [HZ98] S.-C. Huang and Y. Zhou. “Spatially-coordinated regression for image-wise model fitting to dynamic PET data for generating parametric images”. In: *IEEE Trans. Nucl. Sci.* 45.3 (June 1998), pp. 1194–1199 (cit. on p. 136).
- [IBP11] M.-D. Iordache, J. M. Bioucas-Dias, and A. Plaza. “Sparse Unmixing of Hyperspectral Data”. In: *IEEE Trans. Geosci. Remote Sens.* 49.6 (June 2011), pp. 2014–2039 (cit. on pp. 45, 53).
- [Inn+07] R. B. Innis et al. “Consensus nomenclature for in vivo imaging of reversibly binding radioligands”. In: *J. Cer. Blo. Fl. Met.* 27.9 (May 2007), pp. 1533–1539 (cit. on pp. 24, 59, 61).
- [Ira+11] Z. Irace et al. “Bayesian segmentation of chest tumors in PET scans using a Poisson-Gamma mixture model”. In: *Proc. IEEE-SP Workshop Stat. and Signal Processing (SSP)*. June 2011, pp. 809–812 (cit. on pp. 22, 98).

- [Ira+16] Z. Irace et al. “PCA-based approach for inhomogeneous PSF estimation and partial volume correction in PET”. In: *2016 IEEE Nuclear Science Symposium, Medical Imaging Conference and Room-Temperature Semiconductor Detector Workshop (NSS/MIC/RTSD)*. Oct. 2016, pp. 1–3 (cit. on p. 164).
- [Jen+12] T. L. Jensen et al. “Implementation of an optimal first-order method for strongly convex total variation regularization”. In: *BIT Numerical Mathematics* 52.2 (June 2012), pp. 329–356 (cit. on p. 72).
- [JH91] C. Jutten and J. Herault. “Blind separation of sources, part I: An adaptive algorithm based on neuromimetic architecture”. In: *Signal Process.* 24.1 (1991), pp. 1–10 (cit. on pp. 1, 37).
- [JP05] H. Jadvar and J. Parker. *Clinical PET and PET/CT*. Springer, 2005 (cit. on pp. 12, 13, 15, 16).
- [Kam+05] M. E. Kamasak et al. “Direct reconstruction of kinetic parameter images from dynamic PET data”. In: *IEEE Trans. Med. Imag.* 24.5 (May 2005), pp. 636–650 (cit. on p. 136).
- [Kam09] M. E. Kamasak. “Clustering dynamic PET images on the Gaussian distributed sinogram domain”. In: *Comput. Methods Programs Biomed.* 93 (2009), pp. 217–227 (cit. on pp. 22, 34, 98).
- [Kar+15] N. A. Karakatsanis et al. “Clinical evaluation of direct 4D whole-body PET parametric imaging with time-of-flight and resolution modeling capabilities”. In: *2015 IEEE Nuclear Science Symposium and Medical Imaging Conference (NSS/MIC)*. Oct. 2015, pp. 1–6 (cit. on p. 83).
- [Kes03] N. Keshava. “A Survey of Spectral Unmixing Algorithms”. In: *Lincoln Laboratory Journal* 14 (2003), pp. 56–78 (cit. on p. 45).
- [Kim+01] K. M. Kim et al. “Noninvasive Estimation of Cerebral Blood Flow Using Image-Derived Carotid Input Function in  $H_2^{15}O$  Dynamic PET”. In: 2001, pp. 1282–1285 (cit. on pp. 2, 43).
- [Kle+10] R. Klein et al. “Kinetic model-based factor analysis of dynamic sequences for 82-rubidium cardiac positron emission tomography”. In: *Medical Physics* 37.8 (2010), pp. 3995–4010 (cit. on p. 137).
- [Kom07] R. Kompass. “A Generalized Divergence Measure for Nonnegative Matrix Factorization”. In: *Neural Comput.* 19.3 (2007), pp. 780–791 (cit. on p. 109).
- [KP00] J. Klingseisen and M. Plumbley. “Towards musical instrument separation using multiple-cause neural networks”. In: *Proceedings of the International Workshop on Independent Component Analysis And Blind Signal Separation, 19-22 June 2000, Helsinki, Finland*. 2000, pp. 447–452 (cit. on p. 37).
- [KR09] T. Kernane and Z. A. Raizah. “Fixed point iteration for estimating the parameters of extreme value distributions”. In: *Communications in Statistics-Simulation and Computation* 38.10 (2009), pp. 2161–2170 (cit. on p. 103).

- [Kre+03] K. Kreutz-Delgado et al. “Dictionary learning algorithms for sparse representation”. In: *Neural Comput.* 15.2 (2003), pp. 349–396 (cit. on p. 38).
- [KS48] S. S. Kety and C. F. Schmidt. “The nitrous oxide method for the quantitative determination of cerebral blood flow in man: theory, procedure and normal values”. In: *The Journal of clinical investigation* 27.4 (1948), pp. 476–483 (cit. on pp. 24, 25, 34).
- [KTR06] E. Krestyannikov, J. Tohka, and U. Ruotsalainen. “Segmentation of Dynamic Emission Tomography Data in Projection Space”. In: *Int. Workshop Comput. Vision Approaches Med. Image Anal.* Vol. 4241. 2006, pp. 108–119 (cit. on p. 34).
- [Lav+15] S. Lavis et al. “Optimized quantification of translocator protein radioligand 18F-DPA-714 uptake in the brain of genotyped healthy volunteers”. In: *J. Nuc. Med.* 56.7 (2015), pp. 1048–1054 (cit. on p. 20).
- [LBO97] T.-W. Lee, A. J. Bell, and R. Orglmeister. “Blind source separation of real world signals”. In: *Neural Networks, 1997., International Conference on.* Vol. 4. 1997, pp. 2129–2134 (cit. on p. 37).
- [Lee+01a] J. S. Lee et al. “Blind Separation of Cardiac Components and Extraction of Input Function from  $H^{15}_2O$  Dynamic Myocardial PET Using Independent and Component Analysis”. In: *J. Nuc. Med.* 42.6 (2001), pp. 938–943 (cit. on p. 43).
- [Lee+01b] J. S. Lee et al. “Non-negative Matrix Factorization of Dynamic Images in Nuclear Medicine”. In: 2001 (cit. on pp. 1, 35, 43, 60, 98).
- [LH96] A. A. Lammertsma and S. P. Hume. “Simplified reference tissue model for PET receptor studies”. In: *NeuroImage* 4.3 (1996), pp. 153–158 (cit. on pp. 24, 26, 34, 136).
- [Lin+14] Y. Lin et al. “Sparsity Constrained Mixture Modeling for the Estimation of Kinetic Parameters in Dynamic PET”. In: *IEEE Trans. Med. Imag.* 33.1 (Jan. 2014), pp. 173–185 (cit. on p. 137).
- [LL15] H. Li and Z. Lin. “Accelerated proximal gradient methods for nonconvex programming”. In: *Advances in neural information processing systems*. 2015, pp. 379–387 (cit. on p. 164).
- [Log00] J. Logan. “Graphical analysis of PET data applied to reversible and irreversible tracers”. In: *Nuclear Medicine and Biology* 27.7 (2000), pp. 661–670 (cit. on p. 28).
- [LS00] D. D. Lee and H. S. Seung. “Algorithms for non-negative matrix factorization”. In: *Adv. in Neural Information Processing Systems*. 2000 (cit. on pp. 38, 40, 77).
- [MAI12] J.-A. MAISONOBE. “Caractérisation des tumeurs et de leur évolution en TEP/TDM au 18F-FDG pour le suivi thérapeutique”. PhD thesis. Université Paris-Sud, 2012 (cit. on pp. 21, 164).

- [Mar+08] R. Maroy et al. “Segmentation of Rodent Whole-Body Dynamic PET Images: An Unsupervised Method Based on Voxel Dynamics”. In: *IEEE Trans. Med. Imag.* 27.3 (Mar. 2008), pp. 342–354 (cit. on p. 34).
- [Mar+10] M. Margadan-Mendez et al. “ICA Based Automatic Segmentation of Dynamic  $H_2^{15}O$  Cardiac PET Images”. In: *IEEE Trans. Inf. Technol. Biomed.* 14.3 (May 2010), pp. 795–802 (cit. on p. 43).
- [McK+98] M. J. McKeown et al. “Analysis of fMRI data by blind separation into independent spatial components”. In: *Human brain mapping* 6.3 (1998), pp. 160–188 (cit. on p. 37).
- [Meg+14] I. Meganem et al. “Linear-Quadratic Mixing Model for Reflectances in Urban Environments”. In: *IEEE Trans. Geosci. Remote Sens.* 52.1 (Jan. 2014), pp. 544–558 (cit. on p. 50).
- [Meh+17] A. Mehranian et al. “PET image reconstruction using multi-parametric anato-functional priors”. In: *Phys. Med. Bio.* 62.15 (2017), p. 5975 (cit. on pp. 65, 75).
- [MHO17] T. Mou, J. Huang, and F. O’Sullivan. “The Gamma Characteristic of Reconstructed PET Images: Implications for ROI Analysis”. In: PP.99 (2017), pp. 1–1 (cit. on pp. 22, 98, 119).
- [Min+84] M. A. Mintun et al. “A quantitative model for the in vivo assessment of drug binding sites with positron emission tomography”. In: *Annals of neurology* 15.3 (1984), pp. 217–227 (cit. on pp. 24, 25).
- [MOM00] S. M, M. OR, and L. M. “Partial volume effect correction: Methodological considerations”. In: *Physiological Imaging of the Brain with PET*. Ed. by G. A et al. San Diego: Academic, 2000. Chap. 11, p. 413 (cit. on pp. 22, 98).
- [Mor90] D. Morrison. “Multivariate statistical methods”. In: McGraw Hill, New York, 1990. Chap. 7 (cit. on p. 41).
- [Mos11] W. W. Moses. “Fundamental Limits of Spatial Resolution in PET”. In: *Nuclear instruments and methods in physics research* (2011) (cit. on p. 21).
- [Mou+13] S. Mouysset et al. “Segmentation of dynamic PET and images with kinetic spectral clustering”. In: *Phys. Med. Bio.* 58 (2013), pp. 6931–6944 (cit. on p. 34).
- [Mou05] S. Moussaoui. “Séparation de sources non-négatives. Application au traitement des signaux de spectroscopie”. PhD thesis. Université Henri Poincaré-Nancy I, 2005 (cit. on p. 37).
- [Muz+05] M. Muzi et al. “Kinetic Modeling of 3’-Deoxy-3’-Fluorothymidine in Somatic Tumors: Mathematical Studies”. In: *J. Nuc. Med.* 46.2 (2005), pp. 371–380 (cit. on p. 61).
- [Muz+12] M. Muzi et al. “Quantitative assessment of dynamic PET imaging data in cancer imaging”. In: *Magn. Resonance Imag.* 30.9 (Nov. 2012), pp. 1203–1215 (cit. on pp. 1, 10, 20).

- [NB09] J. M. Nascimento and J. M. Bioucas-Dias. “Nonlinear mixture model for hyperspectral unmixing”. In: *Image and Signal Processing for Remote Sensing XV*. Vol. 7477. International Society for Optics and Photonics. 2009, p. 74770I (cit. on pp. [2](#), [49](#), [51](#)).
- [NB85] K. S. Nijran and D. C. Barber. “Towards automatic analysis of dynamic radionuclide studies using principal-components factor analysis”. In: *Phys. Med. Bio.* 30.12 (1985), p. 1315 (cit. on pp. [41](#), [137](#)).
- [NB86] K. S. Nijran and D. C. Barber. “Factor analysis of dynamic function studies using a priori physiological information (nuclear medicine)”. In: *Phys. Med. Bio.* 31.10 (1986), p. 1107 (cit. on p. [41](#)).
- [NB88] K. Nijran and D. Barber. “The importance of constraints in factor analysis of dynamic studies”. In: *Information processing in medical imaging*. Springer. 1988, pp. 521–529 (cit. on p. [41](#)).
- [ND05a] J. Nascimento and J. Dias. “Does independent component analysis play a role in unmixing hyperspectral data?” In: *IEEE Trans. Geosci. Remote Sens.* 43.1 (Jan. 2005), pp. 175–187 (cit. on pp. [37](#), [39](#), [43](#)).
- [ND05b] J. Nascimento and J. Dias. “Vertex component analysis: a fast algorithm to unmix hyperspectral data”. In: *IEEE Trans. Geosci. Remote Sens.* 43.4 (Apr. 2005), pp. 898–910 (cit. on pp. [46](#), [78](#), [116](#)).
- [Nes83] Y. E. Nesterov. “A method for solving the convex programming problem with convergence rate  $O(1/k^2)$ ”. In: *Dokl. Akad. Nauk SSSR*. Vol. 269. 1983, pp. 543–547 (cit. on p. [164](#)).
- [NSK89] M. Nakamura, Y. Suzuki, and S. Kobayashi. “A method for recovering physiological components from dynamic radionuclide images using the maximum entropy principle: a numerical investigation”. In: 36.9 (Sept. 1989), pp. 906–917 (cit. on p. [41](#)).
- [OF96] B. A. Olshausen and D. J. Field. “Emergence of simple-cell receptive field properties by learning a sparse code for natural images”. In: *Nature* 381.6583 (1996), p. 607 (cit. on p. [38](#)).
- [OP08] P. D. O’Grady and B. A. Pearlmutter. “Discovering speech phones using convolutive non-negative matrix factorisation with a sparseness constraint”. In: 72.1 (2008), pp. 88–101 (cit. on p. [105](#)).
- [Oue+14] W. S. B. Ouedraogo et al. “Non-Negative Blind Source Separation Algorithm Based on Minimum Aperture Simplicial Cone”. In: *IEEE Trans. Signal Process.* 62.2 (Jan. 2014), pp. 376–389 (cit. on p. [44](#)).
- [Pad+12] M. Padilla P. and López et al. “NMF-SVM Based CAD Tool Applied to Functional Brain Images for the Diagnosis of Alzheimer’s Disease”. In: *IEEE Trans. Med. Imag.* Vol. 31. 2. Feb. 2012, pp. 207–216 (cit. on pp. [35](#), [43](#), [98](#)).

- [Pad03] A. Padhani. “MRI for assessing antivasular cancer treatments”. In: *The British journal of radiology* 76.suppl\_1 (2003), S60–S80 (cit. on p. 137).
- [Paj+98] S. Pajevic et al. “Noise Characteristics and of 3D and 2D PET and Images”. In: *IEEE Trans. Med. Imag.* Vol. 17. 1. Feb. 1998, pp. 1–23 (cit. on p. 101).
- [Pao+82] R. D. Paola et al. “Handling of Dynamic Sequences in Nuclear Medicine”. In: *IEEE Trans. Nucl. Sci.* 29.4 (Aug. 1982), pp. 1310–1321 (cit. on pp. 1, 41).
- [PBF15] M. Pereyra, J. M. Bioucas-Dias, and M. A. Figueiredo. “Maximum-a-posteriori estimation with unknown regularisation parameters”. In: *Proc. European Signal Process. Conf. (EUSIPCO)*. 2015, pp. 230–234 (cit. on p. 164).
- [PBF83] C. S. Patlak, R. G. Blasberg, and J. D. Fenstermacher. “Graphical evaluation of blood-to-brain transfer constants from multiple-time uptake data”. In: *J. Cer. Blo. Fl. Met.* 3.1 (1983), pp. 1–7 (cit. on p. 28).
- [PDH14] S.-U. Park, N. Dobigeon, and A. O. Hero. “Variational semi-blind sparse deconvolution with orthogonal kernel bases and its application to MRFM”. In: *Signal Process.* 94 (Jan. 2014), pp. 386–400 (cit. on p. 64).
- [Pen+08] J. Y. Peng et al. “Dynamic Positron Emission Tomography Data-Driven Analysis Using Sparse Bayesian Learning”. In: *IEEE Trans. Med. Imag.* 27.9 (Sept. 2008), pp. 1356–1369 (cit. on p. 136).
- [PH01] A. R. Padhani and J. E. Husband. “Dynamic contrast-enhanced MRI studies in oncology with an emphasis on quantification, validation and human studies”. In: *Clinical radiology* 56.8 (2001), pp. 607–620 (cit. on p. 137).
- [Phe+79] M. Phelps et al. “Tomographic measurement of local cerebral glucose metabolic rate in humans with (F-18) 2-fluoro-2-deoxy-D-glucose: validation of method”. In: *Annals of neurology* 6.5 (1979), pp. 371–388 (cit. on pp. 24, 34).
- [Pin+02] L. H. Pinborg et al. “Quantification of [123I]PE2I binding to dopamine transporters with SPET”. In: 29.5 (May 2002), pp. 623–631 (cit. on p. 146).
- [Pla+04] A. Plaza et al. “A quantitative and comparative analysis of endmember extraction algorithms from hyperspectral data”. In: *IEEE Trans. Geosci. Remote Sens.* 42.3 (2004), pp. 650–663 (cit. on p. 46).
- [Pla+12] J. Plaza et al. “On endmember identification in hyperspectral images without pure pixels: A comparison of algorithms”. In: *J. Math. Imag. Vision* 42.2-3 (2012), pp. 163–175 (cit. on p. 49).



- 
- [PMS86] M. E. Phelps, J. C. Mazziotta, and H. R. Schelbert. *Positron Emission Tomography and Autoradiography (Principles and Applications for the Brain and Heart)*. Raven, New York, 1986 (cit. on pp. [75](#), [115](#)).
- [Pow73] M. J. D. Powell. “On search directions for minimization algorithms”. In: *Math. Program., Ser. B* 4.1 (Dec. 1973), pp. 193–201 (cit. on p. [69](#)).
- [Raz+05] P. Razifar et al. “Noise correlation in PET, CT, SPECT and PET/CT data evaluated using autocorrelation function: a phantom study on data, reconstructed using FBP and OSEM”. In: *BMC Med. Imag.* 5.1 (Aug. 2005) (cit. on pp. [22](#), [98](#)).
- [Rey07] M. Rey. “Etude du Tomographe de Haute Résolution pour Petits Animaux ClearPET par la Méthode de Monte Carlo”. PhD thesis. Ecole Polytechnique Fédérale de Lausanne, 2007 (cit. on p. [17](#)).
- [RQS13] A. Rahmim, J. Qi, and V. Sossi. “Resolution modeling in PET imaging: theory, practice, benefits, and pitfalls”. In: *Medical Physics* 40.6 (June 2013) (cit. on pp. [65](#), [75](#)).
- [RT13] A. Rahmim and J. Tang. “Noise propagation in resolution modeled PET and imaging and its impact on detectability”. In: *Phys. Med. Bio.* 58 (2013), pp. 6945–6968 (cit. on p. [101](#)).
- [RTZ] A. Rahmim, J. Tang, and H. Zaidi. “Four-dimensional (4D) image reconstruction strategies in dynamic PET: Beyond conventional independent frame reconstruction”. In: *Medical Physics* 36.8 (), pp. 3654–3670 (cit. on p. [20](#)).
- [Sam+87] M. Samal et al. “Rotation to simple structure in factor analysis of dynamic radionuclide studies”. In: *Phys. Med. Bio.* 32.3 (1987), p. 371 (cit. on p. [41](#)).
- [SBB07] M. Soret, S. L. Bacharach, and I. Buvat. “Partial-Volume Effect in PET Tumor Imaging”. In: *J. Nuc. Med.* 48 (June 2007), pp. 932–945 (cit. on p. [22](#)).
- [SC13] S. Stute and C. Comtat. “Practical considerations for image-based PSF and blobs reconstruction in PET”. In: *Phys. Med. Bio.* 58.11 (2013), p. 3849 (cit. on p. [116](#)).
- [Sch+07] C. Schiepers et al. “<sup>18</sup>F-fluorothymidine kinetics of malignant brain tumors”. In: 34.7 (Feb. 2007), pp. 1003–1011 (cit. on p. [61](#)).
- [Sch13] D. Schulz. “Non-Negative Matrix Factorization Based Input Function Extraction for Mouse Imaging in Small Animal PET - Comparison with Arterial Blood Sampling and Factor Analysis”. In: *J. Molecular Imag. Dynamics* 02 (2013) (cit. on pp. [35](#), [43](#), [98](#)).
- [Sch79] P. Schmidlin. “Quantitative evaluation and imaging of functions using pattern recognition methods”. In: *Phys. Med. Bio.* 24.2 (1979), p. 385 (cit. on p. [41](#)).

- [SDG00] A. Sitek, E. V. R. Di Bella, and G. T. Gullberg. “Factor analysis with a priori knowledge - application in dynamic cardiac SPECT”. In: *Phys. Med. Bio.* 45 (2000), pp. 2619–2638. (Cit. on pp. [1](#), [42](#), [60](#), [146](#)).
- [SGH02] A. Sitek, G. T. Gullberg, and R. H. Huesman. “Correction for Ambiguous Solutions in Factor Analysis Using a Penalized Least Squares Objective”. In: *IEEE Trans. Med. Imag.* 21.3 (2002), pp. 216–225 (cit. on p. [43](#)).
- [Sok+77] L. Sokoloff et al. “The [14C] deoxyglucose method for the measurement of local cerebral glucose utilization: theory, procedure, and normal values in the conscious and anesthetized albino rat”. In: *Journal of neurochemistry* 28.5 (1977), pp. 897–916 (cit. on pp. [24](#), [34](#)).
- [Som+09] B. Somers et al. “Nonlinear Hyperspectral Mixture Analysis for tree cover estimates in orchards”. In: *Remote Sens. Environment* 113.6 (2009), pp. 1183–1193 (cit. on p. [51](#)).
- [Som+11] B. Somers et al. “Endmember variability in Spectral Mixture Analysis: A review”. In: *Remote Sens. Environment* 115.7 (2011), pp. 1603–1616 (cit. on p. [52](#)).
- [Som+12] B. Somers et al. “Automated extraction of image-based endmember bundles for improved spectral unmixing”. In: *IEEE J. Sel. Topics Appl. Earth Observ. in Remote Sens.* 5.2 (2012), pp. 396–408 (cit. on p. [53](#)).
- [Ste81] C. M. Stein. “Estimation of the mean of a multivariate normal distribution”. In: *The annals of Statistics* (1981), pp. 1135–1151 (cit. on p. [164](#)).
- [Stu+15] S. Stute et al. “Analytical Simulations of Dynamic PET Scans with Realistic Count Rates Properties”. In: *2015 IEEE Nuclear Science Symposium and Medical Imaging Conference (NSS/MIC)*. Nov. 2015 (cit. on pp. [75](#), [115](#)).
- [Stu10] S. Stute. “Modélisation avancée en simulations Monte Carlo de tomographie par émission de positons pour l’amélioration de la reconstruction et de la quantification”. PhD thesis. Université Paris-Sud, 2010 (cit. on p. [19](#)).
- [Sub16] R. Subramaniam. *Molecular Imaging and Precision Medicine, Part 1, An Issue of PET Clinics*. Elsevier, 2016 (cit. on p. [61](#)).
- [SV82] L. Shepp and Y. Vardi. “Maximum likelihood reconstruction for emission tomography”. In: *IEEE Trans. Med. Imag.* (May 1982), pp. 113–122 (cit. on pp. [65](#), [98](#)).
- [Sza+93] Z. Szabo et al. “Noncompartmental and compartmental modeling of the kinetics of carbon-11 labeled pyrilamine in the human brain”. In: *Synapse* 15.4 (1993), pp. 263–275 (cit. on p. [137](#)).

- [TDT16a] P.-A. Thouvenin, N. Dobigeon, and J.-Y. Tournet. “Hyperspectral Unmixing with Spectral Variability Using a Perturbed Linear Mixing Model”. In: *IEEE Trans. Signal Process.* 64.2 (2016), pp. 525–538 (cit. on pp. 3, 55, 63).
- [TDT16b] P.-A. Thouvenin, N. Dobigeon, and J.-Y. Tournet. “Online unmixing of multitemporal hyperspectral images accounting for spectral variability”. In: *IEEE Trans. Image Process.* 25.9 (2016), pp. 3979–3990 (cit. on p. 55).
- [Tey+12] A. Teymurazyan et al. “Properties of Noise in Positron Emission Tomography Images Reconstructed with Filtered-Backprojection and Row-Action Maximum Likelihood Algorithm”. In: *J. Digit. Imag.* 26.3 (Aug. 2012), pp. 447–456 (cit. on pp. 22, 98, 101, 119).
- [TF13] V. Y. F. Tan and C. Févotte. “Automatic Relevance Determination in Nonnegative Matrix Factorization with the /spl beta/-Divergence”. In: *IEEE Trans. Pattern Anal. Mach. Intell.* 35.7 (July 2013), pp. 1592–1605 (cit. on pp. 113, 114).
- [Thi+06] T. Thireou et al. “Blind source separation for the computational analysis of dynamic oncological PET studies”. In: *Oncol Rep* 15 (2006), pp. 1007–1012 (cit. on p. 65).
- [Tho17] P.-A. Thouvenin. “Modeling spatial and temporal variabilities in hyperspectral image unmixing”. PhD thesis. Institut National Polytechnique de Toulouse, 2017 (cit. on p. 55).
- [Tib96] R. Tibshirani. “Regression Shrinkage and Selection via the Lasso”. In: *J. Roy. Stat. Soc.* 58.1 (1996), pp. 267–288 (cit. on p. 40).
- [Tom+08] G. Tomasi et al. “Novel reference region model reveals increased microglial and reduced vascular binding of 11C-(R)-PK11195 in patients with Alzheimer’s disease”. In: *J. Nuc. Med.* 49.8 (2008), pp. 1249–1256 (cit. on p. 35).
- [Tro59] H. Trotter. “An elementary proof of the central limit theorem”. In: *Archiv der Mathematik* 10.1 (1959), pp. 226–234 (cit. on p. 22).
- [TS15] O. Tichy and V. Smidl. “Bayesian Blind Separation and Deconvolution of Dynamic Image Sequences Using Sparsity Priors”. In: *IEEE Trans. Med. Imag.* (2015) (cit. on p. 65).
- [TTA12] G. Tomasi, F. Turkheimer, and E. Aboagye. “Importance of Quantification for the Analysis of PET Data in Oncology: Review of Current Methods and Trends for the Future”. In: *Molecular Imaging and Biology* 14.2 (Apr. 2012), pp. 131–146 (cit. on p. 23).
- [Tur+03] F. Turkheimer et al. “A linear wavelet filter for parametric imaging with dynamic PET”. In: *IEEE Trans. Med. Imag.* 22.3 (Mar. 2003), pp. 289–301 (cit. on p. 65).
- [Tur+07] F. E. Turkheimer et al. “Reference and Target Region Modeling of [11C]-(R)-PK11195 Brain Studies”. In: *J. Nuc. Med.* (2007) (cit. on p. 35).

- [Uez+16a] T. Uezato et al. “Incorporating Spatial Information and Endmember Variability Into Unmixing Analyses to Improve Abundance Estimates”. In: *IEEE Trans. Image Process.* 25.12 (Dec. 2016), pp. 5563–5575 (cit. on p. 53).
- [Uez+16b] T. Uezato et al. “A novel endmember bundle extraction and clustering approach for capturing spectral variability within endmember classes”. In: *IEEE Trans. Geosci. Remote Sens.* 54.11 (2016), pp. 6712–6731 (cit. on p. 53).
- [Van03] P. Vanroose. “Blind source separation of speech and background music for improved speech recognition”. In: *The 24th Symposium on Information Theory*. 2003, pp. 103–108 (cit. on p. 37).
- [Veg+14a] M. A. Veganzones et al. “A new extended linear mixing model to address spectral variability”. In: *Proc. IEEE GRSS Workshop Hyperspectral Image Signal Process.: Evolution in Remote Sens. (WHISPERS)*. June 2014, pp. 1–4 (cit. on p. 55).
- [Veg+14b] M. A. Veganzones et al. “Hyperspectral image segmentation using a new spectral unmixing-based binary partition tree representation”. In: *IEEE Trans. Image Process.* 23.8 (2014), pp. 3574–3589 (cit. on p. 53).
- [Vin+03] E. Vincent et al. “A tentative typology of audio source separation tasks”. In: *4th Int. Symp. on Independent Component Analysis and Blind Signal Separation (ICA)*. 2003, pp. 715–720 (cit. on p. 37).
- [VO00] R. Vigário and E. Oja. “Independence: A new criterion for the analysis of the electromagnetic fields in the global brain?”. In: 13.8-9 (2000), pp. 891–907 (cit. on p. 37).
- [WEG87] S. Wold, K. Esbensen, and P. Geladi. “Principal component analysis”. In: *Chemometrics and intelligent laboratory systems 2.1-3* (1987), pp. 37–52 (cit. on p. 39).
- [Win99] M. E. Winter. “N-FINDR: an algorithm for fast autonomous spectral end-member determination in hyperspectral data”. In: *Proc. SPIE Imaging Spectrometry V*. Vol. 3753. 1. 1999, pp. 266–275 (cit. on pp. 73, 115, 145).
- [Won+02] K.-P. Wong et al. “Segmentation of Dynamic PET Images Using Cluster Analysis”. In: *IEEE Trans. Nucl. Sci.* 49.1 (Feb. 2002) (cit. on p. 34).
- [Wri15] S. J. Wright. “Coordinate descent algorithms”. In: *Math. Program., Ser. B* 151.1 (2015), pp. 3–34 (cit. on p. 164).
- [WTB94] D. Wilson, B. Tsui, and H. Barrett. “Noise properties of the EM algorithm. II. Monte Carlo simulations”. In: *Phys. Med. Bio.* 39 (1994), pp. 847–871 (cit. on pp. 22, 65, 98).
- [Wu+95] H.-M. Wu et al. “Factor Analysis for Extraction of Blood Time-Activity Curves in Dynamic FDG-PET Studies”. In: *J. Nuc. Med.* 36.9 (Sept. 1995), pp. 1714–1722 (cit. on pp. 35, 37, 42, 60).

- [XB99] J. Xavier and V. Barroso. “Blind source separation, ISI cancellation and carrier phase recovery in SDMA systems for mobile communications”. In: *Wireless Personal Communications* 10.1 (1999), pp. 53–76 (cit. on p. 37).
- [Yaq+12] M. Yaqub et al. “Optimization of supervised cluster analysis for extracting reference tissue input curves in (R)-[11C]PK11195 brain PET studies”. In: *J. Cer. Blo. Fl. Met.* 32.8 (May 2012), pp. 1600–1608 (cit. on pp. 35, 75, 86, 115).
- [YL06] M. Yuan and Y. Lin. “Model selection and estimation in regression with grouped variables”. In: *J. Roy. Stat. Soc. Ser. B* 68 (2006), pp. 49–67 (cit. on p. 68).
- [Yu+09] H. Yu et al. “Automated radiation targeting in head-and-neck cancer using region-based texture analysis of PET and CT images”. In: *Int J Radiat Oncol Biol Phys.* 75.2 (2009), pp. 618–625 (cit. on p. 61).
- [ZGC13] A. Zare, P. Gader, and G. Casella. “Sampling piecewise convex unmixing and endmember extraction”. In: *IEEE Trans. Geosci. Remote Sens.* 51.3 (2013), pp. 1655–1665 (cit. on p. 53).
- [ZH14] A. Zare and K. Ho. “Endmember Variability in Hyperspectral Analysis: Addressing Spectral Variability During Spectral Unmixing”. In: *IEEE Signal Process. Mag.* 31.1 (Jan. 2014), pp. 95–104 (cit. on pp. 2, 49, 52, 63).
- [Zha+11] L. Zhang et al. “Robust non-negative matrix factorization”. In: *Frontiers of Electrical and Electronic Engineering in China* 6.2 (2011), pp. 192–200 (cit. on p. 55).
- [Zho+02] Y. Zhou et al. “Improved Parametric Image Generation Using Spatial-Temporal Analysis of Dynamic PET Studies”. In: *NeuroImage*. Vol. 15. 2002, pp. 697–707 (cit. on p. 34).
- [ZP09] M. Zortea and A. Plaza. “A Quantitative and Comparative Analysis of Different Implementations of N-FINDR: A Fast Endmember Extraction Algorithm”. In: *IEEE Geosci. Remote Sens. Lett.* 6.4 (Oct. 2009), pp. 787–791 (cit. on p. 46).
- [Zub+94] I. G. Zubal et al. “Computerized three-dimensional segmented human anatomy”. In: *Medical Physics* 21.2 (1994), pp. 299–302 (cit. on pp. 73, 115).
- [ZXY09] Y. Zheng, X. Xie, and L. Yang. “Cooperative spectrum sensing based on blind source separation for cognitive radio”. In: *Future Information Networks, 2009. ICFIN 2009. First International Conference on.* 2009, pp. 398–402 (cit. on p. 37).